A CRYOGENIC LOW NOISE AMPLIFIER FOR FOURIER TRANSFORM MASS SPECTROMETRY

RAMAN MATHUR

Dissertation submitted in partial fulfillment
of the requirements for the degree of
Doctor of Philosophy

BOSTON UNIVERSITY

BOSTON UNIVERSITY

COLLEGE OF ENGINEERING

Dissertation

A CRYOGENIC LOW NOISE AMPLIFIER FOR FOURIER TRANSFORM MASS SPECTROMETRY

by

RAMAN MATHUR

M.S., Boston University, 2003

Submitted in partial fulfillment of the

requirements for the degree of

Doctor of Philosophy

2008

Approved by

First Reader

Peter B. O'Connor, Ph.D.
Professor of Electrical and Computer Engineering and
Research Associate Professor of Department of Biochemistry

Second Reader

Ronald W. Knepper, Ph.D.
Professor of Electrical and Computer Engineering

Third Reader

Mark Horenstein, Ph.D.
Professor of Electrical and Computer Engineering

Fourth Reader

Enrico Bellotti, Ph.D.
Professor of Electrical and Computer Engineering

Acknowledgments

I would like to thank my advisor, Dr. Peter B. O'Connor for his guidance and support. He taught me how to apply my knowledge of electrical engineering to build real-working circuits. The valuable time he spent on me explaining mass spectrometry and instrumentation is greatly appreciated. His ever lasting patience and dedication while working on Cryogenic FTMS during weekends and nights, gave all of us an example to follow. He is the one who instigated me to put effort in learning chemistry and biology (consisting of C60 and Ubiquitin). His pool lessons have made me a better player and a beer lover. It is a privilege to be his student and a great honor to work on his creation, the Cryogenic FTMS.

I would also like to thank my Co-Advisor Dr. Ronald W. Knepper. He was always keen on helping me solve problems which came during my projects. His support and suggestions is the only reason i could finish my dissertation. Dr. Knepper has been always available to discuss research ideas and reviewing my papers.

Besides my academic advisors, I want to acknowledge my committee members, Dr. Mark Horenstein and Dr. Enrico Bellotti for their encouragement and time. Dr. Bellotti has helped me to conduct noise measurements for the low noise amplifiers and Dr. Horenstein's advice to resolve oscillations in the preamplifier was invaluable. I would also like to thank Dr. Cathy Costello for her generous support. Here I would acknowledge Dr. Alan Rockwood and Dr. Saikat Ray for numerous useful discussions during the course of my Phd. Dr. Rockwood shared his ideas regarding the preamplifier design for ICR and contributed greatly to my dissertation. I would like to thank Dr. Randall Kirschman, Dr. D. V. Camin, Carl Ijames, and Dr. Heinrich Kochling for their valuable suggestions for low temperature and high frequency preamplifier design.

The assistance of Dr. Cheng Lin and Konstantine Aizikov in the design, construction and testing of the cryogenic instrument is greatly appreciated. Support and help from all my current and former colleagues at Boston university, Dr. Jason Pittman, Dr. Bogdan

Budnik, Dr. Vera Ivleva, Jason Cournoyer, Dr. Parminder Kaur, Dr. Cheng Zhao, Dr. Chunxiang Yao, Li Xiaojuan, Nadezda Sargaeva, Michael Bowman, Mark McComb, David Perlman, Jia Chen, and Terry Lin is greatly appreciated. I thank Carly Marchioni, Kirsten Levy, Denise Neves, and Patricia Bullock for their help in taking care of administrative issues. I thank Dr. Steve Beu, Dr. Gerald Gabrielse, Dr. Ron M. A. Heeren, Dr. Chris Hendrickson, and Dr. Lutz Schweikhard for valuable comments, Adam Berryhill and Mike Coffey for the magnet design and operation, and Boston University Scientific Instruments Facility for building critical components for the instrument.

I want to thank my parents whom I love the most, they have always been supportive and caring. I acknowledge my sister's and brother-in-law's (Meetu & Amit) support, who have been my personal advisor and guardians in Boston, and gave me a home away from home. I am indebted to my sister Dr. Ritika Mathur and my brother-in-law Dr. Ramnik Mathur, and dear Anushka for caring for me at all times. Dr. Hua Huang's support and friendship have been very important. I greatly appreciate the advice and guidance I received from her.

Finally, I would like to thank National Institute of Health, National Council for Research Resources, (Grant No. P41RR10888), the National Heart Lung and Blood Institute (N01HV28178), and MDS-Sciex for supporting my work.

A CRYOGENIC LOW NOISE AMPLIFIER FOR FOURIER TRANSFORM MASS SPECTROMETRY

(Order No.)

RAMAN MATHUR

Boston University, College of Engineering, 2008

Major Professor: Dr. Peter B. O'Connor, Ph.D.,
Department of Biochemistry,
Department of Electrical and Computer Engineering

ABSTRACT

Recent success of proteomics, which involves study of cellular proteins, in developing drugs to counteract life threatening diseases has illustrated its significance in clinical applications. The complexity and low abundance of proteins necessitates the use of sensitive techniques such as mass spectrometry for these proteomic experiments. Among several kind of mass spectrometers, the Fourier transform mass spectrometer (FTMS) has emerged as an instrument of choice for biological studies due to its combination of flexibility, high mass accuracy, superior mass resolution, sensitivity, and wide dynamic range. Furthermore, an FTMS that can reliably detect the presence of a single ion with unit charge in a sample can potentially revolutionize proteomics, and consequently our ability to discover new protein based drugs. One way of detecting single ions with unit charge is operating the FTMS at ultra-low temperature where its detection capability would be enhanced substantially. One of the main challenges towards achieving this goal is designing a electronic system (especially a low noise, wide-band, high gain amplifier) that can work at cryogenic temperatures (4 Kelvin).

At Boston University School of Medicine we are developing a unique cryogenic Fourier transform mass spectrometer with a 14 Tesla actively shielded superconducting magnet.

This design has the FTMS constructed inside the vertical cold bore of a superconducting magnet to have dramatic advantages in effective magnetic field, noise figures, and base pressure over current commercially available FTMS systems. The vacuum system cooled to 4 Kelvin cryopumps itself, dropping the pressures to less than 10^{-10} mbar. The development of the cryogenic FTMS provides an opportunity to improve the detection electronics of an FTMS by cooling the preamplifier to reduce the thermal noise in the circuit. In this dissertation we present the challenges involved in the design of such a cryogenic preamplifier and how we have solved them.

We have designed and built a GaAs MESFET-based amplifier for cryogenic FTMS. The preamplifier has a voltage gain of 250 with -3db roll off at 850 kHz. The cryogenic preamplifier circuit has shown about 20 times improvement in SNR, over the room temperature version. Several electronic components which are required for ion transfer and manipulation in Cryogenic FTICRMS were also developed here.

Contents

List of Tables

List of Figures

List of Abbreviations

FTMS	....	Fourier Tranform Mass Spectrometer
FTICRMS	....	Fourier Transform Ion Cyclotron Resonance Mass Spectrometry
FWHM	....	Full-Width at Half Maximum
ICR	....	Ion Cyclotron Resonance
FET	....	Field Effect Transistor
ADC	....	Analog to digital Converter
ESI	....	Electrospray Ionization
MALDI	....	Matrix-Assisted Laser Desorption/Ionization
PXI	....	PCI eXtensions for Instrumentation
ESD	....	Electrostatic Discharge
RF	....	Radio Frequency
SNR	....	Signal-to-Noise Ratio

Chapter 1

Introduction

The study of cellular proteins, specifically, how they interact with one another, is believed to hold the keys for discovering drugs to combat today's incurable diseases (Warrick et al., 1999; Dobson, 1999; Thomas et al., 1995; Kelly, 1998). Protein analysis, which involves characterizing protein structure, functionality and behavior in different environments, as well as cataloging them, is a fundamental step towards achieving this goal (Smith et al., 1991; Stadtman and Berlett, 1998).

However, the studies of cellular proteins pose significant challenges due to the high degree of complexity of cellular proteome, and due to the low abundance of many of the proteins, which necessitates highly sensitive analytical techniques (Aebersold and Mann, 2003). Various methods of protein analysis have been proposed in the literature, such as, mass spectrometry, two-dimensional gel electrophoresis, high performance liquid chromatography, infrared spectroscopy, etc (Tonge et al., 2001; Shen et al., 2001; Harry et al., 2000; Lee and Lee, 2004; Smith, 2000). Among these technologies, mass spectrometry has established itself as an indispensable tool for identifying proteins and significant other subsets of biological molecules (Aebersold and Mann, 2003; Nettleton et al., 1998; Reinders et al., 2004; Qian et al., 2006; Shen and Smith, 2000; Shen et al., 2000). It provides a rapid and reliable way to quantitate a large number of proteins (Neubauer et al., 1997; Jensen et al., 1997). The ease of coupling mass spectrometry with other separation techniques multiplies the information which can be obtained about complex molecular pathways within a relatively small time duration (Shen et al., 2001; Belov et al., 2004; Henzel et al., 1993; Martinovic et al., 2000; Gao et al., 2000).

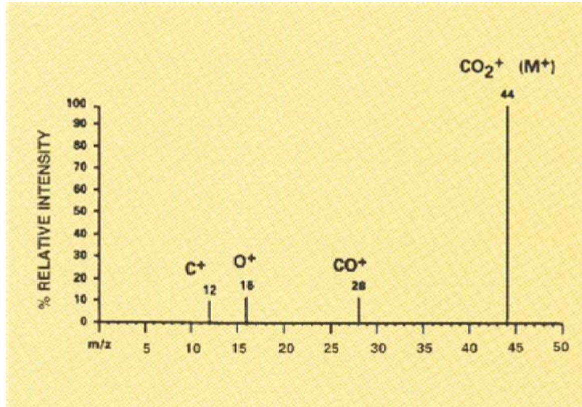

Figure 1·1: A Mass Spectrum of CO_2 (ASMS, 2005)

A mass spectrometer measures the mass to charge ratio (m/z) of an ion of a given substance. Then, by knowing the charge of the ion, its mass can be determined (McLafferty and Turecek, 1993; Horn et al., 2000). Fig 1·1 shows a typical mass spectrum of a CO_2 molecule. In this figure, the horizontal axis shows the m/z and the vertical axis shows the intensity of the ion with the given m/z. For example, in Fig. 1·1, the ion at $m/z = 44$ Da [1] is a CO_2 ion with a single charge.

Another important advantage of a mass spectrometer is that tiny amounts (10^{-12} to 10^{-18} grams) of sample are sufficient to detect many compounds (Wilm et al., 1996; Valaskovic et al., 1995; Beavis and Chait, 1990). Thus, low abundant proteins can be detected using most modern mass spectrometers. [2]

There are several types of mass spectrometers available such as, Time of Flight Mass Spectrometer (Cotter, 1997), Quadrupole Mass Spectrometer (March and Todd, 2005), Fourier Transform Ion Cyclotron Resonance Mass Spectrometer (Marshall and Comisarow, 1974). Each of these existing mass spectrometers has its own advantages and disadvantages. However, recently the Fourier Transform Ion Cyclotron Resonance Mass Spectrometer (in

[1] Dalton (Da), is a unit of mass and is equal to 1/12 of the mass of most abundant isotope of carbon (C^{12}).

[2] In mixtures of proteins it is often difficult to detect such small amounts, when there are other ions from abundant impurities or other proteins, necessitating chromatographic seperation.

short FTICRMS) has emerged as the popular choice for biological samples due to its high mass accuracy, high resolution and wide dynamic range (Marshall and Comisarow, 1974; Comisarow and Marshall, 1974; Comisarow and Marshall, 1976; Shen et al., 2000; Martinovic et al., 2000; Maier et al., 2000; Bruce et al., 2000).

One important performance measure of an FTICRMS is its sensitivity. The sensitivity of the FTICRMS mass analyzer can also be expressed in terms of limit of detection, the lowest number of molecular ions that can be detected. Limit of detection as defined by Limbach et. al. (Limbach et al., 1993) is *the minimum number of ions, in a single scan, required to produce a signal whose FT magnitude-mode peak height is 3 times the noise level for a 1-s observation period of an ICR time-domain signal whose exponential decay time constant is at least 10s, for ions at an initial average postexcitation ICR orbital radius of half the maximum allowed radius.* Thus, the lower the detection limit, the better the sensitivity of the mass analyzer. Currently, the best case detection limit in FTICRMS is approximately 30 charges (Anderson et al., 1995). By improving the sensitivity of FTICRMS, we can further reduce the number of ions required to determine the mass of a protein accurately. Again, this allows us to identify low abundant proteins, which often have important biological significance. Of course, the best that can be done is to detect a single ion with unity charge. This level of sensitivity is referred to as *unit charge detection sensitivity*. If we can achieve unit charge detection sensitivity, then we can:

- Increase the dynamic range [3] of the FTMS.
- Improve the mass accuracy of the FTMS from 1 parts per million (ppm) to ≈1 parts per billion (ppb) (Difilippo et al., 1995).

However, there are many obstacles, which currently prevent achieving unit charge detection sensitivity in an FTMS. These primary limiting factors are the different sources of noise

[3] Dynamic range of an FTMS is defined as the ratio of the least and most abundant species which the FTMS can detect in a single scan.

(chemical or electrical) which makes it difficult to discern the signal from a single charge in an FTMS.

The first and most common noise source is “chemical noise”, which is a real ion signal from unwanted sample contaminants. Many techniques have been proposed in literature to control the chemical noise in FTMS (Krutchinsky and Chait, 2002; Ramsey et al., 1993). These techniques include better sample preparation, use of a heated metal capillary, etc. Using such methods, chemical noise can be reduced to a negligible level.

Electronic noise is related to the various components which are used for signal detection in an FTMS. Also, interference in FTMS can be reduced by using proper shielding and grounding techniques. Thermal noise is intrinsic to electrical devices (Johnson, 1928). Thermal noise can only be reduced by cooling the electrical circuit as close as to 0 K as possible. In conventional FTMS, cooling the electrical circuit turns out to be difficult, since a convenient thermal conductive path cannot be established between the coolant (liquid helium) and the electrical circuit, which is normally is situated in vacuum. However, recently O’Connor have designed an FTMS in which the complete FTICRMS mass analyzer will be cooled to 4 K using liquid helium to reduce the base pressure (O’Connor, 2002). This new FTMS presents us an opportunity for reducing the thermal noise using cryogenic electrical circuits. This research is directed towards achieving this goal.

In an FTMS, the primary electrical circuit is an amplifier that amplifies the very weak raw signal (Comisarow, 1978). In this research, our objective has been to build an amplifier that satisfies the following design constraints. The bandwidth of interest in the unamplified output signal from an FTMS is about 1 MHz and the signal has a typical amplitude of a few pA. Thus, the amplifier is required to have a transimpedance gain of approximately $10^9\Omega$ and a bandwidth of 1 MHz.

In our preliminary work, in order to gain experience and identify design challenges, we first designed two room temperature amplifier circuits. We built these amplifiers using low noise Junction Field Effect Transistors (JFETs) at the input stage connected in a cascode configuration, and Bipolar Junction Transistors (BJTs) in the later stages.

We characterized various aspects of our amplifier designs by conducting a series of tests on a test-bench. Moreover, we compared these designs with an existing commercial amplifier in terms of (i) gain, (ii) power consumption, (iii) noise, and (iv) bandwidth performance.

The room temperature amplifiers cannot work at cryogenic temperatures since these amplifiers are made of silicon based transistors, and carriers freeze at 4 K in silicon (Kirschman et al., 1992). Thus, after these preliminary investigations, we continued our work towards building an amplifier that can work at 4 K. Towards this end, we chose GaAs based Metal Semiconductor Field Effect Transistors (MESFETs) (Lilienfeld, 1930; Weinreb, 1980; Weinreb et al., 1982; Prance et al., 1982). Active devices made from GaAs can operate at cryogenic temperatures without carrier freeze-out (Keyes, 1977). In addition, GaAs MESFETs have very low gate to drain capacitance (C_{gd}=20 fF), which reduces the need for the use of a cascode pair at the input. We have designed and built a GaAs MESFET-based amplifier for cryogenic FTMS. The cryogenic amplifier has been tested and compared with the room temperature designs.

We have also designed a cryostat—a double-lined container used for holding the electrical circuit at a fixed, low temperature maximizing the radiative and conductive heat flow from the circuit to the coolant.

A printed circuit board design methodology for high power circuits was developed. Using the same technique, a PCB was developed for an RF oscillator circuit which can be used to drive multipole ion guides in an FTMS.

Finally several printed circuit board designs are presented which were fabricated for cryogenic FTMS. These PCBs branch out the analog and digital voltages from PXI cards to be connected conveniently to the ion optics and also implements ESD and over voltage protection circuits.

Chapter 2

Background

In this section we review some of the background material as well as survey the literature that is related to this research. Specifically, we describe the operation of a typical FTICRMS with the objective to establish the relation between the m/z ratio of the ions present in a sample and the frequency spectrum of the electrical signal provided by the instrument. The advantages and challenges involved in the design of the cryogenic Fourier transform mass spectrometer are also presented.

2.1 Fourier Transform Ion Cyclotron Resonance Mass Spectrometer

A Fourier Transform Ion Cyclotron Resonance Mass Spectrometer (FTICRMS) block diagram is shown in Fig. 2·1. Primarily, it consists of (i) an ion source, (ii) an ion guide, (iii) a mass analyzer, which is also called an Ion Cyclotron Resonance (ICR) cell, and (iv) a superconducting magnet surrounding the ICR cell. The samples are placed in the ion source and ionized. Then, these ionized samples are transferred to the ICR cell using ion guides. Finally, the m/z ratio of these ions are determined in the ICR cells which is placed in a uniform magnetic field with intensity B.

The ICR cell consists of three pairs of electrodes (plates) as shown in Fig. 2·2. Two pairs among these electrodes are placed parallel to the magnetic field B. The first pair is called the excitation electrodes and the second pair is called the detection electrodes. The third electrode pair placed perpendicular to the magnetic field is called the trapping plates. The magnetic field confines the motion of the ions to the xy plane. The motion of ions in the z direction is controlled by the trapping plates. Note that, these plates act like a capacitor and typically have 10-30 pF of capacitance to ground.

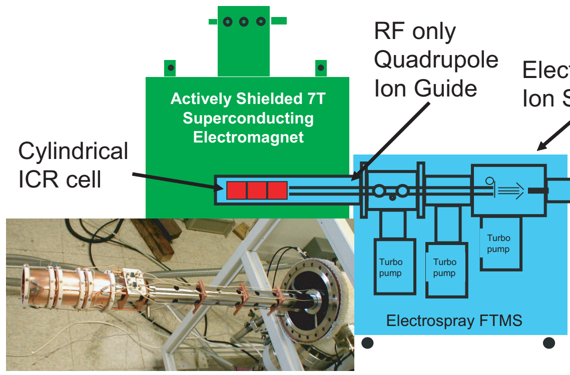

Figure 2·1: A Fourier Transform Mass Spectrometer

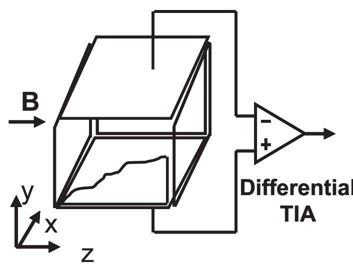

Figure 2·2: An Ion Cyclotron Resonance Cell (Marshall et al., 1998)

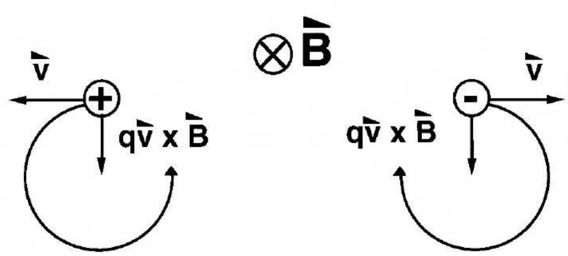

Figure 2·3: Ion Cyclotron Resonance (Marshall et al., 1998)

The FTMS operation is based on *Ion Cyclotron Resonance* (Lawrence and Livingston, 1932), from where it derives its complete name, *Fourier Transform Ion Cyclotron Resonance Mass Spectrometer*. An ion of mass m and charge q, moving in a uniform magnetic field B, experiences the Lorentz force F, $\vec{F} = q\,(\vec{v} \times \vec{B})$, perpendicular to the direction of motion of the ion and the magnetic field. As shown in Fig. 2·3, the Lorentz force rotates the ion in circular orbits perpendicular to B. This circular motion of ions is called the *cyclotron motion*, and the frequency of rotation of ions, ω_c, is called the *cyclotron frequency*. The cyclotron frequency of the ions with mass to charge ratio m/z is given by [1],

$$\omega_c = \frac{qB}{m} \tag{2.1}$$

In FTICRMS, the ions of general interest with m/z 100 to 10 kDa have cyclotron frequency for a 7 Tesla magnetic field ranging from 1 MHz to 10 kHz. This frequency range lies in the AM radio band of the electromagnetic spectrum. Thus the electronic components which are needed for FTMS are readily available off-the-shelf, making assembly of an FTMS system in principle, quite simple (Beu and Laude, 1991).

A typical FTMS experimental sequence is initiated by first transferring the ions from the source to the cell. The transferred ions are trapped in the ICR cell along the z-axis in which they undergo low amplitude, thermal, non-coherent cyclotron motion due to the applied magnetic field. Then, a sinusoidal oscillating potential is applied across the excitation electrodes, which form a roughly spatially uniform electric field in the x-y plane. The ions with cyclotron frequency equal to that of the excitation electric field absorb energy and spiral up into a large ($>$ 1 cm radius) cyclotron orbit. The excitation field is then switched off. The excited ions continue to precess at their final cyclotron orbital radius. The periodic cyclotron motion of the ions in the ICR cell induces a resonant sinusoidal image current on the detection electrodes with frequency equal to the cyclotron frequency

[1] Relation between m/z and cyclotron frequency in Eq. 2.1 is exact only in the absence of any electrostatic field.

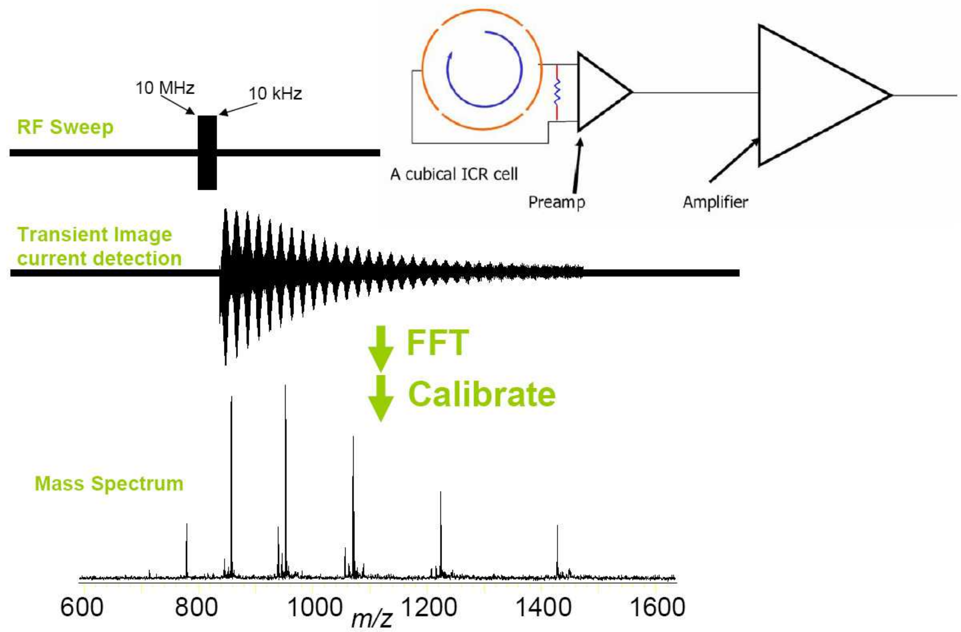

Figure 2·4: FTMS Signal Generation

of the ion packet. This current is amplified, digitized, and stored in computer memory. The Fast fourier transform of the detected signal gives the frequency spectra which is then calibrated to yield the mass spectrum of the sample ions (Fourier, 1878), Fig. 2·4, using Eq. 2.1.

In FTMS all the ions are excited at once by an application of an RF sweep voltage. And the detection is performed by a broadband amplifier which amplifies all the spectral components during the period of detection. This feature in FTMS termed as Fell gett advantage provides FTMS higher signal to noise ratio. The higher resolution and mass accuracy, which are distinct advantages in FTMS compared to other scanning type mass spectrometers, are due to several reasons:

- Mass resolving power of a mass spectrometer is defined by the peak width at half the maximum height. For an FTMS it is calculated by Eq. 2.2;

$$ResolvingPower = \frac{m}{\Delta m_{FWHM}} \tag{2.2}$$

where, Δm_{FWHM} is the full width of the peak at half maximum. The mass resolution in most mass spectrometers such as TOF MS is limited by the spread in the kinetic energy of the ions. However from Eq. 2.1, in FTMS, ions with the same m/z rotate at the same cyclotron frequency independent of their kinetic energy. Thus the width of the peak is not defined by the kinetic energy spread of the ions.

- In FTMS, the m/z of ions manifests as frequency peaks in the spectrum. And as frequency can be measured more accurately than any other physical quantity such as voltage, this provides higher mass accuracy in FTMS than other forms of mass measurements. The accuracy with which the frequency can be measured is governed by the classical uncertainty principle, i.e. the uncertainty in frequency is inversely proportional to the observation time. The finite peak width or the mass resolution in a MS obtained with FTMS is thus limited by the duration of the ion observation time. This duration is principally limited by the background pressure as discussed below.

- From Eq. 2.1, the cyclotron frequency of the ions only depends on their m/z and B. The stability of B which is the magnetic field of a superconducting magnet is typically $\ll$ 10 ppb during the length of an ICR detection. Thus unlike magnetic sector instruments where magnetic field is scanned/ramped for detection of ions of different m/z, in an FTMS a superconducting magnet with superior field stability provides mass spectra with higher resolution.

One of the major differences between FTICRMS and other mass spectrometers is its method of non destructive detection of ions. In ICR experiments the ion packets which are excited to rotate in cyclotron orbits collide with background neutrals, while they are being detected, and lose their kinetic energy which is given by Eq. 2.3.

$$
\begin{aligned}
K.E. &= \frac{1}{2}mv^2 && (2.3)\\
&= \frac{1}{2}\frac{q^2B^2r^2}{m} && (2.4)
\end{aligned}
$$

As the ions lose energy, their cyclotron radius decreases and they slowly spiral to the center of the ICR cell. As the ions come back to the center they are too far from the detection plates to induce any image charge. This loss of ICR signal with time due to decay in the orbital radius depends on the pressure in the ICR cell. Thus ultra high vacuum is required in the ICR cell to achieve longer detection times which ultimately improves SNR and mass resolution. Once the ions cool back to the center of the ICR cell, these ions can be excited again by an RF sweep and detected again. Remeasurement and accumulating multiple detection scans (say N scans), improve the signal to noise ratio by a factor of $\sqrt{N}$ (Pitsenberger et al., 1996). In this non destructive detection scheme, the ions are not lost during detection, they can also be be used to conduct fragmentation studies (MSn); this would be discussed further.

Besides these distinguishing characteristics of FTICRMS, one of the main reasons they are not ubiquitous in mass spectrometry is their cost. This is primarily due to the necessity of the high field superconducting magnet for ICR. Wires which are used to wind coils for these superconducting magnet are made of a special alloy of niobium-titanium or niobium-tin. These wires and the low temperature epoxy which is used to hold these wires in place around the magnet core, makes these magnets expensive [2]. However, the engineering aspects in magnet design are continuously evolving to make higher field magnets available at lower cost/Tesla. More importantly, the development of the cryogenic FTMS, with narrower bore diameter magnet, have addressed this issue to an extent (O'Connor, 2002; Lin et al., 2007).

[2] A 7 Tesla superconducting magnet with 6 in room temperature bore costs around 100,000 US$ (2005)

2.2 Cryogenic Fourier Transform Ion Cyclotron Mass Spectrometer

As mentioned in the previous section, FTICRMS performance in terms of mass resolution and mass accuracy is far superior compared to other mass spectrometers. The highest resolving power of 8,000,000 has been reported in literature on an FTICRMS with a 9.4 Tesla superconducting magnet (Shi et al., 1998). On FTICRMS mass accuracy of 1 ppm are routinely attainable (Easterling et al., 1999), with a best case of 0.1 ppb (Gabrielse et al., 1990a). Sensitivity of the FTMS mass analyzer is more appropriately defined by the limit of detection (Limbach et al., 1993), and is typically equal to 100 charges (Anderson et al., 1995). These results reported in literature do not match to the fundamental performance limit which can be achieved with an FTICRMS. Since the advent of FTICRMS (Marshall and Comisarow, 1974) there has been a continuous considerable effort to push these numbers higher.

The primary fundamental limiting factors in an FTICRMS are:

- Magnetic field strength of the superconducting magnet.
- Pressure in the ICR cell region.
- Equivalent input noise of the detection amplifier.

It is important to realize here that the performance parameters are significantly improved by increasing the magnetic field strength in an FTICRMS (Marshall and Guan, 1996). Or in other words the fundamental limiting factors which are mentioned above are relaxed to a great extent in FTICRMS with higher magnetic fields. Merely doubling the magnetic field results in simultaneous improvement in several parameters: resolution (2x), mass accuracy (2x), sensitivity (2x), and dynamic range (2x), and space charge limit (4x) (Marshall and Guan, 1996).

However as the magnets are designed with higher field strengths, the cost/Tesla increases quadratically (or more) with field. This is primarily due to the increase in the

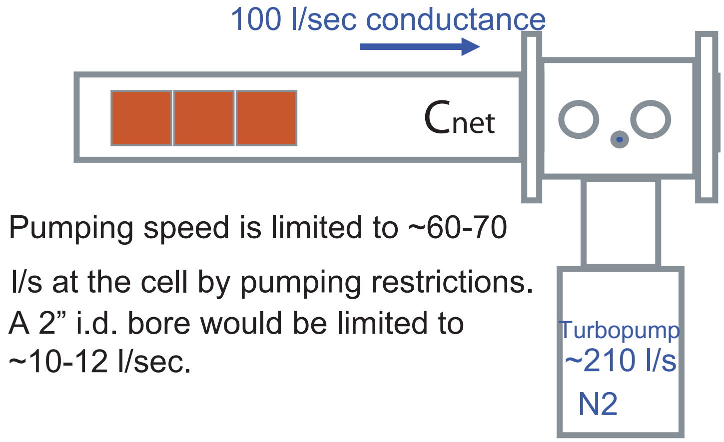

Figure 2·5: Bore Tube Diameter limitation

length of the wire wound for the magnet coil. One approach to decrease the length of the wire used for winding is by reducing the bore diameter of the magnet. Conventional actively shielded 7 Tesla room temperature magnets for FTICRMS have room temperature bore of 15.24 cm and cost around US$ 100k. A 14 Tesla magnet with 15.24 bore will cost around US$1M and a proposed 21 Tesla would cost more than US$15M. Less expensive high field magnets such as 21 Tesla, 900 MHz superconducting magnet, with smaller bore diameter are available and used for nuclear magnetic resonance experiments. Although NMR magnets satisfy the magnetic field homogeneity requirement, their smaller bore limits the ultra high vacuum performance which is required in the FTMS, discussed below.

2.2.1 Bore Tube Diameter Trade-off

The block diagram of a traditional FTICRMS was shown in Fig. 2·1. The FTMS mass analyzer, the ICR cell, and ion transfer optics are enclosed inside a titanium tube which is inserted into the bore of the superconducting magnet.

To attain ultra high vacuum (less than 1×10^{-9} mbar) in the ICR cell region, the vacuum system is pumped by turbo molecular pumps which are at the other end of this tube, outside the magnet as shown in Fig. 2·5. The pressure in the cell is, therefore, partially defined by the pumping speed in the cell region, S_{net}. If we assume the conductance of the tube of length L and i.d. D (cm), is equal to C (L/s) and the pumping speed of the turbo molecular pump is S_{pump} (L/s), then S_{net} (L/s) can be calculated by Eq. 2.5 and Eq. 2.6 (Moore et al., 2002).

$$C = 12\frac{D^3}{L} \tag{2.5}$$

$$\frac{1}{S_{net}} = \frac{1}{C} + \frac{1}{S_{pump}} \tag{2.6}$$

For an NMR magnet with a bore diameter of 25 mm, the conductance of the ion optics tube of length 0.5 m is 3.75 L/s. With a turbo pump placed at the end of the tube with S_{pump} = 210 L/s, the achieved S_{net} is equal to 3.68 L/s. It is clear that the base pressure at the cell region will be limited by the gas conductance of the tube. No matter how powerful is the turbo pump, it would be difficult to attain higher pumping speed, unless the tube diameter is increased. However a bigger tube requires a larger magnet bore diameter, increasing the cost of the magnet. This pumping speed is also limited because of the presence of the ion optics and wires which reduces the effective diameter of the tube. Moreover the out gassing of the ion optics and inner surface of the tube makes it difficult to attain base pressures below 1×10^{-9} mbar.

Thus in FTICRMS there is a trade-off for the size of the magnet bore - a larger bore is desired to improve the pumping speed but a small bore allows use of high field superconducting magnets which are easier to design at lower cost.

However if the FTMS is constructed inside the cold bore of the superconducting magnet and chilled to 4 K, the ion optics and surfaces inside the vacuum start cryopumping. The gases which are present in the vacuum system condense on these surfaces, reducing pressures to very low values. Cryopumps have been used to obtain high pumping speeds on the order of 10^5 L/s in room temperature FTMS systems (Winger et al., 1993). Also single particle physics experiment are regularly performed in Penning traps which are cooled cryogenically in cold bore magnets and achieve base pressures below 1×10^{-16} mbar in a narrow bore magnet (Gabrielse et al., 1990b). Thus construction of FTMS inside the cold bore of a superconducting magnet eliminates the bore diameter trade-off.

2.2.2 Advantages of Cryogenic FTICRMS

Once the bore diameter trade-off is eliminated in the FTMS, the superconducting magnet can be designed with smaller (currently available) bore diameter and much lower cost. The various advantages which are associated with the development of the cryogenic FTICRMS are enumerated below,

- 10^2–10^3 fold improvement in base pressure and pumping speed due to the cryopumping of the FTMS system.
- The narrower cold bore allows the use of high field superconducting magnets, up to 21 Tesla with current magnet technology, increasing mass resolving power, mass accuracy, sensitivity and dynamic range of FTMS.
- The detection preamplifier can be mounted on the ICR cell which is chilled to 4 K, thus reducing the thermal noise in its components. This improves the limit of detection of the FTMS mass analyzer.

2.2.3 Challenges in the design of the Cryogenic FTMS

However, there are several design issues involving the superconducting magnet as well as FTMS system, which have to be solved in the development of the cryogenic FTICRMS. These challenges are discussed below and the ways in which they were overcome prior/during the development of this instrument are also described here.

Heat Load (helium boil-off)

– Insertion of the FTMS inside the cold bore of the superconducting magnet will add significant heat load on the cryogenic dewar. Liquid helium which is used a cryogen for cooling superconducting magnets, is always limited in supply, and is relatively expensive. This requires extensive and careful design optimization to reduce the heat load as low as possible. The three modes of heat transfer are conduction, radiation, and convection. The magnet dewar is a two stage dewar, one stage is at 40 K and the other is at 4 K. This requires the calculation of heat load in two steps, once from 300 K to 40 K and then from 40 K to 4 K. The total heat load on the magnet dewar at 4 K can be calculated by Eq. 2.7. The convective heat transfer by background gas inside the FTMS insert can be neglected as convection requires mass transfer and cryo-pumping prevent it by making it a UHV system.

$$\dot{Q}_{net} = \dot{Q}_{conductive} + \dot{Q}_{convective} + \dot{Q}_{radiative} + \dot{Q}_{dewar} \tag{2.7}$$

- Conductive heat load ($\dot{Q}_{conductive}$) – This is primarily caused by the ion optics enclosure tube, transfer hexapole, and connecting wires. Using Eq. 2.8, we can estimate the conductive heat transfer, $\dot{Q}$ due to each of these components.

$$\dot{Q} = k(T)A\frac{\delta T}{\delta x} \tag{2.8}$$

  where, $k(T)$ is the heat transfer coefficient, A is the cross-sectional area, and $\delta T/\delta x$ is the temperature gradient. The calculation for conductive heat load becomes cumbersome as the heat transfer coefficient, $k(T)$, for all metals is not constant from 4 K to 300 K. However, empirical values of thermal conductivity in a form of a plot or a table are available. Thermal integrals for some of the materials are shown in Table 2.1 (Instruments, 2000). Then Eq. 2.9, can be used to estimate the heat load.

$$\dot{Q} = \frac{A}{L}\int K(T)\delta T \tag{2.9}$$

  where, A is the cross sectional area, and L is the length.

  1. Stainless steel enclosure tube – The current design uses 0.9 mm thick, 7.6 cm

Table 2.1: Thermal Conductivity Integrals

Material	300 K to 0 K	77 K to 0 K
Stainless Steel	30	3.2
Copper	1620	690
G10 (fiberglass	1.5	0.17

o.d., 78 cm long stainless steel tube. The conductive heat load due to this tube is around 0.23 W. Current modifications are underway to reduce the o.d. of this tube to 2.5 cm and thickness to 0.5 mm, which will drop the heat load to 0.04 W.

2. Transfer hexapole – Hollow titanium rods which are 0.8 mm wall thickness and 0.125 o.d. have been used for construction of the transmission hexapole. The net heat load due to six rods is around 0.012 W.

3. Connecting wire – Phosphorus bronze alloy wire is used to carry electrical signals to/for from the ICR cell. This wire which is 1 mm thick, has very low thermal conductivity coefficient and 12 of these wire add only 0.016 W of heat load.

Therefore, the total conductive heat load, $\dot{Q}_{conductive} = 0.068$ W (with new tube), and 0.258 W (with current tube design).

- Radiative heat load ($\dot{Q}_{radiative}$) – Radiative heat load depends on the emissivity and area of the hot and cold surfaces and calculated by the following equation.

$$\dot{Q}_{radiative} = \sigma\epsilon_2 A {T_2}^4 - \sigma\epsilon_1 A {T_1}^4 \tag{2.10}$$

where, σ is the Stefan-Boltzman constant (5.67×10^{-8}), and A_1, A_2 and T_1, T_2 are the areas (m^2) and temperature (K) of the two surfaces, respectively.

Radiative heat load in magnet dewar design is minimized by mirror polishing the metal surfaces. However the line of sight from the source at 300 K to the ICR cell at

4 K can add significant radiative heat load. To minimize this, polished copper discs (baffles) have been added along the bore tube to reflect IR radiation (especially from the source). These baffles have been staggered, to eliminate line of sight except at the ion optical axis. This has reduced the radiative heat load, $\dot{Q}_{radiative}$ to less than 1 mW.

- Magnet Dewar heat load ($\dot{Q}_{dewar}$)– This has been estimated to be around 0.042 W on a 7 Tesla magnet with room temperature bore.

Thus using Eq. 2.7, the net heat load on the cryogen at 4 K is around, 100 mW. This corresponds to a helium boil-off rate of 5 L/day. And at the current cost of $7 per liter, the annual cost of $13,000. This cost is in par with the cryogen use of the conventional room temperature superconducting FTMS instruments. However, in this design a cryo-refrigerator from Sumitomo Heavy Industries (Tokyo, Japan) is included to compensate for the heat load on the cryogen. The cryo-refrigerator has 2 stages, 1st (≈50 K) stage and another 2nd stage (≈4 K), which are connected thermally to the 2 inner magnet Dewars. The cryo-refrigerator provides a cooling power of 80 W at 77 K stage and 1.5 W at 4 K stage. High cooling capacity of the 1st stage allows interception of the heat transferred from the room temperature components (300 K) to the 40 K stage in the design with the provided thermal anchors.

The cooling capacity of the cryo-refrigerator thus will exceed the heat load of the system, the liquid helium boil-off will be reduced to zero, making the Cryogenic FTICRMS a zero loss system.

MS/MS

– Collisionally activated dissociation (CAD) in the ICR cell will be difficult because of the high pumping speed. However, the accumulation hexapole can be used for CAD experiments and the product ions can be sent down to FTMS for analysis as is currently done on our custon ESI-qQq FTMS (O'Connor et al., 2006). Photodissociation (either IR or UV) can be used by guiding the laser via the view port which is provides access to the ICR cell. Electron Capture Dissociation can be performed in cell by using electron beam from field emitter cathodes or photo electrons generated off a metal surface.

Cryogenic Preamplifier

– Conventional silicon based low noise transistors cannot be used due to carrier "freeze-out" below 60 K. Also generic passive components such as capacitors do not behave well at cryogenic temperatures. However GaAs FETs have been used for cryogenic applications. This is discussed in later chapters.

Physical Contraction

– Cooling from room temperature to 4 K contracts all the components to a degree depending upon their material of construction. Stainless steel which has been used for constructing vacuum tube contracts by 0.3%. The design allows sufficient flexibility in components, thus preventing any stress which can cause mechanical damage.

ICR Cell Size

– In high performance FTMS experiments requiring ultra high mass resolving power and sub ppm mass accuracy, the homogeneity of the magnetic field becomes critical. Lower field NbTi superconducting magnets with room temperature bore routinely achieve spatial field homogeneity of around 10 ppm over the cell diameter and magnetic field drift of around 10 ppb/day.

In cryogenic FTMS the bore diameter is reduced to lower the cost/Tesla. When the ions are trapped in the ICR cell sitting inside the small bore, the coulumbic repulsion between these ions can cause mass measurement errors due to space charge (Easterling et al., 1999). Thus space charge in a smaller ICR cell could become a limitation in the performance of cryogenic FTMS.

However in the current cold bore magnet design there is no insulation layer around the magnet bore which usually is up to 15 mm in thickness. Thus the ICR cell for the cryogenic FTMS has an o.d. of 7 cm to utilize the 5 cm by 5 cm homogenous magnetic field region. This cell diameter is comparable to many conventional ICR cells used with room temperature bore 7 Tesla magnets, thus not causing severe errors due to space charge. Moreover doubling the magnetic field to 14 Tesla from 7 Tesla, quadruples the ion storing capacity in the current cryogenic FTMS (Marshall and Guan, 1996).

However this design also puts the ions (while they are excited) closer to the wires of the magnet coil as compared to the room temperature bore magnet. At these ion orbits closer to the magnet coil, the discreteness in the physical spacing of these wires can potentially lead to additional field inhomogeneities. This concept has not yet been explored completely. And experiments to test this are being designed.

Connections on the ICR cell

– In FTMS having the ICR cell at room temperature, all connections are made mechanically, with wires tightened between screws and nuts. In cryogenic FTMS, after making connections at room temperature, the ICR cell is inserted into the cold bore, and chilled to 4 K. The large temperatures change results in shrinking of the screws and nuts, which resulted in unreliable, loose connections. In the current set up electrical connections were silver soldered on the ICR cell plates for reliability.

A 15-Tesla actively shielded superconducting magnet with a vertical cold bore was developed at Cryomagnetics (Oak Ridge, TN). For high performance FTMS experiments, the magnet was designed with a homogeneity of about 12 ppm over a 5×5 cm cylindrical region. A CAD drawing of the magnet is shown in Fig. 2·6. It consists of 3 concentric cylinders which are insulated from each other. The inner-most dewar acts as a reservoir to contain liquid He and also houses the magnet coils. The outer two dewars are radiation-shielded ultrahigh vacuum chambers to isolate the surrounding environment from the magnet dewar.

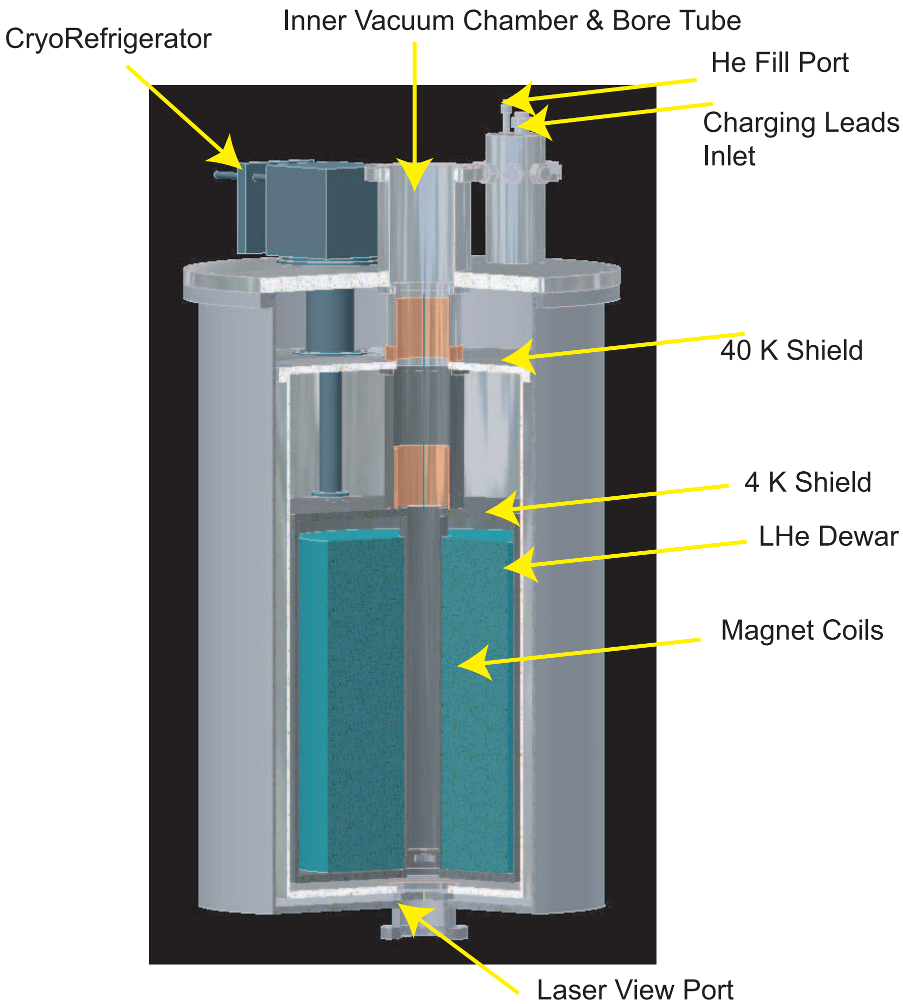

Figure 2·6: 15-Tesla Superconducting Magnet

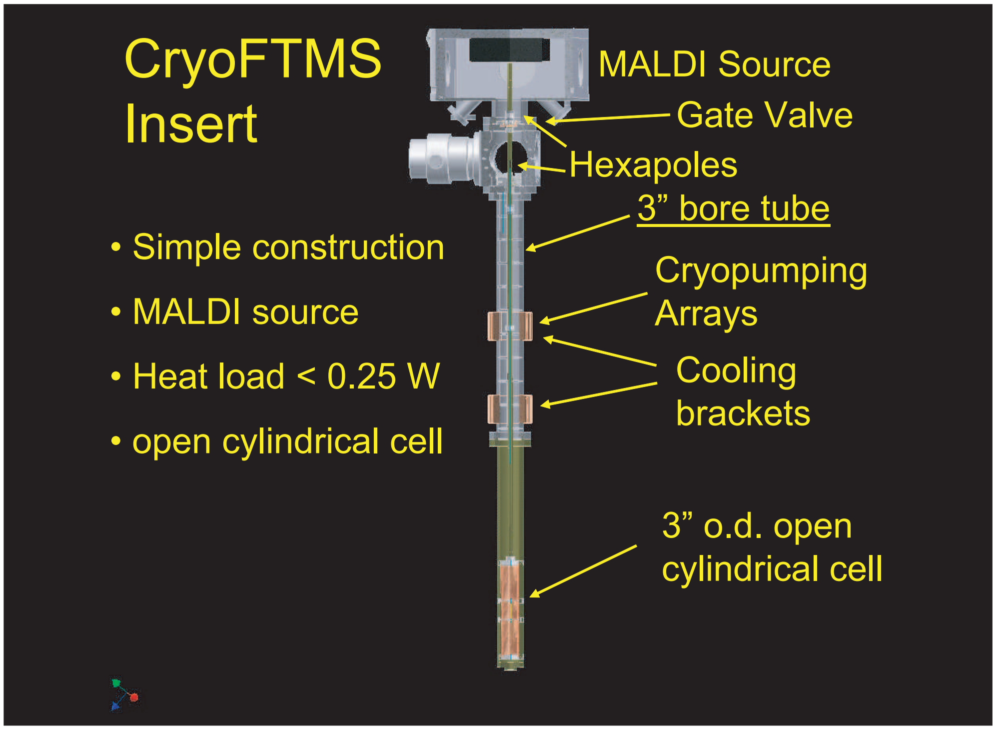

Figure 2·7: Cryogenic FTMS Insert

The FTMS consists of a MALDI source, a pair of hexapoles and an open cylindrical ICR cell. The first hexapole can be used for accumulation of ions from multiple laser shots. The second hexapoles, transmission hexapole, guide the ions from the external source to the ICR cell which sits inside the high magnetic field. A CAD drawing showing the ion optics is shown in Fig. 2·7.

The ICR cell is designed with an o.d. $\approx$ 60 mm with excite and detect plates in the homogeneous magnetic field. The complete Cryogenic FTICRMS system 3D CAD drawing is shown in Fig. 2·8. The system has been assembled, tested and undergoing continuous development at Boston University medical campus (Lin et al., 2007).

In this dissertation we present the design and development of the electronic components for the cryogenic Fourier transform mass spectrometer. We describe in detail the electronics which is used to manipulate electric potential on various ion lenses, ion guides, and ICR cell. Three key electronic circuits which are essential for the high performance of cryogenic

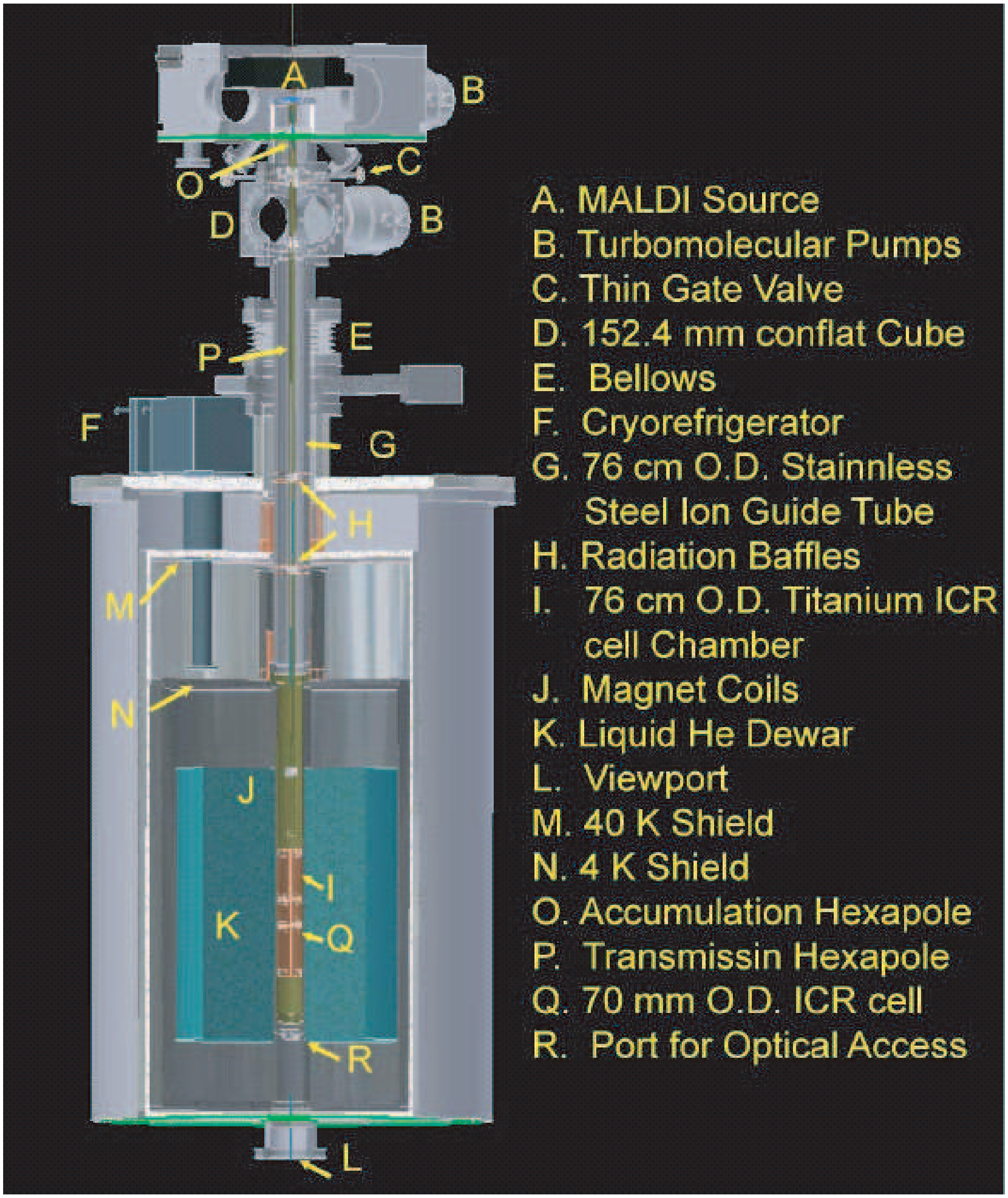

Figure 2·8: Cryogenic FTMS Cutaway View

FTMS are designed, implemented, tested in the course of this research. They are:

- Detection Preamplifier for ion signal detection.
- RF power generator PCB for driving multipole ion guides.
- Datasystem to control timing and provide analog voltages.
- Break out and protection PCBs for ESD protection of datasystem.

Chapter 3

The ICR Signal

3.1 Ion Motion in an Ion Cyclotron Resonance Cell

Equation of cyclotron frequency, Eq. 3.1, can be used to convert a frequency spectrum to mass spectrum. However this linear relation not exact for practical ICR cells used in FTMS.

$$\omega_c = \frac{qB}{m} \tag{3.1}$$

In the ICR cell, the magnetic field B, along the z axis, Fig. 2·2, restricts the motion of ions in the x-y plane. However the ions have to be trapped in the z direction, i.e. parallel to the magnetic field for sufficient time for the excite and detect events. For this purpose 2 end plates are placed at $z = \pm a/2$ to create a potential well along the z-axis. A static potential V_T, typically 1 volt, is applied to the end plates to trap the ions axially. However this trapping field has a radial component that opposes the Lorentz force from the applied magnetic field. Thus the equation of motion of ions in the presence of magnetic field and this trapping field becomes (Marshall et al., 1998),

$$F = m\omega^2 r = qB\omega r - \frac{qV_T\alpha}{a^2} r \tag{3.2}$$

Here, F is the net force on the ion in the radial direction, m/q is the mass to charge of the ion, r is the cyclotron radius, and α is a constant which depends on the trap geometry. Rearranging Eq. 3.2:

$$\omega^2 - \frac{qB\omega}{m} + \frac{qV_T\alpha}{ma^2} = 0 \tag{3.3}$$

Thus the trapping field perturbs this motion splitting this fundamental frequency into two modes which are obtained by solving the Eq. 3.3; the reduced cyclotron frequency (ω_+) and the magnetron frequency (ω_-).

$$\omega_+ = \frac{\omega_c}{2} + \sqrt{\left(\frac{\omega_c}{2}\right)^2 - \frac{\omega_z^2}{2}} \tag{3.4}$$

$$\omega_- = \frac{\omega_c}{2} - \sqrt{\left(\frac{\omega_c}{2}\right)^2 - \frac{\omega_z^2}{2}} \tag{3.5}$$

in which

$$\omega_z = \sqrt{\frac{2qV_{trap}\alpha}{ma^2}} \tag{3.6}$$

where ω_c is given by eq. 3.1, α and a are constants depending on the geometry of the ICR cell, V_{trap} is the trapping potential.

3.2 Comisarow ICR Detection Model

In the ICR cell of an FTMS, ions are excited into a coherent cyclotron orbit by the application of a resonant or swept frequency RF voltage to the excitation electrodes. These coherent, rotating packets of ions induce image charges on the detection electrodes of the ICR cell (Comisarow, 1978). The induced image current is amplified using a transimpedance amplifier. This detection amplifier is typically divided into two stages: (i) a first "preamplifier" stage, which is mounted close to the detection plates of the ICR cell to minimize the capacitance, and (ii) a second stage, "amplifier". The output of the second stage is sent to the analog-to-digital converter that samples the analog signal and stores it in a digital format. Fast Fourier transform of the digital data yields the frequency domain spectrum of the ion signal (Fourier, 1878). Finally, the frequency spectrum is converted into a mass spectrum using a calibration equation (Ledford et al., 1984; Francl et al., 1983; Zhang et al., 2005). The detection plates, the preamplifier & amplifier, and the ADC

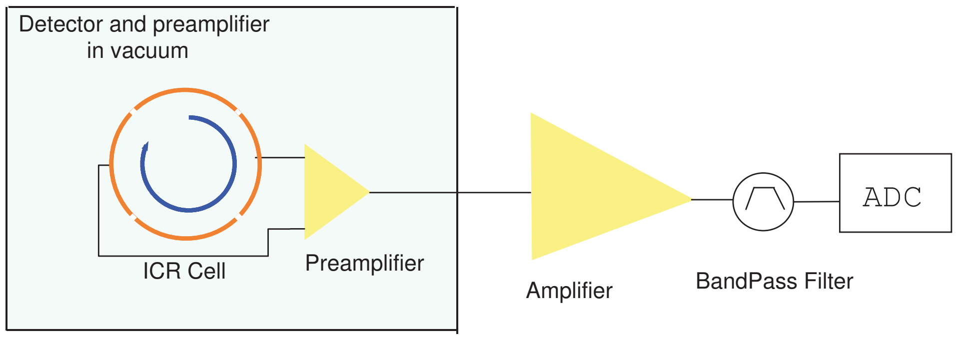

Figure 3·1: FTMS Detection Scheme

constitute the detection circuitry of the FTMS, Fig. 4·1. Enhancing the limit of detection involves careful analysis and optimization of these 3 components. Typically, it is the detection amplifier which is engineered for optimal performance (low noise, high gain, low output impedance), given the existing ICR cell and the ADC specifications.

The equivalent electrical model for the detection scheme in the ICR experiments was first presented by Comisarow, as shown in Fig. 3·2 (Comisarow, 1978). In this approach, the resonantly excited coherent ion packet was modeled as a rotating electric monopole. Comisarow calculated the image current, I_s, induced on the plates of a cubic ICR cell (assuming infinitely long electrodes) due to the cyclotron motion of the ions, as given by Eq. 3.8 (Comisarow, 1978). The theory was based on the work of Shockley, who calculated the induced current in electrodes in proximity of a moving charge (Shockley, 1938).

$$I_s(t) = \frac{Nq^2rB}{md} sin\omega t \tag{3.7}$$

$$I_s(r.m.s) = \frac{Nq^2rB}{\sqrt{2}md} \tag{3.8}$$

where, N is the number of ions with mass to charge ratio m/q, rotating in an orbit with cyclotron radius r in a magnetic field of strength B, and d is the distance between the plates of the ICR cell.

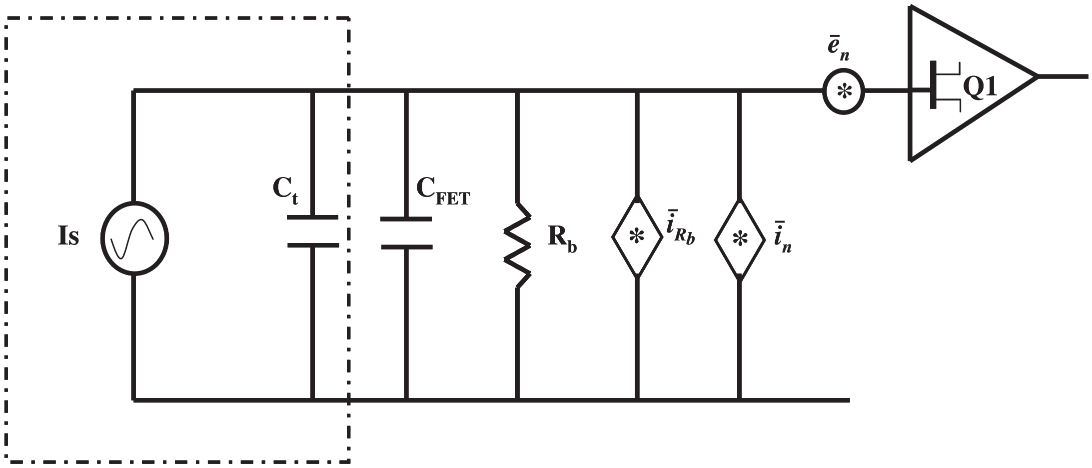

Figure 3·2: Equivalent Electrical Model for ICR detection. (I_s = induced image current, $C_t = C_c + C_{cw}$, C_c = intrinsic Cell capacitance, C_{cw} is the connecting wire capacitance, C_{FET} = preamplifier input capacitance, R_b = preamplifier input bias resistance, i_{R_b} = Johnson noise due to R_b, i_n = preamplifier equivalent input noise current, e_n = preamplifier equivalent input noise voltage)

Now, the cyclotron frequency, ω_c, is given by Eq. 3.9.

$$\omega_c \equiv \frac{qB}{m} \tag{3.9}$$

Thus, using Eq. 3.9 in Eq. 3.8,

$$I_s(r.m.s) = \left(\frac{Nqr}{\sqrt{2}d}\right)\omega_c \tag{3.10}$$

From the signal model presented in Fig. 3·2, the voltage induced on the plates (i.e. at the input of the preamplifier), V_s is given by,

$$V_s = I_s(R_b||X_c) \tag{3.11}$$

where, X_c is the reactance due to the total capacitance at the input of the preamplifier C,

R_b is the input bias resistor as defined in Fig. 3·2.

$$|X_c| = \frac{1}{\omega_c(C_t + C_{FET})} \equiv \frac{1}{\omega_c C} \tag{3.12}$$

Hence,

$$V_s = \left(\frac{Nqr\omega_c}{\sqrt{2}d}\right)\sqrt{\left(\frac{R_b^2}{1+\omega_c^2 C^2 {R_b}^2}\right)} \tag{3.13}$$

If the bias resistor R_b is selected such that: $R_b \gg X_c$ at minimum frequency of interest, then $(R_b||X_c) \approx X_c$. Therefore,

$$V_s = \left(\frac{Nqr\omega_c}{\sqrt{2}d}\right)\left(\frac{1}{\omega_c C}\right) \tag{3.14}$$

Thus, the r.m.s. induced signal voltage in the ICR cell is given by:

$$V_s = \frac{Nqr}{\sqrt{2}dC} \tag{3.15}$$

As noted by Comisarow, the intriguing aspect of Eq. 3.15 is the absence of the frequency term, ω_c. This independence of induced voltage on frequency ensures a flat response of the detection circuit, (over the working range in m/z) which simplifies ion quantification, provided the detection amplifier is designed with a flat gain in this bandwidth of interest. For a 7 T FTMS, the relevant frequency range is generally from 10 kHz ($m/z \approx$ 10k) to 1 MHz ($m/z \approx 100$). Hence, an R_b greater than about 1 MΩ will ensure a flat response in this frequency range, as evident from Fig. 3·3. This value of R_b also determines the Johnson noise as discussed below.

In the derivation it was assumed that the parallel detection plates were infinitely long. This assumption is naturally not true and error from this approximation becomes significant when the dimensions of the cell plates are comparable to the spacing between them. From the analysis by Comisarow the induced ion current is dependent on its distance from the ICR plates, however it was deduced that besides distance the ion current also depends on the angular position in the trap. Nikolaev showed that this results in the presence of higher

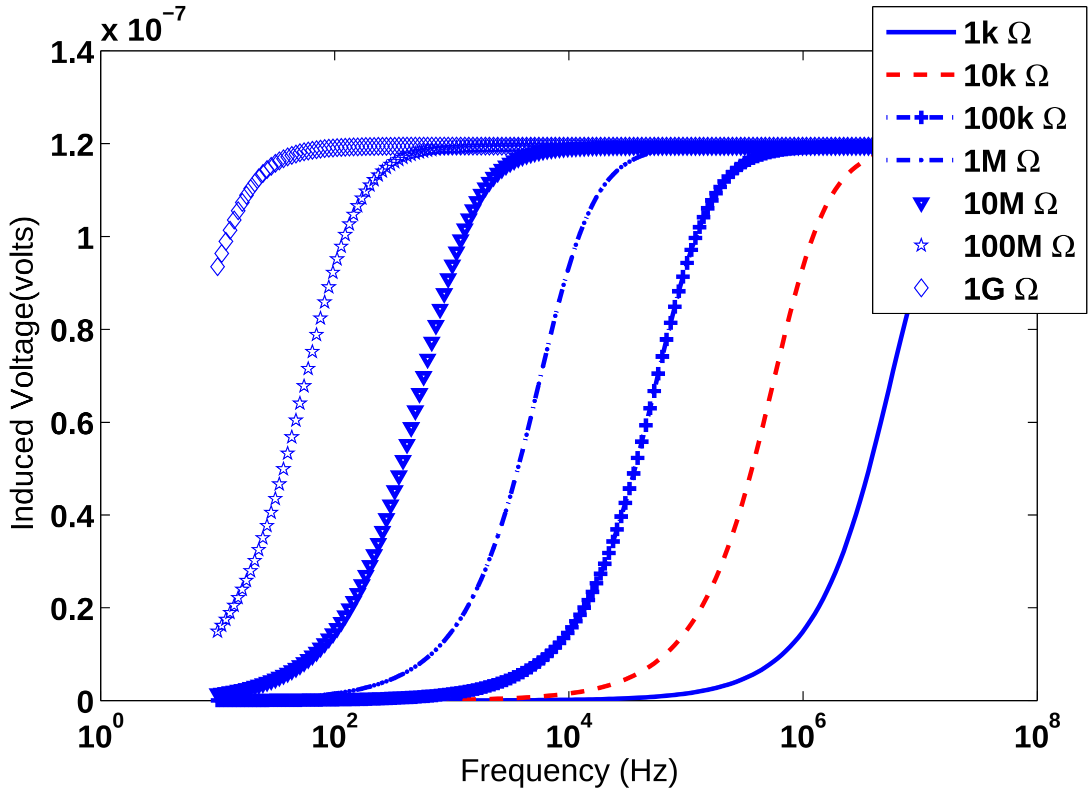

Figure 3·3: Dependence of ICR voltage on Frequency for different bias resistor values.

order odd harmonics in the ICR detection (Nikolaev and Gorshkov, 1985).

A comprehensive analytical solution for the induced differential charge in an ICR cell with arbitrary geometry was derived by Grosshans (Grosshans et al., 1991). Using reciprocity, Grosshans computed the magnitude of the Fourier coefficients of the signal induced by an ensemble of ions in a circular orbit in a trap. For a cylindrical trap with electrodes at coordinates $z = 0$ and c, and at $\rho = a$, the induced differential charge on the detection electrodes is given by the following equation,

$$\frac{\Delta Q}{q} = \sum_{m=0}^{\infty}\{\frac{-16}{\pi^2}\sum_{n=0}^{\infty}\frac{sin[(2m+1)\pi/4]sin[(2n+1)\pi z/c]I_{2m+1}[(2n+1)\pi\rho c]}{(2m+1)(2n+1)I_{2m+1}[(2n+1)\pi a/c}\}cos[(2m+1)\phi] \tag{3.16}$$

or,

$$\frac{\Delta Q}{q} = \sum_{m=0}^{\infty} A_{2m+1}(\rho, z)cos[(2m+1)\phi] \tag{3.17}$$

Here, A_{2m+1} are the Fourier coefficients of the ICR signal induced by an ion packet rotating with angular velocity ω at fixed z coordinate. The intensities of the harmonic peaks arising at $(2m + 1)\omega$ frequency can be calculated using Eq. 3.16.

These equivalent electrical model makes it possible to develop an analytical solution for the design of the low noise preamplifier for Ion cyclotron resonance mass spectrometer.

A pioneering step to enhance the limit of detection by improving the detection amplifier was taken by Anderson *et. al* (Anderson et al., 1995), which is further based on the work of Jefferts and Walls (Jefferts and Walls, 1987). Anderson presented a design of a low noise amplifier for the FTMS using a JFET input differential stage. Various factors which determine the signal/noise ratio of the amplifier were analyzed.

In Anderson designs and the room temperature amplifier designs, which were developed in our research at Boston University, silicon transistors were used as active devices. The development of cryogenic FTMS provides an opportunity to improve these designs by cooling them. The input transistors of these amplifiers have thermal noise and the leakage current which can be reduced considerably by cooling them to 4 Kelvin. Designing for low temperature applications requires review of cryogenic electronics and many experiments to understand the component behavior at 4 Kelvin. These will be discussed further.

3.3 Thermal Noise Model

Thermal noise, also referred to sometimes as Johnson noise, is generated by the random fluctuations of the current in a conductor caused by the thermal motion of the charge carriers (Johnson, 1928). Thermal noise in a resistor can be represented by a series voltage source, given by the following equation:

$$\bar{v_n}^2 = 4k_bTRB \tag{3.18}$$

This, can also be expressed by an parallel equivalent current source, given by:

$$\bar{i_n}^2 = \frac{4k_bTB}{R} \tag{3.19}$$

where, k_b is the Boltzman constant, T is the temperature, R is the equivalent resistance of the component, and B is the noise bandwidth of the measuring device. Thermal noise is intrinsic to the electrical component and is typically independent of the frequency, hence comes in category of white noise (Gray et al., 2001). For example, a 1 $k\Omega$ resistor, sitting on a bench, will generate an rms voltage noise approximately equal to 4 $nV/\sqrt{Hz}$. This thermal noise is proportional to the square root of the bandwidth and the square root of resistance, as well as the square root of temperature. This means that in order to reduce the contribution of thermal noise in a broadband circuit, either temperature, or the resistance itself, must be lowered. As discussed in section 2.1, it is not helpful in terms of SNR to reduce the resistance and the bandwidth in an FTMS.

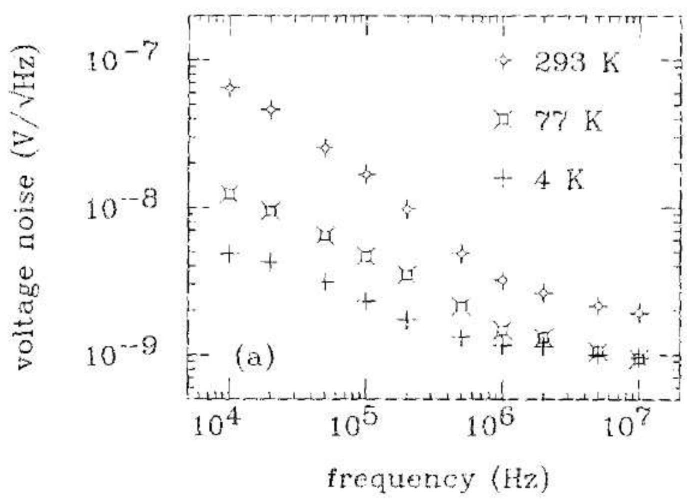

Figure 3·4: Spectral noise voltage vs Temperature (Lee, 1989).

3.4 Preamplifier operation at Room Temperature and Cryogenic Temperature

Suppose the ambient temperature is denoted by T. Then, the thermal noise power spectral density is proportional to the T and can be reduced by cooling the electrical component to low temperatures. For example, in (Lee, 1989), authors have measured the temperature dependence of the voltage noise in a cryogenic amplifier. As shown in the Fig. 3·4, the input voltage noise decreases as the amplifier is cooled to cryogenic temperatures. Also, the improvement in noise performance from room temperature to 77°K was significant, where as further cooling to 4°K was comparatively less.

The designed cryogenic FTMS uses liquid helium to cool the FTMS mass analyzer, to achieve low base pressure in the order of 10^{-12} mbar (Gabrielse et al., 1990a). The detection preamplifier connected to the cell plates can be cooled simultaneously by placing it in contact with the same cryobath. Cooling of the detection circuit will enhance the SNR by reducing the thermal noise in the circuit (Tanskanen et al., 2000; Kok et al., 1999; Wang et al., 1998).

3.5 Power Consideration at 4 K

The cryogenic FTMS has distinct advantages. It enhances the signal to noise ratio for better sensitivity and lowers the base pressure for better mass resolution (O'Connor, 2002). However, the advantages of cooling the preamplifier and the FTMS come at the cost of liquid helium. The more power dissipated in the preamplifier circuit, the more the heat load on the cooling system and hence, more difficult it is to keep the circuit at 4 K. This also increases the liquid helium boil off rate. Liquid helium, which will be used as the coolant, costs about $5 per liter. Thus, the power dissipation in the detection circuit is one of the principal reason to keep only the preamplifier stage of the detection circuit, with minimal power dissipation, close to the detection plates. The second stage with very high gain sits outside the cryogenic system with much less stringent power constraints. In the current cryogenic FTMS, 100 mW has been set as the upper limit for the power dissipation in the preamplifier circuit (O'Connor, 2002). This level of power dissipation will translate into 3.36 lt/day of liquid helium boil-off if the amplifier is run continuously.

3.6 Choice of Semiconductor

The carrier mobility in a semiconductor is governed primarily by the scattering of the carriers and the collisions which the carriers go through in the conduction channel. The principle scattering processes which occur in a semiconductor material are:

- Lattice scattering : This type of scattering is caused by the collisions of carriers due to lattice vibrations. The lattice vibration is proportional to the thermal energy, thus causing more collisions at higher temperature.

- Impurity scattering : This occurs by the scattering of the carriers due to the columbic effect of the ionized impurities as the carriers travel in the conducting channel. High doping densities implies more impurity scattering and lower carrier mobility.

At room temperature, in devices with low or medium doping levels, the carrier mobility due to lattice scattering dominates and impurity scattering is negligible. However, as

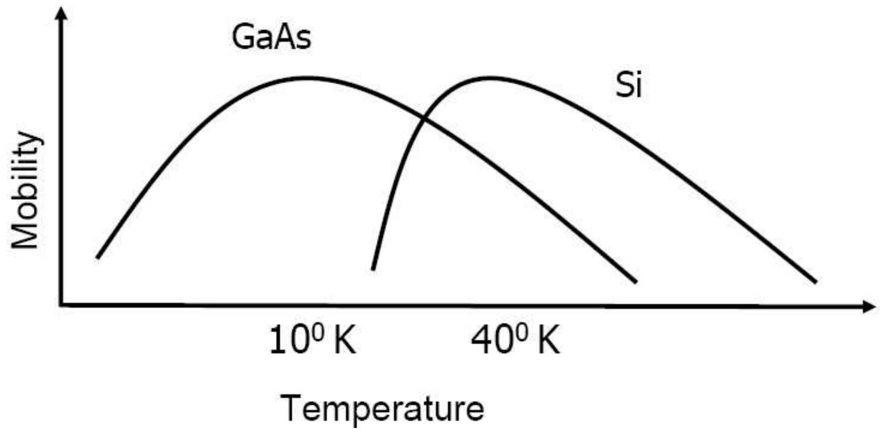

Figure 3·5: Schematic diagram representing the mobility of GaAs versus Silicon. Adapted from (Keyes, 1977; Jonsher, 1964).

the temperature is decreased, the lattice vibration decreases, so does the collisions of the carriers with the lattice. This increases the net carrier mobility of the semiconductor device at low temperatures. However at still lower temperatures, the mobility due to impurity scattering increases and limits the net carrier mobility. Ultimately at very low temperatures, the carriers freeze-out.

As seen in Fig. 3·5, as the temperature is decreased from room temperature towards 0 K, the mobility of silicon first increases due to reduced lattice vibrations. However, around 40 K, the mobility of silicon starts to decrease and around 20 K the carriers in silicon freeze-out. On the other hand, although the mobility of carriers in GaAs exhibit a similar trend, the carrier freeze-out doesn't happen in these devices until about 2 K. Thus, GaAs devices can be operated at 4 K—the temperature of interest to us.

3.7 Gallium Arsenide Devices

Gallium Arsenide is a compound semiconductor, and due to its high mobility, it is used to fabricate microwave devices operating at GHz frequencies. Two type of GaAs devices which are commercially available are discussed next.

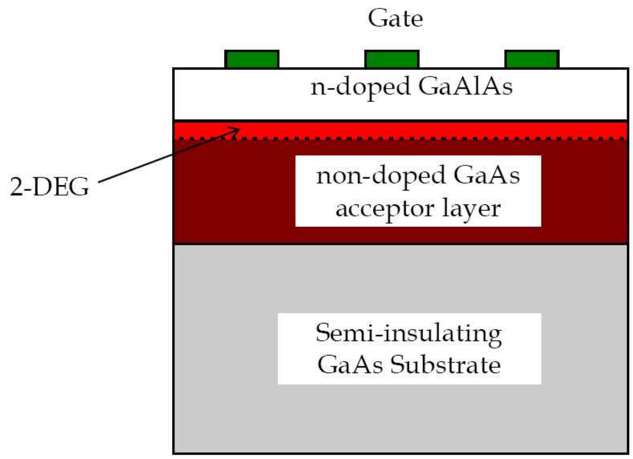

Figure 3·6: Schematic representation of a GaAs HEMT device.

3.7.1 High Electron Mobility Transistor (HEMTs) or Modulation Doped FETs (MODFETs)

HEMTs are heterojunction transistors, which are usually made using AlGaAs and GaAs. A simple HEMT device cross-section is shown in Fig. 3·6. HEMTs have superior electron transport properties due to the formation of two-dimensional electron gas (2DEG). Thus, HEMTs show high mobility, high transconductance and ultra low noise. The high carrier mobility in GaAs HEMTs make them suitable for low temperature applications. HEMT devices show improvement in electron transport properties and reduction in thermal noise when cooled to cryogenic temperatures. These devices have a unity gain frequency in the order of tens of GHz, e.g. the device FHX35LG has an f_T of 12 GHz (Eudyna Devices, Inc., 2005). Thus, they are widely used for radio frequency applications.

3.7.2 Metal Semiconductor Field Effect Transistor (MESFET)

MESFETs are field effect transistors which are fabricated by placing a conducting channel between the source and drain region. In MESFET a metal-semiconductor junction, known as Schottky contact, is used to control the flow of carriers in the channel. The bias on the Schottky gate is used to change the width of the depletion layer controlling the drain to source current in a MESFET. A cross section of a MESFET is shown in Fig. 3·7.

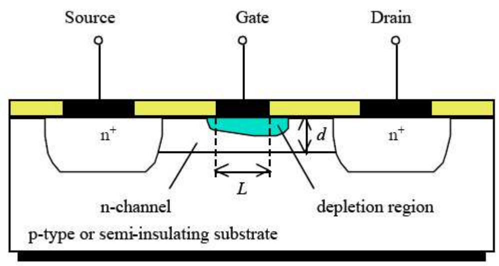

Figure 3·7: Schematic representation of a GaAs MESFET device.

Several cryogenic low noise amplifier designs using GaAs MESFETs have been published in the literature. However, none of these designs satisfy the bandwidth and the gain requirement of an FTMS at the same time. For instance, Lee et al. has proposed the design of a low noise cryogenic preamplifier using GaAs MESFETs in (Lee, 1989). This design has four MESFETs in parallel. These MESFETs are operated at cryogenic temperature and cascoded with a Si-JFET kept at room temperature. The input stage is followed by three inverting amplifiers. The amplifier has 3 dB bandwidth from 100 kHz to 10 MHz with a gain of 59 dB. This gain-bandwidth product is not sufficient for FTMS.

Similarly, Yang et al. have suggested a design of a low noise cryogenic transimpedance amplifier with a bandwidth of 32 kHz. A GaAs MESFET is used in a source-follower configuration at the input followed by a high gain room temperature stage (Yang and Change, 2002). Various other similar designs have been explored in the literature (Weinreb, 1980; Weinreb et al., 1982; Prance et al., 1982; Gregg et al., 1987).

The previous designs use GaAs MESFETs. However, GaAs HEMTs have been shown to perform better for low noise amplifiers (Duh et al., 1988; Hanyu et al., 1988; Joshin et al., 1983; Wenger et al., 1991). The high carrier mobility achieved in the GaAs HEMTs allows these devices to be used for very high frequency applications (Shumaker et al., 2001). Tanskanen et al. has shown that HEMTs potentially have the lowest noise at frequencies below 100 GHz (Tanskanen et al., 2000). The design in (Tanskanen et al., 2000) uses Indium-phosphide HEMT, which exhibits a noise figure lower than 5.5 dB with a gain higher than 14 dB over the 50-68 GHz range at room temperature. In (Kok et al., 1999), authors have fabricated a monolithic low-noise amplifier (LNA) using pseudomorphic (PM) InAlAs-InGaAs-InP HEMT. The measured gain of the LNA is 9 dB with a 3 dB bandwidth of 164 GHz to 192 GHz. In (Wang et al., 1998; Kwon et al., 1996; Itoh et al., 1995), authors have presented various low noise amplifier designs, which are based on high mobility heterojunction active devices.

Although, these amplifiers can be operated at cryogenic temperatures with few design modifications, none of them are suitable for operation between 10 kHz to 1 MHz (Pospieszalski and Wollack, 2000; Pospieszalski et al., 2000; Risacher and Belitsky, 2003), as required for an FTMS.

3.8 Motivation for Low Noise Amplifier

3.8.1 Increased Dynamic Range

Dynamic range is defined by the ratio of minimum and the maximum number of ions which can be reliably detected in an FTMS mass analyzer. So, if we can detect single ions we can detect proteins that exists in small quantities, whose signal is generally lost in the noise. Thus providing more information to the biologists.

Time of flight and ions traps routinely detect single ions with unit charge because they use particle detectors such as electron multipliers and dynodes. This allows them to achieve dynamic range of the order of 10^6. For FTMS the best case limit of detection which has been reported in literature is 30 charges (Anderson et al., 1995).

An example for the need to improve dynamic range is shown in the mass spectrum in Fig. 3·8. The glycan which is the sample for analysis has been dissociated into small fragments using electrons, this phenomenon is termed as Electron Detachment Dissociation (Adamson and Hakansson, 2007; Budnik et al., 2001). The identification of the fragments provides characteristic information about the unknown sample and the list of the fragments can be used to uniquely identify the structure of the glycan. However, as is

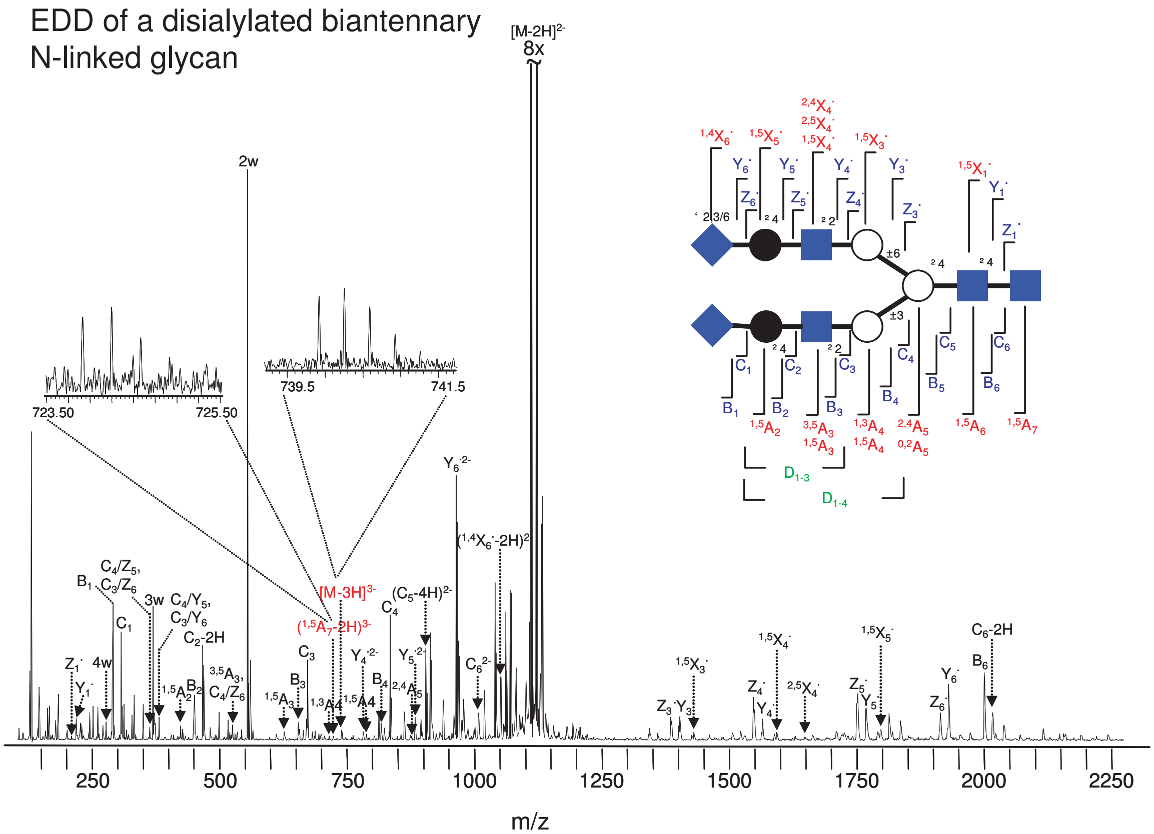

Figure 3·8: EDD Spectrum of N-linked Glycan

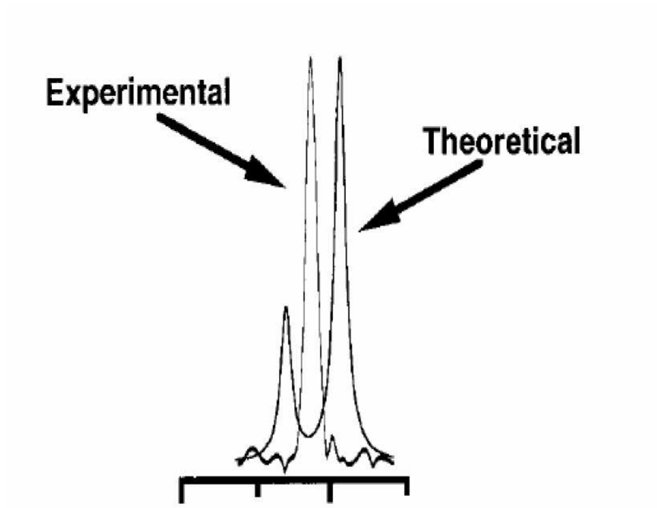

Figure 3·9: Peak Coalesce due to Space Charge effects (Amster, 1996)

evident from the insets in the Fig. 3·8, the signal to noise ratio of the fragment peaks is generally very low. There are several peaks with useful information that are submerged in the noise of the detection circuit, Fig. 3·8. These peaks which arise due to small number of ions can be readily detected if the preamplifier noise can be reduced.

Thus achieving unit charge detection sensitivity which is limited by the detection amplifier noise, the dynamic range of the FTMS can be increased several times.

3.8.2 Space charge effects

High ion densities in an ICR cell during detection, for large induced current, causes a space charge effect. The space charge is caused by the columbic repulsion between ions, which results in:

- frequency shift due to effective trapping potential, V_T, reduction (Marshall et al., 1998).
- expansion and distortion of the lineshape from averaging the effective frequency over time (Marshall and Verdun, 1990; Aizikov and O'Connor, 2006).
- peak coalescense due to columbic entrapment of different ion clouds (Amster, 1996).

For example in the extreme case of peak coalescence, the ions are excited for detection, and they first orbit with other ions with same cyclotron frequency. However, with time, they start to move in synchrony with other ions, that have similar cyclotron frequencies. This is caused by the columbic interaction between the ions rotating at cyclotron frequencies very close to each other. In this phenomenon, peaks that are closely spaced in the mass spectrum, coalesce into a single peak, as shown in Fig. 3·9. This will cause the incorrect interpretation of the m/z peaks causing errors in mass analysis (Ledford et al., 1984).

Space charge is the main limitation to achieving high mass resolving power [1] and mass accuracy in an FTMS. This problem can be addressed by reducing the ion population, which will reduce the columbic interaction between the ions, hence the space charge effects. However, reducing the number of ions, decreases the induced current on the detection plates. To efficiently detect this weaker ion signal, it is required to have an amplifier with improved signal to noise ratio. Thus, if unit charges can be detected in an FTMS, the mass resolution, as well as mass accuracy, is improved.

Many techniques have been developed to study small unit charged particles, such as protons (Weisskoff et al., 1988; Difilippo et al., 1995). However, the amplifiers used in these particle detectors are not suitable for FTMS. In particular, the *Single Ion cyclotron Resonance* technique is commonly used in physics laboratories for determination of the mass of small ions, such as CO^+ (Brown and Gabrielse, 1986). Most of these ICR detectors use high Q,[2] high gain, narrowband amplifiers (Cornell et al., 1989; Weisskoff et al., 1988). Authors of (Difilippo et al., 1995; Gerald Gabrielse, 2005) have reported accurate relative mass measurements of a single ion using a Penning trap mass spectrometer with an accuracy exceeding 1 parts per trillion.[3] The advantages of single charge detection are clear from the above mentioned applications. However, in an FTMS unknown ions with a range of m/z

---

[1]Mass resolving power is defined as the dimensionless ratio of the mass of the peak to the width of the peak at half maximum intensity $\frac{m}{\Delta m}$(fwhm).

[2]Q or Quality factor of a circuit is defined by the ratio of resonant frequency to its bandwidth.

[3]This level of performance is achieved in the absence of columbic effects that can arise if multiple ions are to be analyzed simultaneously.

values are excited and then detected. This requires a low noise wide-bandwidth amplifier.

The primary goal of this thesis is to develop a wideband low noise amplifier for FTICRMS to be able to detect single charges. We have designed a room temperature amplifier which has been tested on room temperature FTICRMS. And development of the FTICRMS in the cold bore of a superconducting magnet provided an opportunity to develop a cryogenic preamplifier which was cooled to 4 Kelvin to reduce the thermal noise.

These low noise amplifiers have led to higher sensitivity in FTICRMS which has provided significant improvements in the quality of data.

Chapter 4

ICR Amplifier Design Constraints

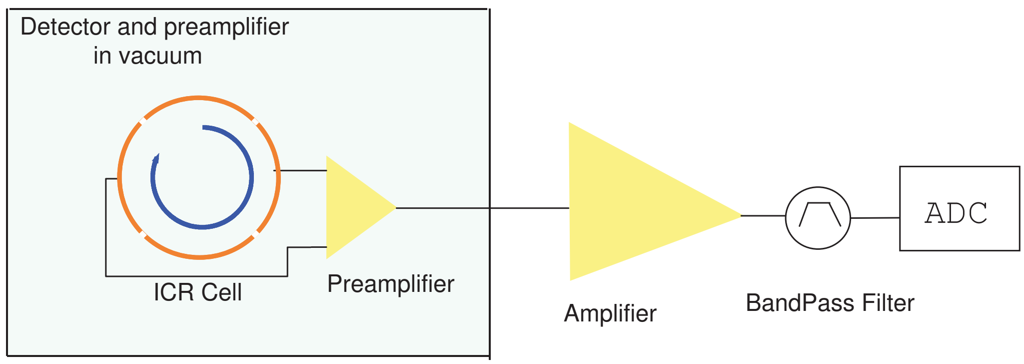

Figure 4·1: FTMS Detection Scheme

4.1 Amplifier Design Constraints

The previous section details the model for the ICR detection circuit, Fig. 4·1. Here in this section we will describe several design constraints or requirements which drive this development of the low noise preamplifier for the FTICRMS.

4.1.1 Gain Distribution

A simple amplification system representing different stages of an amplifier is shown in Fig. 4·2. For example the first stage could be the preamplifier and second stage could be the amplifier and so on. $k1$ and $k2$ are the power gains and $n1$ and $n1$ are the noise power of the first and second stage respectively.

The total output signal can be calculated to be equal to $s_1 \times k_1 \times k_2$. The total output noise is $(n_1 \times k_1 \times k_2) + (n_2 \times k_2)$. Thus to optimize signal to noise ratio of the

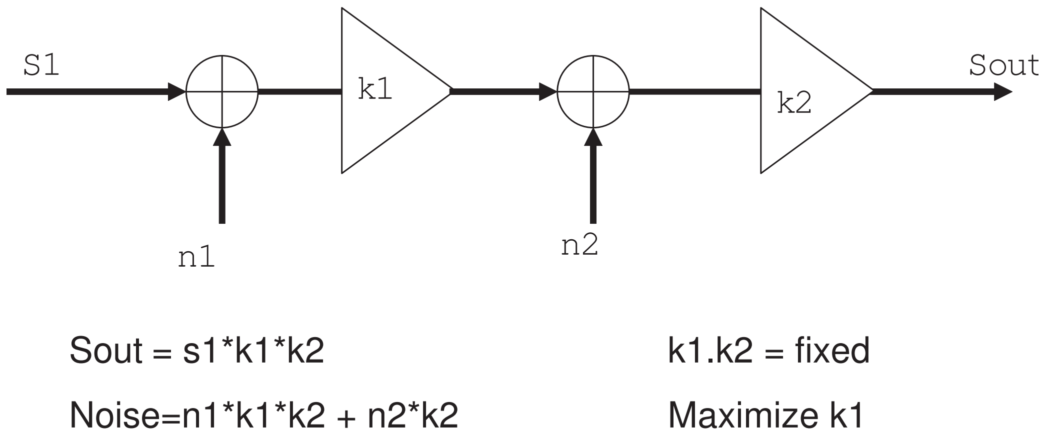

Figure 4·2: Analysis for Gain Distribution

amplification system, the gain of the first stage k_1 should be maximized. However, the power dissipation limit of the circuit imposes a limit on the achievable gain per stage in an amplifier. Typically the first stage is designed with a gain high enough to raise the level of the signal above the noise floor. This ensures that the noise contribution from the second and later stages, $n2$ in this case, is negligible to the total noise of the amplifier.

4.1.2 Low Leakage Current

The ICR detector is a capacitor on which charge is induced. In theory the image charge which is induced on the plates, charges the capacitor (the detection plates). This build up of charge on the detection plates produces a voltage which is then amplified. However the amplifier (or input FET) which is used for the amplification also has its intrinsic input leakage current. As the FET is in parallel with the detection plates the leakage current of the FET also changes the detection plate capacitance. Thus the input devices with minimum leakage current should be selected. For the same reason FETs are preferred over Bipolar junction transistors.

Moreover the input leakage current of an FET causes shot noise. Thus, for high impedance sensors, as is the case with ICR detection, input devices with minimum input leakage current are desired. This is further discussed in section 5. Minimizing the input leakage current also allows the selection of the bias resistor, R_b, with maximum value as discussed below.

4.1.3 Input Bias Resistor

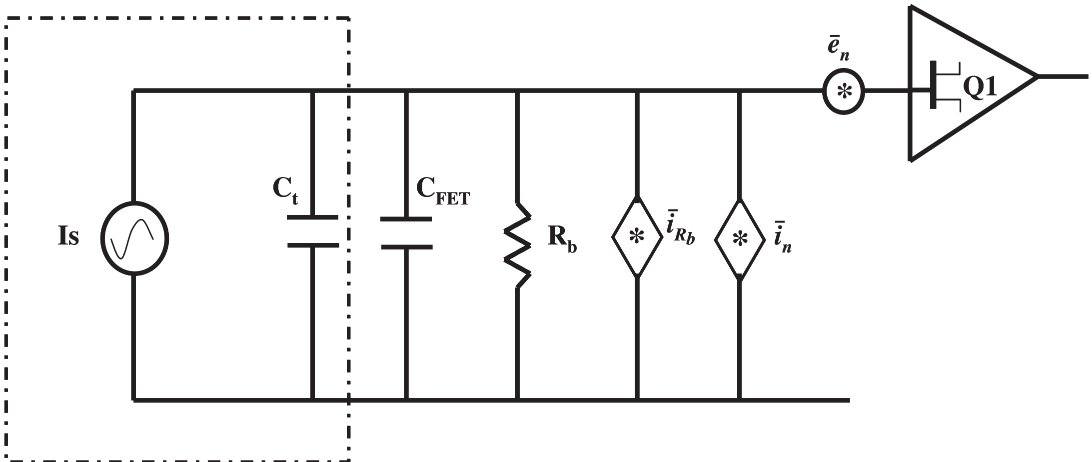

Figure 4·3: Equivalent Electrical Model for ICR detection. (I_s = induced image current, $C_t = C_c + C_{cw}$, C_c = intrinsic Cell capacitance, C_{cw} is the connecting wire capacitance, C_{FET} = preamplifier input capacitance, R_b = preamplifier input bias resistance, i_{R_b} = Johnson noise due to R_b, i_n = preamplifier equivalent input noise current, e_n = preamplifier equivalent input noise voltage)

If we recall from previous chapter, various noise sources in the ICR detection circuit are presented in the signal model by Comisarow, Fig. 4·3. The total input referred noise in the ICR detection circuit can be calculated from the following equation (for high value of R_b),

$$\begin{aligned}\bar{e^2}_{ni} &\approx (\bar{i}^2_{R_b} + \bar{i}^2_n)|X_c|^2 + \bar{e^2}_n \\ &\approx \frac{4kT\Delta f}{R_b}\left(\frac{1}{\omega_c C}\right)^2 + \left(\frac{\bar{i}^2_n}{{\omega_c}^2 C^2}\right) + \bar{e^2}_n\end{aligned}$$

Thus to minimize noise, we have to select a bias resistor, R_b with highest value.

The maximum value of R_b which can be used is defined by the intrinsic input leakage current of the FET used in the preamplifier. The primary purpose of the R_b in the ICR preamplifier circuit, shown in Fig. 4·4 is to set the d.c. bias at the gate of the input FET (and the detect plates) to ground potential. However, due to intrinsic leakage current from the gate of the FET, a charge starts to build up on the input capacitance of the preamplifier. This accumulation of charge floats the d.c. potential at the gate of this FET, eventually driving it to the power supply rails, thus making the preamplifier non-operational. Moreover, this leakage current also causes an ohmic voltage drop across R_b, which is directly connected to the detection plates, and as a result will perturb ion motion. One Volt of potential developed on the detection plates (10 pA of leakage current with a 100 GΩ bias resistor) can potentially cause a complete loss of detected ICR signal.

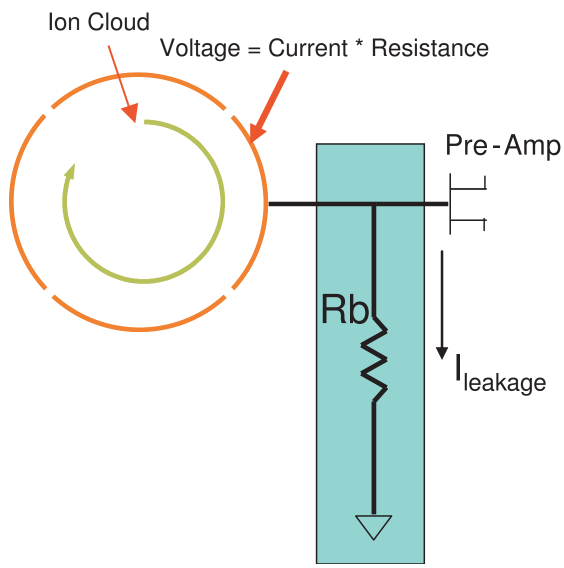

Figure 4·4: Selection of Input Bias Resistor

In this work 10 mV was taken to be permissible on the detection plates and has been verified experimentally to be non detrimental for signal detection. As a result, the maximum value of R_b that can be used with a FET with 10 pA of leakage current is equal to 1 GΩ. A general conclusion which can be made is to select a FET with minimum leakage current, thus permitting maximization of the R_b, and hence, minimization of the input equivalent noise to the intrinsic noise of the input FET.

Increasing the value of R_b to reduce its noise contribution only helps up to the point where the intrinsic noise of the FET, e_n, becomes significant. For example, the noise contribution of a 1 GΩ bias resistor at the input of the preamplifier is merely 0.6 nV/rtHz at 100 kHz (T = 290 Kelvin, and C = 10 pF). This is already below the input noise voltage of most of the commercial low noise JFETs used for the ICR preamplifier designs. Thus, increasing the bias resistor further, does not enhance the net ICR signal/noise ratio.

It is evident that infinite resistance at the input of the preamplifier would provide the lowest noise from the R_b. Thus for this ideal case a mechanical switch can be used between the inputs of the preamplifier and ground. During the ICR signal detection the switch can be opened, allowing the accumulation of charge at the input FET, thus recording the ICR signal. After the detect event the switch can be closed to bleed-off the charge from the FETs to ground. However finding a reliable mechanical switch which can operate in 7 Tesla magnetic field is non trivial. And electrical switches would add capacitance and noise to the ICR signal and must be avoided. Some piezoelectric switches have been shown to be working in the high magnetic fields and have low capacitance. This will be explored in future.

4.1.4 Input Device Selection

The above discussion shows that the selection of the input FET is the most significant design choice for the optimization of the ICR detection preamplifier. The ICR signal is modeled as a current source in parallel with a capacitance (Comisarow, 1978). In such a high impedance source, the leakage current of the input transistor can potentially have a dominant influence on the input-referred electronic noise.

Thus, for room temperature preamplifier designs, it is desirable to use Junction Field Effect Transistors (JFETs) at the input stage, which have lower leakage currents than bipolar junction transistors (BJTs) (Jefferts and Walls, 1987). JFETs have leakage currents on the order of 1 pA, allowing a high value for the input bias resistor, which helps minimize noise as discussed above. Moreover, the low 1/f noise cut-off frequency in JFETs, typically below 1 kHz, has significant implication in low noise ICR detection where spectral frequencies of interest are usually above 10 kHz.

Noise sources in a JFET can be attributed to the following sources (Van Der Ziel, 1970):

- 1/f noise caused by generation recombination of charge carriers in the depletion region of the FET. In modern JFETs the 1/f noise roll-off is typically below a kHz, hence this component of noise in neglected at higher frequencies.
- Shot noise due to the leakage current of the gate of the JFET. This can be calculated by the Schottky formula ${I_{shot}}^2/\Delta f = 2qI_{GSS}$, where q is the charge of an electron, I_{GSS} is the gate leakage current (Schottky, 1918).
- Channel noise due to thermal fluctuations in the drain to source channel. This noise can be calculated by determining the equivalent value of the channel resistance as shown in section 4.1.5.
- Channel thermal noise, capacitively-coupled to gate (input) by C_{gd}. This noise is represented as a shunt resistance ($R_n \approx 1/(\omega^2 r_{ds}^2 g_m C_{gd} C_{ds})$) in parallel with the C_{gs} at the input of the FET. The contribution of the thermal noise current due to R_n is typically less than 10 fA/rtHz at frequencies below 1 MHz, becoming significant only at higher frequencies, and is neglected for most practical applications (Van Der Ziel, 1970; Levinzon, 2000).

Thus in the ICR frequency range of operation, the primary contribution to the noise of the JFET comes from the thermal noise in the channel. Hence to obtain optimum noise performance it is proper to consider channel thermal noise of the device, as discussed below.

However for the cryogenic preamplifier Si JFETs do not work due to carrier "freeze-out" (Jonsher, 1964). The GaAs MESFETs selected for the amplifier placed at 4 Kelvin generally have 1/f noise corner frequency at around 100 kHz which increases the noise contribution due to the FETs, decreasing the signal to noise ratio of the ICR signal.

4.1.5 Matching Input Capacitance

The ICR signal arises by integrating the image current over the total input capacitance. This total input capacitance consists of sum of capacitances due to the cell plates, connecting wires, and the FETs input capacitance, Fig. 4·5. Hence, reducing this capacitance increases the ICR signal, which is evident from Eq. 4.1. Now the capacitance of the cell plates can be reduced by making the cell smaller. This is not usually advisable as in smaller ICR cells, the ion spatial density increases, and the space charge effects, which arise due to the columbic interactions of the ions with each other becomes worse. This effectively reduces the number of ions which can be stored in the cell. Typically the ICR cell geometry is made to be equal to the homogenous region of the superconducting magnet.

$$V_s = \frac{Nqr}{\sqrt{2}dC} \tag{4.1}$$

Again, as the geometry of the ICR cell plates is fixed, it is of interest to minimize the connecting wire capacitance and the FET input capacitance for maximizing the ICR signal. The wire capacitance is minimized by placing the preamplifier in vacuum, near the ICR cell. However, the electronic noise of a FET, which primarily consists of the Johnson noise in the intrinsic channel resistance, increases as the FET intrinsic capacitance decreases, or in other words, as the device is made smaller. As a result, the scaling down of the device to reduce the capacitance makes it noisier. Selection of a FET with an input capacitance for optimal ICR signal/noise ratio can be done on the basis of the following analysis.

The FET equivalent channel noise resistance between drain and source terminal in the saturation region is $3/(2g_m)$, where g_m is the transconductance of the FET (Gray et al., 2001). As a result, the equivalent input noise voltage in a FET (referred to the gate) can be expressed as:

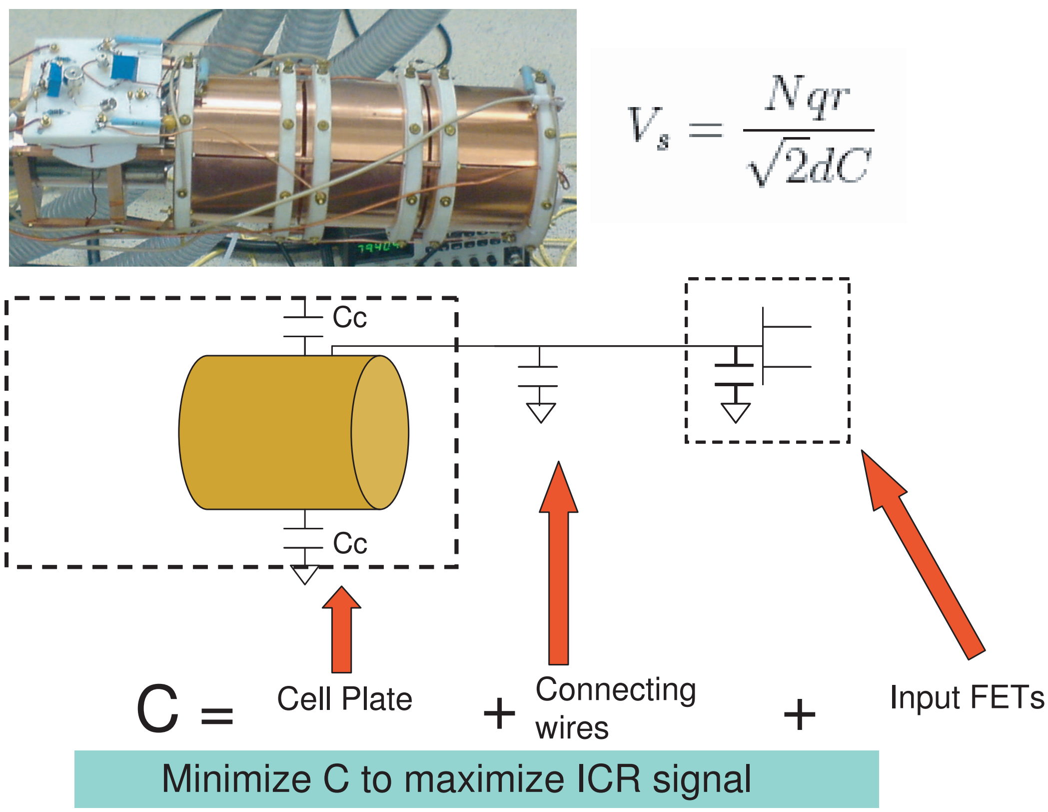

Figure 4·5: Input Capacitance at the ICR cell

$$\bar{v_n}^2 = 4kT(2/(3g_m))\Delta f \tag{4.2}$$

Hence, using Eq. 4.1 the signal/noise ratio (Signal Power/Noise Power) of the ICR signal at the input of the preamplifier can be calculated by,

$$signal/noise = \frac{V_s{}^2}{\bar{v_n}^2} = \left(\frac{Nqr}{\sqrt{2}d(C_t + C_{FET})}\right)^2 \left(\frac{3g_m}{8kT\Delta f}\right) \tag{4.3}$$

Eq. 4.3 can be rearranged as:

$$signal/noise = \left(\frac{3N^2q^2r^2}{16d^2kT\Delta f}\right)\left(\frac{g_m}{C_{FET}}\right)\left(\frac{1}{C_{FET}(1 + C_t/C_{FET})^2}\right) \tag{4.4}$$

The transconductance, g_m, and the input capacitance of the FET, C_{FET}, both scale linearly with the width of the FET channel for a given device fabrication process (Gray et al., 2001). This ratio of g_m to C_{FET} is generally used as a figure of merit to compare various device processes used for the fabrication of a FET. Therefore, the set of terms in the first two parenthesis are constant for a given ICR signal and a given device process. To find optimal device geometry, taking the derivative of the last term with respect to C_{FET} and equating to zero, gives:

$$C_t = C_{FET} \tag{4.5}$$

Therefore, in ICR signal detection, the optimal signal/noise ratio is obtained when the total capacitance due to the cell plates and connecting wires is minimized and matches the total input intrinsic capacitance of the FET. Hence, in the preamplifier design, a FET with a capacitance slightly smaller (≈2 pF to account for the connecting wire capacitance) than that of the capacitance of the cell plates is selected and with a device process for maximum g_m/C_{FET} ratio.

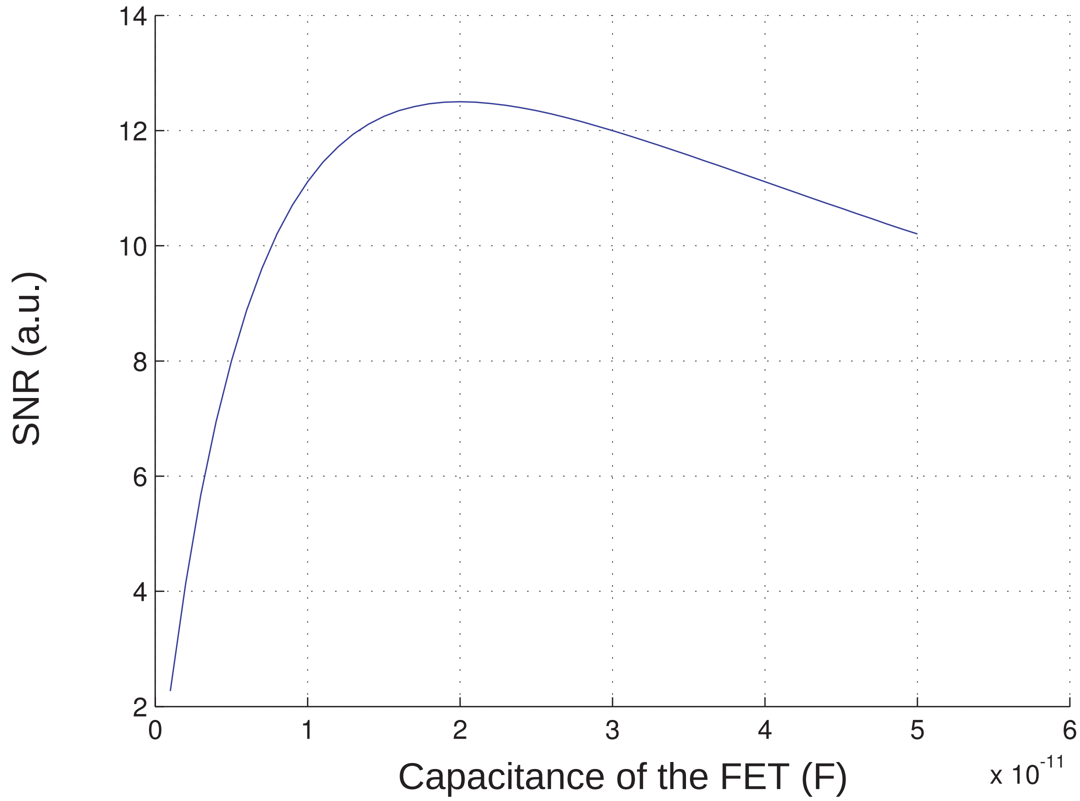

Figure 4·6: Optimal Capacitance of the input FET, with Cin=15 pF

As an example, consider an ICR cell plate capacitance of 12 pF and connecting wires with 3 pF, in total 15 pF capacitance at the input of FET. If we plot the signal to noise ratio from Eq. 5.1 with respect to the FET capacitance we obtain a plot as shown in Fig. 4·6. It is clear that for optimal SNR the input FET should have intrinsic input capacitance equal to 15 pF.

4.1.6 Functionality in High Magnetic Field

As discussed earlier, from Eq. 5.1 it is best to mount the preamplifier as close to the the detection plates as possible. This not only minimizes the parasitic capacitance of the connecting wires but also converts the impedance of the ICR signal lines from high to low. The high impedance nature of the ICR detector makes this signal more vulnerable to radio frequency interference (RFI). Specially as there are many sources of RFI in a mass spectrometer, such as pumps, RF oscillators, phonic pick up due to magnetic field, it is best to transform the impedance as early as possible to minimize RFI pick up.

Thus the preamplifier should be mounted on the detect plates of the ICR cell. However, the ICR cell is placed inside the bore of the superconducting magnet such that the detection plates are in the strongest and most homogenous part of the magnetic field. Placing the preamplifier close to the detector brings the FETs inside this magnetic field. It is found that most of these JFETs which are optimal for room temperature FTMS do not work well in the presence of such high magnetic field. This is due to the Hall effect (Hall, 1879). A possible solution is to design the preamplifier such that the FETs are mounted with their channel aligned to the magnetic field.

4.1.7 Rapid Overload Recovery

The preamplifier inputs are connected to the detect plates which are in close proximity to the excite plates. The excite plates carry typically 200 Vp-p of RF for few msec during an ion excitation event. The quadrature placement of detect plates with respect to the excite plates should minimize this RF getting coupled onto the detect plates. However, as the plates are not perfectly aligned/balanced some small part of this RF is picked up by the detect plates and thus appears at the input of the preamplifier. It was measured to be 5 Vp-p ($\approx$ 2.5%) in one case on a ESI FTMS at Boston University. This 5 Vp-p of RF at the input of the preamplifier almost certainly saturates the preamplifier, the amplifier, and the Analog to digital converter (ADC). This is termed as "overloading" of the amplifier.

As soon as the excitation field is switched-off, the ions are rotating in the cyclotron orbits with maximum radius. This is the time when they are closest to the detect plates and induce the maximum charge. Slowly, depending upon the pressure, ions come back to the center of the cell which causes the decay of the signal induced on the plates. Thus it is important to integrate the charge which is accumulated on the detect plates when the ions are at their highest orbit, right after (less than few msec) the excitation is removed.

For the same reason it is required for the preamplifier and the amplifier to recover from the saturation promptly to collect/amplify induced signal.

In our amplifier designs at Boston University we have used low capacitance Schottky diodes at the input of the FETs to clamp this coupled RF voltage, discussed further in chapter 5.

4.1.8 Vacuum Compatible PCB

The signal in an FTMS arises on the detection plates by the coherent motion of the ions in cyclotron orbits inside the ICR cell. These ions collide with the gas particles in the cell, loose their energy and come back to the center. From Eq. 4.1 the signal induced is proportional to the radius of cyclotron motion of ions. Thus, the longer the ions stay in higher orbits, the longer and stronger is the voltage induced on the plates. In FTICRMS this is done by keeping the pressure in the ICR cell ultra low ($< 10^{-9}$ mbar). To accomplish this the use of any component (including electronic parts) which outgasses is avoided inside the vacuum system housing the ICR cell.

For fabrication of electronic circuits on printed circuit boards, FR4 fiberglass is the most common material (see Fig. reffig:fr4). A PCB is made of fiber glass and cladded with a thin layer of copper which is etched to make traces on the board. FR4 is easily machinable and is less lossy at high frequency. However FR4 when manufactured is left with several inclusions (air bubbles) and striations. The gas trapped in these pores act as a virtual leak when placed in UHV systems and take a long time to pump out. This limitation due to outgassing prevents their use for preamplifier circuits which are to be mounted near the ICR cell.

Fortunately there are a few high density ceramics such as MACOR which are developed as substrates for high power circuits. MACOR is ultra high vacuum (UHV) compatible and it also has a thermal conductivity 5 times that of FR4. This is highly advantageous as the heat dissipation is a concern for circuits in UHV systems as discussed further in section

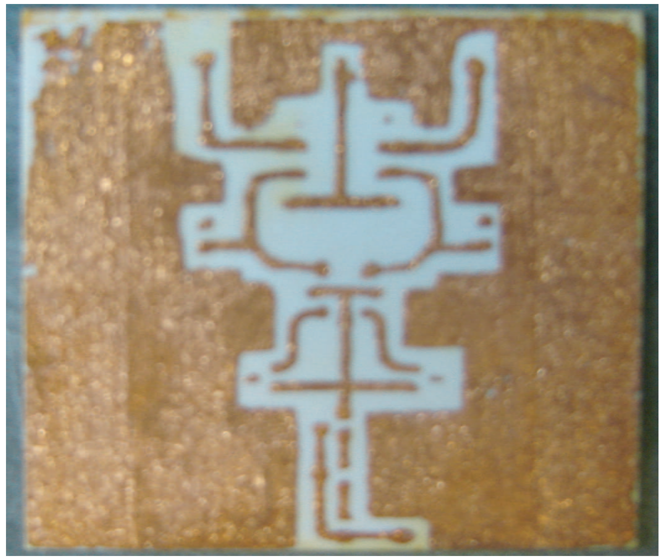

Figure 4·7: Etched Direct Bonded Copper.

4.1.9. A sample circuit board using direct bonded copper (DBC) etched in house is shown in Fig. 4·7

Outgassing of FR4 is not a concern in cryogenic FTMS, since when cooled to 4 Kelvin all the gas in the pores of the board freezes, thus not outgassing.

4.1.9 Low power dissipation

From section 4.1.1, we know that for higher SNR, the gain of the first stage is to be maximized. However increasing the gain generally increases the power dissipation in the preamplifier, which is the first stage of amplification. The preamplifier is placed inside the UHV for ICR signal detection. Under these low pressures, the convective cooling of the electronic components is essentially nonexistent. This severely restricts the allowable power dissipation in the preamplifier which in turn limits the gain and SNR of the preamplifier. A solution to this is to attach heat sinks to the preamplifier components which are in turn thermally anchored to the body of the instrument. However this is not always possible with surface mount components having micro packages.

In the cryogenic preamplifier power dissipation is also limited by the maximum allowable helium boil off. A 10 mW of heat load can dissipate approx. .336 liters of helium per day. Thus heat generated by the preamplifier is to be minimized.

4.1.10 Temperature Cycles

The preamplifier is placed inside the ultra high vacuum near the ICR cell. The complete ion optics and the ICR cell is enclosed in a titanium tube which is pumped down using several turbo molecular pumps. As discussed above it is important to achieve ultra high vacuum in the FTMS. Any water droplet or oil due to finger prints can act as a source of virtual leak that can take a long time to be pumped out. Thus, to clean the surface and facilitate quick pumping out of such particles, the chamber is baked to 100 °C using heating blankets for approx. 12 hours.

Baking of the chamber is generally done everytime the optics, circuits, and components inside the vacuum system are exposed to air. Thus the preamplifier PCB and the electronic components are subjected to several baking/temperature cycles. This can effect the performance of certain components of the preamplifier, specially the transistors. Extensive testing of the preamplifier under such conditions had to be conducted while monitoring the bias, gain and noise of the ICR detection amplifier for any deterioration. Only those components which can withstand such cycles can be used for the ICR preamplifier.

4.1.11 RF Shocks

The preamplifier inputs are connected to the detect plates which are in close proximity to the excite plates. A part of this excitation (200 Vp-p) gets coupled to the detect plates and thus appear at the input of the preamplifier. A preamplifier which uses Field Effect Transistors (FETs), and is designed to detect signals less than uVs, can get damaged when exposed to such sudden RF voltages. Also, transfer optics and multipoles which are used to get ions to the ICR cell, can carry around 1 kVp-p (1 MHz) RF. The preamplifier, which is in proximity to these components, should be able to sustain these electrical shocks.

4.2 Amplifier Specifications

We have identified several design requirements for our amplifier arising from various considerations. These requirements are described below.

4.2.1 Gain Requirement

Typically, the current detected on the ICR cell plates is in the order of few pA or less (Comisarow, 1978). This current is converted into a voltage signal before feeding it to the digitizer. The digitizer currently in use, which uses a 12-bit analog to digital converter, has voltage range of 400 mV. Hence, the quantization noise is approximately 100 μV. Thus, to take advantage of the full dynamic range of the digitizer, a transimpedance gain of approximately $10^9\Omega$ is required. In all designs, to convert the detected current into voltage, 1 $M\Omega$ resistors are connected at both the inputs of the preamplifier. A single charge, orbiting at half the cell radius in a 7 Tesla field at 54 kHz will generate around 20 nV of signal across this resistor. This voltage is then amplified with the preamplifier and the second stage amplifier. With a 1 $M\Omega$ resistor at the inputs, the preamplifier and the amplifier are required to have a combined voltage gain of approximately 1000 or 60 dB to provide an overall transimpedance gain of $10^9\Omega$.

4.2.2 Bandwidth Requirement

An FTMS is usually required to analyze ions in m/z range of 100 Da to 10 kDa. This is equivalent to a signal spectrum of approximately 10 KHz to 1 MHz. Thus, the amplifier is required to have a 3-dB lowpass bandwidth of approximately 1 MHz.

4.2.3 Power Constraints

The limit for power dissipation in the cryo-preamplifier has been set to 100 mW. Recall that this level of power dissipation will translate into 3.36 lt/day of liquid helium boil off. Although it is desirable to put more gain in the first stage of amplification, as previously this also increases the heat generated in the circuit. An effective trade off must therefore be made.

We have implemented two set of FTMS amplifier designs, room temperature designs using silicon FETs which were tested on FTMS with room temperature bore magnets, and the cryogenic amplifiers using GaAs FETs for the cryogenic FTMS. These amplifier designs were based on the issues discussed above and were evaluated on the bench for their bandwidth, gain and noise performance. The following chapters describe the results.

Chapter 5

Room Temperature FTMS Amplifier

This chapter has been reproduced in part with permission from the article, A Low-Noise, Wideband Preamplifier for a Fourier-Transform Ion Cyclotron Resonance Mass Spectrometer Journal of the American Society for Mass Spectrometry, Volume 18, Issue 12, December 2007, Pages 2233-2241 Raman Mathur, Ronald W. Knepper and Peter B. OConnor. Copyright 2007 Journal of The American Society for Mass Spectrometry.

In order to gain experience and acquaintance with the design issues several low noise wideband amplifiers using silicon components were designed for room temperature FTMS. These amplifiers developed for an FTMS are based on the discussed design rules earlier. Here we classify them as first generation amplifiers and the second generation amplifiers. The performance of these amplifiers was evaluated in terms of gain, bandwidth, and noise on the bench. Satisfactory designs were then tested on a MALDI-FTMS, and compared to a commercial amplifier.

As discussed earlier, the ICR detection amplifier is divided into 2 stages: An in-vacuum preamplifier and a second stage amplifier which is at atmospheric pressure. The preamplifier is used primarily to convert the high impedance of the ICR signal to a low impedance, with a corresponding current gain and very low noise. Further, the voltage amplification, which requires more power, is done outside the vacuum. This is done because the extremely low pressure in the FTMS (order of 10^{-10} mbar) hinders efficient cooling of the devices which ultimately can cause power derating or device failure. Thus, most of the signal amplification is done in the second stage. However, the equivalent input noise of the ICR detection circuit is primarily defined by the in-vacuum preamplifier.

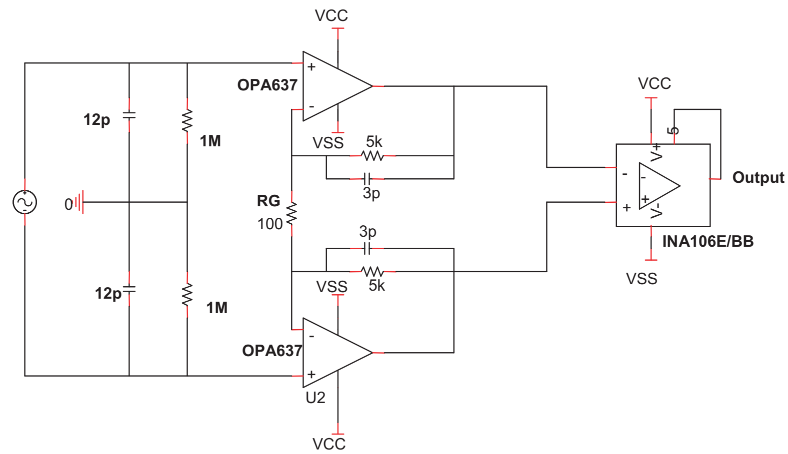

Figure 5·1: Classical-Instrumentation Amplifier

5.0.4 First Generation BUSM Amplifiers

Classical-Instrumentation Amplifier

The first attempt at an improved amplifier design used a classic instrumentation amplifier, primarily to understand the gain and the stability issues that need to be addressed. Fig. 5·1 shows an op-amp based classical–instrumentation amplifier circuit. This topology uses three op-amps and was the first obvious choice, because of its following salient features:

1. It has high input impedance at both the differential inputs.

2. It has high Common Mode Rejection Ratio (CMRR).

3. A High and simple Gain selection.

Design

The input op-amps are used to buffer the input signal. The high input impedance is achieved by using FET input op-amp, $U1$ and $U2$ in Fig. 5·1 (OPA637). The input resistance of the OPA637BB (Burr Brown) is approximately 10^{13} Ω in parallel with 8 pF, and it has a very low bias current (1 pA). These characteristics make OPA637 well-suited for the input stage. The full differential voltage appears across R_G, which can be varied to change the differential gain. The complete symmetry of the input circuit ensures that any common mode signal which comes at the two summing points, will not flow through RG, hence won't be amplified. Therefore, the differential signal is amplified by a factor of (1+2 $* R_G/R_F$) but common mode signals are passed with unity gain. These common mode signals are canceled at the second stage by using a difference amplifier. INA106, $U3$ is used as a difference amplifier, which is a low noise, precision gain, difference amplifier, with a gain of 10. The voltage gain of the circuit is equal to $(1 + 2 * R_F/R_G) * 10$.

Measurement and Testing

1 Mohm resistors were used in all designs to have a fair comparison in terms of signal to noise ratio, between all the designs. A 20 pF capacitor was connected at the input of the preamplifiers being tested to model the capacitance due to detection plates.

The instrumentation amplifier was constructed on a circuit board and tested on bench. The measured gain versus frequency plot is shown in Fig. 5·2. The measured gain of the instrumentation amplifier was approximately 32 dB and bandwidth was 580 KHz.

We also measured the input short circuit rms voltage noise of the instrumentation amplifier. The noise voltage measured was 423 $nV/\sqrt{Hz}$ at 10 KHz. The power dissipated in the instrumentation amplifier was measured to be 280 mW.

The instrumentation amplifier thus designed and tested didn't meet the requirements for FTMS. The bandwidth of 580 KHz was not sufficient to cover the required m/z range of 100 Da to 10 KDa, the power dissipation was too high, and the voltage noise was also high.

5.0.5 Si-based JFET Amplifier

The analysis above showed that the classical instrumentation amplifier performed well on gain, but poorly on noise and bandwidth. Thus a three-stage low noise amplifier was built as a basic preliminary design for the cryo-preamplifier.

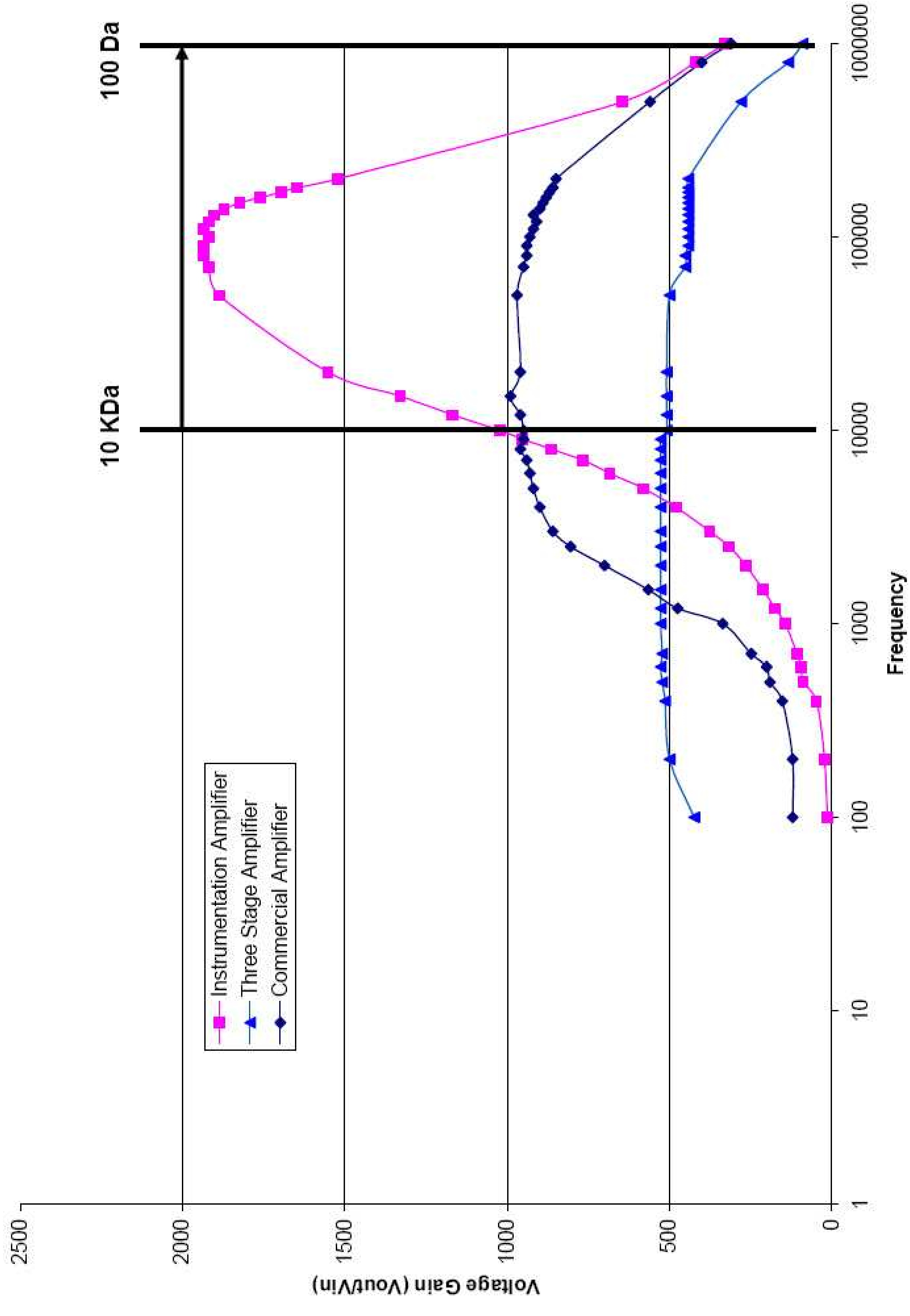

Figure 5·2: Measured Gain Plot of Instrumentation Amplifier

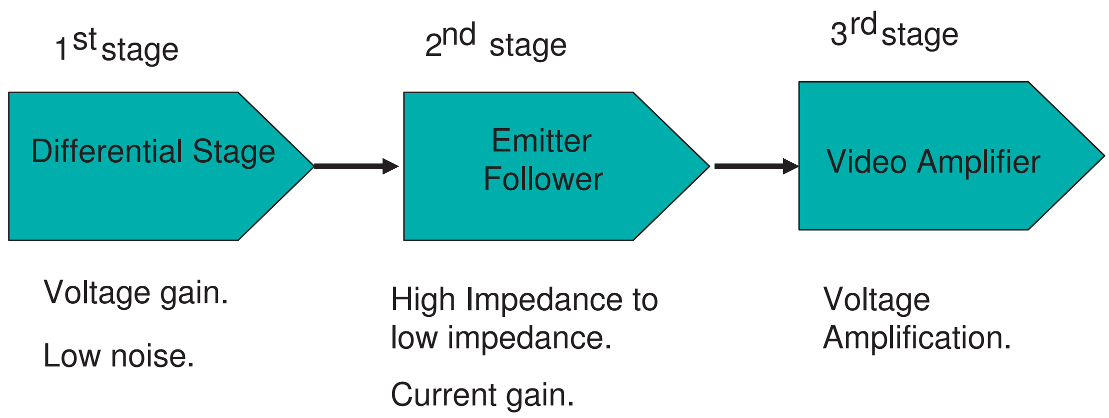

Figure 5·3: Block diagram of the 3 Stage Amplifier

Design

Block Diagram of the Si-based JFET amplifier is shown in Fig. 5·3 describes primary attribute of each stage. The circuit diagram of the Si-based JFET amplifier design is shown in the Fig. 5·4. The first stage consists of a differential cascode, with a self biased constant current source. The cascode pair increases the achievable bandwidth by reducing the Miller effect (Jefferts and Walls, 1987). Then the signal is fed into a BJT emitter follower. The emitter follower has a low output impedance, which decreases the resistive loading on the last stage. INA106 (Texas Instruments, 2005), a precision gain amplifier is used as the final output stage.

The gain of the input differential stage is approximately $g_m \times R_D = 60$. The emitter follower stage is a unity gain stage, followed by the INA106.

Measurements and Testing

The Si-based JFET amplifier was mounted on a printed circuit board for electrical testing, Fig. 5·5. The measured ac response is shown in Fig. 5·2. The voltage gain of the amplifier was equal to 54 dB with a bandwidth of 800 KHz. The measured input rms noise voltage was equal to 29 $nV/\sqrt{Hz}$ at 10 KHz.

The noise performance of the Si-based JFET amplifier was around 15 times better than

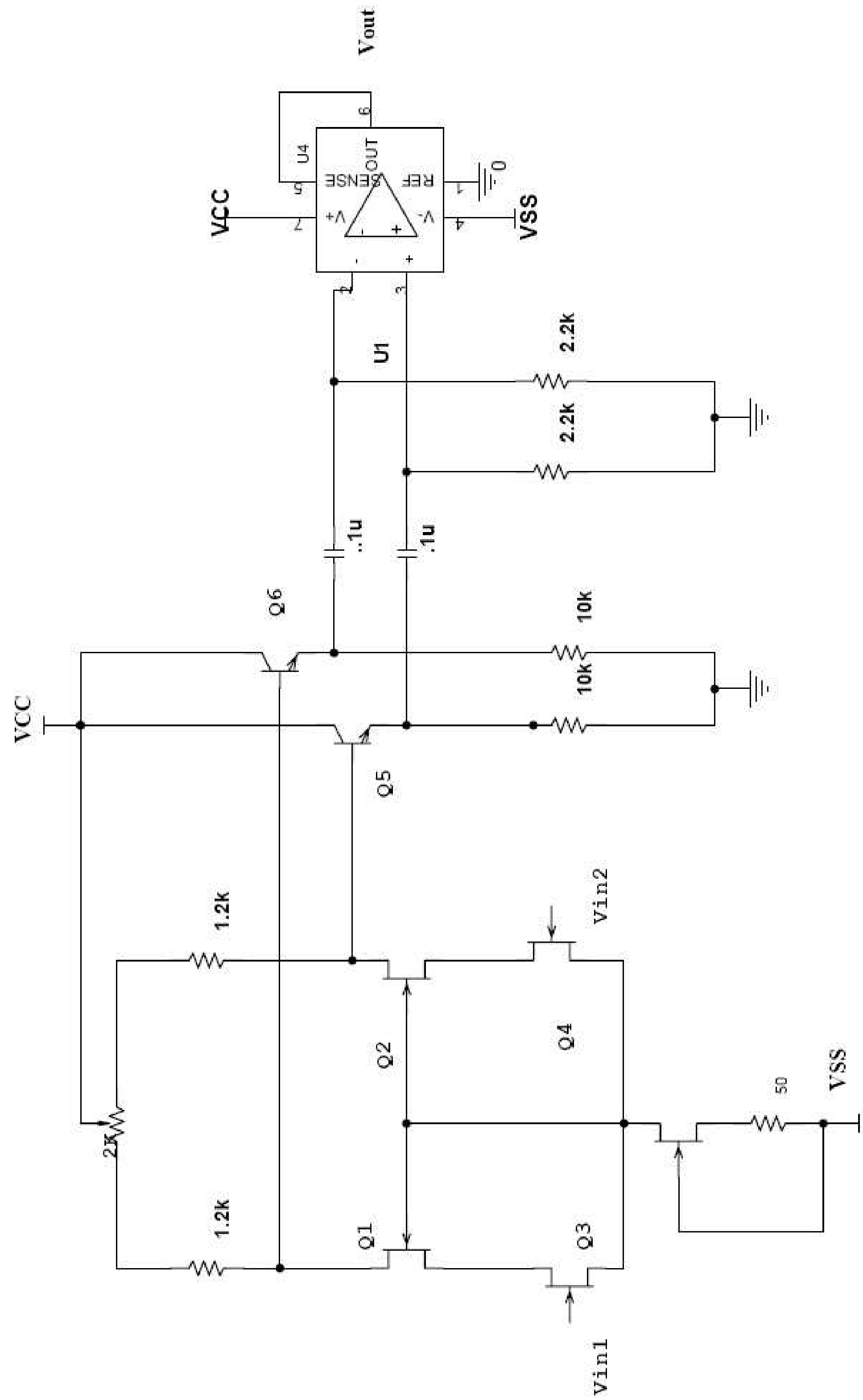

Figure 5·4: Three stage Amplifier

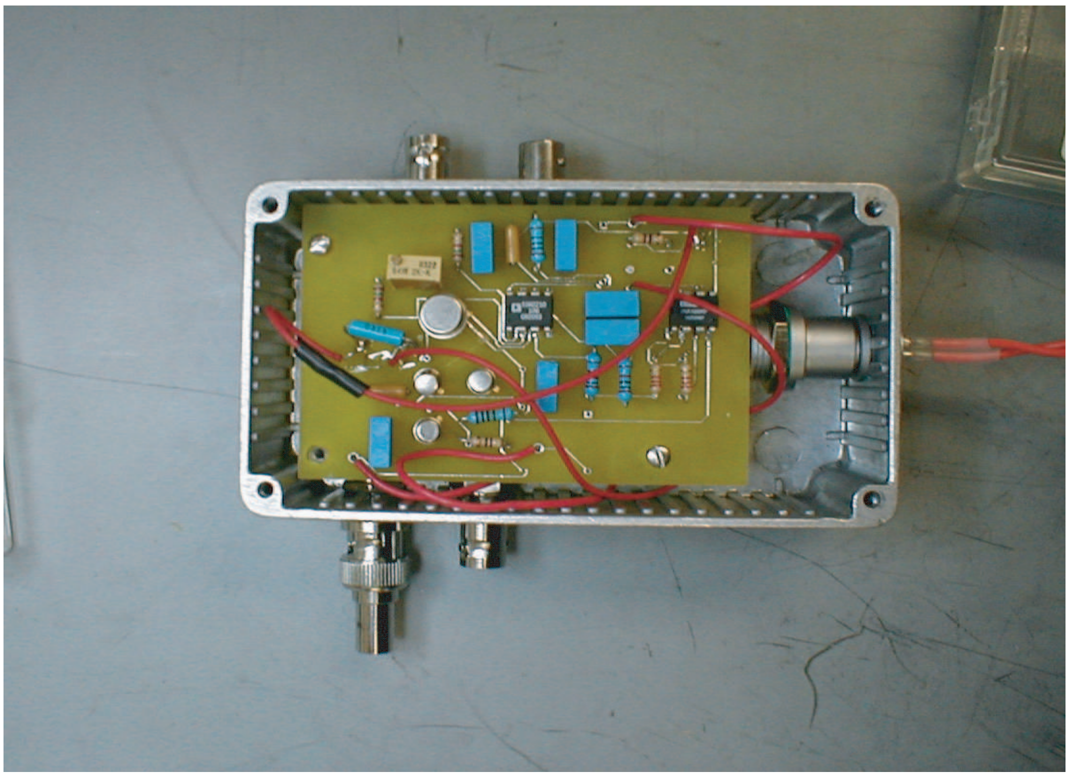

Figure 5·5: Three stage Amplifier

Table 5.1: Performance of Transimpedance Amplifiers (TIA's) at Room Temperature

Amplifier Type	Voltage Gain	Bandwidth	Input noise voltage @10KHz
Commercial TIA	970	400K Hz	415 $nV/\sqrt{Hz}$
Instrumentation Amplifier	1800	180K Hz	423 $nV/\sqrt{Hz}$
Si-based JFET TIA	500	380K Hz	28 $nV/\sqrt{Hz}$

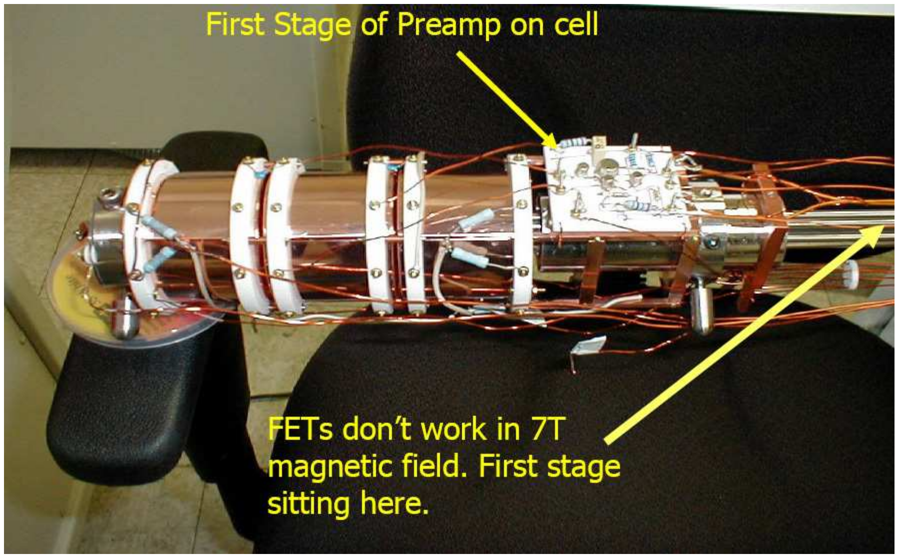

Figure 5·6: First Stage of the three stage design on cell

the instrumentation amplifier and the commercial amplifier (IonSpec Inc.).

A summary of results which compare the first generation amplifiers with the existing commercial amplifier in terms of (i) gain, (ii) power consumption, (iii) noise, and (iv) bandwidth performance, as summarized in Table 5.1.

Comparison of Si-based JFET amplifier design with commercial amplifier on FTMS

To evaluate the performance of the Si-based JFET amplifier further, a comparative study between the Si-based JFET amplifier and a commercial FTMS amplifier from Ionspec Inc. was done. For this purpose a vacuum compatible version of Si-based JFET amplifier

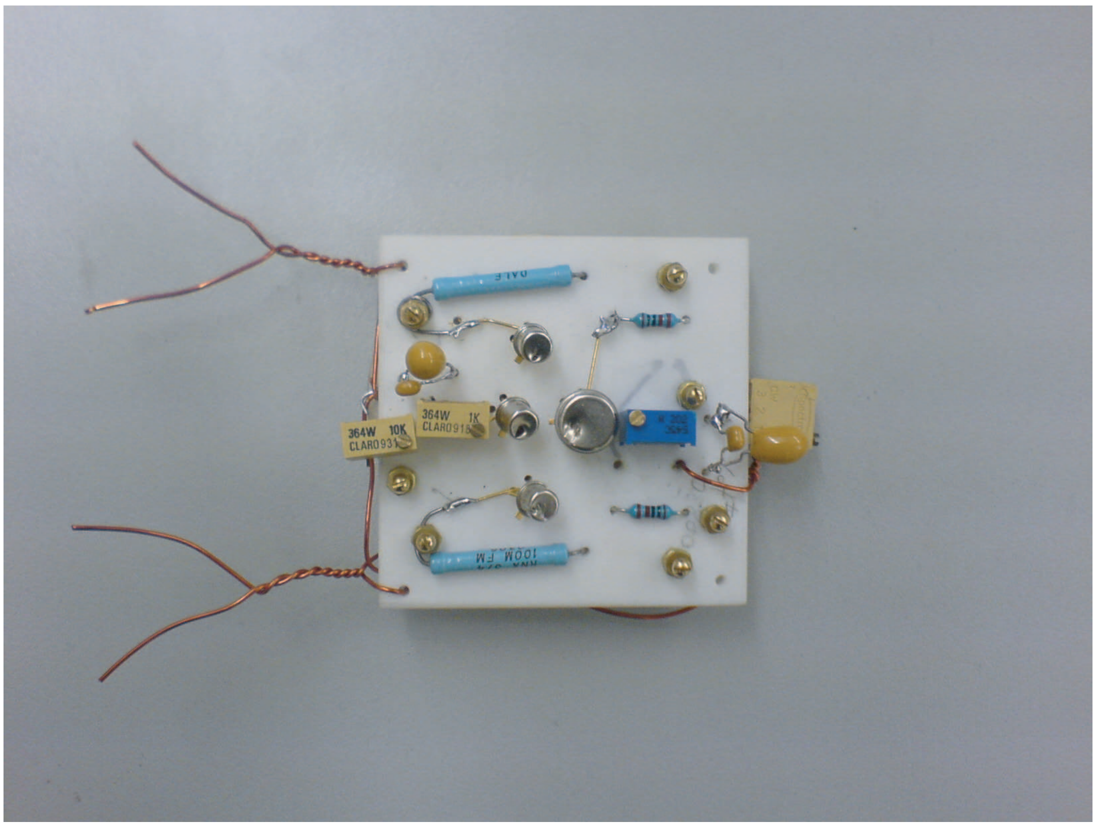

Figure 5·7: First Stage of the three stage design on MACOR Block was developed. As we know FR4 outgasses and is not recommended for ultra-high vacuum (UHV) systems. Instead, MACOR was used. MACOR is a kind of machinable ceramic with high density. The preamplifier circuit mounted on the MACOR block is shown in Fig. 5·7. Testing of both the amplifiers was done under identical conditions, on the home built Electrospray Fourier Transform Mass Spectrometer (ESI-FTMS). The input differential stage of the Si-based JFET amplifier design was mounted on the cell, as shown in Fig. 5·6. The second and third stage were mounted on a PCB and placed outside the vacuum chamber.

Zinc ions were generated in the ICR cell, excited to higher cyclotron orbits and then detected using the amplifier. The acquired mass spectra showing the isotopic distribution of Zinc are shown in Fig. 5·8, using each of the amplifiers, one by one.

Overall the signal to noise ratio of the detected signal from the Si-based JFET amplifier was found to be approximately 2.5 times better than that of the commercial amplifier. The presence of many high frequency noise peaks was also noticed in the mass spectra. These peaks were mainly due to interference and were eliminated by proper shielding and grounding of connecting cables.

5.0.6 Second Generation BUSM Amplifiers

The circuit diagram of the second generation BUSM (Boston University School of Medicine) in-vacuum preamplifier is shown in Fig. 5·9. The cascode configuration was used to reduce the Miller effect, hence enhancing the bandwidth of the preamplifier (Miller, 1920).

The gate of the cascode device is tied to the source of the input device, to minimize the input gate leakage current. The source to drain voltage of Q1 and Q2 now becomes the gate to source voltage of the Q3 and Q4. This requires for the drain to source voltage of the input devices (Q1, Q2) to be much less in magnitude than the pinch off voltage of the cascode devices (Q3, Q4). This configuration limits the drain to source voltage of Q1, Q2 to small values which keeps the leakage current negligible in the JFETs, independent

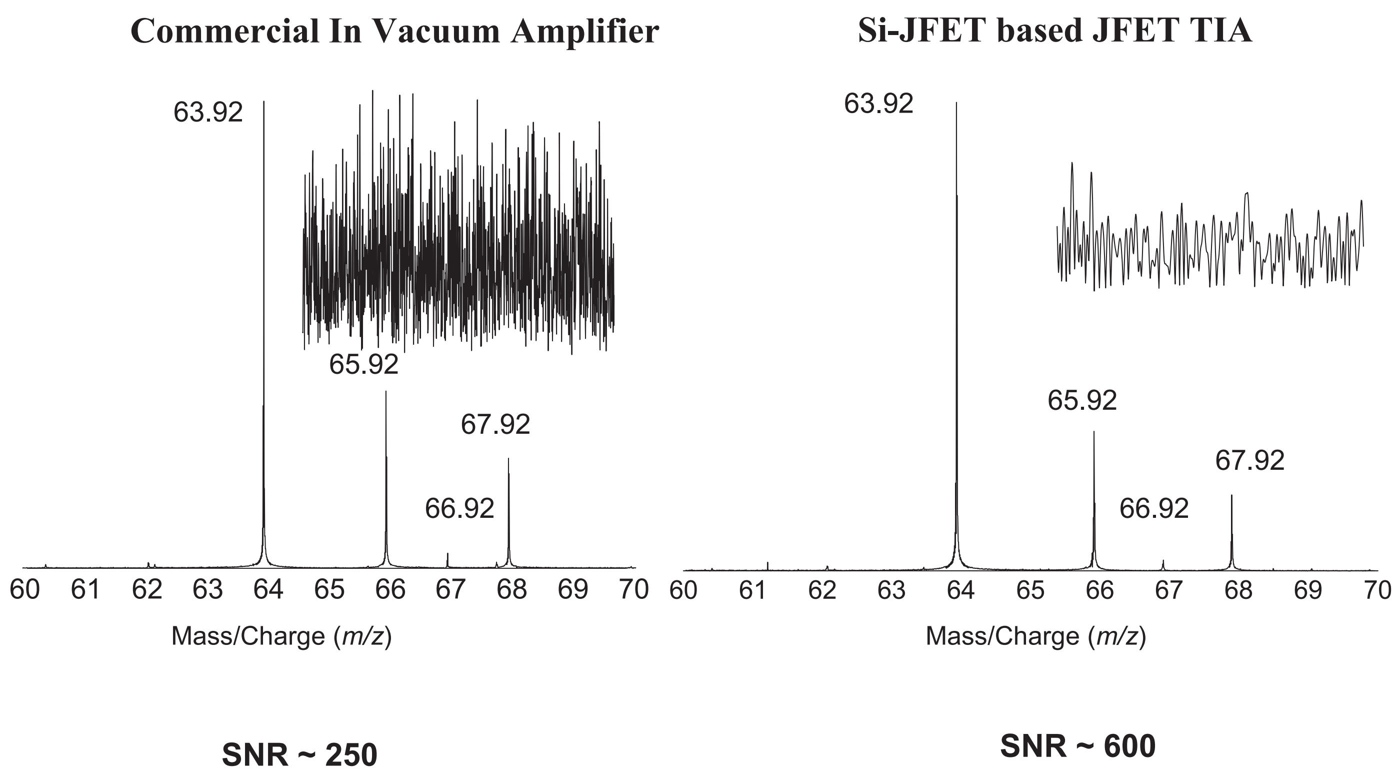

Figure 5.8: Mass Spectrum of Zinc isotopes

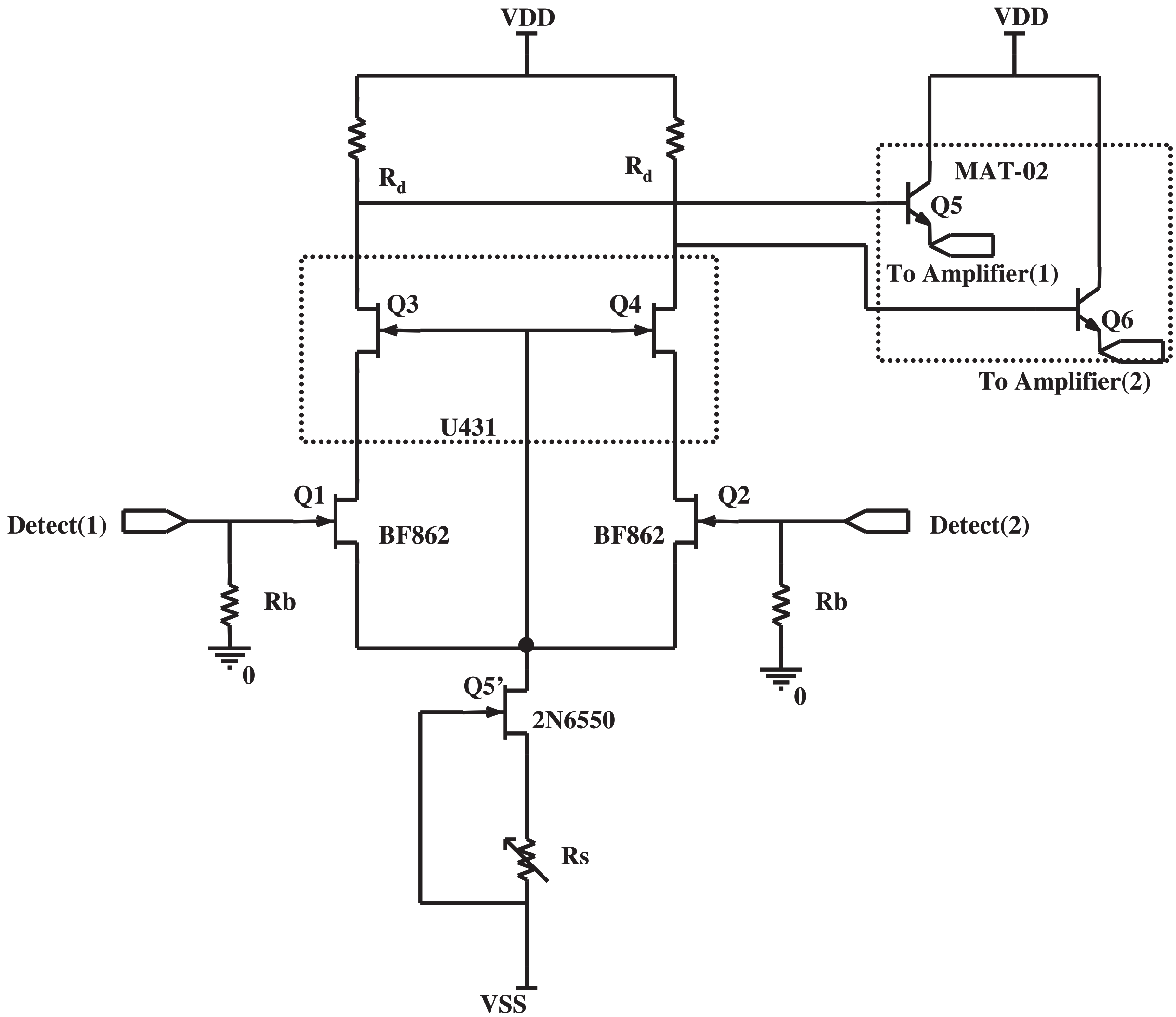

Figure 5·9: Schematic of the BUSM low noise wideband transimpedance Preamplifier.

of the drift in the supply voltage. A current mirror using matched npn's was used to bias the JFETs. The high output impedance of the current mirror enhances the CMRR of the differential stage as discussed previously.

Emitter followers, Q5 & Q6, are used for impedance transformation of the ICR signal (from high to low). Low impedance on the long lines running from preamplifier to the electrical feed-through makes the amplifier less susceptible to interference pick up and noise coupling. Once the impedance level of the signal is low, a generic low noise operational amplifier (opamp) can be used for further amplification. A low noise instrumentation amplifier configuration is used for this purpose, using standard opamps as shown in Fig. 5·10. Finally, the output of the amplifier is fed to an ADC for digitization.

5.1 On Bench Circuit Testing

JFETs from NXP Inc. (Eindhoven, The Netherlands), BF862, were used as input transistors. The ICR signal is inherently a differential signal, and thus, the amplifier is a differential design. A close symmetry (matching) of the components in the 2 legs of the differential amplifier is required for a high common mode rejection ratio, and because commercial JFETs show wide variation in characteristics, several of these were tested to find a pair with closely matched DC characteristic curves. The set of curves for the 2 of these matched JFETs are shown in Fig. 5·11. The operating curves of U431's is shown in Fig. 5·12.

Matched JFETs U431 from Vishay Intertechnology, Inc. (Malvern, PA) were used as the cascode devices. BF862 has an input capacitance of 10 pF and input noise voltage of 0.8 nV/rtHz, and represents the optimal trade off between noise and input capacitance. Low leakage JFETs and the above configuration allowed the use of high value input bias resistors, 1 GΩ, to elevate the signal/noise ratio. BF862's were biased at VDS=1.5 volts and IDS=8mA giving a g_m of approx. 35 mS. From Eq. 5.1 derived in previous chapter, it is desired to operate the input JFET at IDSS where the gm is maximum, thus minimizing

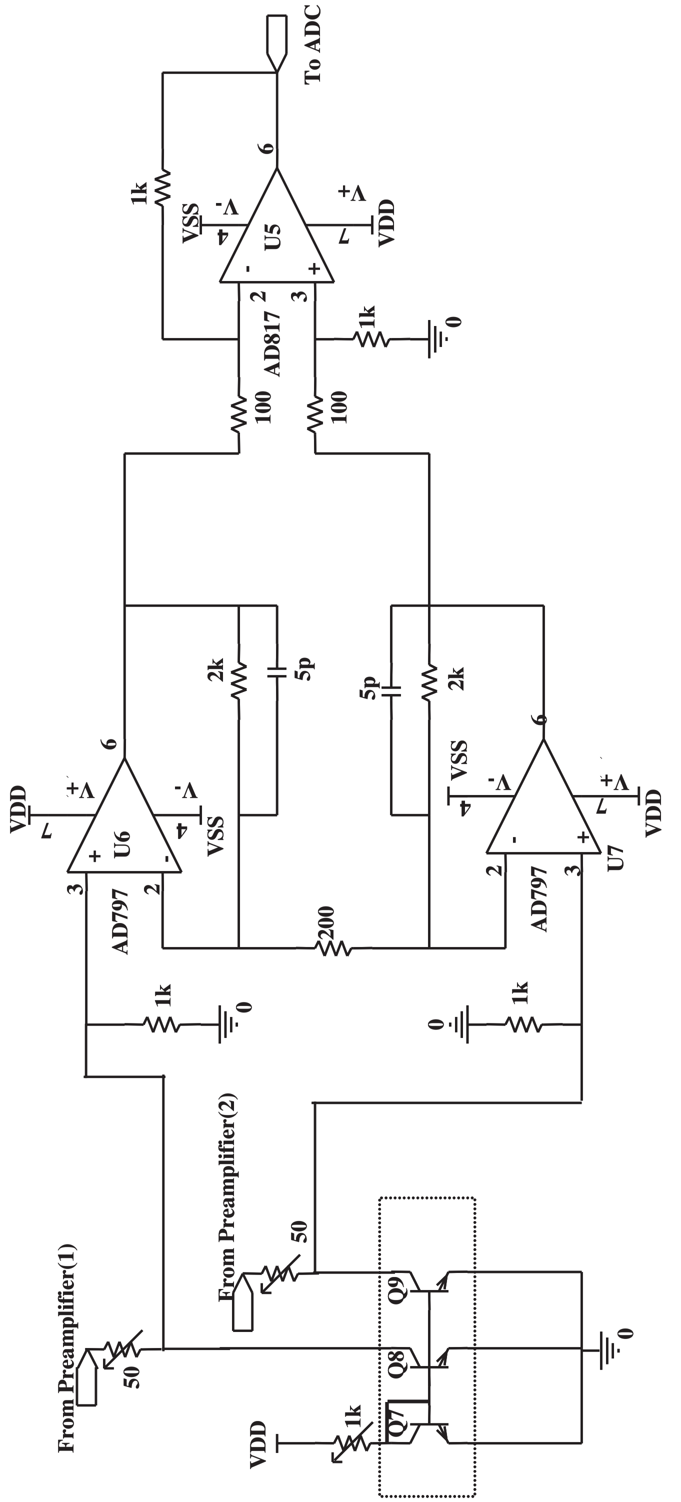

Figure 5·10: Schematic of the BUSM Instrumentation Amplifier.

the channel thermal noise. However the power dissipation in the JFET can cause the device to heat, specially as it is in vacuum. This would result in an increase in the leakage current [1]. The 750 Ω R_d provided a voltage gain of approx. 25 in the first stage. The emitter follower reduced the signal impedance level to approx. 50 ohms, primarily due to the balancing potentiometer at the emitter of Q5 & Q6. The constant current sources, Q7 – Q9, kept the base-emitter voltage of Q5 & Q6 equal and constant. This ensures that the current gain (CMRR/differential gain) is identical for each signal line.

$$signal/noise = \left(\frac{3N^2q^2r^2}{16d^2kT\Delta f}\right)\left(\frac{g_m}{C_{FET}}\right)\left(\frac{1}{C_{FET}(1+C_t/C_{FET})^2}\right) \tag{5.1}$$

The voltage gain versus frequency characteristic plot of the BUSM amplifier is shown in Fig. 5·13. The -3dB high frequency roll-off of the transimpedance amplifier is at 2.81 MHz which corresponds to approx. 30 Da on a 7 Tesla FTMS. The midband voltage gain of the amplifier is $\approx$ 3500.

The electrical noise performance of the BUSM transimpedance amplifier was compared with that of a commercial amplifier from Ionspec Inc., Fig. 5·14. The commercial amplifier consists of a unity gain source follower, using OPA637, as a preamplifier followed by a high gain instrumentation amplifier. The BUSM transimpedance amplifier was powered either by switching power supplies (Agilent Technologies, Santa Clara, CA) with unshielded cables in the room or by 9 volt batteries. The commercial amplifier was powered by linear power supplies (Varian Inc., Lakeforest, CA).

The equivalent input rms noise voltage was measured by shorting the inputs of the preamplifiers to ground. A Tektronix spectrum analyzer (Tektronix 2712) was used to obtain the short circuit output noise spectrum from 10 kHz to 1 MHz. To compare the two amplifiers the output noise spectrum was divided by the corresponding voltage gain spectrum to obtain the input equivalent rms noise voltage density as shown in Fig. 5·14.

[1] Leakage current increases exponentially with temperature in a JFET.

The BUSM transimpedance amplifier has shown approximately 40 times lower rms noise voltage using the batteries (at 100 kHz), compared to the commercial amplifier. Also, the 1/f noise corner frequency is more than 10 times lower in the case of the BUSM transimpedance amplifier.

5.2 Instrument Testing

A custom MALDI-FTMS was used to evaluate the low noise ICR amplifier (O'Connor et al., 2004). The instrument has an open cylindrical ICR cell geometry with 3 inch O.D. The BUSM preamplifier was fabricated by etching the circuit layout on Direct Bonded Copper (DBC) in house using Ferric Chloride. DBC is essentially consists of a high density ceramic such as MACOR or Alumina coated with a layer of copper, typically used for high power circuits because its thermal conductivity is higher than FR4. It is UHV compatible and provides the use conventional etching or lithography techniques to fabricate complex circuits. The etched DBC and the preamplifier circuit mounted on the DBC is shown in Fig. 5·15.

The preamplifiers were mounted close to the detection plates minimizing the connecting wire parasitic capacitance. Magnet wire from McMaster-Carr (Princeton, NJ), which is enamel coated copper, is used for all in-vacuum electrical connections. The outputs from the in-vacuum preamplifier are connected to the instrumentation amplifier via a con-flat BNC electrical feed-through (MDC Vacuum Products, Hayward, CA). It is always recommended to remove any noise component outside the desired bandwidth using a filter. Thus, a low pass, 11th-order Butterworth filter from TTE Inc. (Los Angeles, CA.) is used before the digitizer to remove any unwanted noise above 1 MHz. Several sets of mass spectra were obtained to compare the signal/noise ratio of the current amplifier with the commercial one.

C_{60} was used as a standard for the studies on a custom MALDI-FTMS (O'Connor et al., 2004). A 1 μM solution of C_{60} in toluene was spotted onto a stainless steel plate and allowed to dry. Spectra were generated using a single shot of a 355 nm Nd:YAG laser from Continuum Inc. (Santa Clara, CA.) at 50 μJ/pulse. The ions were transferred to the ICR cell using a pair of hexapoles driven by high voltage RF oscillators (O'Connor et al., 2002; Mathur and O'Connor, 2006) and were trapped using gated trapping. After 50 ms of thermal stabilization, the ions were resonantly excited into coherent cyclotron orbits by the application of a broadband RF sweep. The RF sweep voltage of 200 V_{p-p} was applied for 8 ms and swept from 150 Da to 3000 Da. The excitation was followed by image current detection using the amplifier under test. 512K samples were taken from the amplified ICR signal at a rate of 2 MHz (total transient length of 0.262 seconds). The digitized data was zero filled to 1024K points and Fast Fourier transformed without apodization (Aarstol and Comisarow, 1987). The resulting magnitude mode frequency spectra were converted to a mass spectra and are shown in Fig. 5·16. The detected signal, using the BUSM low noise differential amplifier, Fig. 5.16(b), demonstrated approximately a 25 fold reduction in noise compared to the commercial one, Fig. 5.16(a). In this comparison, the commercial in-vacuum amplifier was powered with linear power supplies, but the BUSM transimpedance preamplifier was powered with unshielded switching power supplies. Subsequent tests showed an additional ≈ 4 fold reduction in noise when the power supplies were swapped to a shielded battery powered supply (Fig. 5·14). The plots in Fig. 5·14 represent the short circuit input noise, while this C_{60} comparison is for an open, capacitive input impedance, so the plots are not directly comparable.

Although Fig. 5.16(b) shows an apparent ≈ 30 fold improvement in signal/noise ratio. But, due to shot-to-shot instability in laser desorption/ionization, this may be a less useful comparison. It should be noticed that the family of peaks which appear besides the C_{60} isotopes in Fig. 5.16(b) are due to several reasons; namely, the characteristic Lorentzian line shape of the isotopic peaks, Gibbs oscillations, and the mixing of axial/magnetron motion frequencies (sidebands) with the cyclotron frequency. Furthermore, RF interference noise can cause (and did in this case) a transient to "clip", which generates further mixing artifacts. Fig. 5·17 shows the complete broadband *m/z* range of the MS in Fig. 5.16(b) obtained with BUSM amplifier.

5.2.1 Low Noise Biasing of the Preamplifier

The noise plot of the room temperature amplifier in Fig. 5·14 clearly states the importance of a clean biasing technique for the preamplifier. The comparison of batteries with power supplies is more contrasting in Fig. 5·14 as switching power supplies were used. Switching power supplies generate output voltage by switching a transistor between its cut-off and saturation region. This switching directly manifests as noise with regular harmonics and apparently also with white noise (as shown in Fig. 5·14) in the output voltage. Thus, switching power supplies are not well suited for biasing low noise preamplifiers.

To achieve ultra low noise performance from preamplifiers, batteries are used to supply the bias currents. One of the major drawbacks using batteries is they have finite power capability or ampere $\times$ hours, and thus requires recharging or replacement. In an FTMS sequence of events, Fig. 5·19, ions are generated in the source and transferred to the ICR cell via multipole ion guides. Then they are cooled, resonantly excited and detected. A typical pulse sequence lasts for 2 to 3 seconds and the detection, which is the duration when the preamplifier is detecting the signal, is approx. 500 msec. Thus, we have used a FET switch, ADG453, from Analog Devices, Inc., to turn-on the preamplifier only during the detection (Fig. 5·18). This preserves the battery power. Another reason to keep the preamplifier on for s short duration, is the power dissipation in the components. If we recall from the previous chapter 4, the cooling of the preamplifier inside the UHV FTMS system is not efficient. Thus if the preamplifier is powered only for short duration using a switch ($\approx$ 500 ms in a 2 sec pulse sequence) the electronic components do not heat up significantly. And they have time to cool down between the detects for consecuteive pulse sequences. The on resistance, R_on of the FET switch is less than 4 ohms, which accounts for only 60 mV of voltage drop, thus providing the complete supply voltage range for the preamplifier. It has fast switching time, around 40 ns, and is controlled using TTL logic from the current datasystem. The maximum current it can pass is around 100 mA; thus, it provides an added protection to the preamplifier from high current surges from the batteries.

Another issue with using batteries to bias preamplifiers is that they contain a large amount of energy, and if released by a fault, either by reverse connections or temporary short, it will source large amount of current which can potentially and permanently damage the circuit. Typically a battery can source amps of current in microsecond a which requires the protection circuit to act fast. This makes regular fuses obsolete as a protection.

5.2.2 Preamplifier Overload Recovery

The rf sweep voltage on the excitation plates to energize the ions is of the order of 50 volts. A portion of this voltage ($\approx$1 volt) gets coupled to the detect plates which are connected to the input of the preamplifier. This voltage completely saturates the preamplifier. For example, in the time domain signal in Fig. 5·20 the preamplifier is saturated for the first 15 msec of the detection period. In other words, the overload recovery time of the amplifier is $\approx$15 msec after an excitation voltage of 100 Vp-p. However, we know that the initial time after the excitation is when the induced signal on the detect plates is maximum as the ion orbital radius is maximum, and if the preamplifier is not recording any signal during that time, it deteriorates the SNR.

To minimize this overload recovery time we have added clamping diodes at the input and the output of the preamplifier as shown in Fig. 5·21. The high impedance nature of the ICR plates requires the diodes with minimal capacitance and leakage. For this purpose Schottky diodes, BAS70 from Vishay Intertechnology, Inc. (Malvern, PA) were used. The input capacitance of these diodes is merely 3 pF, and the low forward voltage, Vf = 0.3 volts ensures that the preamplifier is not overloaded during excite events.

While, the overall performance of the BUSM amplifiers was encouraging, it was designed using Si-JFETs, which cannot be used at cryogenic temperatures. Thus, a further design was done using GaAs MESFETs.

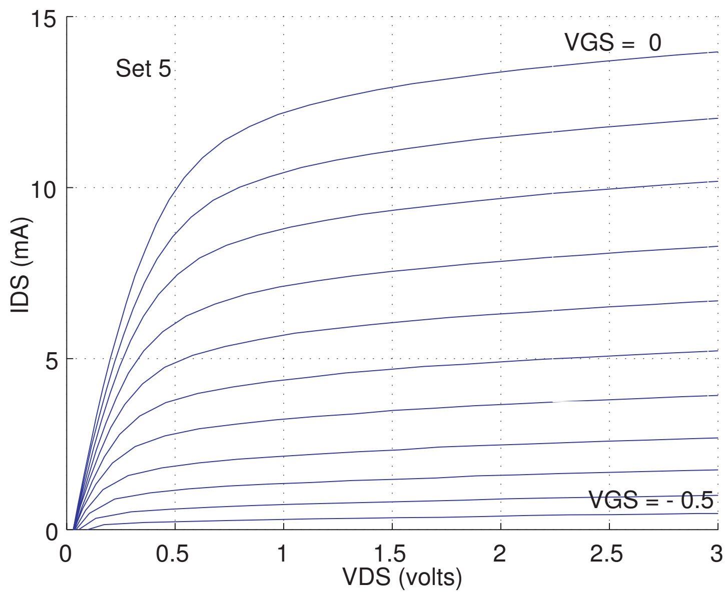

(a) BF862 Set5

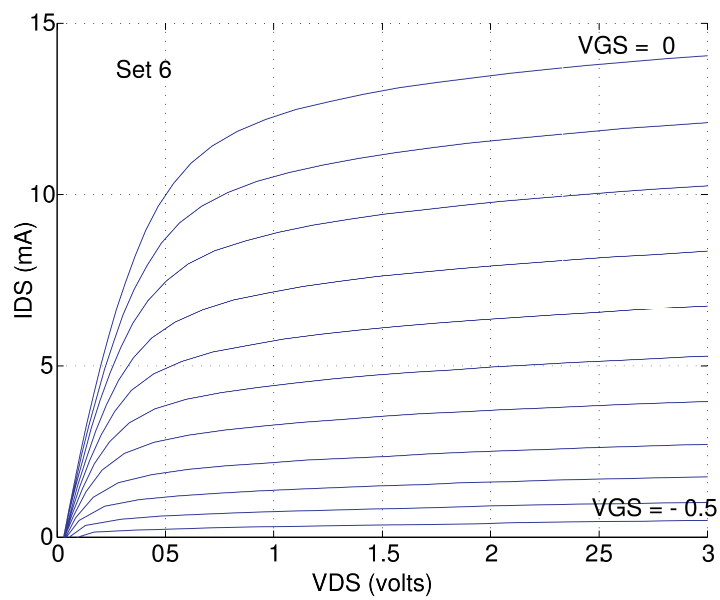

(b) Set6

Figure 5·11: Drain Current versus Drain-source voltage of the selected matched JFET pair

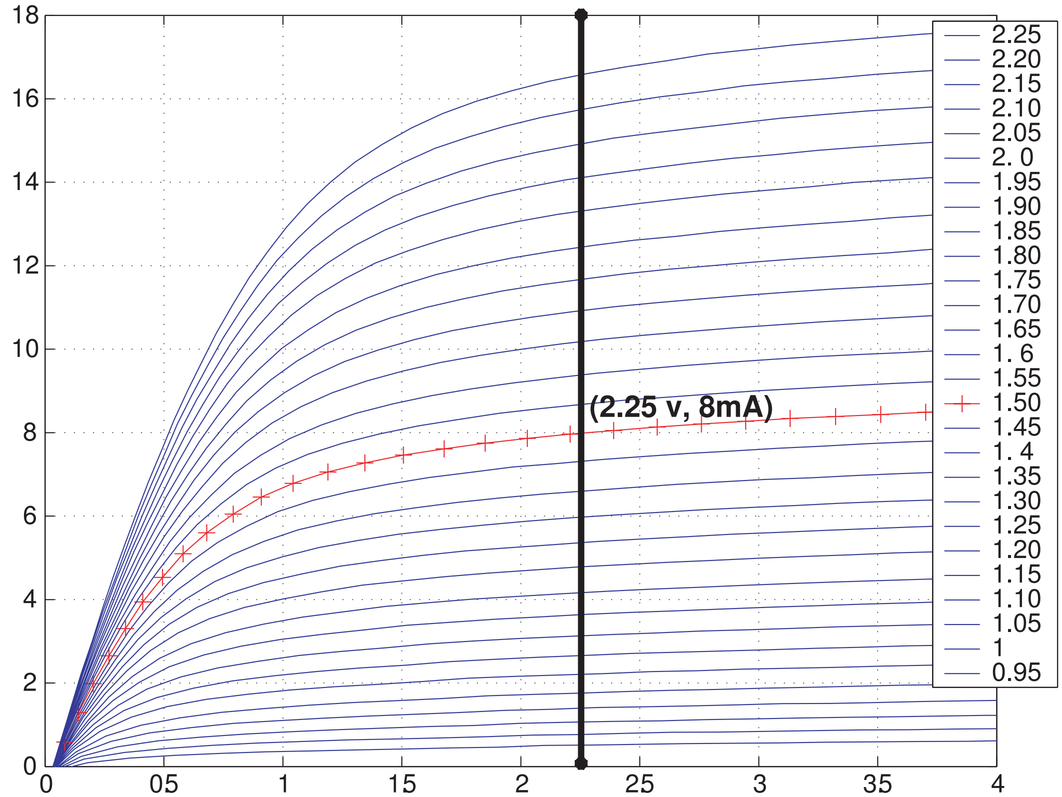

Figure 5·12: DC Characteristics of U431 (Cascode Device).

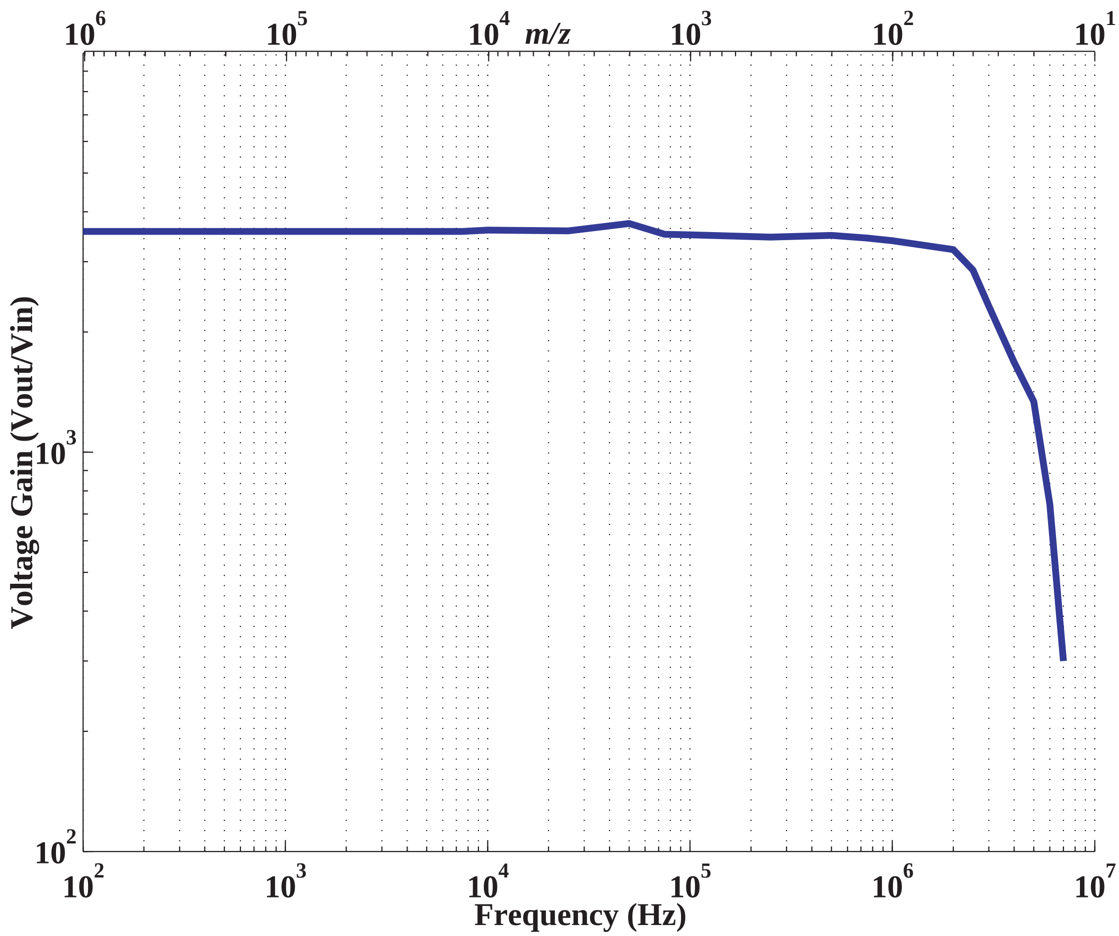

Figure 5·13: Gain Bandwidth plot of the low noise wideband BUSM Transimpedance Amplifier.

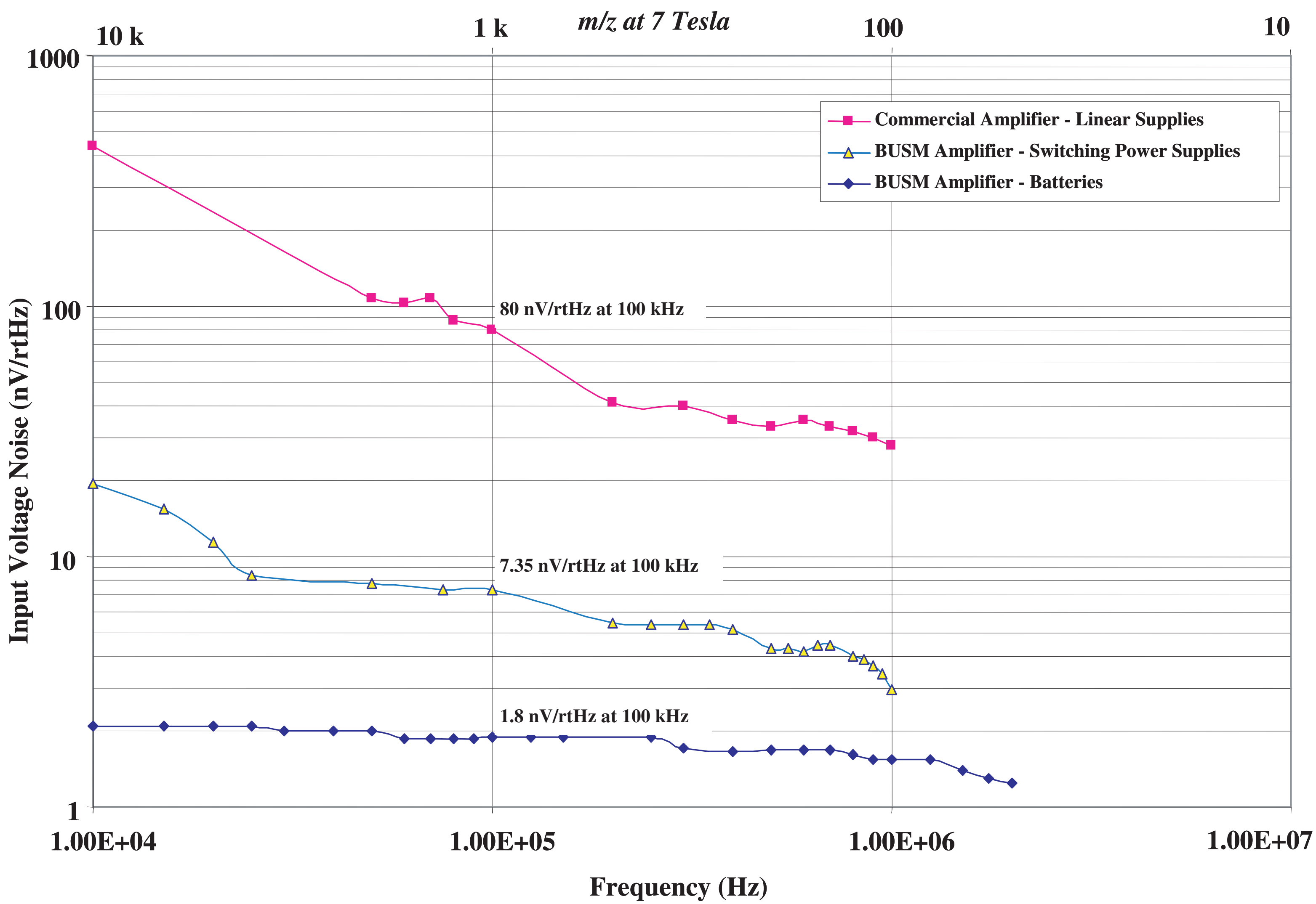

Figure 5.14: Equivalent input r.m.s noise voltage density of the two amplifier designs.

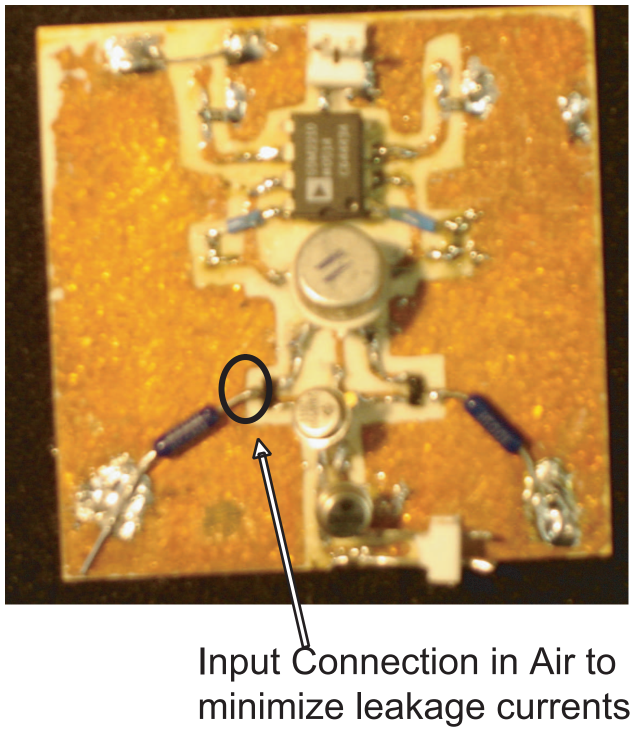

Figure 5·15: Etched Direct Bonded Copper.

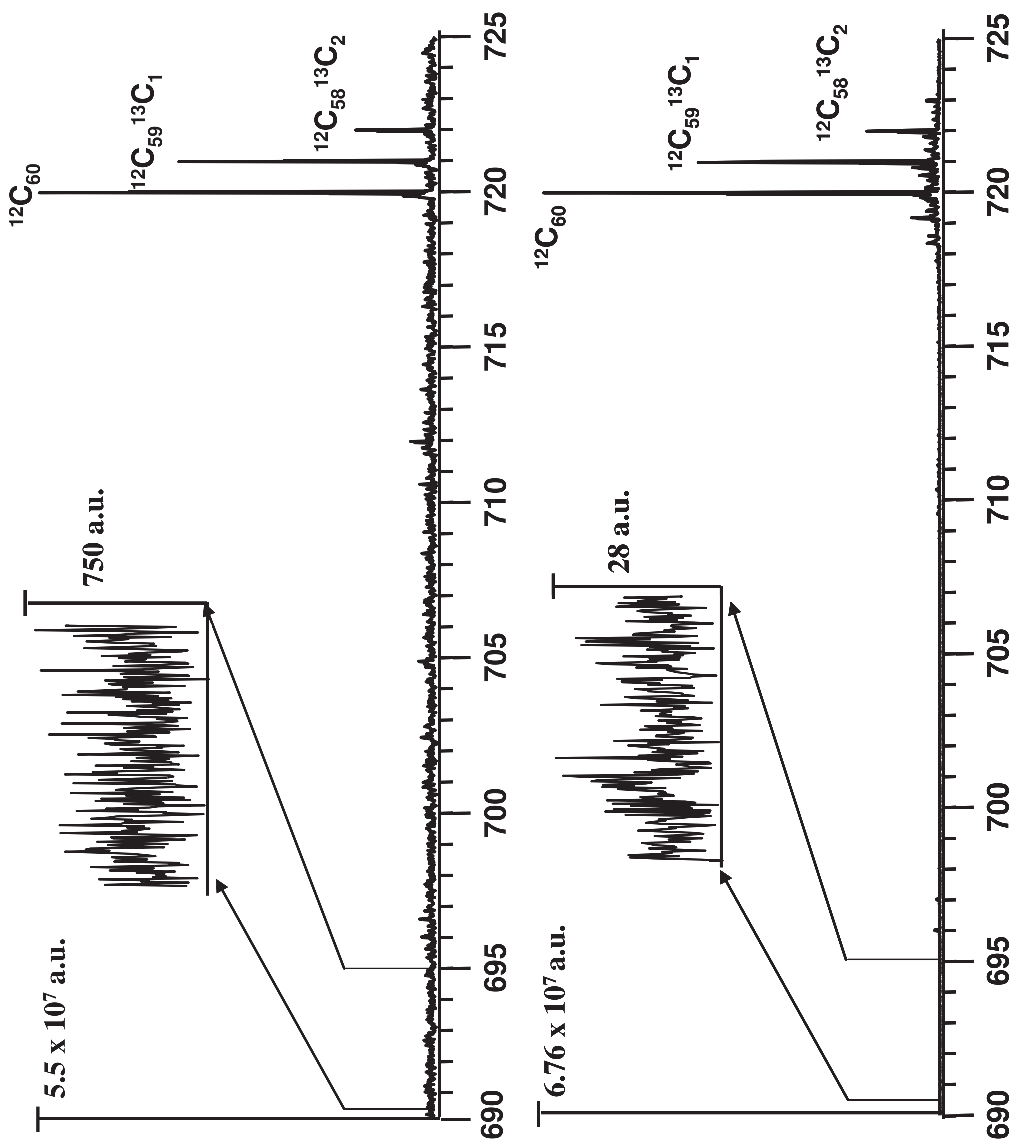

(a) C_{60} MS using Commercial Amplifier (b) C_{60} MS using BUSM Amplifier

Figure 5·16: MS of C_{60} obtained using two amplifiers with identical instrument settings on a MALDI-FTMS

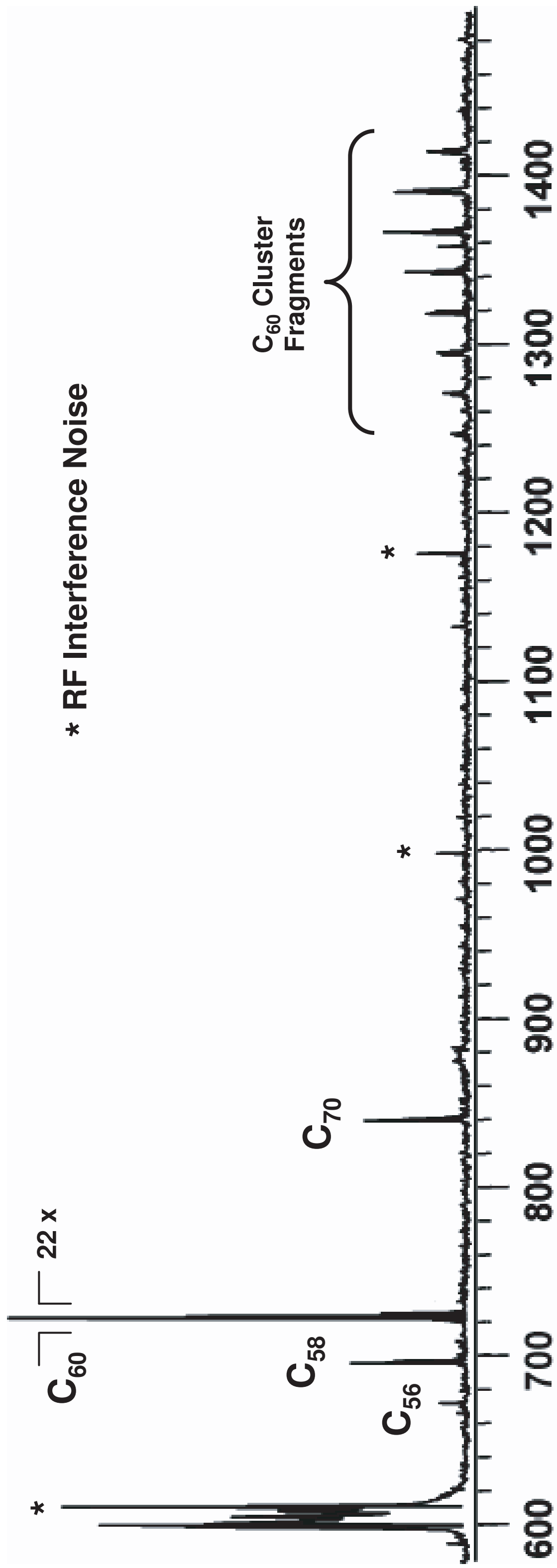

Figure 5·17: The complete broadband m/z range of the MS in panel B Fig. 5.16(b) using the BUSM amplifier.

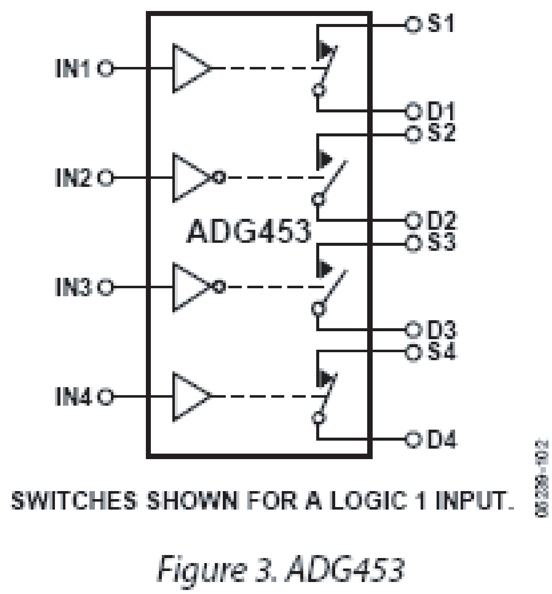

Figure 5·18: FET Switch to control the preamplifier bias.

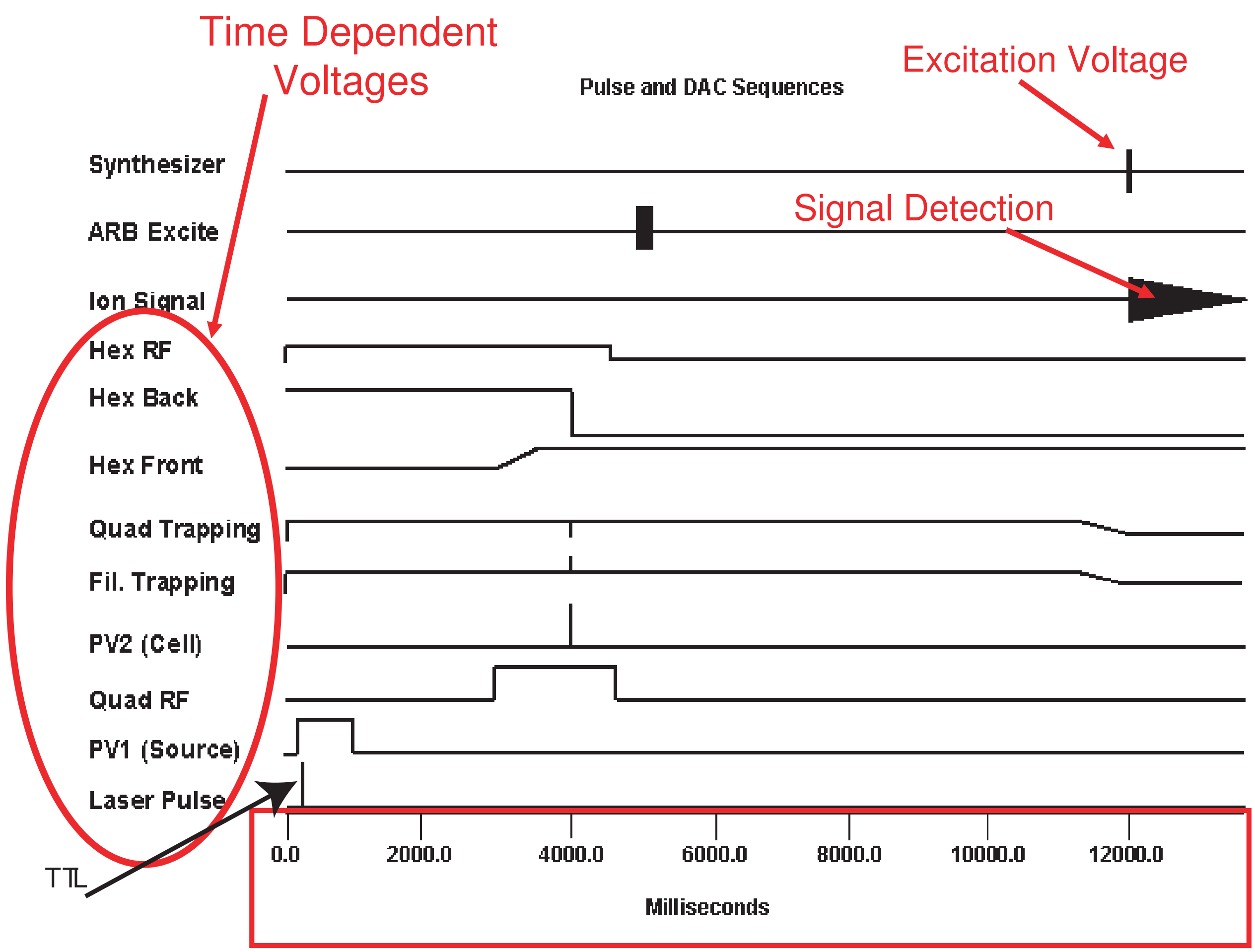

Figure 5·19: FTMS Pulse Sequence.

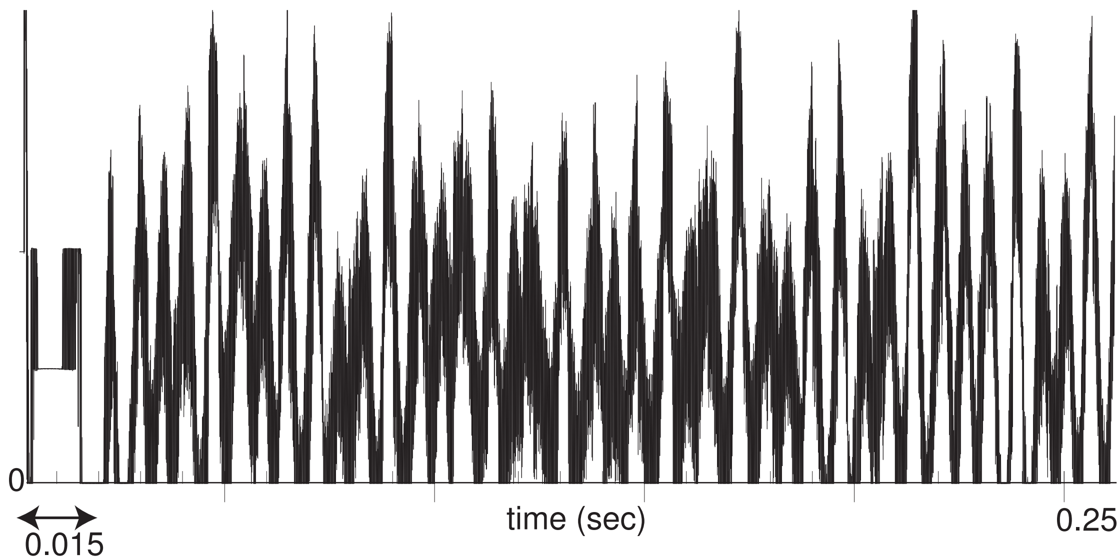

Figure 5·20: Overloading in the Preamplifier (A 100 Vp-p to excite overloads the preamplifier for 15 msec.

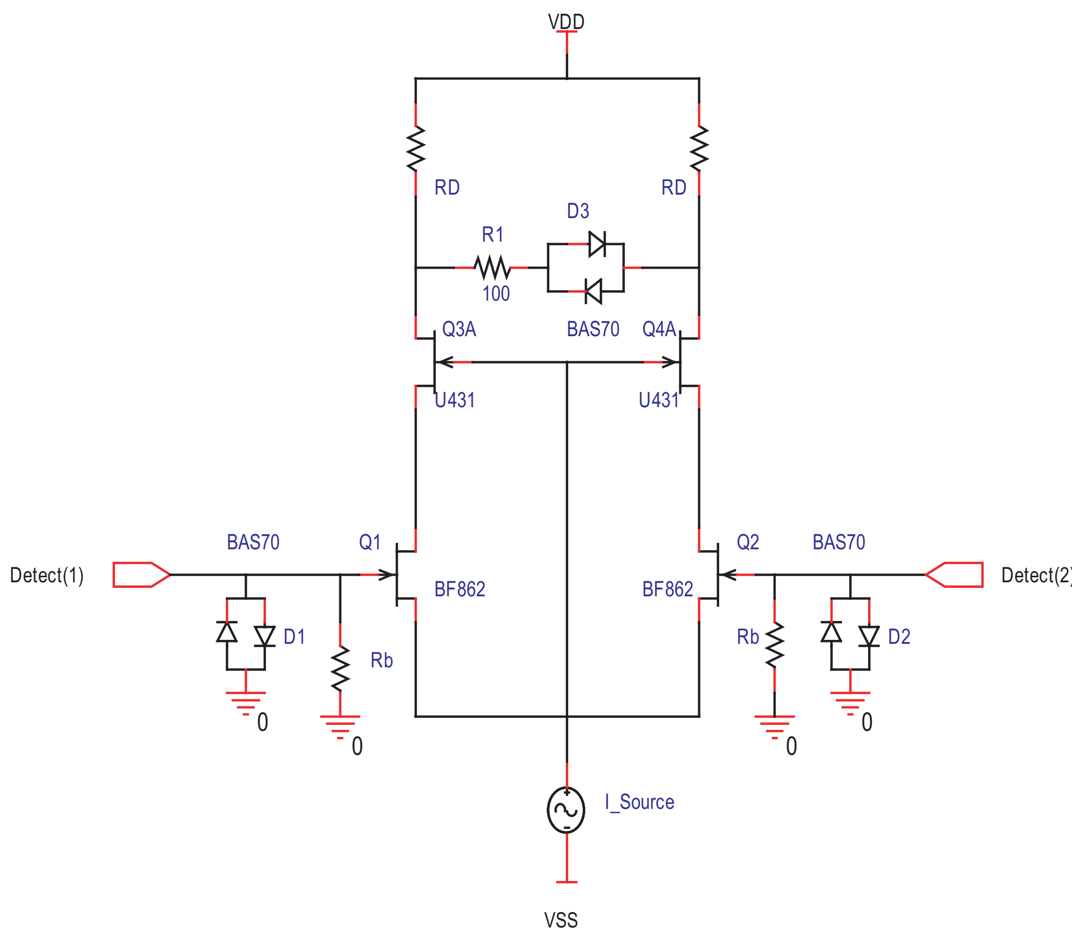

Figure 5·21: Preamplifier with Schottky Diodes at the input to protect against overloading.

Chapter 6

Cryogenic Fourier Transform Mass Spectrometer

This chapter has been reproduced from the article, First Signal on the Cryogenic Fourier-Transform Ion Cyclotron Resonance Mass Spectrometer Journal of the American Society for Mass Spectrometry, Volume 18, Issue 12, December 2007, Pages 2090-2093 Cheng Lin, Raman Mathur, Kostantin Aizikov and Peter B. OConnor.

In this chapter, a discussion about the the construction and achievement of the first signal on a cryogenic Fourier-transform ion cyclotron resonance mass spectrometer (FT-ICR-MS) is reported. If we recall, building the FTICR cell into the cold bore of a superconducting magnet offers several advantages over conventional warm bore design. First, at 4.2 K, the vacuum system will cryopump itself, thus removing the requirement for a large bore to achieve the desired pumping speed for maintaining base pressure. Second, because the bore diameter can be substantially reduced, the amount of magnet wire needed to achieve high field and homogeneity is also reduced, greatly decreasing the cost/Tesla of the magnet. Increased magnetic field strength improves many FTMS performance parameters simultaneously, including the resolving power, mass accuracy, sensitivity, limit of detection, dynamic range, and space charge limit. Finally, cooling the preamplifier will decrease the input resistor Johnson noise by 8.4-fold and the FET leakage current noise by $\approx$10X, improving the limit of detection and dynamic range accordingly. The current instrument implements an actively shielded 15-Tesla magnet of vertical design with an external matrix assisted laser desorption/ionization (MALDI) source. The first signal was obtained by detecting the laser desorbed/ionized (LDI) C_{60} ions, with the magnet at 7

Tesla, unshimmed, and the preamplifier mounted outside of the vacuum chamber at room temperature. A subsequent experiment done with the magnet at 14 Tesla and properly shimmed produced a C_{60} spectrum showing ≈350,000 resolving power at m/z ≈720, with an 8.4 second transient.

6.1 Experimental

6.1.1 Magnet Design

The cut-away view of the complete cryogenic FTMS system with its salient components is shown in Fig 6·1. It incorporates an actively shielded 15 Tesla superconducting magnet (Cryomagnetics, Oak Ridge, TN) with a vertical, cryogenic temperature bore, and homogeneity of ≈12 ppm over a 5 cm by 5 cm cylindrical region. The system is designed to have zero loss in liquid helium under normal operation, with the equipped Sumitomo RDK415 cryo-refrigerator (Sumitomo Heavy Industries, Tokyo, Japan) providing a cooling power of ≈80 W at 77 K and ≈1.5 W at 4.2 K to compensate the heat transfer into the magnet Dewar. The Dewar can hold up to ≈100 Liter of liquid helium, which facilitates initial cool down, and provides a reservoir of cryogen to prevent magnet quenching in case of power outage and/or unaccounted heat loads. Two radiation shielded UHV chambers separate the outer surrounding environment from the magnet chamber, which is also radiation shielded from the 4 K inner chamber housing the FTMS system which allows for short duration temperature shocks. There is a 3.4 cm conflat port at the bottom of the Dewar for optical access offering capability of carrying out IRMPD experiments.

6.1.2 FTMS System

The FTMS system consists of an external MALDI source, multipole ion guides, and an open cylindrical ICR cell. The high pressure MALDI source is similar to the one described previously (O'Connor et al., 2004), where analytes are desorbed and ionized from the target plate mounted on an XY-stage (Fraunhofer USA, Brookline, MA) by focused 355 nm light from a Nd:YAG laser (Continuum, Santa Clara, CA). The ion transfer optics include an accumulation hexapole with front and back trapping plates that can accumulate ions externally, and a transmission hexapole, both driven by custom RF oscillators (Mathur and O'Connor, 2006) but separated by a thin gate valve to maximize ion transmission. The ICR cell has an outer diameter (o.d.) of 7 cm, a central excite/detect region length of 5 cm, 10 cm long inner trapping ring on each side to extend the trapping volume, and two outer trapping plates. After an overnight bakeout of the FTMS insert at 110oC, followed by its insertion into the cold magnet bore and a two-day cool-down, the pressure of the system was measured at $\approx 3 \times 10^{-9}$ mbar in the cube region, and it is expected that the pressure down in the cell should be much lower because of cryopumping.

6.1.3 Data Acquisition

A PXI-based data system developed at FOM-AMOLF (Mize et al., 2004) was used to control the pulse sequence, generate the excite waveform, and acquire the spectrum. The excite waveform was produced using an arbitrary waveform generator, followed by amplification and balancing through an iron-core balun transformer before transmission to the excite plates. The current setup uses an op-amp based standard instrumentation amplifier at room temperature outside of the vacuum system to amplify the induced ICR signal, so the hypothesized noise reduction is not expected with these initial results. The digitized transients were zero-filled once and fast Fourier transformed without apodization to produce the magnitude mode mass spectra shown.

6.2 Results and Discussion

6.2.1 First Signal at 7 Tesla

C_{60} was chosen as the analyte for tuning the cryogenic FTMS instrument. To reduce the tuning space dimension, the LDI mass spectrum of C_{60} was first obtained and optimized on a room temperature 7 T MALDI-FTMS instrument (O'Connor et al., 2004). The data system, excite and detect amplifiers as well as the pulse sequence used in that experiment were then transported to the cryogenic FTMS system, with its magnet also charged half-

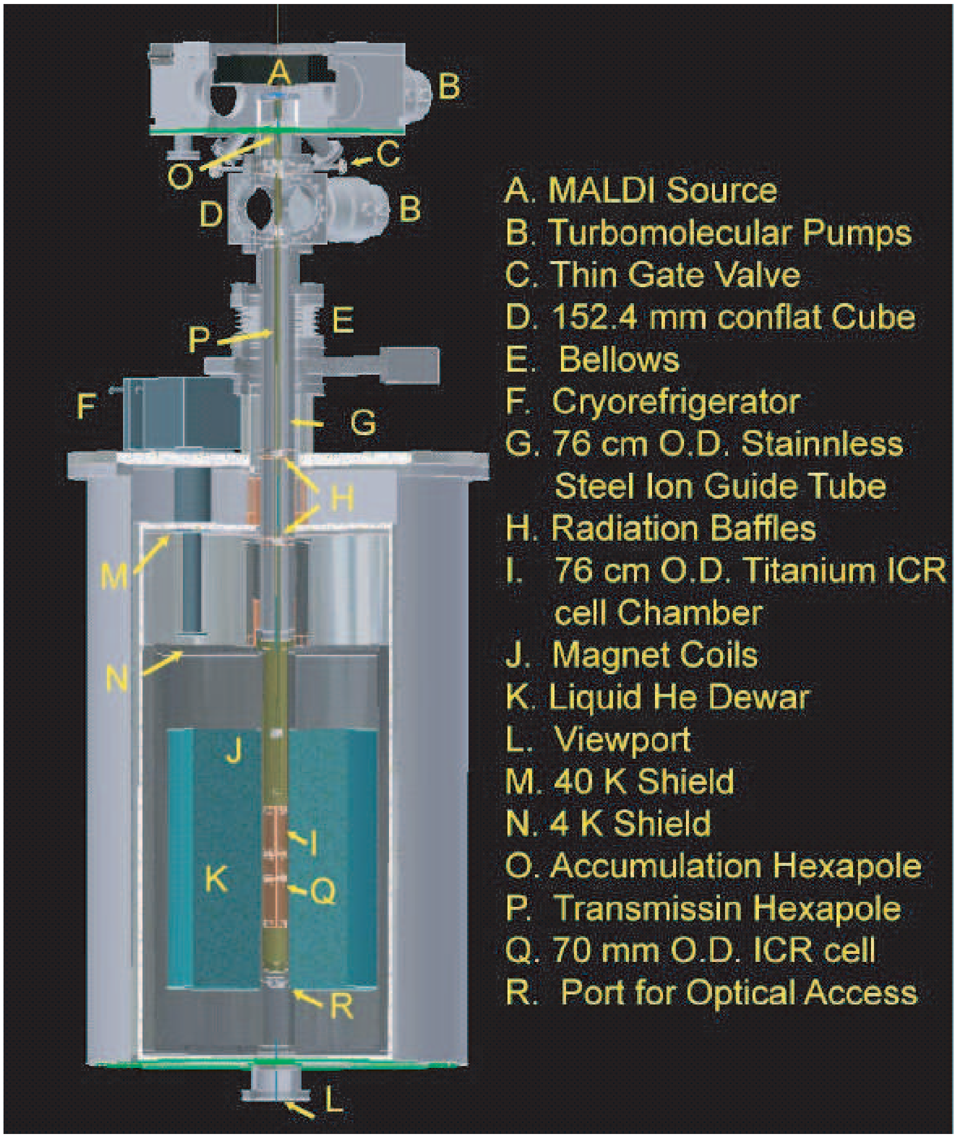

Figure 6·1: Cutaway view of Cryogenic Fourier Transform Ion Cyclotron Mass Spectrometer way to 7 T to minimize the unknown parameters. With parameters such as ion time-of-flight, voltage settings on ion lenses, hexapole RF amplitudes and frequencies, and the excite amplitude and length set near optimal values, acquiring the C_{60} spectrum in the cryo-FTMS system was expected to require minimal tuning. C_{60} molecules were first desorbed from a stainless steel plate and ionized by a single laser shot of around 80μJ (focused to ≈100 m diameter spot) at 355 nm, then transferred to the ICR cell through two hexapoles, both operated at 900 kHz and ≈25 Vpp amplitude. Gated trapping was used to trap the ions in the ICR cell, with the lower inner trapping ring held at 10 V, and the upper one briefly dropped to -1 V to allow the passage of ions into the cell before returning to 10 V, 1.27 msec after the laser fired, corresponding to a 1.27 msec ion flight time. After a short delay of ≈200 msec, the trapped ions were subjected to a broad band chirp excitation (m/z 500-1000 Da, 107-214 kHz at 7T) for 20 msec at 70% attenuation (≈20 Vpp), and the image current was detected at 4 MHz sampling rate and with 1 M point (16-bit) buffer size, corresponding to a 0.26 second transient. Fig 6·2 shows the optimized single scan mass spectrum of C_{60} at 7 T, with the inset showing the time domain signal, which clearly displays the beat pattern of the closely spaced isotopic peaks. The mass resolving power is around 18,000, close to the theoretical Fourier-transform limit (f*t/2) of 19,344. 14 Tesla Spectrum While the current magnet is designed for 15 T, shimming values are only available at 14 T. Thus, after optimizing the C_{60} signal at 7 T, the magnet was brought up to 14 T, and shimmed for optimal overall homogeneity. Fig 6·3 shows a single scan spectrum of C_{60} at 14 T with broad band excitation and an 8.4 second transient. The mass resolving power is ≈350,000, falling far short of the theoretical limit of ≈1,250,000. Such deviation likely results from dephasing of the ion clouds, particularly because the high trapping potentials should increase trapping field inhomogeneities and the magnetron expansion rate. Cell pressure should be very low with the cryopumping, so collisional decay of the transient is not expected to be significant.

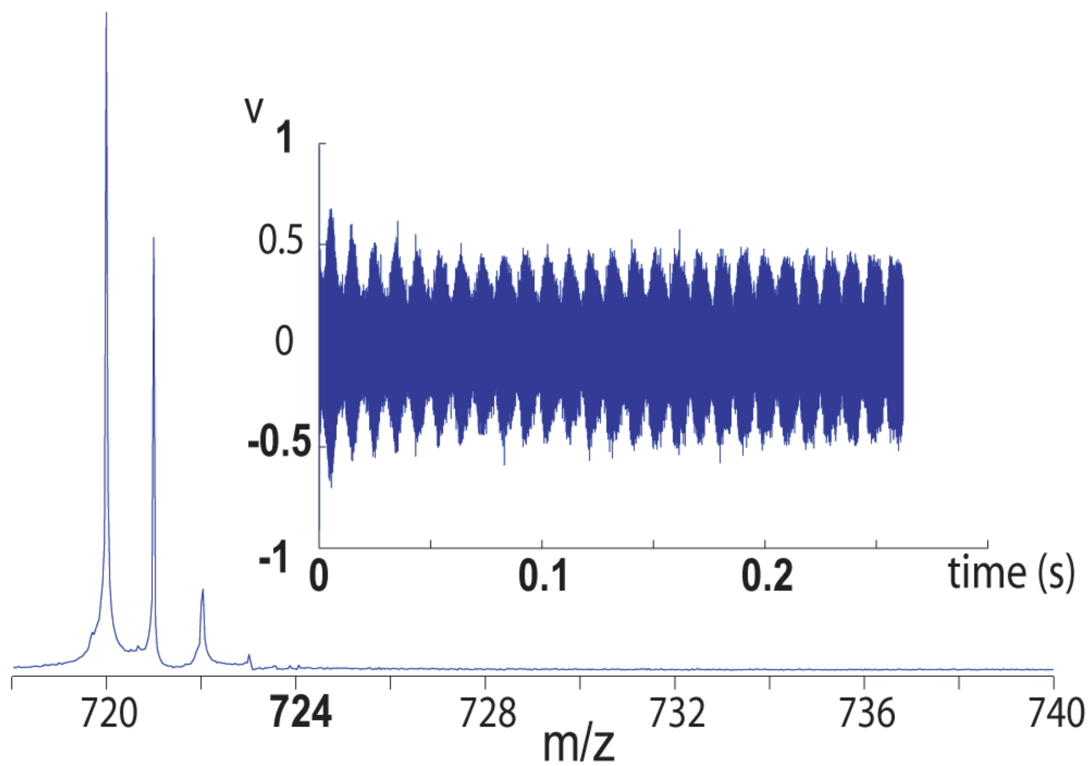

Figure 6·2: First Signal on Cryogenic FTMS at 7 Tesla

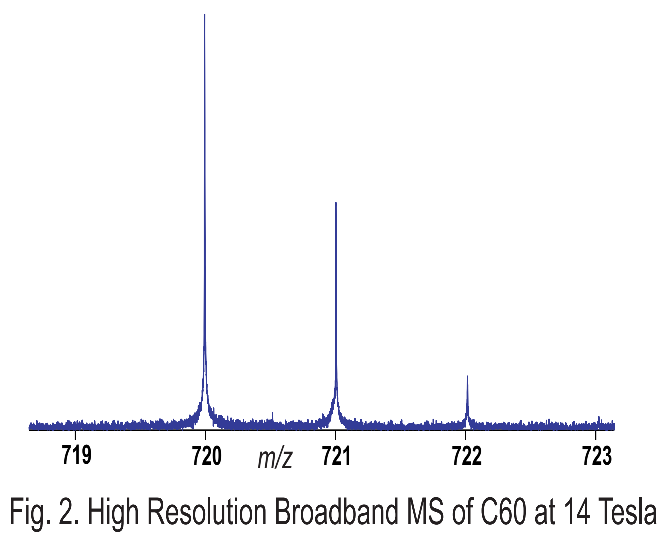

Figure 6·3: High Resolution mass spectrum of C_{60} at 14 Tesla

6.3 Conclusions

A cryogenic FTMS instrument has been constructed with a 15 T magnet, which offers several advantages over the conventional warm bore design, including the field strength, base pressure and preamplifier noise. The helium boiloff rate is currently at a manageable 5 L/day, with modifications under way to reduce the heat transfer further to make it a zero-loss system. First signal has been achieved on this instrument by detecting the LDI C_{60} ions at 7 T, and later at 14 T. While not fully optimized, this signal can be used to tune the instrument. Particularly, replacing the room temperature instrumentation amplifier with the low-temperature preamplifier in proximity to the ICR cell has improved the signal/noise significantly, as shown further.

Chapter 7

Cryogenic Preamplifier

This chapter has been reproduced in part from the article submitted to IEEE Transactions on Applied Superconductivity.

Fourier-transform ion cyclotron resonance mass spectrometry has shown superior performance in terms of mass accuracy, resolving power, and sensitivity for applications in physics, biology and chemistry. Continuous advances in the field of electronics has reflected directly on the improvement and development of better FTICRMS. Recently developed cryogenic FTICRMS has provided an opportunity for improvement in the limit of detection of FTICRMS by cooling the detection preamplifier to 4 K, thus reducing the thermal noise in the preamplifier. In this chapter we describe the development of a low noise cryogenic preamplifier for FTICRMS. The complete amplifier has a voltage gain of 250 with -3db roll off at 850 kHz. The cryogenic preamplifier circuit has shown about 20 times improvement in SNR, over the room temperature version.

Several scientific instruments, such as the electron microscope, particle detectors, and infrared telescopes, have detectors placed inside the cryostat. Sensors from these instruments are intrinsically at cryogenic temperatures and generate output signals typically in the order of a few μVs. This signal must be amplified several orders of magnitude, prior to being converted into digital format for data processing. A simple approach for amplification of such a signal is to use shielded cables to bring the signal out of the cryogenic environment and then amplify using an amplifier at room temperature. In this design, the capacitance of the long cables at the input of the amplifier can severely deteriorate the signal-to-noise ratio (SNR) of such a detection scheme, particularly at higher frequencies. Moreover, with such a scheme, the signal is also prone to interference noise (Lee, 1993). A more challenging, but more effective approach is to use a preamplifier inside the cryogenic system, connected to the sensor output using short, low capacitance leads. The preamplifier transforms the impedance level of the signal, and its signal gain reduces the effective noise contribution of the following amplification stages (Lee, 1989; Lee, 1993; Hu and Yang, 2005).

In addition to improved SNR due to the lower capacitance at the sensor output, there are other significant advantages of using a cryogenic preamplifier in signal conditioning. Namely,

- Johnson Noise in the electronic component decreases as $\sqrt{T}$ (Johnson, 1928).
- The shot noise due to leakage current reduces in the input FETs (Schottky, 1918).
- The life span of the electronic circuit component increases.

As mentioned above, there are challenges involved in the design of amplifiers operable at cryogenic temperatures (Kirschman, 1986). The primary limitation is selection of an active device that can operate at liquid helium temperatures (Kirschman et al., 1992). Almost all commercial low noise operational amplifiers are silicon-based. Recently, we have shown an improved detection amplifier for room temperature FTICRMS which exhibited ≈ 25 fold improved SNR compared to a commercial amplifier (Mathur et al., 2007). However, the room temperature BUSM amplifier uses Si-JFETs which generally cease to work at temperatures < 70 K. The mobile carriers in silicon "freeze-out" at 4 K. Thus for cryogenic applications, FETs fabricated using GaAs are implemented. Metal semiconductor field-effect transistors (MESFETs) and high electron mobility transistor (HEMTs) have been extensively used in circuits at 4 K (Keyes, 1977; Jonsher, 1964). However at low temperatures, GaAs FETs have been shown to exhibit instabilities in their electrical characteristics in terms of discontinuities or hysteresis (Pospieszalski and S., 1987). This often leads to high frequency oscillations in the amplifier circuits. Moreover most of the commercial passive components do not behave well at low temperatures. Components with ceramic packages such as transistors and capacitors can crack due to mechanical sheer stress caused by thermal cycling. As a result the design of a robust and stable cryogenic preamplifier becomes non-trivial.

In this section we describe the development of such a low noise cryogenic amplifier for FTICRMS. The current design has two stages. The first stage, the preamplifier, uses GaAs MESFETs which are cooled to 4 K and mounted close the detection plates. The second stage uses generic silicon JFETs and opamps placed outside the vacuum. The bias point of the FET in the preamplifier is adjusted for optimal gain and suitable power dissipation. For the current design, the power dissipation in the complete differential preamplifier is $\approx$ 10.5 mW. The voltage gain of the amplifier is ≈ 250 with the bandwidth at ≈ 850 kHz. We also report the first ion signal achieved using the GaAs-based BUSM amplifier cooled to 4 K in the cryogenic FTICRMS at Boston University.

7.1 Cryogenic FTICRMS

Conventional FTICRMS instruments use superconducting magnets with the analyzer housed inside the room temperature bore. With such scheme, there is no convenient access for the preamplifier to be cooled to liquid helium temperature. In 2002 O'Connor proposed a design of a novel kind of FTICRMS which uses a custom designed vertical cold bore magnet (Fig. 7·1) (O'Connor, 2002). In this system, the FTICRMS is cooled to 4 K by placing it inside the cold bore of the magnet, thus reducing the needed bore diameter and enabling access to higher magnetic field strengths at significantly lower cost.

Constructing an FTMS with a vertical cold bore magnet facilitates insertion and removal of the FTMS system inside the cold bore by leaking warm helium gas from the bottom, thus minimizing air condensation inside the magnet bore. This is important as the formation of ice (water or nitrogen) inside the magnet dewar can be destabilizing, as it may interfere with insertion or removal of the ICR vacuum chamber. The vertical design also simplifies the construction of the magnet, thus decreasing its cost, but at the expense of requiring an appropriately tall space for the instrument. The 14 Tesla superconducting magnet was developed at Cryomagnetics, Inc. (Oakridge, TN) with a cold bore diameter of $\approx$7.5 cm providing $\approx$ 12 ppm homogeneity over a 5 $\times$ 5 cm cylindrical volume. Magnet stability has not yet been measured, but is expected to be $\approx$100 ppb/hr after several weeks of stable operation.

The FTMS mass analyzer, is a 6 cm o.d. open cylindrical ICR cell inserted inside the vertical cold bore. This design allows a thermal path from the preamplifier to the liquid helium dewar to cool the preamplifier to 4 K. The preamplifier is mounted close to the detection plates of the ICR cell which is also cooled to $\approx$4 K, as shown in Fig. 7·1. The use of a cryogenic preamplifier enhances the SNR for better sensitivity, offering distinct advantages for cryogenic FTICRMS compared to conventional room temperature FTICRMS instruments. This overall instrument design also added complexities, which had to be overcome in the initial development, as discussed below.

7.2 Circuit Design and characteristics

The preamplifier circuit uses GaAs based MESFETs, which have shown a considerable performance improvement for cryogenic applications (Alessandrello et al., 1990; Lee, 1993). Their low leakage current at cryogenic temperatures makes them an ideal choice for high impedance sensors (Alessandrello et al., 1990). Commercially available MESFETs (FSU01LG) from Eudyna Devices Inc. (Freehold, NJ) were obtained (Eudyna Devices, Inc., 2005).

The first set of experiments to determine the drain current versus drain-source voltage of the devices at room temperature were conducted in a common source configuration, Fig. 7.2(a). The power supplies were bypassed with a bank of capacitors ranging from 10 uF to 10 pF. The DC characteristics obtained are shown in Fig. 7.2(b). During the measurements of drain current a kind of hysteresis effect was noticed in the variation of

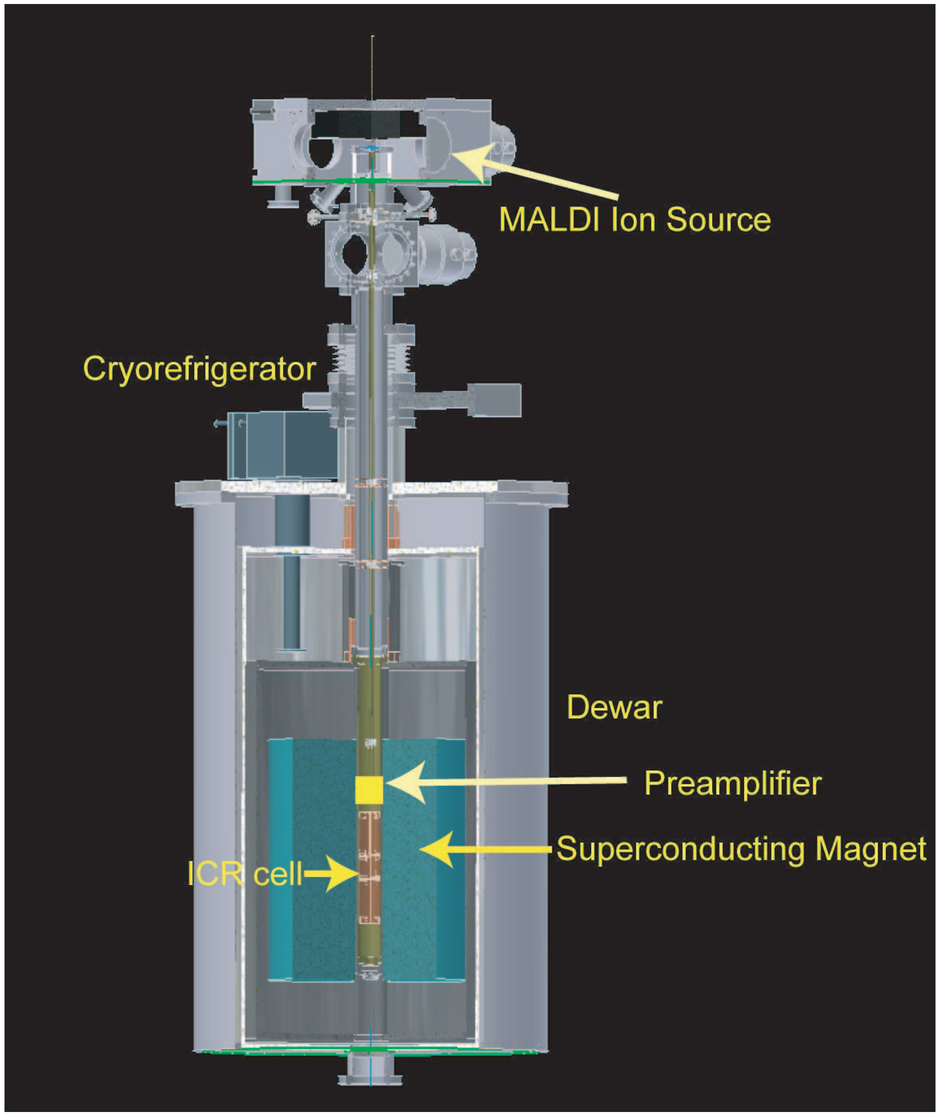

Figure 7·1: Cryogenic FTICRMS Cut Away View drain current with respect to drain to source voltage. The drain current will have a different value for a particular drain to source voltage during ramping up and ramping down of drain bias. As mentioned in (Pospieszalski and S., 1987) this hysteresis in the IV curves is due to the instability/oscillations of the FET under test. Further tests using a spectrum analyzer revealed that the preamplifier circuit in Fig. 7.2(a) would oscillate at 5 GHz with a second and third harmonic at 10 GHz and 15 GHz respectively.

These Eudyna GaAs MESFETs which are being used for the cryogenic preamplifier are high frequency transistors with a unity gain frequency around 12 GHz. After discussions with experienced personal in high frequency RF design, several modifications were done to the original circuit shown in Fig. 7.2(a), which led to the stable (oscillation free) preamplifier circuit. High frequency bypass capacitors (10 pF and 50 pF) which were used in previous circuit, had a series resonant frequency (SRF) at 800 MHz. Due to this the capacitors no longer exhibit a low impedance path to ground for the RF (or noise) at frequencies greater than 800 MHz. This behavior of capacitors is due to the parasitic series inductance of the package of the capacitors, as extensively discussed in an application note by Jim Williams (Williams, 1998). For the same reason high frequency capacitors, HPC0201 series, from Vishay Intertechnology, Inc (Malvern, PA) were incorporated in the design. These surface mount capacitors (1.2 pF, 10 pF) had a small footprint, SM0201, reducing their parasitic inductance to merely .035 nH. This provides them with an ultra high SRF, typically greater than 5 GHz, and extremely stable capacitance value over a wide frequency range. The bypass capacitors were mounted within 1 cm of the FET pins to minimize parasitic inductance of connecting traces. The PCB was etched in-house using Ferric Chloride with short traces between the components, as shown in Fig. 7·4.

DC characterization of the MESFETs was done using the test circuit shown in Fig. 7·3. A printed circuit board (PCB) was fabricated in-house on a fiberglass substrate for testing purposes as shown in Fig. 7·4. The unity gain frequency of the MESFETs is 12 GHz, requiring careful high frequency design and layout. The addition of bypass capacitors and low pass filters on the bias lines minimizes coupling between power supply lines and prevents

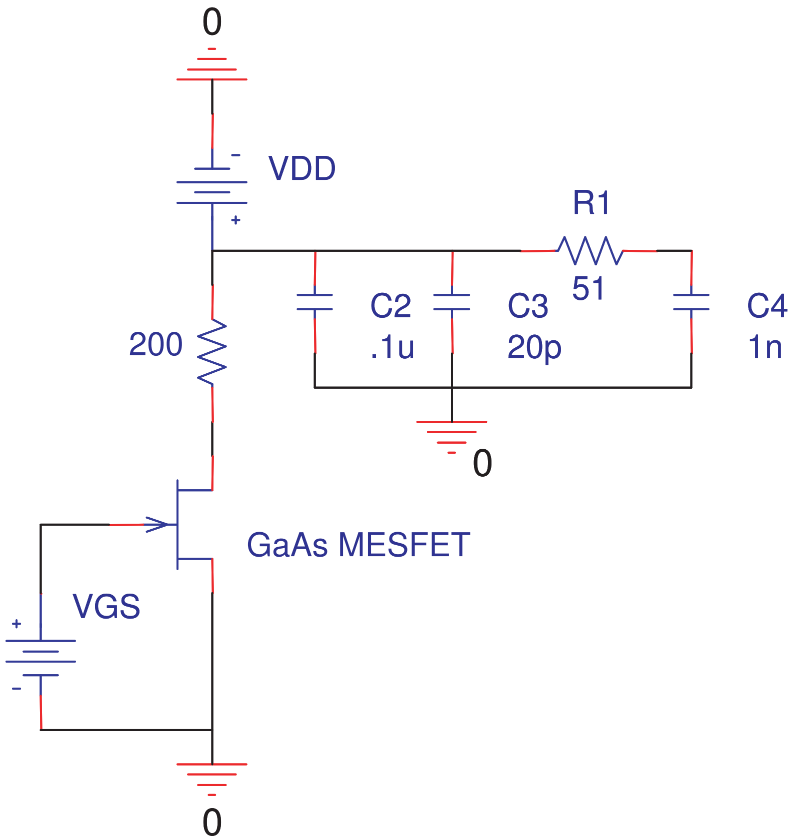

(a) Initial Circuit for GaAs IV Characteristics

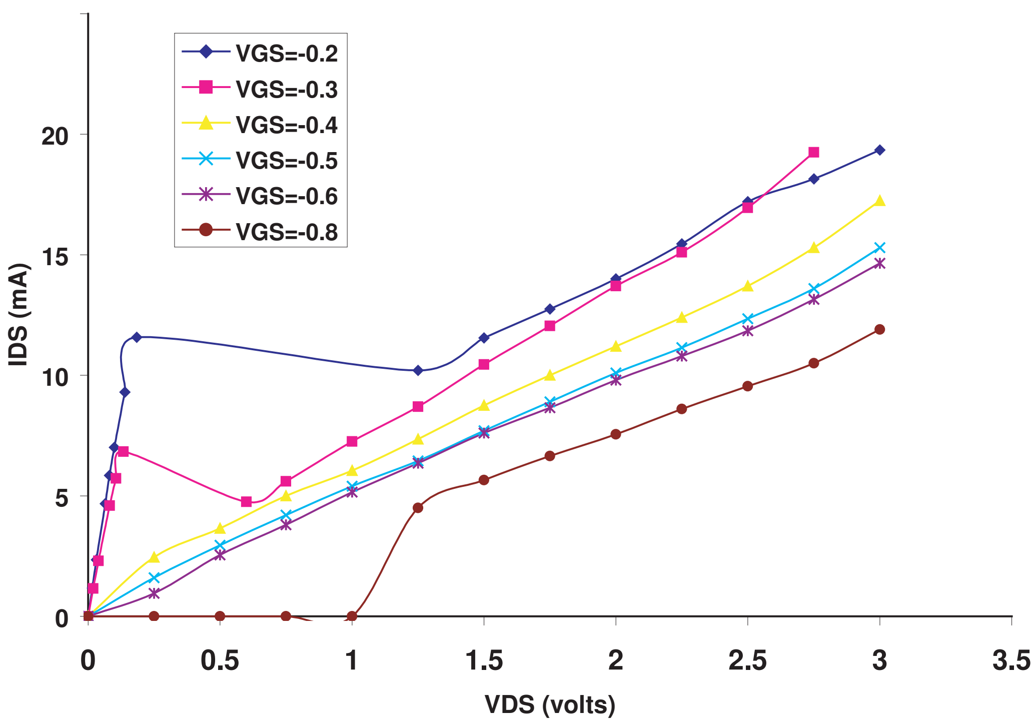

(b) Instability in GaAs Drain Currents

Figure 7·2: Instability in GaAs MESFET Characteristics

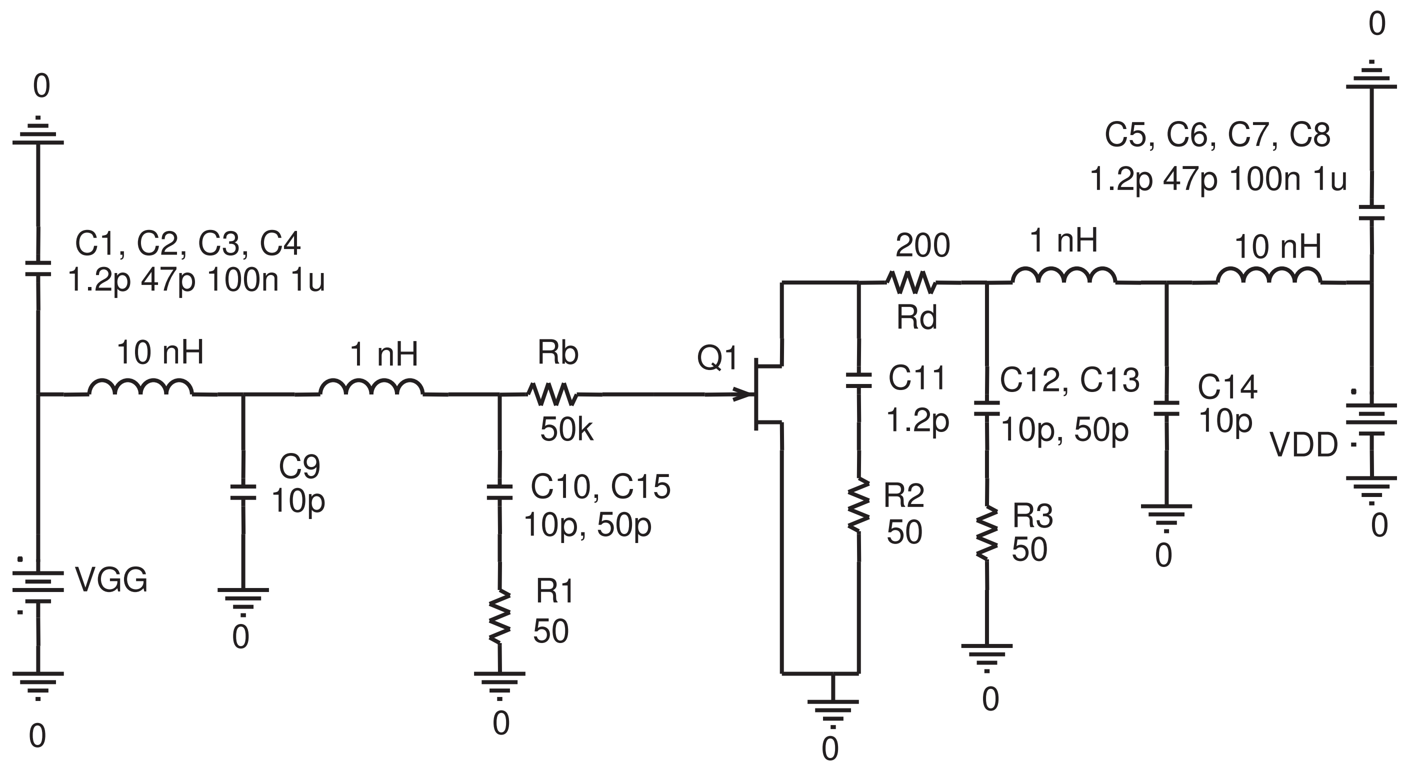

Figure 7.3: Circuit for Device Testing Purposes.

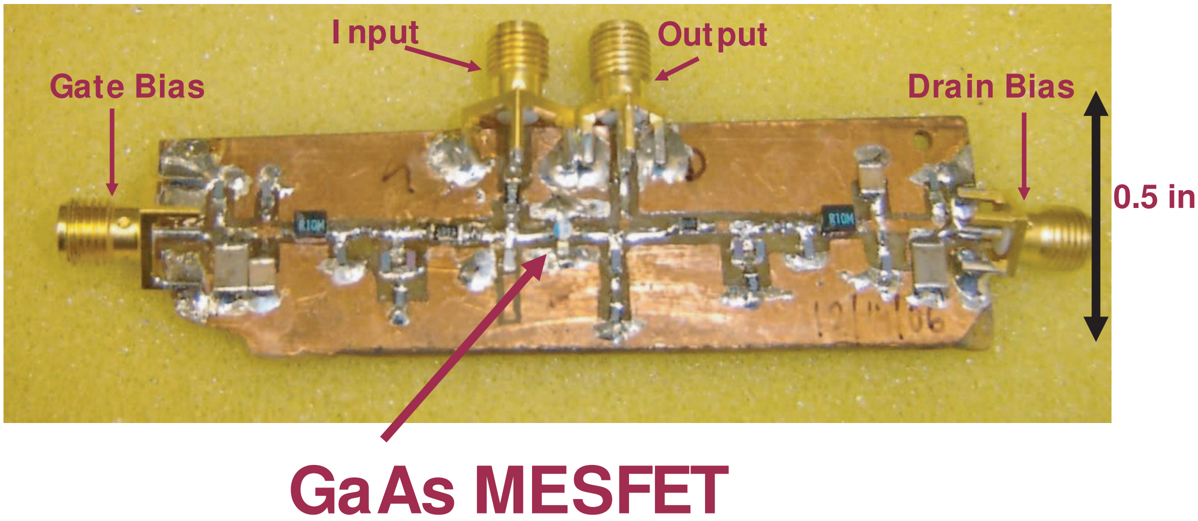

Figure 7·4: PCB for Device Testing purposes.

instability of the transistor. Additionally, for high frequency stability of the MESFET, the drain was terminated with a 1.2 pF capacitor, C11, in series with a 50 ohm load, R2. A 200 Ω resistor, Rd was added to measure the drain current of Q1.

While testing, it was observed that several surface mount passive components did not behave well when subjected to temperature cycling. Specifically, the bypass capacitors, critical for the high frequency stability of the MESFETs, cracked, thus shorting the power rails to ground. Thus, in the development of the preamplifier circuit, capacitors had to be eliminated.

The circuit diagram of the cryogenic preamplifier is shown in Fig. 7·5. A circuit board using FR4 was etched using Ferric chloride solution. To guarantee high frequency stability, 50 ohm surface mount resistors are mounted directly on the terminal of the MESFETs, damping initially observed high frequency oscillations at 5 GHz. GaAs MESFETs Q1 & Q2, input bias resistors, Rb, damping resistors R1–R6 and the current source resistor Rs, constitute the cold stage of the preamplifier and are placed at 4 K. The primary purpose of the preamplifier is the impedance transformation of the signal (from high to low). The output signal from input FETs is fed to a Si JFET cascode pair, Q3 & Q4, which sit

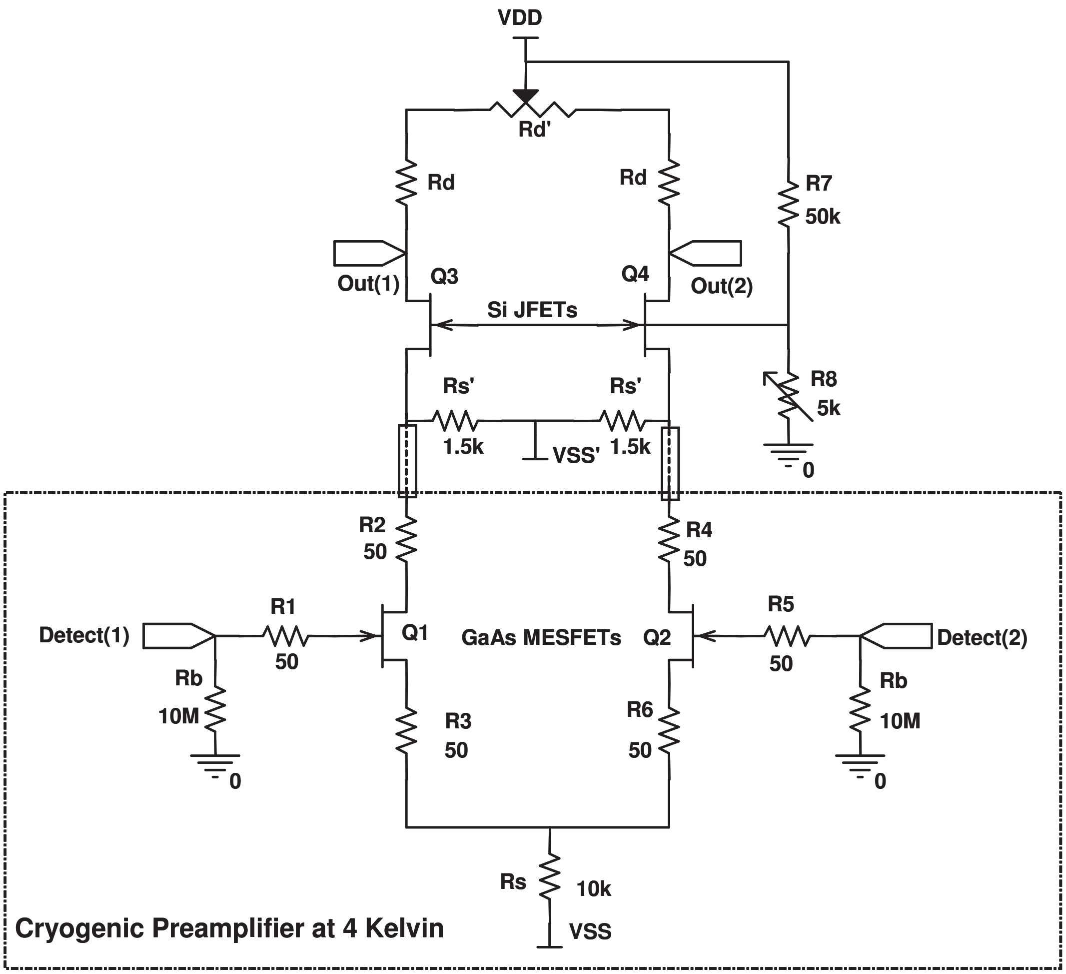

Figure 7·5: Preamplifier Circuit Schematic

outside the vacuum system, via a 1 m long cable. The capacitance of this cable, which was estimated to be ≈ 25 pF, would normally form a high frequency pole with the resistance at the terminating end, limiting the bandwidth of the design. In the current design, the use of a cascode configuration ensures that the terminating resistance looking into the source of the JFET is low – hence pushing this pole to a higher frequency (Miller, 1920). The cascode was followed by a standard instrumentation amplifier, Fig. 7·6.

The high impedance nature of the ICR detection plates poses some requirements on the physical layout of the preamplifier circuit board. Specially, the connection of the detection plates to the gate of the MESFET must be done in a way to minimize the parasitic

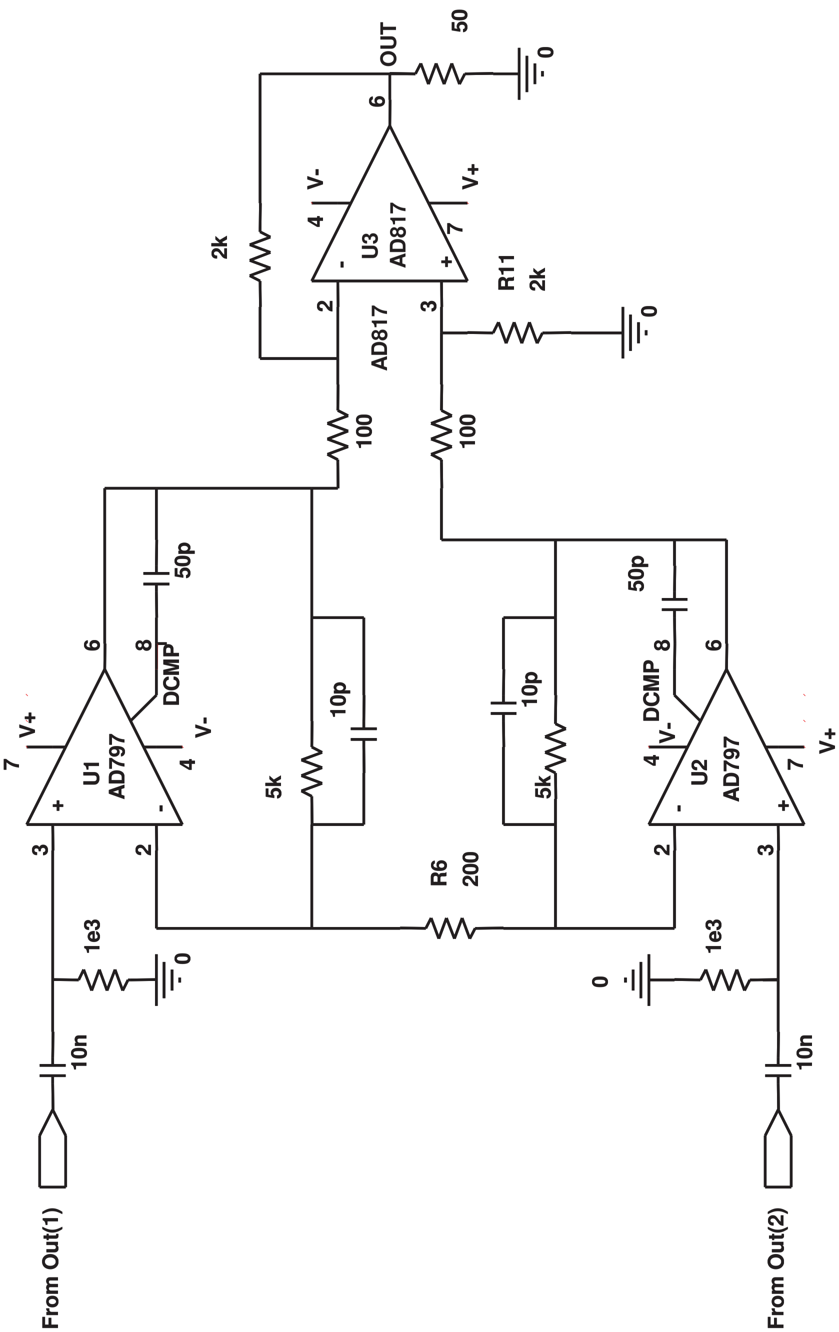

Figure 7·6: Circuit Diagram of the Instrumentation Amplifier capacitance and leakage current (Pease Bob, 1993). This was achieved by flipping the device upside down and making the connections in air using the “Birds nest” scheme described by Jim Williams (Williams, 1998). This also eliminates the possibility of ripping up the traces leading to bad connections when the Fiber glass PCB is cooled to 4 K and subjected to multiple temperature cycles.

7.3 Experiment Results

7.3.1 On-Bench Electrical Testing

All the experiments reported here are done using the set up described in chapter 8. PXI cards from United Electronic Industries, Inc. (Walpole, MA) and National Instruments (Austin, TX) were used to read/write the voltages. Labview (National Instruments, TX) was used as the programming platform to control these PXI cards and for data analysis and plotting.

IV Characteristics

To verify the operability of the commercial GaAs MESFETs, several sets of experiments were conducted on the bench.

The circuit in Fig. 7·3 was used for these tests. The measured DC characteristics of the transistor at room temperature and liquid helium temperature are shown in Fig. 7·7. At liquid helium temperatures, a decrease in drain current for a given gate bias was observed. This is attributed to the reduced number of mobile charge carriers at low temperatures. The plots of the transconductance of the MESFET for VDS = 1.5 volts at room temperature and liquid helium temperature were obtained using the DC characteristics at the respective temperatures, as shown in Fig. 7.8(a). The gain bandwidth plot of the complete amplifier was measured using a test signal from an arbitrary waveform generator, NI 5411 (National Instruments, Austin, TX). The -3 dB high frequency roll-off of the amplifier is at 850 kHz which corresponds to a lowest detectable mass of 117 Da at 7 Tesla. Short-circuit input-referred voltage noise of the common source preamplifier, followed by a low noise

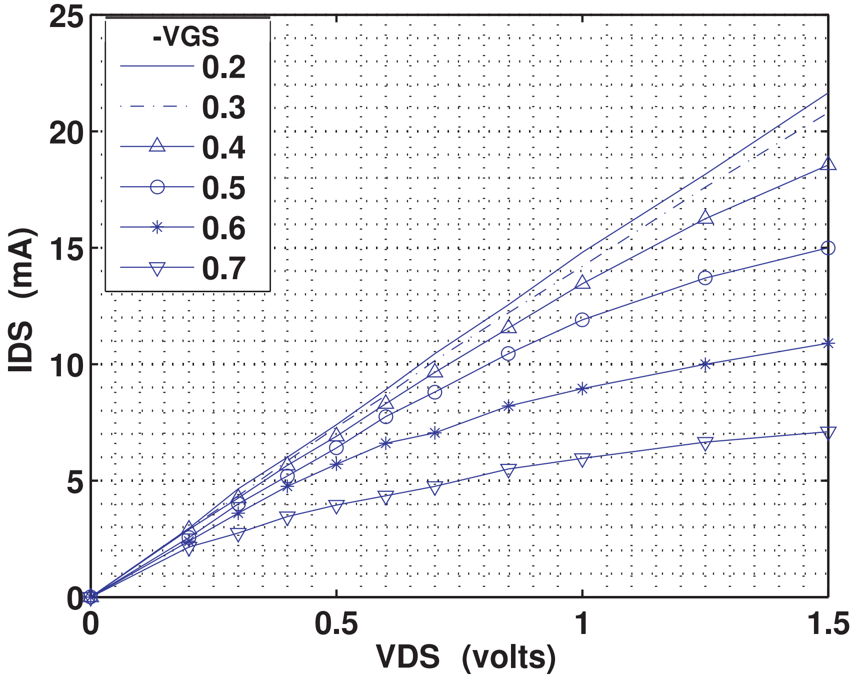

(a) IV Characteristics at 300 K

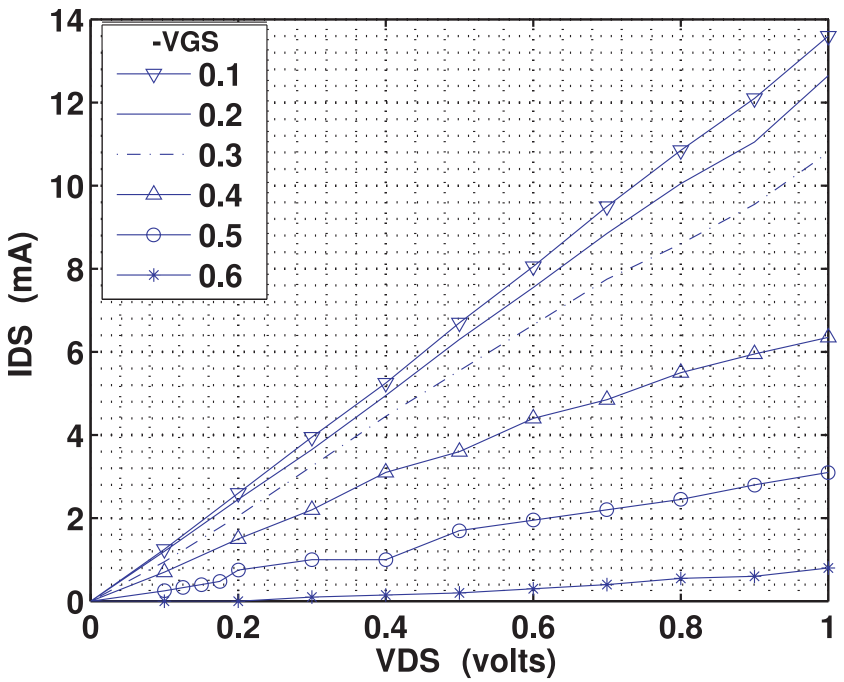

(b) IV Characteristics at 4 K

Figure 7·7: DC Characteristics of MESFETs

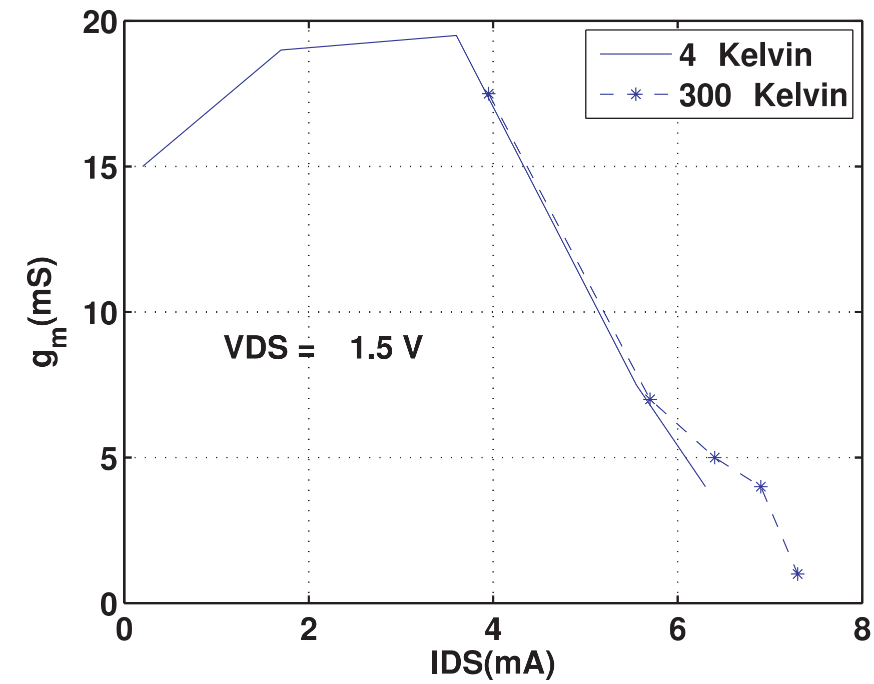

(a) Transconductance of the GaAs MESFET

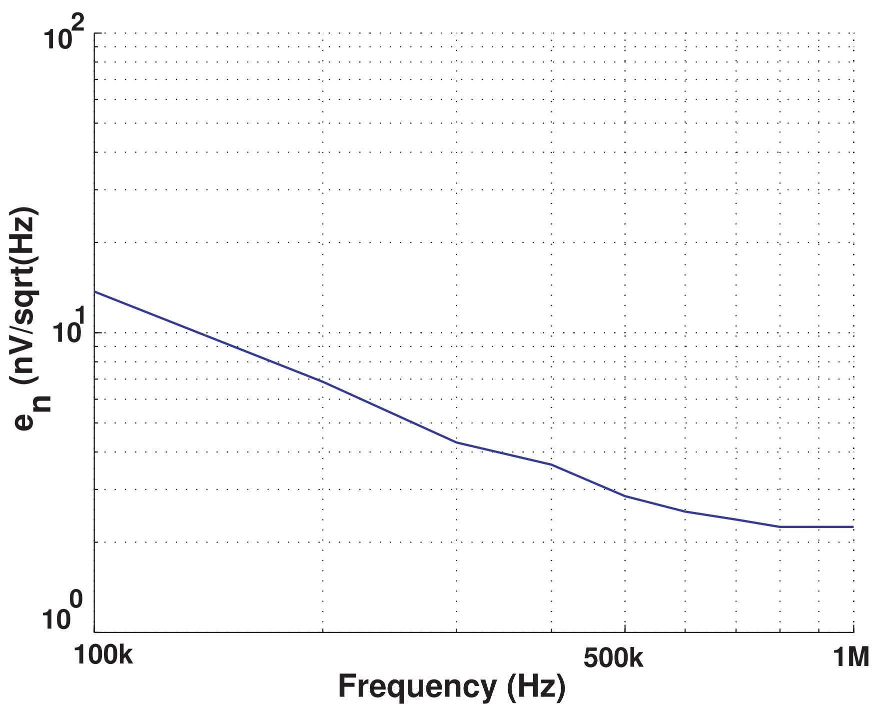

(b) Input Short-Circuit Noise Voltage at 77 K

Figure 7·8: GaAs MESFET Characteristics post amplifier, was measured at liquid nitrogen temperature and is shown in Fig. 7.8(b). A Tektronix spectrum analyzer, Tek 2712 (Tektronix, Richardson, TX) provided the noise plot from 100 kHz to 1 MHz indicating the 1/f noise 'knee' occurring at 700 kHz.

Preamplifier Performance in a High Field Superconducting Electromagnet

In the ICR detection preamplifier, it is optimal to mount the preamplifier in close proximity to the detection plates to minimize the lead wire capacitance. However the high magnetic field in which the ICR cell is placed may adversely affect the performance of the FETs. Most of the commercial JFETs which were tested during the room temperature preamplifier design did not operate well in the magnetic field, due to the Hall effect (Hall, 1879). A general solution is to align the channel of the FETs to the magnetic field; however, the transverse package of the GaAs MESFETs selected here, prohibits such alignment.

For this reason functionality tests were performed on the common source amplifier with a drain resistor of drain resistor equal to 100 Ω, Fig. 7·3 by placing the preamplifier in the presence of the high magnetic field. The preamplifier was inserted inside the room temperature bore of the 7 Tesla superconducting magnet. The gain bandwidth plot of GaAs MESFETs (FSU01LG) was obtained using a function generator and an oscilloscope for the amplifier, once, inside the magnet, and then, outside the magnet. The Bode plot thus obtained is shown in Fig. 7·10. It was noticed that there was minor affect on the gain of the preamplifier when placed in the 7 Tesla field. The preamplifier was also rotated at different angles with respect to the magnetic field in the bore of the magnet, which only resulted in a slight change (less than 0.2 volts) in the bias points and transimpedance of the FETs. This variation (reduction) in drain current is attributed to the change in magnetoresistance of the FET channel (Hall, 1879). The Lorentz force acting on the charge carriers causes them to undergo $E \times B$ motion, leading to a drain current which is dependent on the applied magnetic field. The field dependence generally causes a decrease in transconductance in silicon based junction field effect transistors, which was observed in previous room temperature preamplifier designs (unpublished), in agreement with the

Figure 7·9: Preamplifier Inside the Bore of a Room Temperature 7 Tesla Magnet

literature (Bodart et al., 1998). However, the GaAs MESFETs tested here retained most of their intrinsic gain even in the presence of 7 Tesla and 14 Tesla magnetic field.

Similar tests were conducted by mounting the preamplifier on a wooden stick and inserting it inside the bore of the 14 Tesla magnet filled with liquid nitrogen, Fig. 7·11, Fig. 7·12. The drain resistor in this case was equal to 210Ω. A slight change in the gain of the preamplifier was noticed. However, a drop in drain current from 12 mA at room temperature to 3.6 mA at liquid nitrogen temperatures was noticed as shown in Fig. 7·12. This was expected due to reduced charge carriers in GaAs with the lower temperatures.

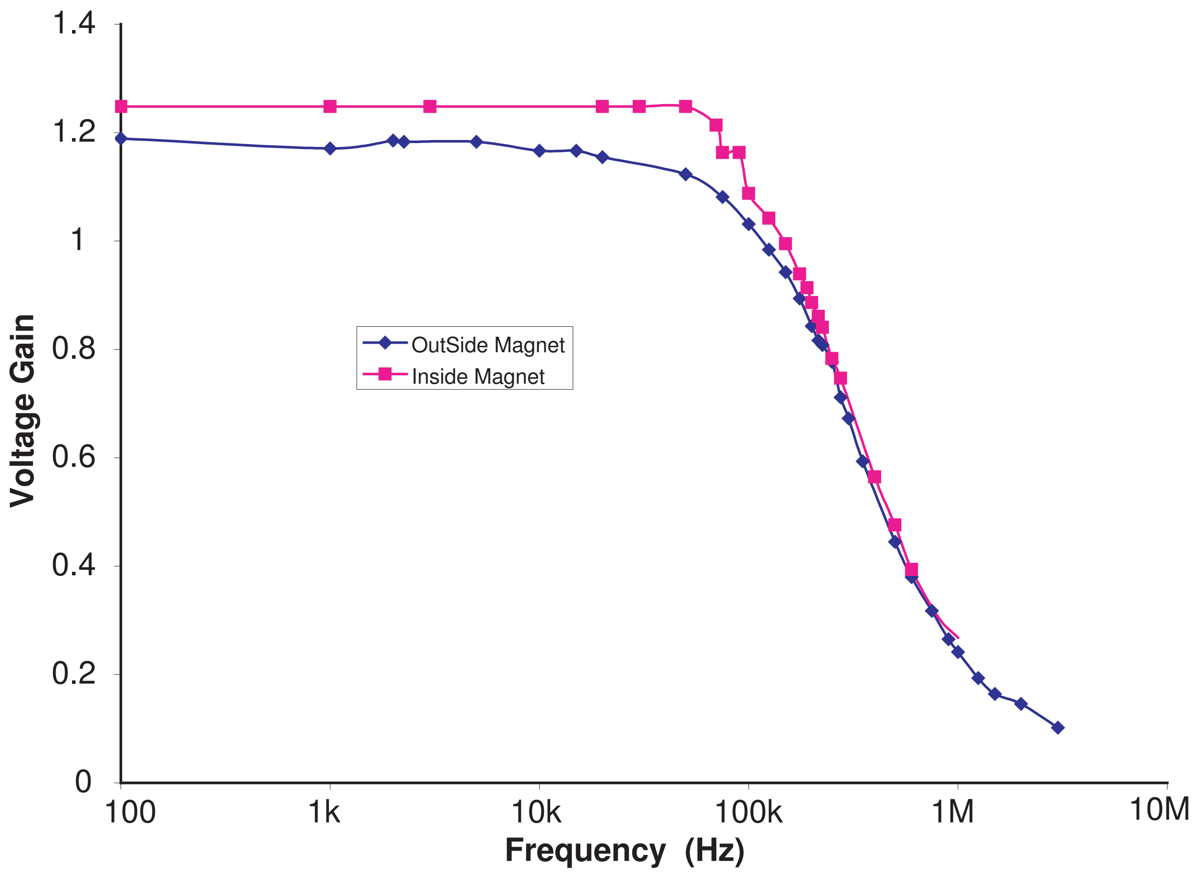

Figure 7·10: CS preamplifier Bode plot in a 7 Tesla magnetic field

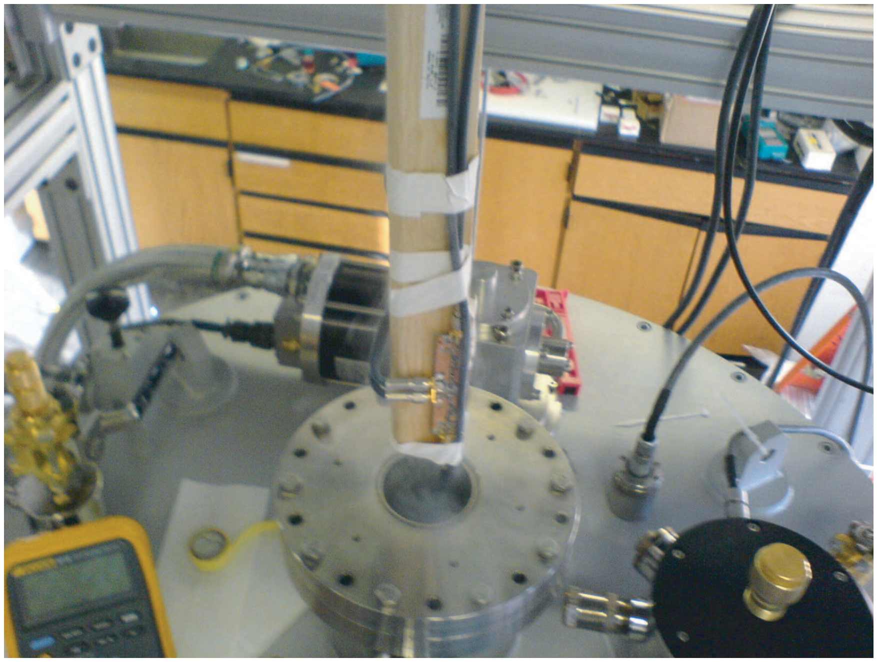

Figure 7·11: Preamplifier being inserted into the bore of a 14 Tesla Magnet

7.3.2 Cryogenic FTICRMS Testing

The performance of the low noise cryogenic preamplifier was evaluated on the first, cryogenic Fourier-transform ion cyclotron mass spectrometer (O'Connor, 2002). Previously, the first experiments reporting an ion signal on the cryogenic FTICRMS used a low performance room temperature instrumentation amplifier (Lin et al., 2007). The inputs of the amplifier were connected using 2 m long wires to the detection plates, which deteriorate the ion signal. The present cryogenic preamplifier is mounted in close proximity to the detection plates and is shown to provide improved SNR.

The cold stage of the preamplifier is mounted on 1 side of an FR4 PCB with a copper ground plane on the other side as shown in Fig. 7·13. Generally for UHV applications FR4 is not used as it out-gasses. However, with temperatures near 4 K, all gas (primarily nitrogen) freezes, and thus, out-gassing is not a limitation for low temperature UHV systems. Outputs of the preamplifier cold stage are extracted via a BNC feedthrough (MDC Vacuum, CA) and connected to a room temperature stage and post-amplifier. The connect-

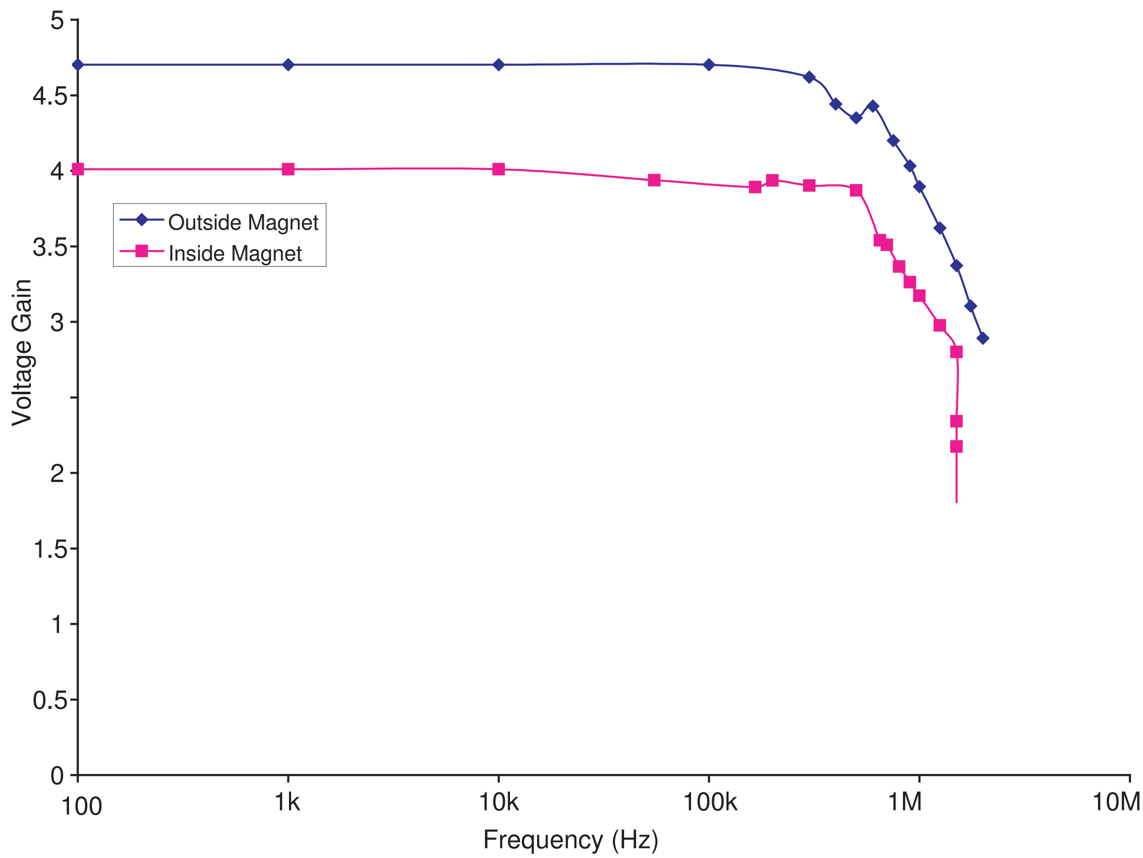

Figure 7·12: Bode plot of the Preamplifier inserted into the bore of a 14 Tesla Magnet ing wires used for this purpose are a special alloy of phosphorous-bronze from Lakeshore (Westerville, OH) which have low thermal conductivity, thus reducing the heat load on the cryogenic system.

The power dissipation in the cold stage is 10.5 mW, out of which the FETs account for the 0.5 mW, the remaining is dissipated across the current source resistor, R_s. The ground plane on the back of the preamplifier PCB partially shields from RF interference due to the hexapoles, which typically carry 300-600 V_{p-p}, at 800 kHz, of AC voltage and are in close proximity to the preamplifier.

A simple test which is often used to test if the preamplifier is working or not, can be done while the preamplifier is connected to the detect plates. The test is performed by applying a small differential RF signal at a particular frequency on the excite plates. Due to the capacitive coupling between the excite and detect plates, a small portion of this RF gets coupled onto the detect plates. This RF signal is picked up by the preamplifier, amplified and can be detected at the output of the amplifier to verify the functionality of the preamplifier. Since in this test, we are applying a excitation voltage on one set of electrodes, and at the same time, detecting on the other pair of the ICR cell, this test is also referred as *Detect During Excite test* (DDE). This test can be done at room temperature and at different stages/temperatures during the cooling of the magnet.

A DDE test was conducted by applying a 30 mVp-p RF signal at 140 KHz (720 Da @ 7 Tesla) generated by a function generator, which was later converted into two out of phase sinusoidal signals by a balun transformer. Hence, the coupled RF signal on the detect plates was amplified by the preamplifier and then by the amplifier. Fourier transforms of the amplified signal at two different temperatures are shown in Fig. 7·14. The baseline noise spectrum between 900 and 950 Da are shown in the inset, which exhibits $\approx$ 2.7 times lower noise at 4 Kelvin as compared to 300 Kelvin. The RF signal intensities appear similar, but when the time domain signal was further investigated, it revealed that the preamplifier gain increased at 4 Kelvin, Fig. 7·15. The transient showed that the digitizer was saturated in both the cases. However, the presence of a third harmonic at 240 Da at 4 Kelvin reflects upon the higher gain and much worse overloading of the digitizer. The DDE test is perhaps the only reliable way to verify the functionality of the preamplifier when it is inside the cold bore of the superconducting magnet.

Various control voltages driving the ion optics and timing triggers were generated using a PXI-based datasystem developed at AMOLF (Mize et al., 2004) which provides a user interface to control the experimental pulse sequence and also acquires, stores and analyzes the data obtained from FTICRMS. C_{60} dissolved in toluene was deposited on a stainless steel plate as a standard to test the functionality of the cryogenic preamplifier at 4 K. C_{60} ions were laser desorbed using a 355 nm Nd:YAG laser (Continuum, Santa Clara, CA) and transferred to the FTICRMS mass analyzer using a pair of hexapoles. These hexapoles were driven by a custom oscillator circuit with an RF signal of 50 V_{p-p} at 800 kHz (O'Connor et al., 2002; Mathur and O'Connor, 2006). Ions were accumulated in the ICR cell using gated trapping. After an initial delay to allow the ions to thermally stabilize, a broadband RF sweep voltage of 20 V_{p-p} was applied on the excitation plates to excite the C_{60} ions into coherent cyclotron orbits. The RF frequencies were swept from 107 to 214 kHz (m/z 500-1000 Da) during the 20 msec excite pulse.

The induced image charge on the detection plates was amplified using the cryogenic preamplifier and the post-amplifier, before being sent to the ADC. The 14-bit ADC sampled the ion signal for 0.26 sec at an acquisition rate of 4 MHz. Fast Fourier-transform of the signal was done in MATLAB and then calibrated into the m/z domain for a magnetic field strength of 7 Tesla. The resulting mass spectrum depicting the C_{60} isotopic distribution is shown in Fig. 11·2. The SNR in the mass spectrum is around 1600 for the C_{60} monoisotopic peak. This represents an improvement of about 20 times compared to the previous results using the room temperature amplifier (Mathur et al., 2007).

Figure 7·13: Cryogenic Preamplifier Mounted on the ICR cell

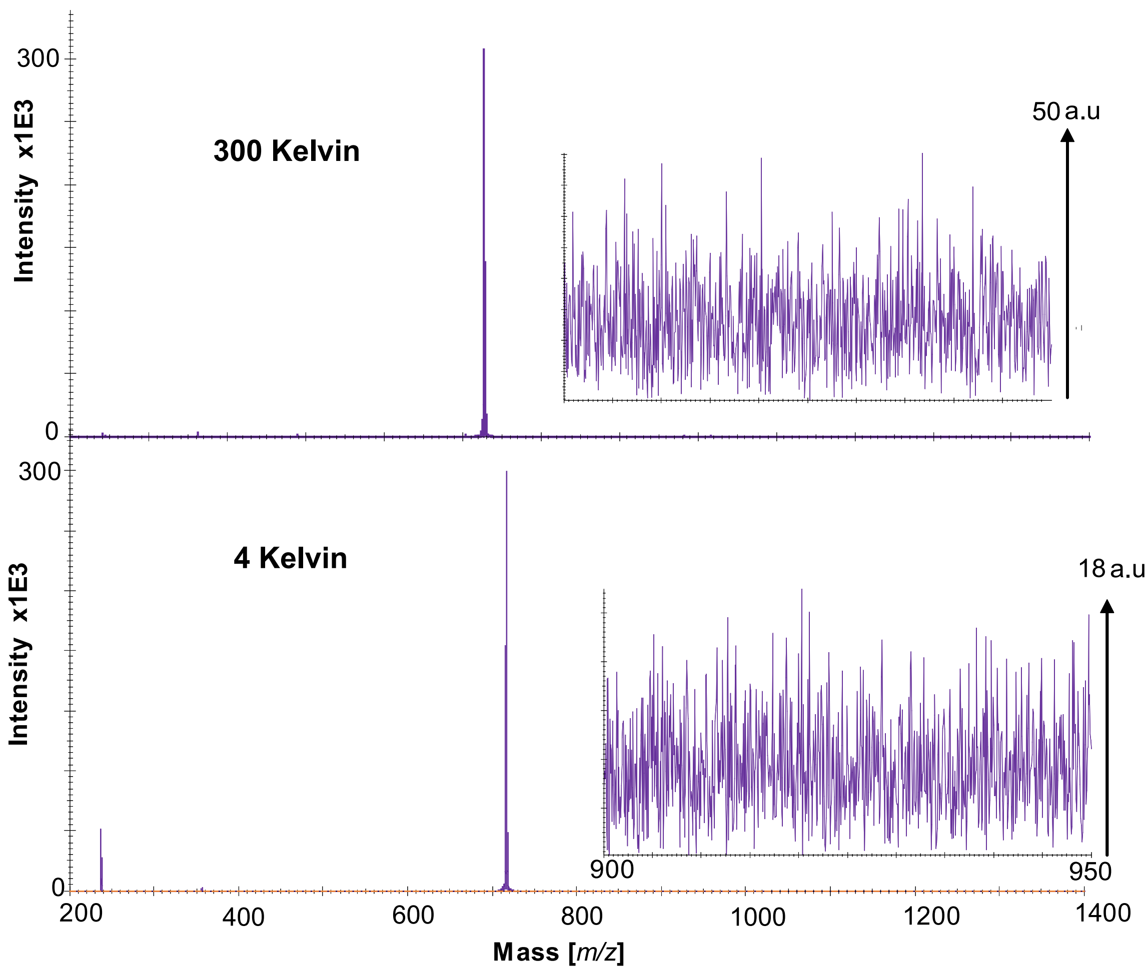

Figure 7·14: Detect During Excite evaluation of Cryogenic Preamplifier showing ≈ 2.5 times lower noise at 4 K

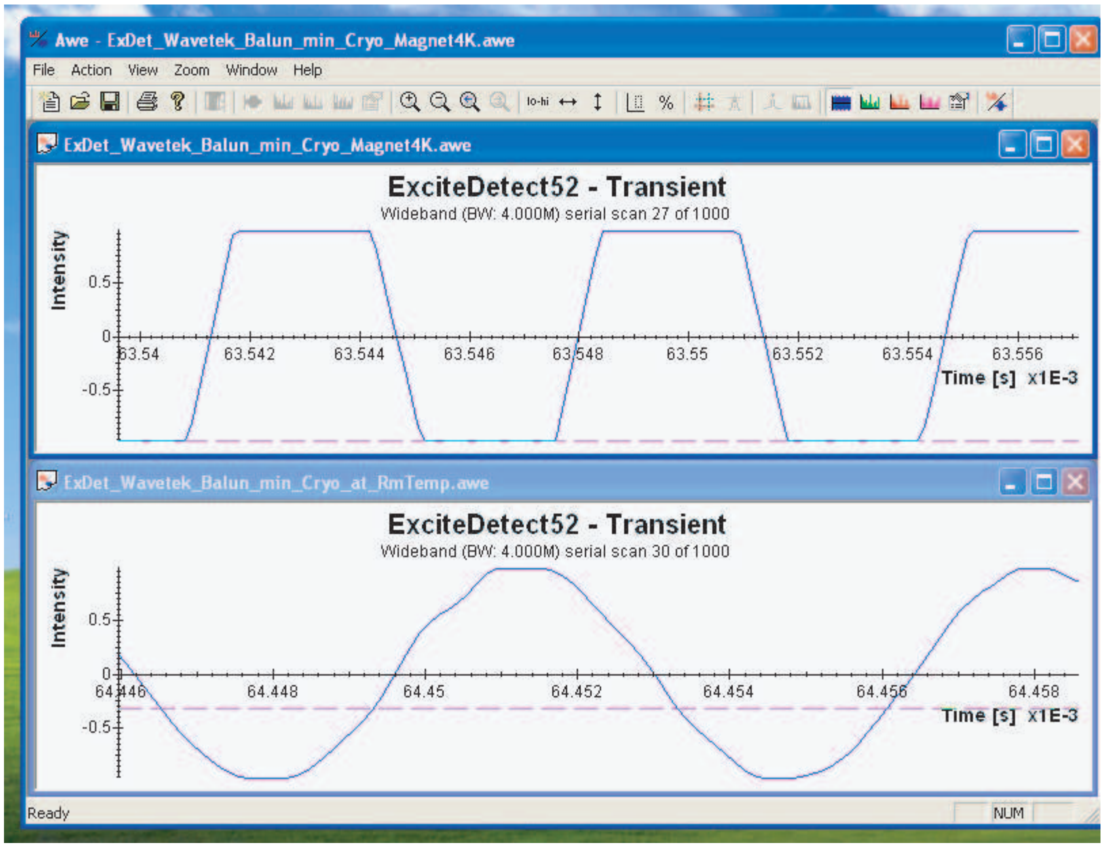

Figure 7·15: Detect During Excite (DDE) Transient showing increased gain at 4 K

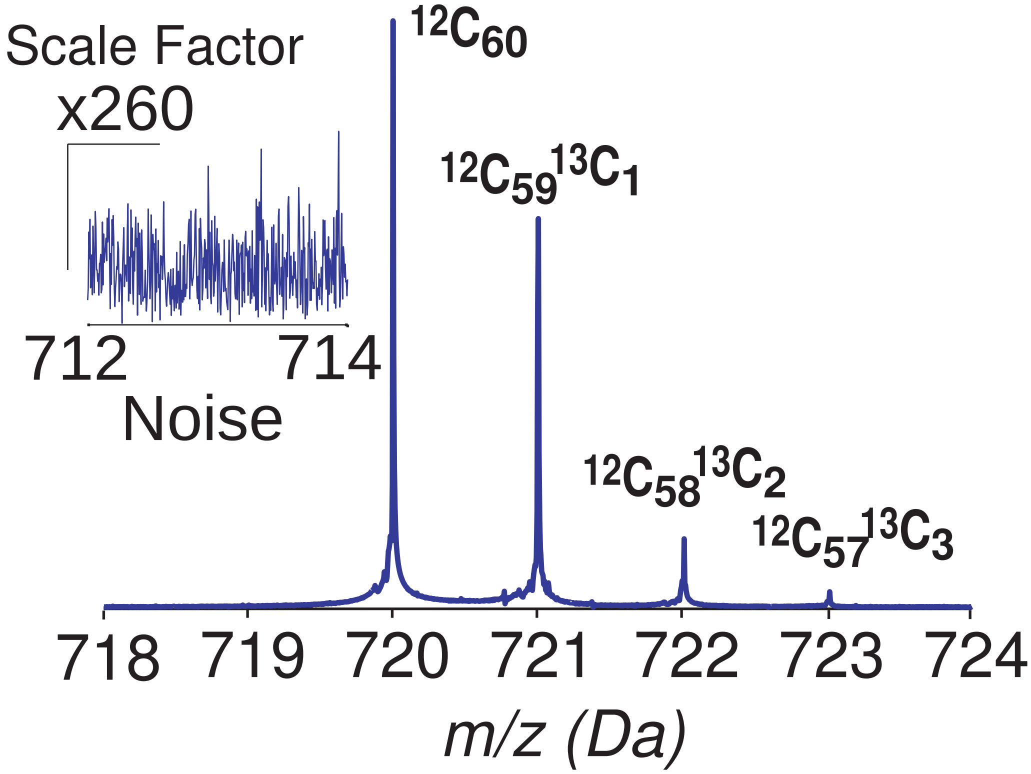

Figure 7·16: C_{60} MS obtained using BUSM Cryogenic Preamplifier

7.4 Conclusion

Cryogenic detectors enable the monitoring of phenomena which are very sensitive to noise from external energy perturbations. The signal from these sensors generally must be amplified prior to signal processing. For such low temperature sensors it is often critical to have a preamplifier in close proximity to the sensors inside the cryogenic system. The minimal length connecting wires between the sensor and the preamplifier inputs ensures low parasitic capacitance, thus minimizing attenuation of high frequency components in the signal. Keeping the preamplifier at low temperature also provides additional advantages in terms of lower Johnson noise and leakage currents.

Conventional low noise silicon based components do not work at 4 K and most of the passive resistors and capacitors behave erratically when subjected to large temperature cycles. This necessitates the use of GaAs devices with non trivial circuit and layout design practices for low temperature amplifiers. Moreover placement of FETs in the high magnetic field of the superconducting magnet can potentially cause performance degradation in terms of their transconductance.

In this chapter we present a cryogenic preamplifier which uses commercial GaAs MESFETs. The preamplifier was completely characterized on the bench for its performance at room temperature and liquid helium temperatures. The cold stage of the preamplifier is followed by a room temperature Si JFET cascode stage and then a opamp based instrumentation amplifier. The complete amplifier has a gain of 250 with a high frequency roll-off at 850 kHz.

The cryogenic preamplifier was tested to detect induced voltage in a cryogenic FTICRMS. The cold stage of the preamplifier uses 50 ohm resistors at gate, drain and source of the GaAs MESFETs, which is critical for stable operation of the FETs. C_{60} ions were desorbed using a laser from a stainless steel plate and transferred to the FTICRMS, inside the cold bore of the superconducting magnet. The C_{60} ion signal in the obtained mass spectrum showed a SNR of ≈ 1600. Further tests, comparing the cryogenic preamplifier to previous room temperature amplifiers, are undergoing.

Chapter 8

Cryogenic Test Set-up

To determine the basic functionality of the GaAs MESFETs at liquid helium temperatures a test set up was designed. The primary requirement was to be able to conduct all the necessary experiments with ease and minimal cryogen loss.

8.1 Set-up for Liquid Helium Testing

A stainless steel test Dewar which consists of 3 concentric tubes was designed, shown in Fig. 8·1. The sample which in this case is the PCB of the cryogenic preamplifier is placed inside the inner most tube. Liquid helium is made to flow between the inner tube and the middle tube via side ports. A nw25 flange is used to pump the region between the middle tube and outer tube to rough vacuum ($\approx 2 \times 10^{-2}$ mbar). This is necessary to prevent extra heat load on the cryogen which may arise due to convective gas flow between the middle tube and outer tube. Dewar is made of stainless steel as it is one of the most suitable alloys for vacuum system construction (Moore et al., 2002). It is easy to machine, strong and contains relatively less volatile impurities. For cryogenic concerns, it has low thermal conductivity which keeps the heat load on the cryogen less.

The 3D computer-aided design (CAD) drawings of the dewar were made using Autodesk inventor (Autodesk, Inc. CA), Fig. 8.1(b). The drawings were supplied in iges format to the Boston University Physics Scientific Instruments Facility where the tubes were welded to the base plates using arc welding (mac, 2007), Fig. 8.1(a).

A simplified set up was established with the suggestion of Dr. Randall Kirschman. This enabled the tests to be carried out with minimal cryogen use. In all the experiments

(a) Cryogenic Dewar

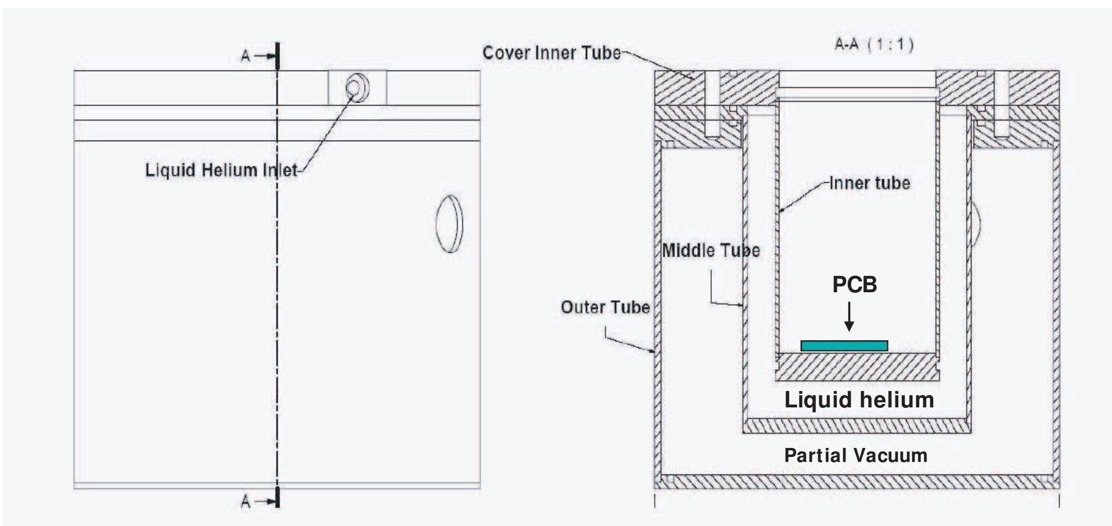

(b) CAD drawing of the Dewar

Figure 8·1: In-house designed Dewar for cryogenic testing

Figure 8·2: Cryogenic dip probe set up

at 4 K, the GaAs FETs were directly immersed in the liquid helium ensuring temperature stability during the testing period.

The GaAs FETs with 50 ohm damping resistors were mounted at the end of a 2 m long 12 mm i.d., 2 mm thick stainless steel tube. All the wires to carry bias voltages and RF were passed through this tube and connected to a terminal block at the end. The stainless steel tube served as the ground. GaAs FETs mounted on the test fixture on one end of the tube were slowly inserted into the liquid helium dewar as shown in Fig. 8·2. Liquid helium boiling off from the storage tank would rise up and cool the top part of the stainless steel tube. The thin walled stainless steel tube could be locked at different heights allowing measurements at different temperatures.

8.2 Labview Automated Test bench

As mentioned before, the electronic testing of circuits at cryogenic temperatures requires a test set up which would utilize the cryogen efficiently in cooling the components. Moreover it is also required to collect the necessary data in short duration. The stainless steel probe and the circuit while emersed in liquid helium causes continuous boil-off and this time has to be minimized. For this reason we developed an automated test set-up which could supply time varying voltages/currents to the device under test (DUT) and similarly read back the values. This test set up is based on PXI cards which were programmed using Labview.

8.2.1 Labview Automated Script for DC characterization

The bias points of the DUT are connected to several PCI eXtensions for Instrumentation (PXI) Input/Output cards (discussed further in section 10. The modular nature of the PXI system provides flexible, yet powerful instrumentation to facilitate electronic testing. PowerDAQ cPCI/PXI Multifunction Data Acquisition (DAQ) Board from United Electronic Industries, Inc. (Walpole, MA) was used to write and read analog voltages to the test fixture. The multifunction card used, has 32 analog output channels and 8 analog input channels. For DC characteristics of the MESFETs, 2 AO channels were used to apply gate and drain bias while 1 AIn channel was used to read back the drain voltage.

Laboratory Virtual Instrumentation Engineering Workbench (LabVIEW) was used as the platform for development of the test programs. Labview provides a visual programming environment to construct subroutines, called virtual instrumentats (VIs) which are used for controlling the PXI boards. It allows the user to input data/voltages into PXI boards and read the output/voltages back for analysis and plotting.

A screenshot of the Labview script, which was used to obtain the DC characteristics of the MESFETs, is shown in Fig. 8·3. The two input parameters to obtain the VDS versus IDS curves are maximum drain to source voltage (VDS) and starting gate to source voltage

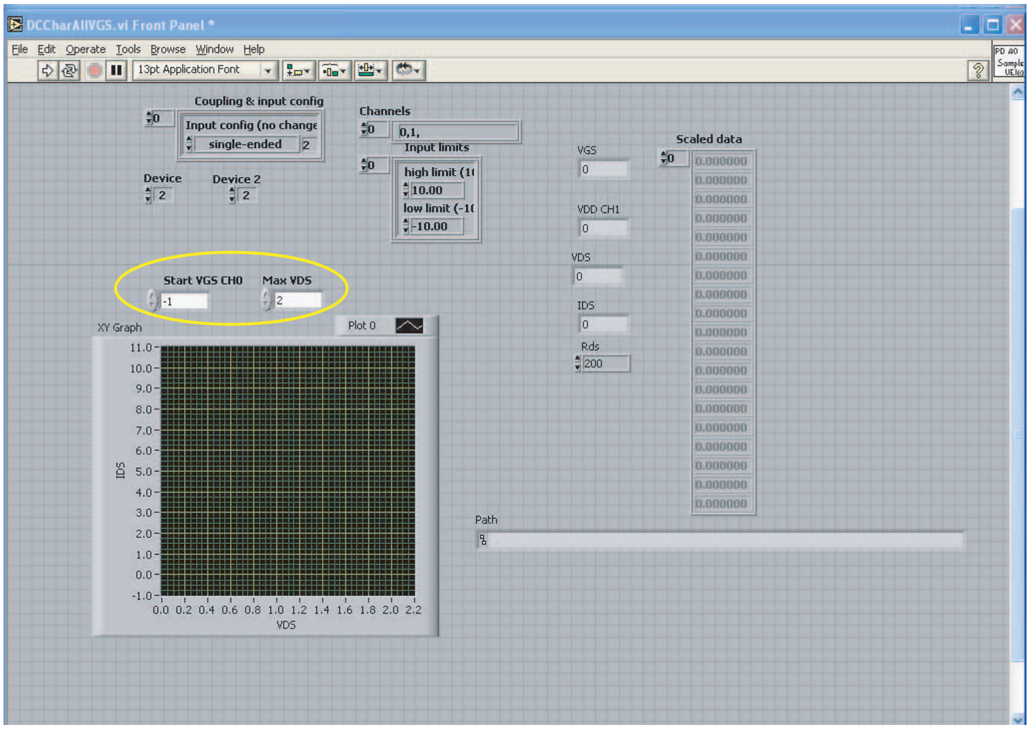

Figure 8·3: Labview VIs to obtain DC Characteristics of FETs

(VGS). The script loops through all the necessary values and read backs the drain voltage for each value of VGS and VDD applied. The block diagram showing all the initialization and control modules is shown in Fig. 8·4.

Similarly Labview scripts in Fig. 8·5 and Fig. 8·6 were used to obtain the Bode plot of the preamplifier at low temperatures minimizing the cryogenic loss. In this set up, a signal generator (PXI 5411) from National Instruments (Austin, TX) was used to apply the test RF signal and a high speed digitizer (PXI 5621) from National Instruments read the RF amplitude at the drain.

The Cryogenic Automated test set up enabled us to conduct functionality and characterization tests on the GaAs MESFETs and the preamplifiers in a reliable and efficient way.

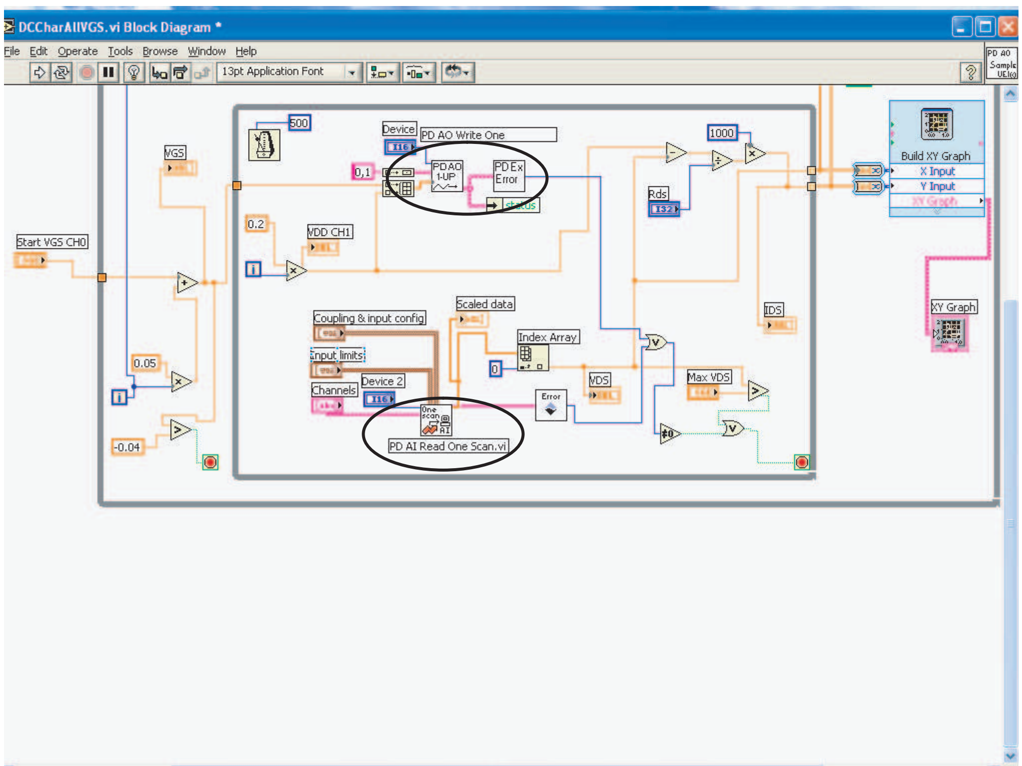

Figure 8·4: Labview Block Diagram for DC Characteristics of FETs

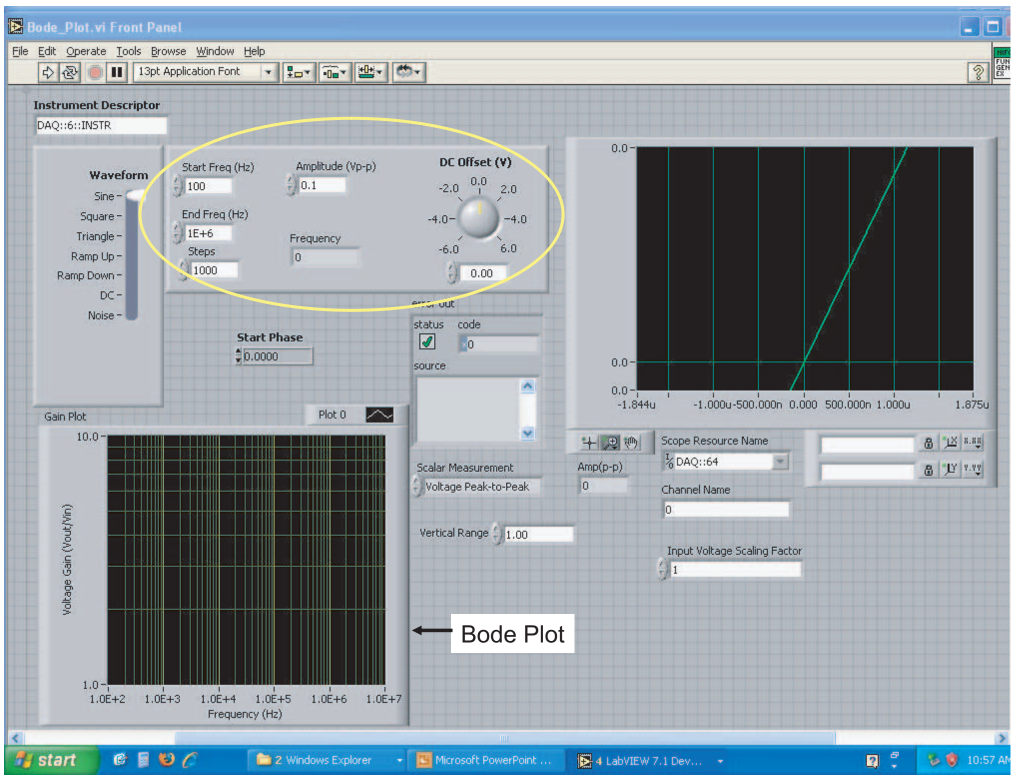

Figure 8·5: Labview VIs to obtain DC Characteristics of FETs

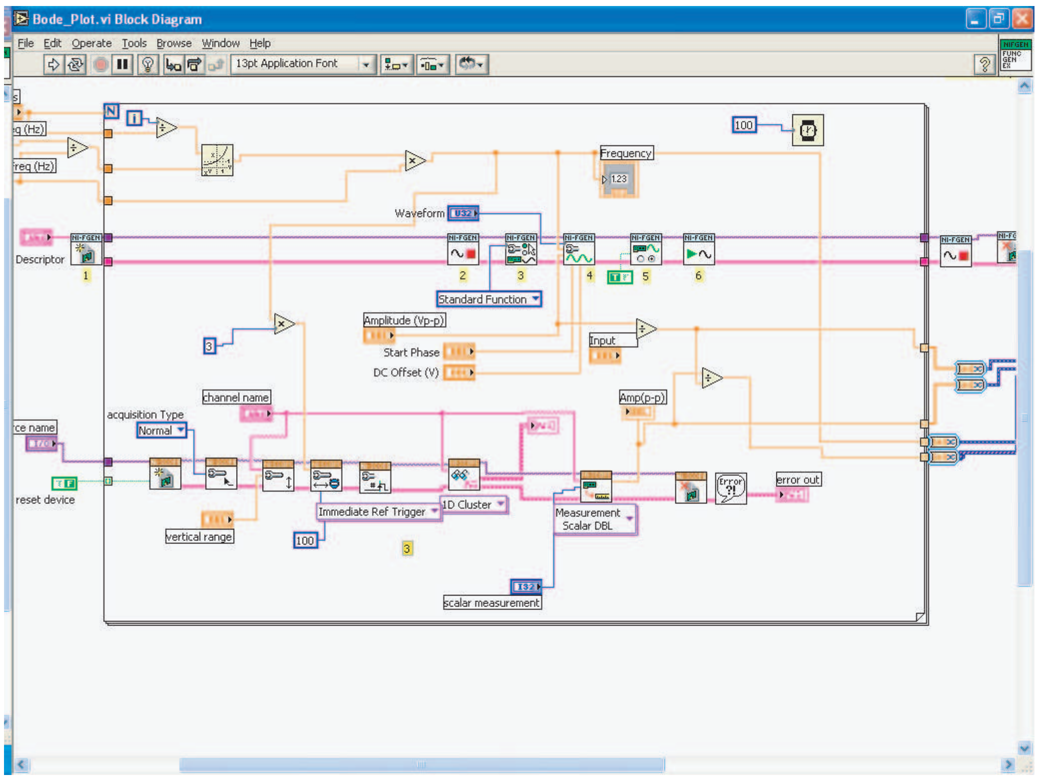

Figure 8·6: Labview Block Diagram for DC Characteristics of FETs

Chapter 9

High Power RF Generator

This chapter has been reproduced in part with permission from4. Raman Mathur, Peter B. O'Connor, "Design and Implementation of a High Power rf Oscillator on a Printed Circuit Board", Review of Scientific Instruments, Vol.77 , 114101 (2006). Copyright 2008 American Institute of Physics.

A construction methodology has been developed for the high voltage r.f. generator to power multipole ion guides. In a previous paper, we proposed an electrical design based on an LC tank oscillator circuit. The circuit can generate upto 1 KV of output voltage which can be linearly controlled by an analog signal. The frequency can be varied by an order of magnitude (kHz to MHz) by tuning either the capacitance or the inductance of the tank circuit. Recently, we have simplified the implementation of the r.f. oscillator by designing a PCB for the circuit. The primary objective of this chapter is to present a practical approach to design and build such a high power RF circuit. Solutions to several design issues are proposed and implemented to construct a PCB for the RF power generator presented earlier. The PCB has a footprint of merely 7 X 5 $inch^2$, and the transformer coil takes 3 inches of headroom. The circuit uses commercially available components which are easy to obtain and inexpensive. These features make the design to be readily integrated on several instruments such as traps and other electrode arrangements. The gerber files for the PCB can be found on www.bumc.bu.edu/ftms/rfOsc.

9.1 Introduction

The use of Multipole ion guides continue to be one of the most popular technique in several scientific experiments involving ion-beam physics(Brown and Gabrielse, 1986; Gerlich, 1992). In mass spectrometers, they are used for accumulation and mass filtering of the ions prior to the mass analysis, and also as collision cells for fragmenting ions (Senko et al., 1997; McIver,). Thus multipole ion guides are an integral part of modern mass spectrometers. The ions in the multipole ion guide are subjected to a time varying RF (radio frequency) signal. The amplitude, the frequency and the D.C. offset of this RF signal is determined by the Mathieu equations for ion trajectories (Gerlich, 1992). Simplified formulae can be derived to determine required frequency and voltage for the transfer of ions (Cermak, 2005). The minimum RF frequency, f_{min} on the multipole ion guide with 2n poles, required for the transfer of ions with mass range, m_{max} to m_{min} is given by,

$$f \geq f_{min} = 2.08\text{MHz}.\frac{(n-1)}{\hat{r}}.\frac{\sqrt{E_m/eV}}{(r_o/cm)^2}.\frac{\sqrt{m_{max}/u}}{m_{min}/u} \tag{9.1}$$

where, r_o is the radius of the multipole, E_m is the maximum kinetic energy of the ions with mass range m_{min} to m_{max}, and $e_o = q$.

The RF amplitude necessary on the multipole can be derived by,

$$V_o = \frac{80(n-1)}{3n.\hat{r}^n}.\frac{E_m}{e_o}.\frac{m_{max}}{m_{min}} \tag{9.2}$$

For small molecules higher frequencies are required which is usually the case for MS/MS studies. And for bigger molecules high RF voltage amplitude is needed to transfer them effectively via multipole.

For typical biomolecular studies a quadrupole ion guide is driven with an RF power generator with a signal frequency around 1 MHz and peak to peak voltage of around 1 KV (O'Connor et al., 2002; Jones et al., 1997).

Previously, we proposed an RF power generator design based on the LC tuned oscillator (O'Connor et al., 2002) . The signal frequency of the RF generator can be adjusted by using tuning capacitors in parallel with the intrinsic capacitance of the trap electrodes. Moreover, the output signal amplitude is linearly adjustable from 0 to 1 KV peak to peak (p-p).

Here, we present the construction methodology for the RF power generator circuit described in (O'Connor et al., 2002). The construction of such a high power and high frequency circuit involves careful designing of the Printed Circuit Board (PCB) with proper RF shielding and thermal management. We note that, although implementing a prototype circuit on a generic prototyping board may sometimes be faster, a custom PCB usually is more convenient in the long run. Moreover PCBs are inexpensive, reliable and easy to reproduce. However, PCB design for the RF power generator is complex. This is because the high power and frequency requirement of these circuits compel us to consider interactions between several complex issues described below.

- As we mentioned before, the electrodes of a multipole ion guide are driven by approximately 1 KV p-p and 1 MHz sinusoidal signal. This high voltage appearing on the printed circuit board traces can be hazardous. The dielectric strength of the board material can be compromised which can lead to local or complete insulation breakdown.

- In the RF generator circuit high currents are used to charge the capacitor of the tank circuit (Cermak, 2005). These high currents cause heat dissipation due to the ohmic loses in the traces. The excessive heating of the copper conductors can eventually melt the copper causing a broken connection (Pan et al., 1993; Friar and McClurg, 1968).

- Since the signal frequency is quite high, it causes the so called skin effect, which in turn increases the resistance of the conductor. This again can lead to significant heating of the conductor as well as signal distortion.

- The devices operating at high frequency and high power generate a significant amount of heat. The temperature rise of the components due this heat causes power derating and eventually may cause device failure [1] (Lee, 1995; Lee, ; Elliot,).

- The radiation of energy from conductors carrying high frequency signals on the PCB causes electromagnetic interference or crosstalk. This may lead to unwanted signal coupling between tracks in proximity.

- The copper conductor on the the PCB introduces some parasitic capacitance which effects the signal at high frequencies. This parasitic capacitance increases with the conductor length and cannot be neglected in high frequency PCB design. The high propagation delay encountered by the signal while traveling on these long traces can cause degradation of the signal.

- The high power RF circuits radiate electromagnetic waves which interfere with the ambient RF signals, such as those generated by cell phones and radio.

- Another important motivation for constructing a PCB of an electrical circuit is space. The area occupied by the circuit can be optimized significantly by properly designing a PCB for the circuit.

Note that the simple minded approaches to deal with the challenges in high power and high frequency circuit design do not provide an optimal trade off between the above mentioned issues. For example, insulator breakdown and crosstalk between conductors can be avoided by increasing the distance between the components. However, this increases the space we need for the components on the PCB. Moreover, longer traces are required to connect the components which leads to higher parasitic capacitance of these traces. The high capacitance in many cases degrades the signal quality. Similarly, in theory heat dissipation and the resulting temperature rise in conductors can be determined using fundamental physical laws. However, in practice the temperature rise is also a function of the heat lost due to conduction, convection and radiation. These non-linear phenomena makes it difficult to estimate the rise in temperature of the conductors. Thus, the high power and

[1] The maximum power a device can handle decreases with the rise in its temperature.

high frequency circuit design requires making tough choices and is a non-trivial task which requires analysis and extensive experimentation.

The goal here is to present the principles of high power RF circuit design which are available in electrical circuit knowledge base and compile them so that they can be used in disparate fields such as mass spectrometry. An approach is developed to deal with the above mentioned issues encountered in high power RF design. We have demonstrated the use of the proposed method to construct a circuit for the RF generator to drive multipole ion guides. The PCB of the oscillator circuit takes 7×5 in. of floor space with a 3 in. high transformer coil. In a typical hybrid FTMS (ESI-QqQ-FMTS) 6 of such RF signal generator circuits are required to drive the different multipole ion guides (O'Connor et al., 2006; Belov et al., 2004). With the current PCB design all of these can be conveniently arranged in a 19 in. rack mountable chassis with proper cooling and power supplies. Although, here we have described the method for the RF oscillator circuit, the approach can be applied to design the PCB for any high power and high frequency circuit.

The rest of the chapter is organized as follows. In Section 9.2.1, we describe the process of designing and fabricating a PCB. In Section 9.2.2, we illustrate the various considerations in PCB design for circuits involving high power and high frequency signals. The selection of proper heat sink for the high power dissipating circuit components is discussed in Section 9.3. This is followed by discussion of parasitic impedance and mixed signal design considerations in Section 9.4 and Section 9.5 respectively. Conclusions and future modifications which are currently being implemented are described in Section 9.8.

9.2 PCB Design

9.2.1 PCB Design Methodology

We have designed a two layer PCB for the RF power generator circuit, as shown in Fig. 9·1. The basic steps followed in the design are same as above, however here we mention some design choices which were made during the process. The minimum clearance for critical high voltage traces were set to be equal to 100 mils, discussed further in Section 9.2.2.

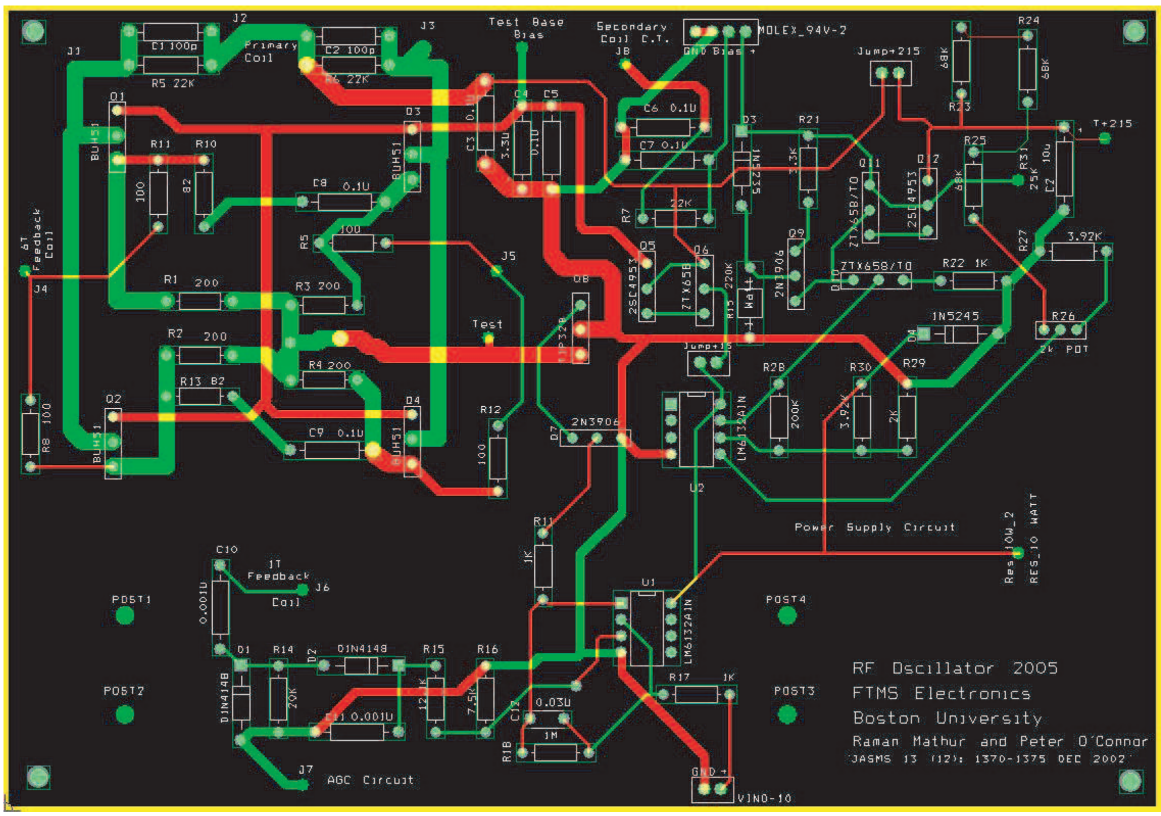

Figure 9·1: RF Generator PCB

Additionally, the width of high current connecting wires (traces) were set to 100 mils, refer Section. 9.2.2. In the component placement step, the components carrying high frequency RF signal were kept spatially separate from the components of the D.C. regulator circuit. The traces carrying the RF signal were routed first for minimal lengths, followed by the transistor bias and the D.C. regulator connections. The generated Gerber files were sent to Advanced Circuits for the PCB fabrication.

9.2.2 PCB design issues

Modern PCB design methodology for high frequency circuits is based on a set of guidelines regarding their physical and electrical characteristics. While in principle these guidelines can be derived from fundamental laws of physics, various practical issues and uncertainities—such as presence of impurities, complex geometry, etc.—make such a derivation impractical. Thus, a body known as *Institute for Interconnecting and Packaging Electronics Circuits* (IPC) publishes recommendations for these guidelines based on extensive suites of controlled experiments. For our design, the publication IPC-2221 (Industries",) is particularly relevant. In the subsequent sections, we describe various aspects of the design of our PCB, the issues that affect these aspects, the design principles derived from fundamental laws of physics and the corresponding IPC recommendations.

Track Spacing Determination

One advantage of using PCB is that it generally reduces the board area, which not only leads to a neat construction, but also makes the circuit functionally more reliable. Reduction of board area requires decreasing the spacing between the tracks and components. However, insufficient clearance between the conductors with a large potential difference can cause electric breakdown of the insulation. Thus, a minimum spatial clearance between any two conductors must be maintained. It is our goal to determine this clearance as a function of the dielectric strength of the insulator and the potential difference between the conductors. Recall that the dielectric strength of an insulator is defined to be the minimum potential difference across two points separated by unit distance that causes insulation break-down.

We used a material called FR4 as our PCB material. FR4's dielectric strength under ideal conditions is 39 KV/mm. However, in practice the dielectric strength depends upon several factors: the ambient temperature, pressure and humidity, structural properties such as voids and types and distribution of impurities, geometry (whether it is layered or granulated), etc. Thus in practice IPC recommendations are used to determine the value of the minimum clearance between the tracks on the PCB.

The maximum output voltage in our circuit appears at the collector of the power transistors, which is around 350 p-p volts. IPC recommendation for this level of potential difference for FR4 is 52 mils. Since our board area budget is not too tight, we designed our PCB with a clearance of 100 mils between high voltage tracks. We have kept 20 mils spacing between tracks with voltages less than 15 volts due to the limitations posed by the PCB manufacturing.

Track Width Determination

After track separation, the next thing that needs to be determined is the track width. Choosing too high a width will introduce a large amount of parasitic capacitance and inductance; choosing too small a track width, on the other hand, will generate too much of heat, since thinner tracks have higher resistance and resistance causes heat dissipation. Excessive heat may hinder normal operation of the circuit, and may even damage it by inducing a cyclic effect called *thermal runaway*, which is described in Section 9.3 in the context of transistors.

Thus, it is desirable to minimize the track width, w, given the maximum allowable temperature rise, ΔT and the current it is required to carry, I. From the first principles of physics, we can derive that the relation between these quantities under ideal conditions is:

$$I = K\sqrt{\Delta T}\sqrt{w \times t} \tag{9.3}$$

Here, K is a proportionality constant and t is the thickness of the track.

However, the actual relation between these quantities differ from the theoretical relation since the generated heat is continually dissipated by various processes—the dielectric cools the track by conduction, the ambient air cools it by convection and the track itself looses heat by black body radiation.

Thus, we rely on an empirical formula proposed by the authors of (Brooks, 1998) by fitting the IPC-published experimental data relating temperature and current for PCB tracks with different cross-section area (Industries",). The proposed formula is shown in Eq. 9.4.

$$I = .065 * \Delta T^{.43} * (w \times t)^{.68} \tag{9.4}$$

In our design, we have used $\Delta T = 20°\text{C}$ and $t = 1.25$ mils for 1 oz. copper. Eq. 9.4 then shows that a track carrying 5 A current should atleast be 70 mils wide. Similarly, for traces carrying less than 1 A of current the trace width is around 7 mils keeping the other parameters same. Typically, a 10% margin is added to the value of the width obtained from the IPC data to account for the variation in conductor thickness, moisture and pollutants on the surface of the board, and the heat conducted into a track by its attachment to a power dissipating components. However, since our area budget is not too tight, we have used 100 mil wide tracks for laying out high current nets, while the width of the tracks carrying low currents was kept 20 mils. The ground track is also made 100 mils to keep the temperature rise within limits and to minimize other parasitic effects as mentioned in Section 9.5.

9.3 Heat sink selection

The power dissipation at the circuit elements is proportional to the power that is delivered at the output. Since the circuit that we construct here delivers a significant amount of power to the multipole ion guides, the circuit elements generate a significant amount of heat. If this heat is not dissipated properly, then it will increase the temperature of the circuit elements. This increase in temperature is detrimental due to various reasons:

1. The life expectancy and reliability of a typical semiconductor device is inversely proportional to its junction temperature.

2. The thermal efficiency of a transistor—maximum allowable power dissipation decreases with temperature.

3. An extreme effect of temperature increase is the following. An increase in the junction temperature increases the junction resistance of a transistor, which further increases the power dissipation (since power dissipation is proportional to the resistance), which in turn increases junction temperature. This cyclic effect, called *thermal runaway*, may destroy the device.

Thus, in the circuit construction, care must be taken to ensure that the heat generated in the circuit elements must be dissipated in the ambiance. Towards this goal, we mount *heat sinks* on the transistors. An heat sink is characterized by its *thermal resistance*, which can loosely be thought of as the resistance it offers to the flow of heat from high temperature to low temperature. In practice, three thermal resistances are considered: (i) the junction-to-case thermal resistance ($R_{\theta_{jc}}$), which is a property of the transistor, (ii) the case-to-sink thermal resistance ($R_{\theta_{cs}}$), which depends on how the heat-sink is attached to the transistor surface, and (iii) the sink-to-ambient thermal resistance ($R_{\theta_{sa}}$), which is a property of the heat-sink. Therefore, selection of the heat-sink boils down to computing $R_{\theta_{sa}}$, given $R_{\theta_{jc}}$ and $R_{\theta_{cs}}$, and choosing a heat-sink whose thermal resistance is the computed value or less.

These three parameters are related by Eq. 9.5,

$$R_{\theta_{sa}} \leq \frac{T_j - T_a}{Q} - R_{\theta_{jc}} - R_{\theta_{cs}} \tag{9.5}$$

Here, T_j is the maximum allowable junction temperature, T_a is the ambient temperature, and Q is the power dissipated in the transistor.

For the transistors we use, the maximum non-destructive junction temperature, $T_j = 150°\text{C}$ and we assume $T_a = 25°\text{C}$. The worst case power dissipation in each transistor at $1000V_{p-p}$ and 500 kHz is 5 Watt. The transistor we use has $R_{\theta jc} = 2.5°\text{C}/W$; $R_{\theta cs} = 0.5°\text{C}/W$ for our heat-sink mounting method. Thus, we need a heat-sink with thermal resistance $R_{\theta sa} \leq 21.5°\text{C}/W$. We chose a commercially available heat sink with $R_{\theta sa} = 15°\text{C}/W$. In addition, we mount a fan to enhance convectional cooling. Our enclosure contains a sufficient number of vents and ducts to ensure proper flow of air. The heat sinks are staggered to ensure non-obstructive flow of air on them for efficient cooling.

9.4 Parasitic Impedances

In high frequency circuit design the undesirable impedance of the signal wires can significantly impair the quality of the RF signal. This parasitic impedance can arise either due to the inductance of the wires or because of their capacitance with respect to the ground plane. The effect of the parasitic impedance increases with the increase of the operating frequency and with the length of the conductor.

At high frequencies a copper wire behaves as a single turn air coil inductor. As a result, the wires in a circuit implementation have a finite impedance between any two connection points. As a rule of thumb, 1 mm of a wire has around 1 nH of inductance. Hence, at 10 MHz the impedance of a 100 mm wire is equal to 6.2 ohms, which will cause a significant potential difference between the connection points. Due to this intrinsic reactance connecting wires cannot provide appropriate RF signal voltages to various circuit components.

Moreover, at high frequency the signal propagation delay due to the capacitance of the interconnects becomes comparable to the rise time of the signal, significantly effecting the signal integrity.

1. For the above mentioned reasons the length of the wires are minimized in the imple-

mentation of RF power generator circuits.

2. Unbroken metallic areas, called as reference planes, are used to provide a short and low impedance path to connect supply pins of the components to the power nets on the PCB. The use of reference planes also reduces the parasitic inductance of the traces on the other layers.

In general we have to consider the effect of several other phenomena for high frequency circuit design such as reflection of the signal due to impedance mismatch. However the signal frequency of the RF power generator circuit design is below the limit when these factors come into effect. Thus they are not discussed here.

9.5 Mixed Signal Circuit Design

One of the most challenging endeavors in electrical circuits is the design of a high speed mixed signal circuit. Mixed signal circuits contain analog and digital components in the same circuit which significantly influence each others behavior. The designer has to address several issues such as electromagnetic interference (EMI) and power distribution in the construction of such circuits.

In the PCB for the RF power generator circuit the high frequency RF components generate RF noise which can couple to the other sensitive bias components effecting voltage levels. Thus the RF components consisting of power transistors and the transformer coil were physically and electrically segregated from the D.C. subcircuit which included the peak detecting circuit and the voltage regulator.

Generally, in mixed signal design separate power and ground connections are used for the digital and analog circuits to prevent any unwanted noise coupling via the power line. In addition to this, the power connection for digital circuit is decoupled to ground using capacitors. In the PCB for the high frequency RF generator the high frequency noise from the collector could get coupled to the base and disturb the bias of the active devices. Thus we have connected ceramic capacitors with a range of values to the base of the power transistors to bypass any coupled noise to ground. Also ground plane was provided to reduce the reactance of the bypassing network to ground.

A wire carrying a high frequency signal radiates electro magnetic waves, thus acting as an antenna. These electro magnetic waves cause unwanted signal coupling between closely spaced signal wires. Moreover in high frequency PCB design, if the field emanating from the surface of a trace is not guided by a controlled return conductor, then they terminate at the adjacent traces. This also leads to undesirable crosstalk between traces. In the RF power generator circuit we have used ground planes along such traces to reduce the E.M.I. These reference plane provide a low impedance return path to the radiating field and, thus also improving the EMI susceptibility of the circuit components.

In practice there are numerous guidelines to be followed while designing high frequency mixed signal circuits. However, by careful evaluation of the above important considerations a functional prototype of a high speed circuit can be designed.

9.6 Methods

The circuit of the RF oscillator was described in the previous correspondence (O'Connor et al., 2002) and is shown in Fig 9·2 with corrections in the connections for the operational amplifier (LM6132) and addition of an input follower for isolation. In the current version of the circuit the obsolete power transistors 2SC5392's have been replaced by BUH51's from On Semiconductor (Phoenix, AZ). The voltage regulator to provide DC power to the oscillator has remained unchanged from the previous article. A two layer PCB for the RF power generator was designed using the layout tool from Cadence (San Jose, CA). The minimum clearance between critical high voltage traces (wires) was set to be equal to 100 mils (1 in = 1000 mils), discussed below. Additionally, the width of high current traces was set to 100 mils, see below. The components carrying the high frequency RF signal were kept spatially separate from the components of the D.C. regulator circuit. The traces carrying the RF signal were routed first for minimal lengths, followed by the transistor bias and the D.C. regulator connections. The PCB was fabricated by Advanced Circuits

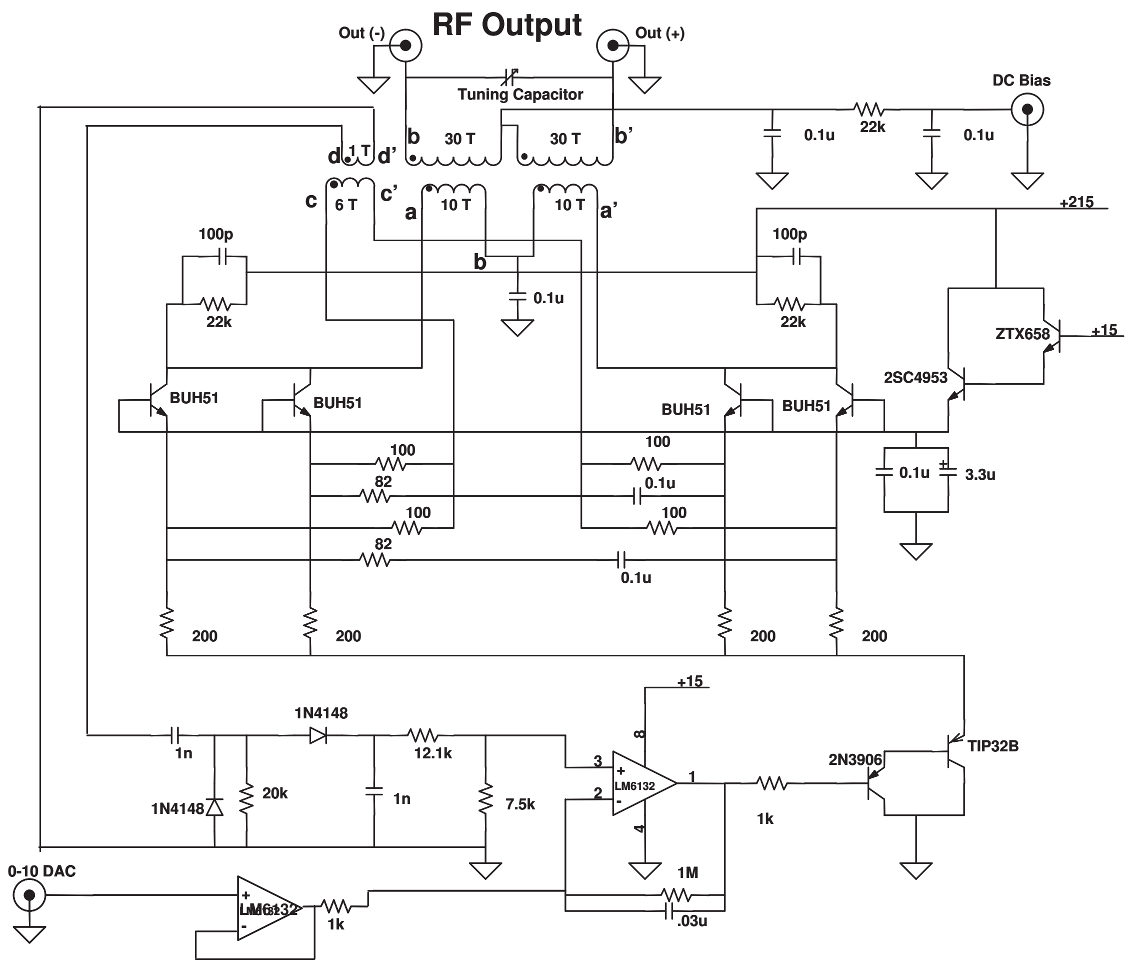

Figure 9·2: Schematic of the RF Oscillator Circuit. The connections of the transformer coils at points a-a', b-b', c-c', and d-d' are elaborated in Fig. 9·5.

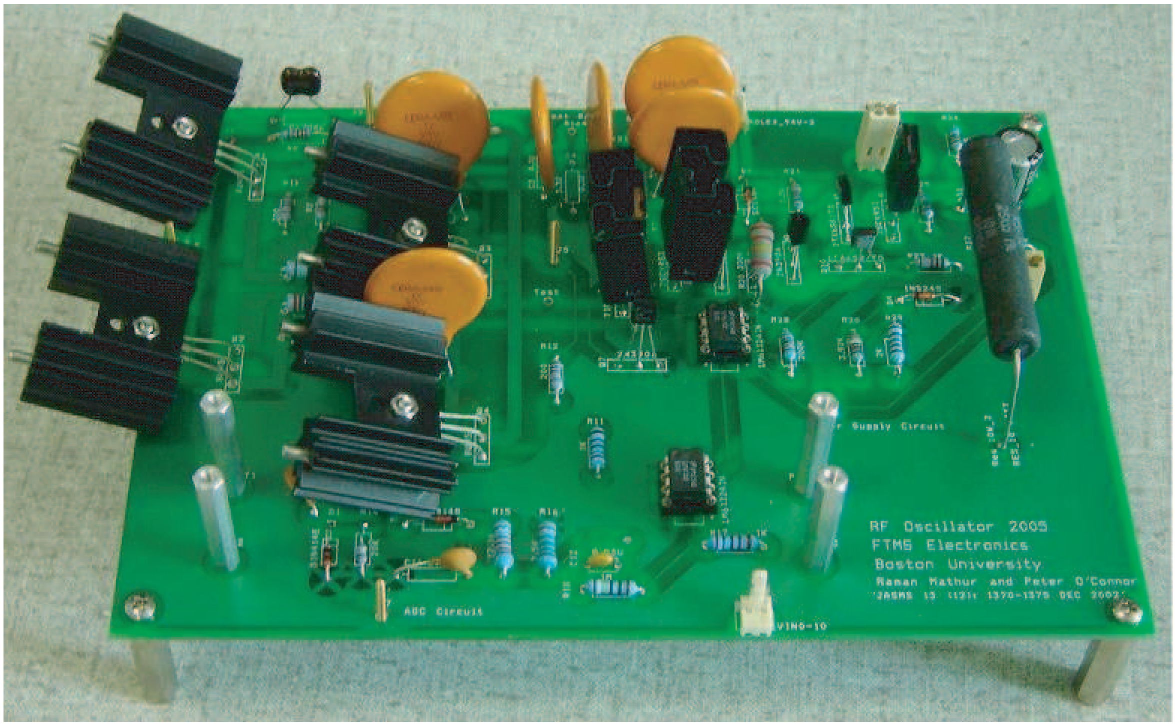

Figure 9·3: RF oscillator Printed Circuit Board

(Aurora, CO) and is shown in Fig. 9·3. Circuit components and the transformer were mounted on the PCB and the complete oscillator was enclosed in a shielded box as shown in Fig. 9·4.

It was critical during the design of the transformer coil with a high coupling factor to ensure minimum losses and high stability as described in the previous communication. A sketch showing the cross section of the transformer is shown in Fig. 9·5. Moreover the construction of the coil in house is a multi-step process and is worth notifying here. A photo of each step is shown in Fig. 9·6. A 90 mm o.d. PVC tube is wound with 30 turns of a 18-gauge magnet wire. A layer of epoxy is spread on the coil to harden and strengthen the winding. Then three layers of 0.1 mm mylar (Dupont, Wilmington, DE) were wrapped around the coil. Another 30 turn coil with 18-gauge wire was wound and coated with epoxy and then mylar. For the primary coil 16-gauge wire was used and all the 20 turns were wound on the same layer, ensuring good coupling and then center tapped. The 6 turns of

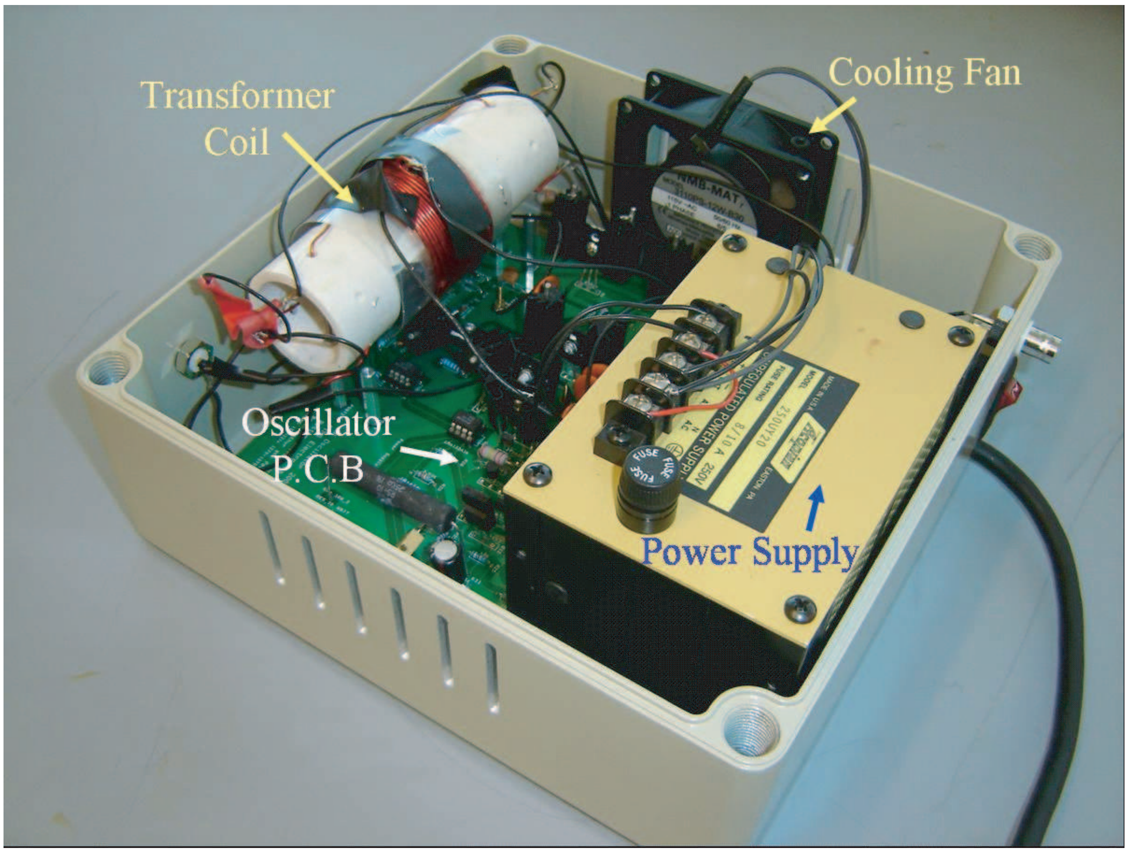

Figure 9·4: RF Oscillator with the transformer coil, Power Supply, and the cooling fan enclosed in a Shielded Box

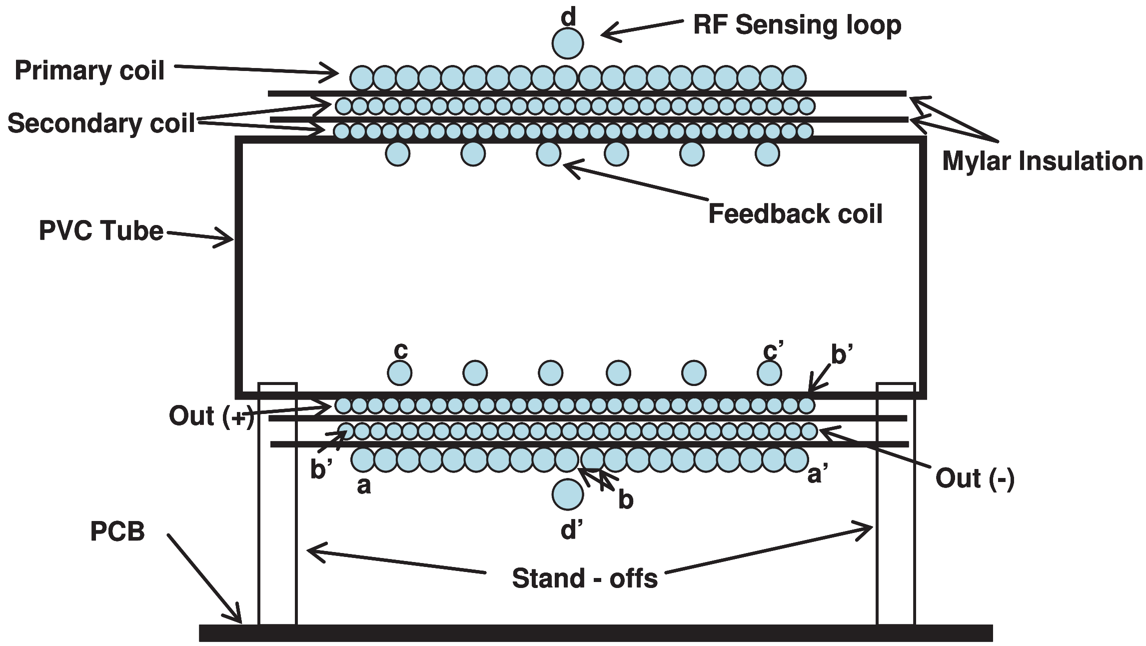

Figure 9·5: Cross Section of the transformer coil. Out(+) and Out(-) are connected to the electrodes of the ion guide. a-a', c-c' and d-d' are the secondary coil, feedback coil and RF sensing loop respectively. b and b' are the center tap of primary and secondary coils respectively. (refer to Fig. 9·2 for connections of the coils.)

the feedback coil were made with the 16-gauge magnet wire and placed inside the hollow PVC tube. The connections of the secondary coil were done according to the schematic shown in Fig. 9·5 to ensure proper flux orientation.

The functionality of the RF oscillator was tested using a custom MALDI-FTMS (O'Connor et al., 2004). The ions were generated using a nitrogen laser and accumulated in a hexapole for 4 seconds in the presence of nitrogen gas. Another long hexapole was used to transfer the ions from the source region to the open cylindrical Ion Cyclotron Resonance (ICR) cell. Several experiments involving detection of large biological proteins and small matrix clusters were performed to test the transfer of ions via the hexapoles driven by the RF oscillator circuit.

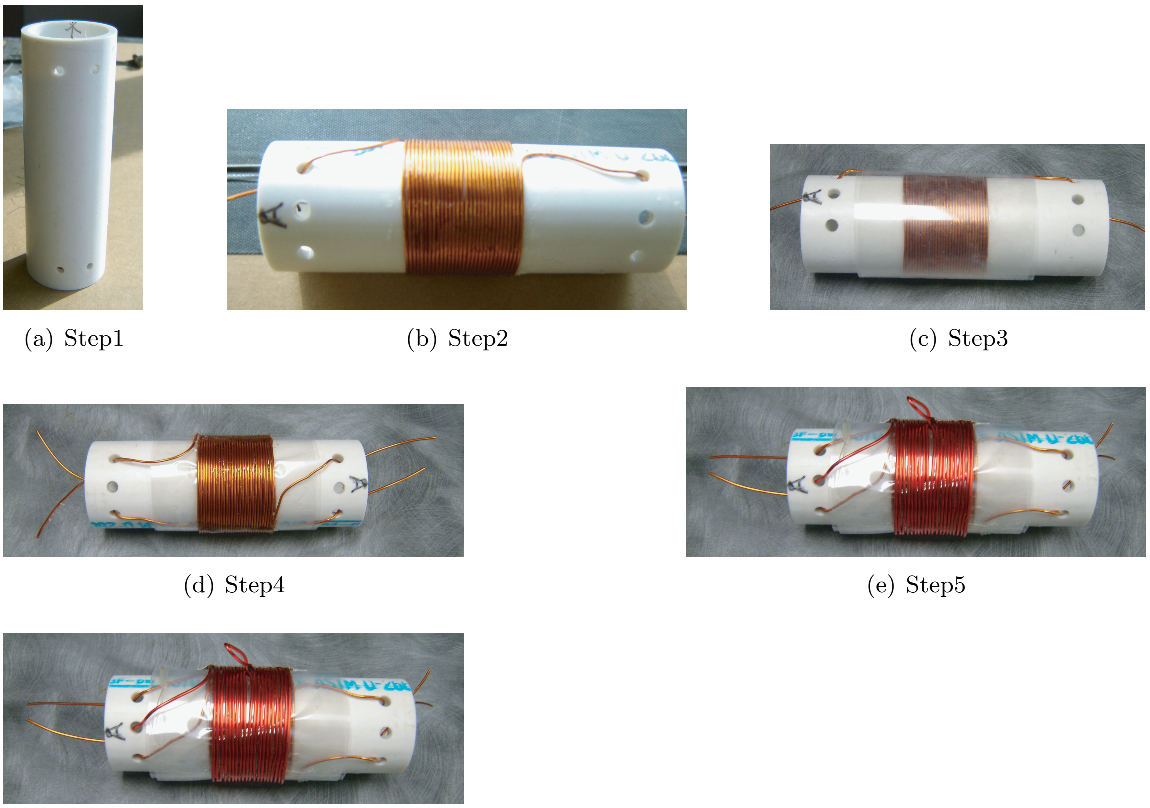

(a) Step1 (b) Step2 (c) Step3

(d) Step4 (e) Step5

(f) Step6

Figure 9·6: Steps to wind the Transformer for RF oscillator

9.7 Results and Discussion

The newly designed RF oscillator PCB was used to drive the accumulation hexapole of the MALDI-FTMS mentioned above. Experiments to test the high mass transmission of ions using RF only hexapoles were conducted with Ubiquitin (UB) which is a protein having monoisotopic mass equal to 8559.60 Da. 1M solution of UB was prepared in methanol : water (50:49) and 1 % formic acid. 2,5 dihydroxybenzioc acid (DHB) was recrystallized and used as the matrix for desorption. 1/2 μl of the protein solution was spotted on top of 1/2 μl of a DHB solution on the target plate. For low m/z experiments only 1/2 μl of DHB was spotted on target and dried. The ions were desorbed using a 337 μm, 3.5 ns pulsed nitrogen laser at 40 μJ/pulse, and a gas pulse was used to increase the trapping efficiency in the Ion Cyclotron Resonance (ICR) cell. After 6 - 8 seconds, (required for the cell pressure to return to $< 1 \times 10^{-9}$ mbar), the ions were resonantly excited and detected in the ICR cell. In experiments with Ub the accumulation hexapole was driven by the RF oscillator circuit with a voltage of 500 Vp-p at 600 kHz, and the transmission hexapole was driven at an RF voltage of 300 Vp-p at 650 kHz using the original oscillator circuit. Similarly for matrix clusters with small m/z both the hexapoles were driven at 1.1 MHz and 200 Vp-p.

Besides tuning the RF voltages on the hexapoles, two other parameters were critical for efficient trapping and detection of ions in the ICR cell, namely the time of flight of ions along the long transmission hexapole and the amplitude and duration of the excitation voltage. Gated trapping was used at the ICR cell, thus the timing of the open and close of the front trap plate potential was critical and the ideal timing varied substantially across the mass range, 1 ms at m/z 200 Da but 3.5 ms at m/z 8.5 kDa for an ion with 20 eV of kinetic energy. The broadband excitation voltage and the sweep rate also had to be adjusted for different ions to generate a coherent, detectable ion packet.

The mass spectrum (MS) of Ub is shown in Fig. 9·7. The peaks corresponding to the matrix adducts were also observed and are assigned in Fig. 9·7. The time of flight

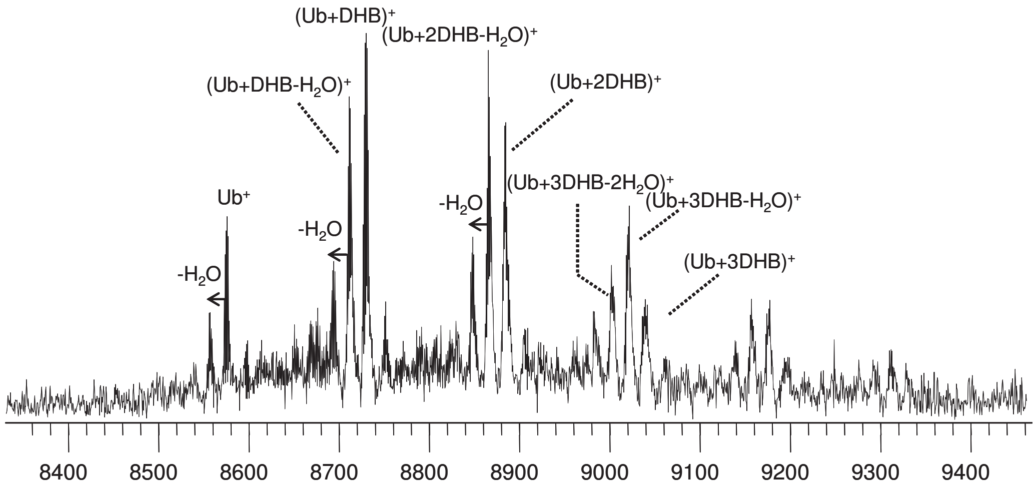

Figure 9·7: Mass Spectrum of Ubiquitin obtained using the RF oscillator to drive the hexapoles

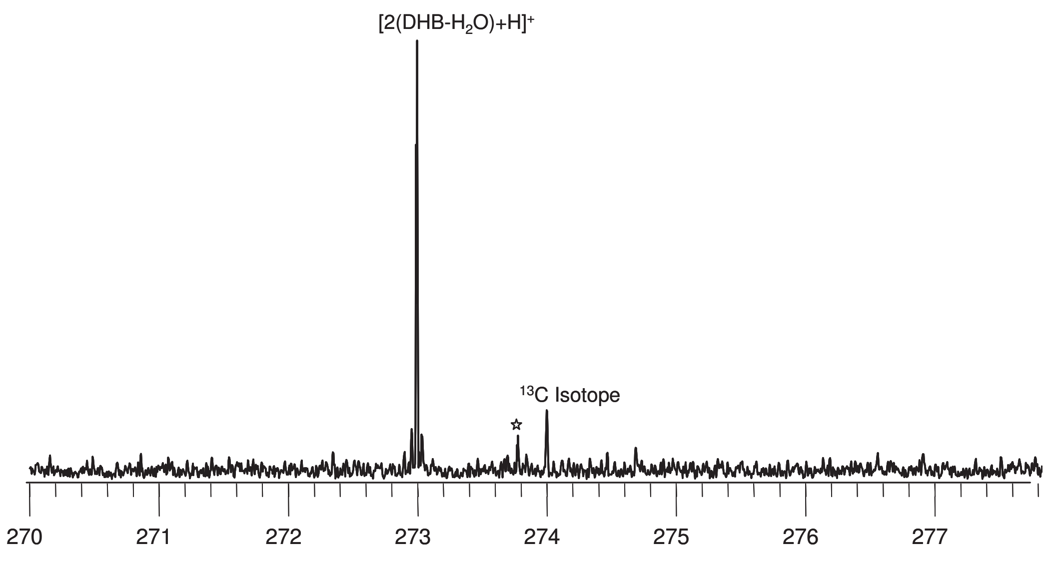

Figure 9·8: Mass Spectrum of DHB dimer of UB ions in the 134 cm long hexapole was approximately 3.5 ms and the excitation voltage on the ICR cell of 100 Vp-p was swept for 8 ms from m/z 1 kDa to 10 kDa. In an attempt to remove the matrix adducts, the ions were heated using a pseudo continuous CO2 laser (Synrad model 48-2, Mukilteo, WA.) for 100 ms in the ICR cell, causing the matrix adducts to dissociate from the molecular ion. The clean spectrum in Fig. 9·7 was however, accompanied by a trade-off with decrease in the overall signal intensity. Presumably this ion loss can be attributed to the infrared multi photon dissociation of the UB molecules.

The MS of matrix clusters in the low m/z window were obtained by using a similar pulse sequence but adjusting the time of flight to 1 ms and excitation sweep voltage to 30 Vp-p from m/z 50 Da to 1000 Da over 8 ms. Several matrix clusters were observed in the MS. The lowest species transferred and detected in the ICR cell had an m/z of 273 Da and is shown in Fig. 9·8. This was attributed to the DHB dimer with a loss of two water molecules (2DHB - 2H20). The m/z cut-off for the operational RF voltage of 200 Vp-p and 1.1 MHz was calculated to be approximately 80 Da from the ion stability equations for hexapoles.

Table 9.1 shows the complete tunable range of the current RF oscillator on the PCB. The tuning capacitors are added externally in parallel with the intrinsic capacitance of the multipole. It is advised to use silvered mica capacitors for tuning as they show high stability with temperature variations.

Table 9.1: Tuning Capacitors for RF Oscillator

Capacitor (pF)	Oscillation Frequency	RF Amplitude
4	1.78 MHz	1 kVp-p
6	1.74 MHz	1 kVp-p
12	1.685 MHz	1 kVp-p
50	1.388 MHz	1 kVp-p
100	1.16 MHz	1 kVp-p
150	1.02 MHz	1 kVp-p
500	632 kHz	1 kVp-p
1000	458 kHz	1 kVp-p

9.8 Conclusions

RF oscillator circuits are commonly used to drive ion guides in several kinds of scientific instruments. An instrument such as an Fourier Transform Mass spectrometer (FTMS) sometimes has multiple ion guides which require a number of RF oscillator. This presents an urgent need to develop circuits for these high power RF oscillators that are robust, simple to implement, and compact. In this chapter an implementation of an RF oscillator circuit which satisfies the above necessities is presented.

Constructing high power, high frequency circuits requires consideration of various design constraints. However, in most cases, intuitive approaches fail to achieve satisfactory solutions. Thus, in this chapter, a systematic methodology that identifies various issues involved and achieves a fair trade-off between them is elaborated. Various parameters which are selected during PCB design and their significance are defined. In particular, a description of how to determine track spacing and track width is given. Values of these parameters cannot precisely be determined from first principles due to various nonideal conditions such as inhomogeneous geometry, but can be estimated based on the experimental data. In this RF oscillator PCB design, a clearance of 20 mils and 100 mils was required for traces with voltages less than 15 volts and 350 volts respectively. The traces carrying high currents in the order of 5 A should be at least 70 mils wide. The selection and position of the heat sink is also important. By using an empirical formula that was proposed in literature, the heat sink for the high power transistors was determined to have a thermal resistance of $= 21.5\ {}^{\circ}C$/W. Effects of parasitic impedance in high frequency circuit design and functional recommendations that mitigate parasitic impedance are discussed. Moreover, it is advised to spatially separate the analog and digital components of the circuit to prevent any unwanted cross talk.

An illustration of the proposed method is shown by constructing a high power RF generator circuit for multipole ion guides; the circuit was presented earlier.10 The performance of the new RF oscillator circuit on the PCB was verified on a home-built MALDI-FTMS.

The RF oscillator was tuned to drive a hexapole with a sinusoidal signal having amplitude equal to 500 Vp-p and frequency 600 kHz to transfer Ubiquitin ions with m/z 8.5 kDa. Similarly the extended mass range towards the smaller m/z was tested using matrix clusters of DHB. The RF voltage was adjusted to 1.1 MHz and 200 Vp-p; transferring a DHB dimer of m/z 273 Da. The current RF oscillator PCB can be tuned down to an output equal to 1 kVp-p with resonant frequency of 400 kHz using a 1000 pF in comparison to the previous prototype which reached the limit at around 500 kHz. This extends the upper mass transmission range of the hexapoles to around 75 kDa.

The complete cost of the circuit implementation, including the PCB fabrication and all components, was less than 300 in parts. The Gerber files of the PCB have been uploaded on the group website; they are made available including the bill of materials and construction photographs.

Chapter 10

FTMS Datasystem

In FTICRMS ions are generated in the ion source and have to be transferred to the ICR cell for mass analysis. This is done using ion transfer optics which generally is a combination of multipole ion guides, static lenses or tubes. For example a schematic showing the ion optics of the cryogenic FTMS is shown in Fig. 10·1. A sample from a stainless steel plate is ionized by a laser pulse and transferred to the ICR cell via a pair of hexapoles. The hexapoles have static lenses at their entrance and exit which are used during ion accumulation. The hexapoles are driven by RF oscillators which in turn are controlled by TTL triggers or time varying analog voltages. The lenses and hexapoles also require bias potential for efficient transfer of ions. In the ICR cell these ions are trapped using the gated trapping. Gated trapping requires pulsing the voltage on the hexapole end trapping plate to a negative value for approximately 3 ms to let the positively charged ion inside the cell (Hofstadler et al., 1995). The positive voltage traps the ions inside a potential well created by the end trapping plates.

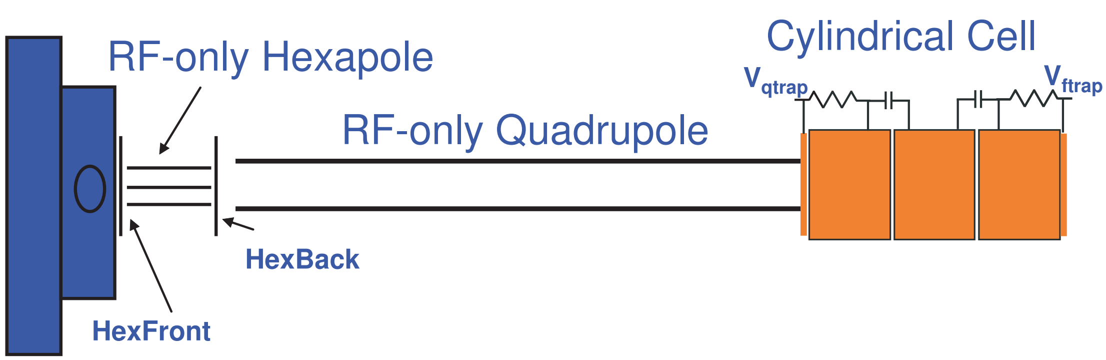

Figure 10·1: Cryogenic FTMS Schematic

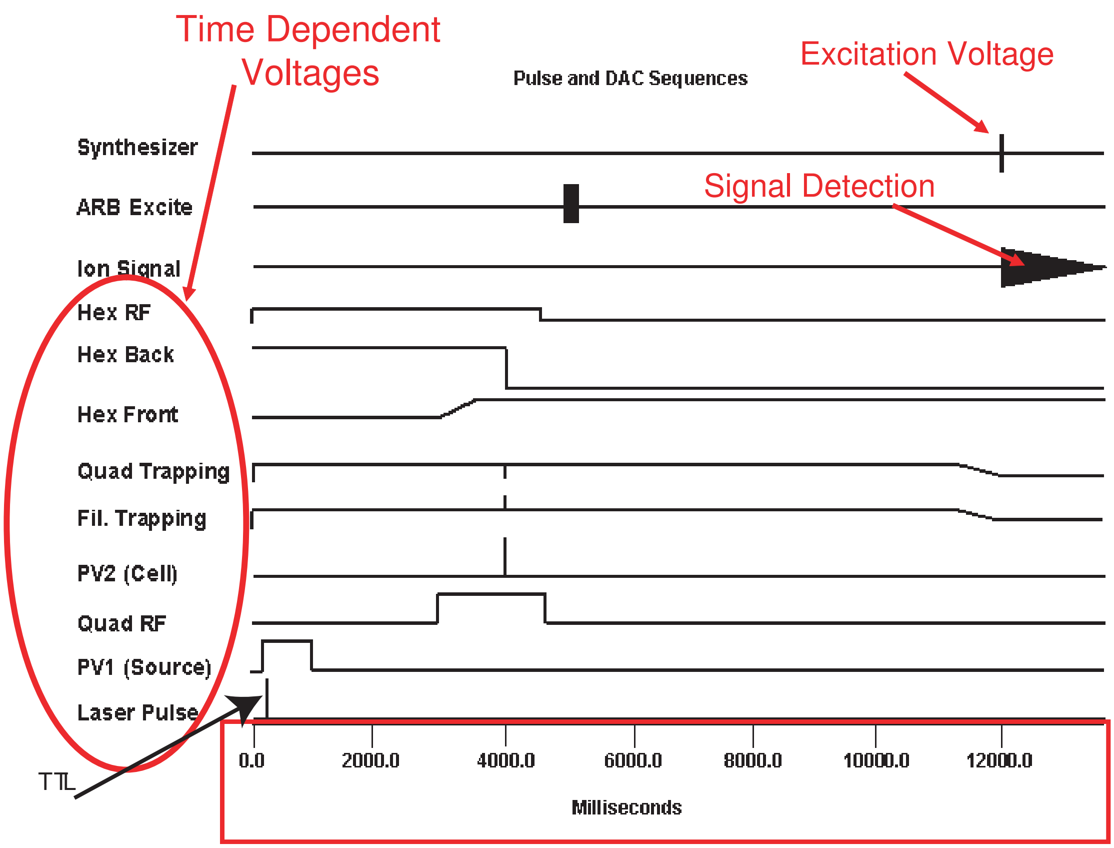

Figure 10·2: FTMS Pulse Sequence

A typical pulse sequence listing most of the voltages which are typically applied and varied during a FTMS experiment are shown in Fig. 10·2. There are several sets of analog (time varying and static) and digital voltages required with precise ($< 100\mu sec$) timing control. Simple off the shelf components can be used to implement a datasystem for FTMS (Beu and Laude, 1991). However to exploit the complete functionality of the FTMS a more sophisticated and well engineered system is necessary (Senko et al., 1996; Mize et al., 2004).

At AMOLF (Mize et al., 2004), a datasystem is being developed specifically for FTICRMS. This system is based on PCI eXtensions for Instrumentation (PXI) which is a modular instrumentation platform originally introduced in 1997 by National Instruments (Austin, TX). PXI provides a common platform to develop electronic instrumentation and automation. The AMOLF datasystem was used to control all the voltages and timing of the events in cryogenic FTMS such as laser shots and TTLs for RF oscillators.

A picture showing all the PXI-cards which were used in the datasystem for the cryogenic FTMS is in Fig. 10·3.

The modules or the PXI cards which were used are as follows:

- PXI-6733 (AO card) - It is the a high speed 16 bit analog output card with 8 channels from National Instruments (Austin, TX). These voltages were used for biasing trapping plates and hexapoles.

- DIO-64 (Digital/timing card) - It is a Digital Event Analyzer/Controller card with 64 digital I/O channels from Viewpoint Systems, Inc.(Rochester, NY). This card was used to generate digital control TTLs to time the events in the FTMS pulse sequence.

- PXI-5411 (Arbitrary Waveform Generator) - It is a high speed arbitrary waveform generator card from National Instruments (Austin, TX). It has 12 bit resolution and update rate of 40 MHz which allows the use of complex SWIFT waveforms for ion selection and excitation (Marshall et al., 1985).

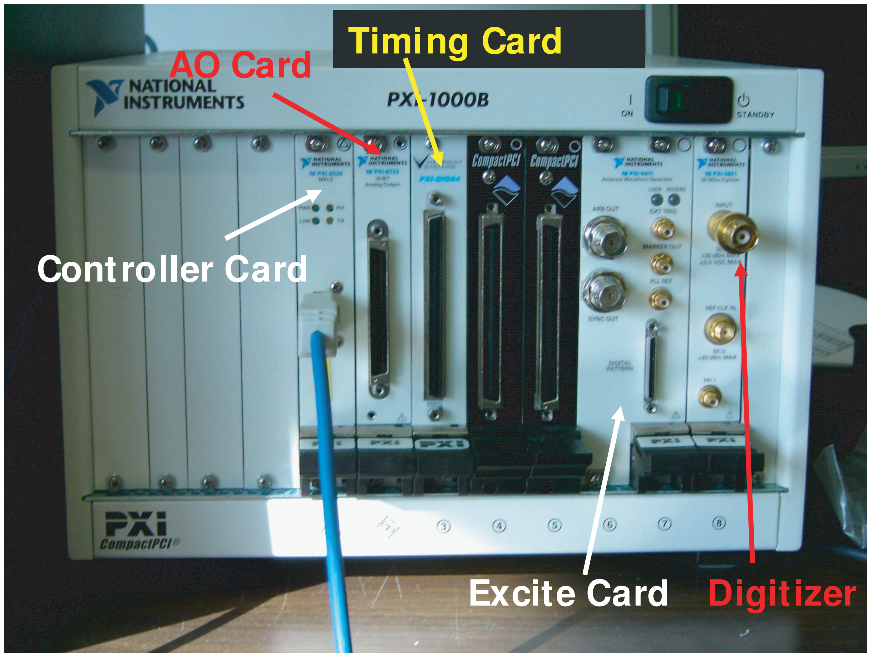

Figure 10·3: PXI Crate with modular cards

- PXI-5411 (Digitizer) - PXI-5621 is the high speed signal digitizer with 14 bit resolution and maximum sampling frequency of 64 MS/s. It is used to digitize the amplified ICR signal for data processing by a PC. The digitizer have an onboard memory of 32 MS which enables to accumulate and add long transients without waiting to transfer data to the PC.

The PXI cards are designed for high performance instrument systems which require modularity and compactness. The output voltages from these cards are typically routed to high density connectors having 96 pins, as is the case in PXI-6733. The compact nature of these connectors makes the access to these pins difficult. A PCB is fabricated which branches out the signal voltages from the high density connector from PXI-6733 to BNC and DB-25 form of outputs which are easily accessible.

Moreover, these cards use conventional but advanced electronic components such as opamps which are highly sensitive to electro-static discharge (ESD). Especially when the signals from these cards are connected to ion optics or high power RF generator, a short

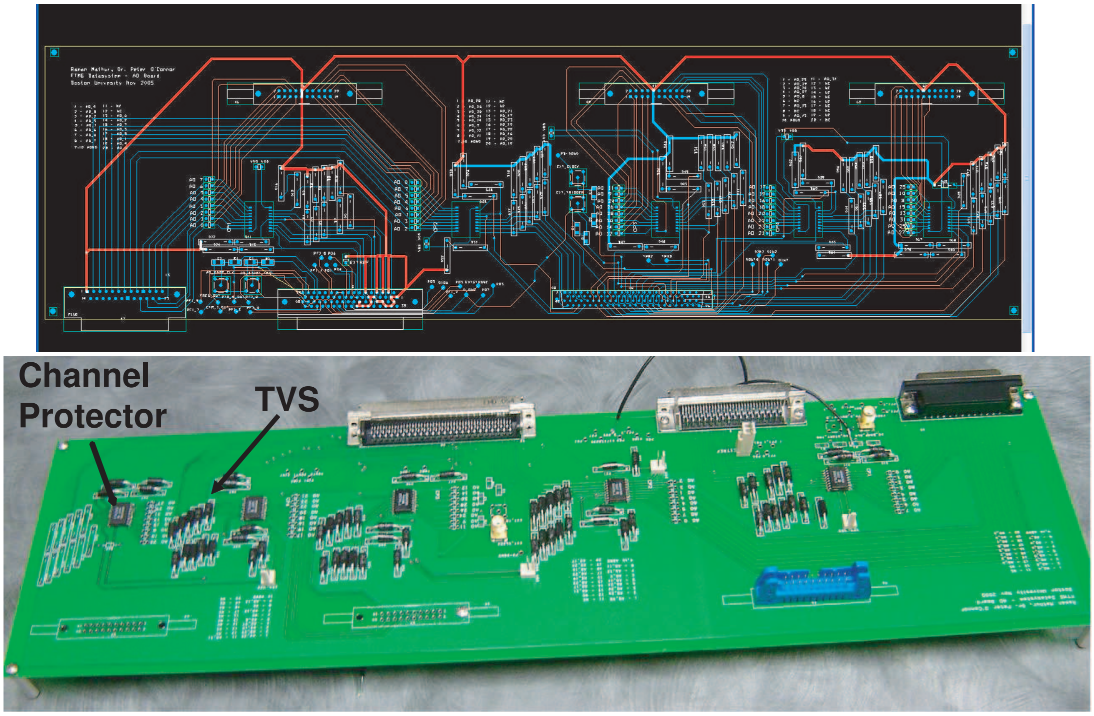

Figure 10·4: Analog Protection Board

circuit or arcing in the instrument can in advertently damage these cards. Thus, to ensure reliability and functionality of the PXI datasystem we have provided protection circuits on the analog breakout board, as shown in Fig. 10·4. The primary idea is to protect the expensive PXI cards by adding protection components between the instrument and PXI modules. For this purpose we have added channel protectors, ADG466 from Analog Devices in series with the signal lines, Fig. 10·5. Generally, protection components protect the circuit by clamping the ESD voltage to a level that the circuit can survive. ADG466 consists of two FETs in series of the signal lines, one n-channel and other p-channel. The ADG466 protects the PXI cards from transient voltage surges and clamps the voltage to around +/- 1.5 volts from supply voltage.

We have also added transient voltage suppressor diodes in parallel with the inputs of the channel protectors as an additional line of protection. These transient voltage suppressors clamp the ESD voltage to +/- 12 volts and shunt the majority of the ESD current away from the signal line to the ground reference. These diodes and channel protector circuits have

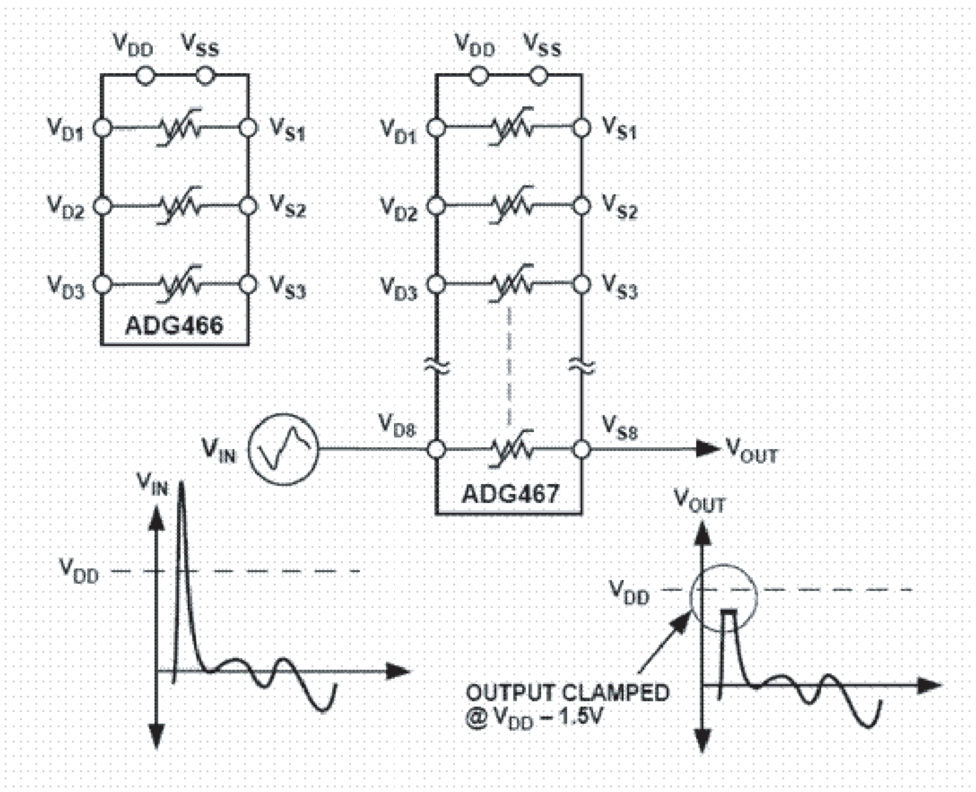

Figure 10·5: Channel Protector (Analog Devices, 2005)

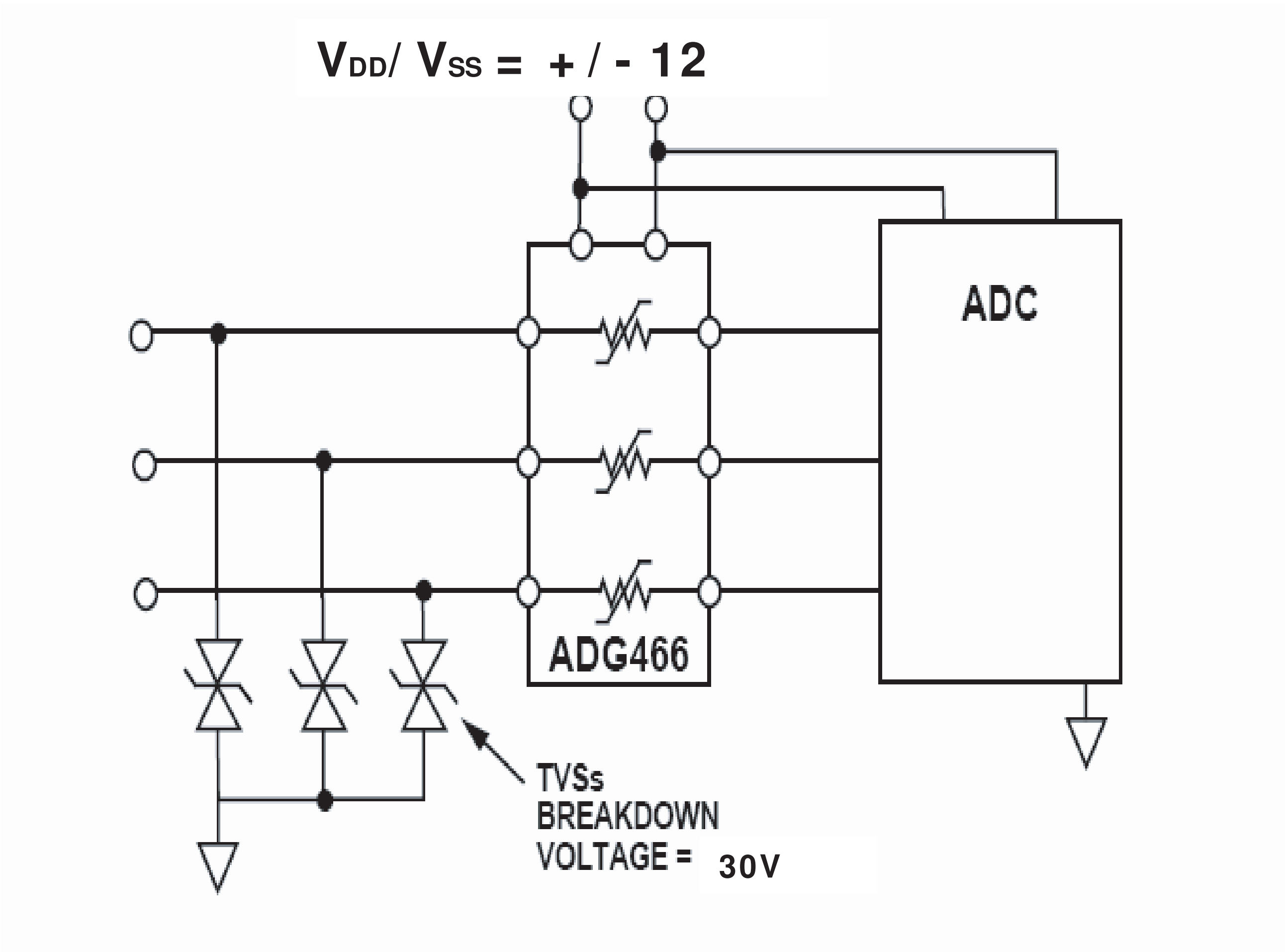

Figure 10·6: ESD Protection for PXI cards

very low stand by current, thus in normal operation they practically appear transparent to the signals. The complete protection scheme which has been implemented in the cryogenic FTMS is shown in Fig. 10·6.

A similar breakout board for routing the timing signal from DIO64 card is fabricated. The TTL outputs from the DIO64 card contain glitches, thus low pass filters were added. To protect the DIO64 card from ESD which can arise in the FTMS, opto-isolators are to be added on the digital PCB.

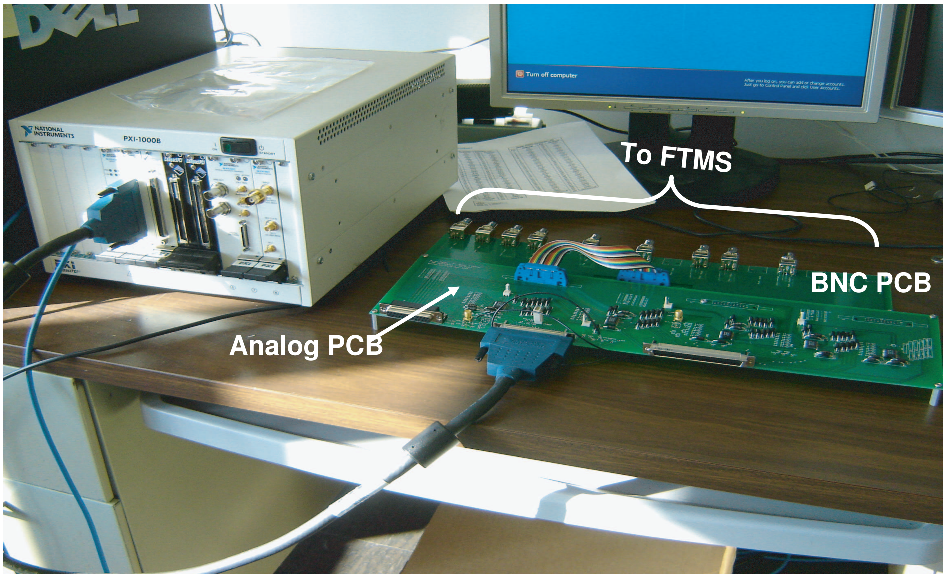

Figure 10·7: Analog Voltage Set up for CryoFTMS

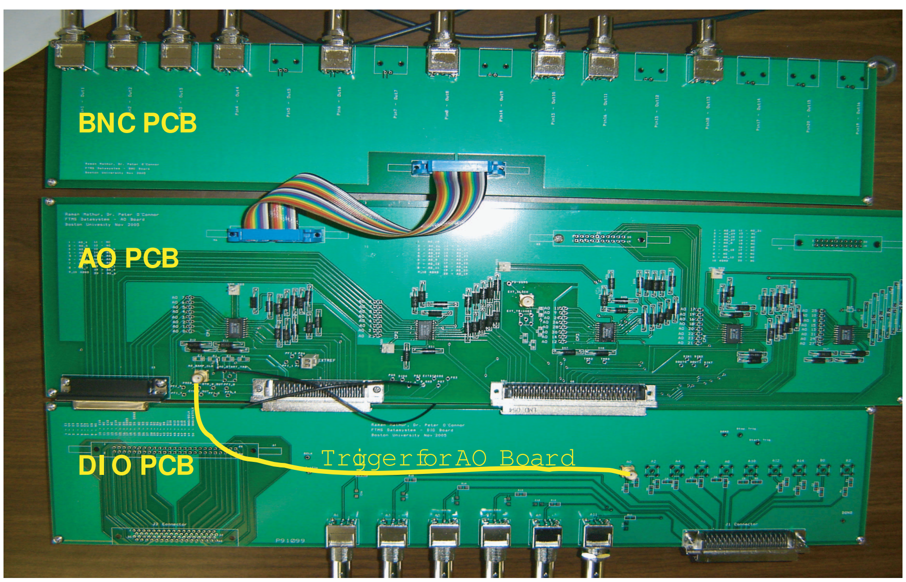

Figure 10·8: Digital Protection Protection Board

Chapter 11

Artifacts in Fourier Transform Mass Spectrometry Detection

This chapter has been reproduced in part from the article submitted to the journal Rapid Communications in Mass Spectrometry.

In our work on a new, higher sensitivity preamplifier design for FTICR MS a number of artifact peaks (spectral features) which do not contain useful chemical information were observed. In order to determine the cause of these artifacts and eliminate them, these severely distorted spectra were compared with similarly distorted signal models. The source of several common signal processing artifacts was thereby determined and correlated to RF noise interference and saturation of the amplifier and/or the digitizer. Under such conditions, the fast Fourier transform generates spectral artifact peaks corresponding to harmonics and mixing frequencies of the real signal peaks, RFI frequencies. While this study was done using FTICRMS data, it is important to stress that these artifacts are inherent to the digitization and FFT process and thus are relevant to any FT based MS instrument, including the orbitrap and FTIR.

11.1 Introduction

Mass spectrometry is a sophisticated, sensitive, and accurate method for the analysis of chemical and biological compounds. A mass spectrometer measures mass to charge ratio (m/z) of samples which provides information about their composition, conformation, and their interaction with other compounds (Gygi et al., 1999; Mann et al., 1993; Cronshaw et al., 2002). Fourier transform ion cyclotron mass spectrometer (FTICRMS) is char-

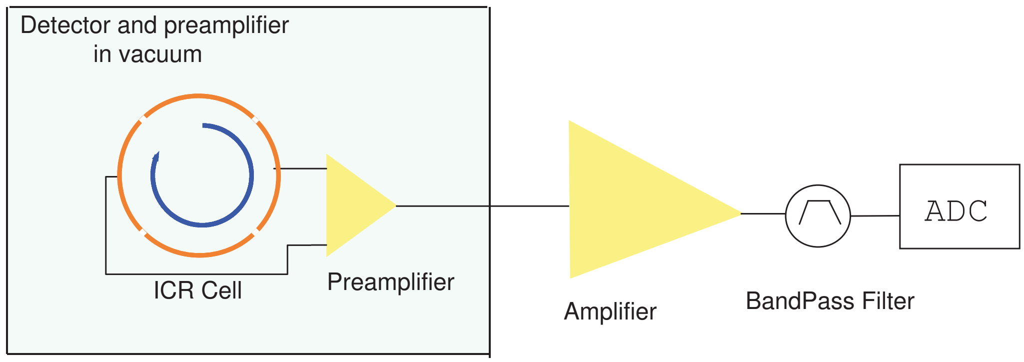

Figure 11·1: FTICRMS detection Scheme.

acterized by its high mass resolving power and mass accuracy compared to other mass spectrometers (Marshall and Comisarow, 1974; Comisarow and Marshall, 1974; Amster, 1996).

$$\omega_c = \frac{qB}{m} \tag{11.1}$$

In an FTMS sample compounds are energized to rotate in cyclotron orbits as coherent packets of ions in the presence of external magnetic and electric field (Marshall and Comisarow, 1974). The rotating ion packets induce an alternating image current on the plates of the ICR cell with a frequency corresponding to their cyclotron frequencies given by Eq. 11.1. The induced signal is the superposition of all the spectral components due to various ion packets of different m/z. This signal is amplified using a low noise amplifier and digitized using an Analog to digital converter (ADC) (Shockley, 1938; Comisarow, 1978; Nikolaev and Gorshkov, 1985; Grosshans et al., 1991; Mathur et al., 2007),Fig. 11·1. The spectral components in this time domain signal are extracted by a fast Fourier transform (FFT) algorithm using a PC (Cooley and Tukey, 1965). These frequency components are then calibrated to provide a mass spectrum (Comisarow and Marshall, 1976; Ledford et al., 1984; Francl et al., 1983; Zhang et al., 2005).

The peaks in the mass spectrum represent the frequency of cyclotron motion of ions.

However, in the commonly used open cylindrical and cubic ICR cell in FTMS the electric field which the ions experience is not perfectly hyperbolic. The finiteness of the electrodes of the ICR cell results in the appearance of signal peaks at the odd harmonics of the cyclotron frequency (Grosshans et al., 1991; Nikolaev and Gorshkov, 1985). Though these harmonics can provide vital information such as ion cyclotron radius (Grosshans et al., 1990), their presence increases the complexity of the mass spectra, making data interpretation difficult.

Often in FTMS there are non-real peaks which arise in a mass spectrum which are not due to any physical phenomenon/imperfections but are the result of errors in sampling by analog to digital converter (ADC) or because of calculation of the fast Fourier transform (FFT) of the ion signal (Marshall and Verdun, 1990). Recently these artifacts were observed during the evaluation of an ultra sensitive detection amplifier for a room temperature FTMS (Mathur et al., 2007). The presence of such non-real peaks makes the mass spectrum interpretation far more complex and prone to identification errors. Thus it becomes important to understand these artifacts, their cause and ways to avoid them. This short communication discusses such artifacts in mass spectra obtained on FTMS which are related to sampling and signal processing. Strategies to avert these errors in signal processing are also presented. These methods are equally applicable to any instrument which uses Fourier transform as a tool for data analysis such as an orbitrap (Hu et al., 2005), Fourier transform infrared spectroscope etc. Various cases with relevant examples of mass spectra obtained on a MALDI-FTMS (O'Connor et al., 2004) and simulated in MATLAB (The MathWorks Inc., MA) are presented.

11.2 Method

A custom MALDI-FTMS (O'Connor et al., 2004) was used for all the experiments which has a ultra low noise BUSM detection preamplifier (Mathur et al., 2007). A saturated solution of C_{60} in toluene was spotted onto a stainless steel plate. Spectra were generated using a single shot of a 355 nm Nd:YAG laser from Continuum Inc. (Santa Clara, CA.)

at 50–150 μJ/pulse. A pair of hexapoles driven by RF oscillators (O'Connor et al., 2002; Mathur and O'Connor, 2006) were used to transfer the ions to the ICR cell. After 200 ms of thermal stabilization, the ions were resonantly excited into coherent cyclotron orbits by the application of a broadband RF sweep. The RF sweep voltage of 80 V_{p-p} was applied for 8 ms and swept from 150 Da to 3000 Da. 256K samples were taken from the amplified ICR signal at a rate of 1 MHz (total transient length of 0.262 seconds). The digitized data was fast Fourier transformed without apodization. The standard detection scheme for an FTMS is shown in Fig. 11·1.

Simulated spectra were generated using a MATLAB script (The MathWorks Inc., Natick, MA). The DFT routine defined in MATLAB was used to obtain the spectral information from the time domain data. The frequency spectrum was converted into the mass-to-charge domain using calibration constants for a 7 Tesla magnetic field (Ledford et al., 1984; Francl et al., 1983; Zhang et al., 2005).

11.3 Results and Discussion

In these set of experiments, C_{60} was chosen to be the compound of interest. The simulated intermodulation of time domain signals due to the first 3 isotopes of C_{60} is shown in Fig 11·2a. The induced image signal from the 3 isotopes interferes constructively and destructively with each other causing the generation of the beat pattern. The spacing between these beats is determined by the frequencies of the neighboring isotopes (Hofstadler et al., 1994). The Fourier transform of the simulated time domain signal from Fig 11·2a is shown in Fig 11·2b, where f_c, 149 kHz, is the cyclotron frequency of C_{60} ion at 7T. A simulated mass spectrum and experimental mass spectra of C_{60} is shown in Fig 11·2c and Fig 11·2d respectively. The simulated time domain signal in Fig 11·2 does not account for any damping of the ion signal caused by columbic repulsion or collisions with background gases. For this very reason the simulated MS does not show Lorentzian line shapes as is the case in the experimental MS. Also as the physical model of the electric field inhomogeneity

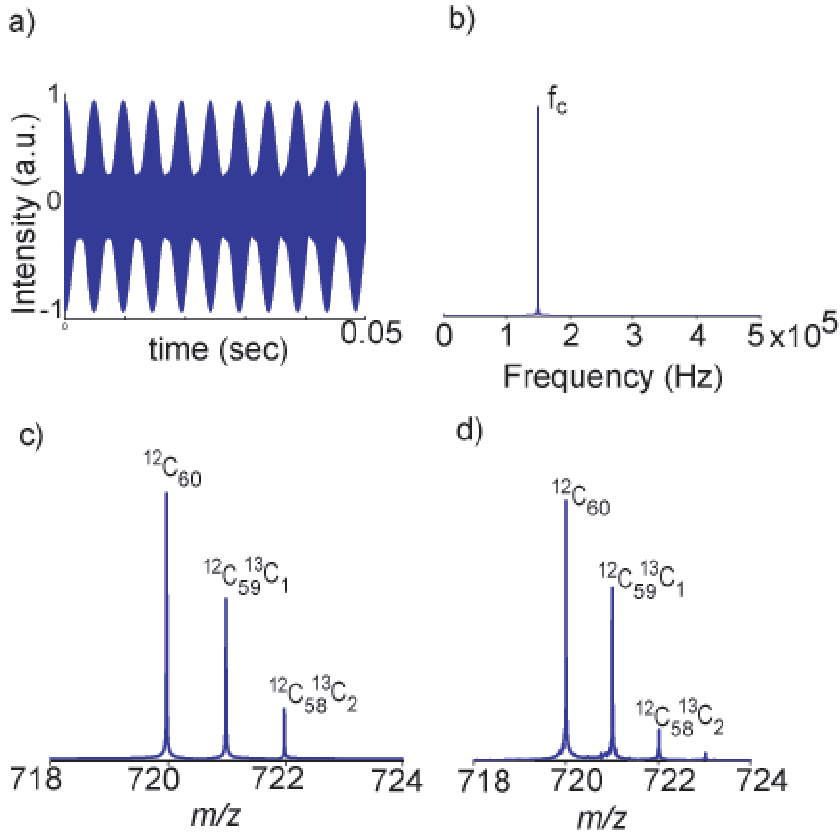

Figure 11·2: C_{60} Signal on an FTMS. a) Simulated Transient. b) Simulated Frequency Spectrum, FFT of "a". c) Simulated MS, calibrated m/z spectrum of "b" using 7 T calibration constants. d) MS obtained on MALDI-FTMS.

is not modeled here the odd harmonics which are present in real spectra are not seen in Fig 11·2b.

In FTICRMS, the detection amplifier sends the signal to the analog to digital converter (ADC). In a case when the detection amplifier is highly sensitive (high gain & low noise), saturation of the amplifier or over loading of the ADC can occur, which generates additional spectral artifacts. Fig 11·3a shows the C_{60} beat pattern with a DC offset causing the saturation/clipping of part of the negative signal. The dc offset could be caused by the temperature drift in electronic components of the amplifier, or imbalance of the two FETs (mismatch) (Mathur et al., 2007). The frequency spectrum of the simulated transient is shown in Fig 11·3b. The spectral components due to C_{60} are present, f_c , however, the so-called "clipping" of the time domain signal generates the harmonics of the cyclotron frequency within the spectrum. Ideally ICR detection is a differential scheme and no even harmonics should appear in the resulting mass spectra. However, in this case the clipping, which is caused by the imbalance in the ICR detection circuit, gives rise to the even harmonics. The first harmonic (f_c), second harmonic ($2f_c$) and the third harmonic ($3f_c$) at $\approx$ 149 kHz, $\approx$ 298 kHz, and $\approx$ 447 kHz respectively are seen in Fig 11·3b. The frequency of the fourth harmonic is more than the Nyquist frequency of 500 kHz, this results in the under sampling (aliasing), and a fold over peak at 404 kHz ($4f_{cf}$ = 1 MHz–596 kHz) appears in the spectrum. Similarly, fold over peaks up to the seventeenth harmonic, $17f_{cf}$, are visible and labeled in the frequency spectrum. The list of all harmonics in Fig 11·3b is given in Table 11.1. It should be recalled that these even harmonics are not due to any physical phenomenon but are caused during the signal processing of the induced ion signal. Thus an anti-aliasing filter, the low pass part of the bandpass filter in Fig 11·1, implemented in an ADC prior to sampling will not attenuate these artifacts. In the mass spectrum besides the C_{60} isotopic cluster there are several peaks at 1 Da spacing below the monoisotopic peak. These peaks shown in Fig 11·3c and Fig 11·3d (marked with $\star$) arise due to inter modulation of the C_{60} isotopes and lead to the distortion of the C_{60} isotopic

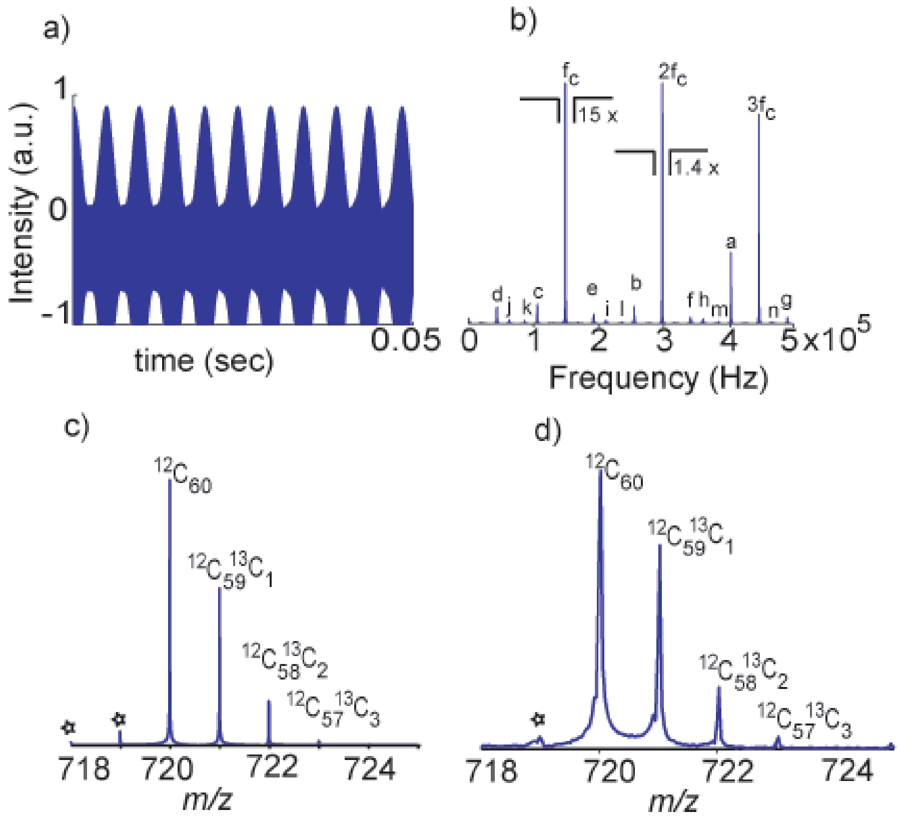

Figure 11·3: C_{60} signal with asymmetric overloading of the ADC. a) Simulated Transient. b) Simulated Frequency Spectrum showing artifacts at odd and even harmonics of the cyclotron frequency, FFT of "a". c) Simulated MS with 1 Da spacing artifacts due to intermodulation of the C_{60} isotope signals. d) Experimental MS obtained on MALDI-FTMS showing the 1 Da neighboring artifacts, "$\star$".

distribution.

The offset in the signal can be avoided by implementing a high pass filter prior to the ADC. However over loading of the ADC can still occur due to the high gain of the detection amplifier. A time domain signal showing such a case is shown in Fig 11·3a in which truncation of the signal is caused by the amplitude of the ICR signal going beyond the dynamic range of the ADC. The frequency spectrum in Fig 11·3b shows the presence of odd harmonics only. As previously mentioned, the odd harmonics in ICR arise from the non-hyperbolic detection electrodes in the trap, and their amplitudes are proportional to

Table 11.1: List of artifact peaks at harmonics of the fundamental cyclotron frequency, f_c

a=4f_{cf}	h= 11f_{cf}
b=5f_{cf}	i= 12f_{cf}
c=6f_{cf}	j=13f_{cf}
d=7f_{cf}	k=14f_{cf}
e=8f_{cf}	l=15f_{cf}
f=9f_{cf}	m=16f_{cf}
g=10f_{cf}	n=17f_{cf}

the ion cyclotron radius (Marshall and Verdun, 1990). This non linearity is not modeled here, so the odd harmonics in Fig 11·3b are due to clipping only. In the case of the C_{60} mass spectrum obtained on the FTMS, the clipping of the transient increases the intensities of the odd harmonics, which were originally barely visible in the un-clipped mass spectrum in Fig 11·2b. The simulated and the experimental mass spectrum in Fig 11·3c and Fig 11·3d also shows the isotopic intermodulation artifacts with $\approx$ 1 Da spacing below the C_{60} isotopes.

Often in FTMS experiments, too many ions in the ICR cell or high amplifier gain can lead to an extreme case of saturation of the ADC, commonly referred as a "Black Bar Transient". An example of such a transient for C_{60} ions is shown in Fig 11·5a. The Fourier transform of the simulated signal indicates the presence of dominant third harmonic and also a second harmonic component of the ICR signal. The experimental mass spectrum was generated by accumulating C_{60} ions from multiple laser shots. The increased number of C_{60} ions induced a voltage which after amplification was high enough to overload the ADC. The mass spectrum also exhibits the train of isotopic intermodulation artifacts at $\approx$ 1 Da spacing around C_{60} isotopes as in the previous case, however with much higher intensities. The A+1 and A+2 isotope peaks have their abundances severely altered by this mixing, Fig 11·5c and Fig 11·5d.

All of the above artifacts were based on saturation of the ADC normally caused by the

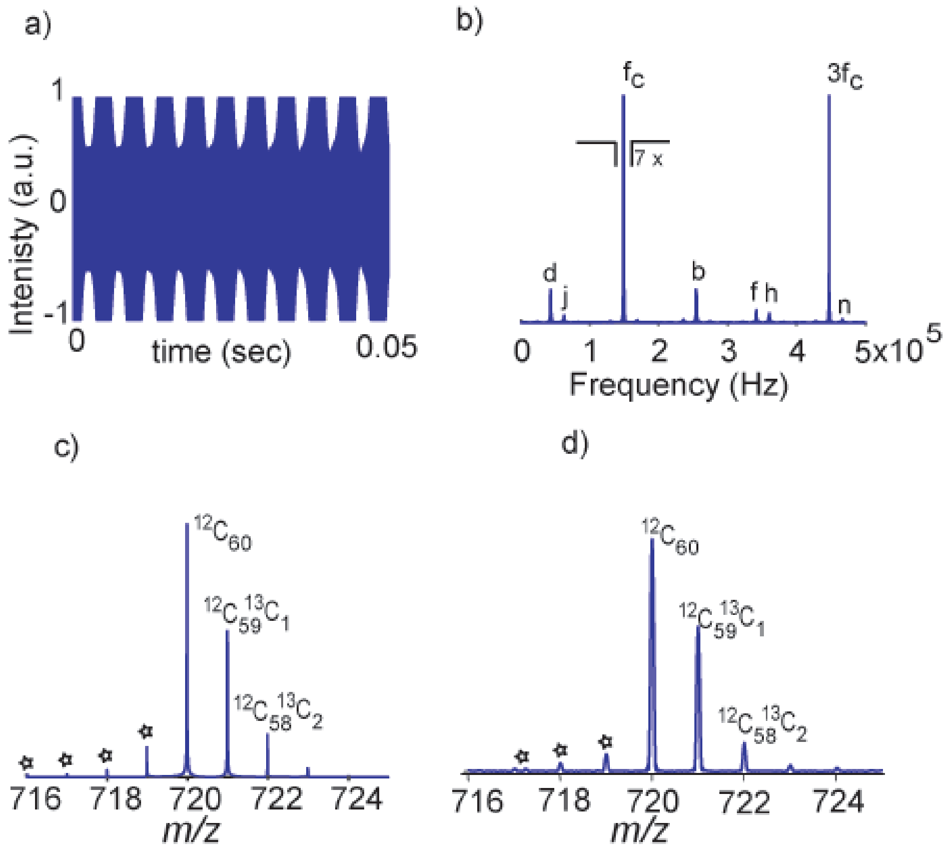

Figure 11·4: Fig.4. C_{60} signal with symmetric overloading of the ADC. a) Simulated Transient. b) Simulated Frequency Spectrum showing artifacts at only odd harmonics of the cyclotron frequency, FFT of "a". c) Simulated MS with 1 Da spacing artifacts due to intermodulation C_{60} isotope signals. d) Experimental MS obtained on MALDI-FTMS showing the 1 Da neighboring artifacts, "$\star$".

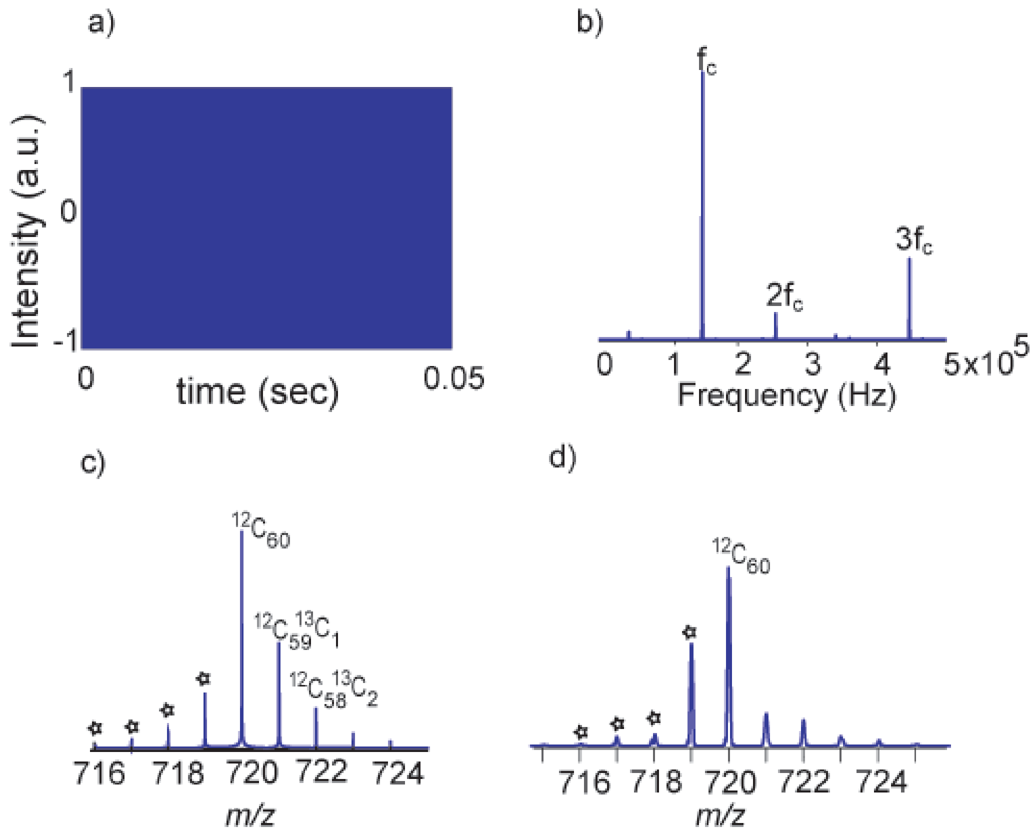

Figure 11·5: C_{60} "Blackbar" Transient. a)Simulated Transient. b) Simulated Frequency Spectrum showing artifacts at odd and even harmonics of the cyclotron frequency, FFT of "a". c) Simulated MS with 1 Da spacing artifacts due to intermodulation C_{60} isotope signals. d) Experimental MS obtained on MALDI-FTMS showing the 1 Da neighboring artifacts, "⋆".

high amplitude of the ICR signal compared to the dynamic range of the ADC. In this case, the amplifier had an output range of $\pm$ 6 volts, while the ADC had an input range of $\pm$ 0.5 volts, guaranteeing the saturation of the ADC prior to that of the amplifier. But it is important to note, that in other configurations these signals can also be generated by the saturation of the amplifier itself. A variable gain element with a feedback control can be implemented to prevent the amplifier saturation. However, reducing the gain of the amplifier sacrifices the dynamic range and also degrades the limit of detection of the ICR detection circuit. Signal saturation can also be avoided by implementing automatic gain control (AGC) in an FTMS. In such an scheme a survey scan or current measurement is performed to estimate the number of ions in FTMS. Then the ion accumulation time is adjusted accordingly to prevent over loading the ICR cell (Belov et al., 2003).

Another significant cause of artifacts in FTMS, which originally led to these investigations, are artifacts induced by radio frequency interference (RFI) on the detect lines. In a mass spectrometer, power supplies, vacuum pumps, RF oscillators driving ion guides, ion gauges, and even noise of the DC voltages on the ion optics can be a source of RFI, corrupting the ion signal. The high impedance nature of the ICR detector makes it prone to microphonic pick up at the input of the preamplifier (Mathur et al., 2007). Typically, RFI noise leads to electronic noise peaks in the frequency/mass spectrum which are readily recognizable as they have no isotopes and do not interfere in the analysis, if they do not overlap with the peaks of interest. However one scenario is of special interest which results in distinct artifacts in a mass spectrum, as discussed below.

Fig 11·6a shows that particular case, where RFI noise at 167 Hz and 120 Hz were intentionally added to the C_{60} isotopes, in MATLAB, causing asymmetric over-loading of the ADC. Without any saturation, the 167 Hz and 120 Hz peak would correspond to 598 kDa and 833 kDa, respectively, and normally would be out of the range of interest on a 7 Tesla FTMS, thus not interfering with the data analysis. However as evident from Fig 11·6 the saturation has caused the intermodulation of these RF interference frequencies with the isotopes of C_{60}, complicating the spectrum.

More realistically, the RFI coupled to the ICR time domain signal can affect the signal to noise ratio as evident in Fig 6c. Fig 6c shows a real time domain signal obtained on a MALDI FTMS using the low noise BUSM preamplifier (Mathur et al., 2007). This preamplifier was powered by switching power supplies which introduced RFI noise peaks, predominantly at 120 Hz and 167 Hz. This low frequency signal was amplified and saturated the ADC on the negative side. The prominent artifacts from this saturation are labeled in Fig 6d. These clusters of small peaks made the spectrum appear noisy near the C_{60} isotopes, deteriorating the signal to noise ratio. Thus, it becomes important to use low noise power supplies or even better, batteries, for superior performance of the ICR detection preamplifier. Proper bypassing and grounding of the preamplifier power rails eliminates RFI, which can manifest as spectral artifacts in a mass spectrum. Moreover, mounting the preamplifier as close as possible to the ICR detect plates greatly reduces the potential of RFI as the preamplifier's output is a low impedance line, which significantly reduces microphonic and inductive pick ups.

11.4 Conclusions

Fourier transform mass spectrometer provides data with high mass accuracy and resolution which is rich in information. To ensure superior level of performance it is necessary to optimize the gain of the detection amplifier according to the ADC specification. In this communication it is shown that imbalance in the gain or bias of the amplifier can lead to overloading of the ADC which results in appearance of harmonics in the mass spectra. Severe over loading of the ADC can also cause distortion in the isotopic distribution of ions thus making the automated interpretation of the mass spectra difficult. Radio frequency interference on the ICR signal can also cause imbalance and/or overloading of the ADC. A low noise amplifier mounted close to the detect plates can minimize this.

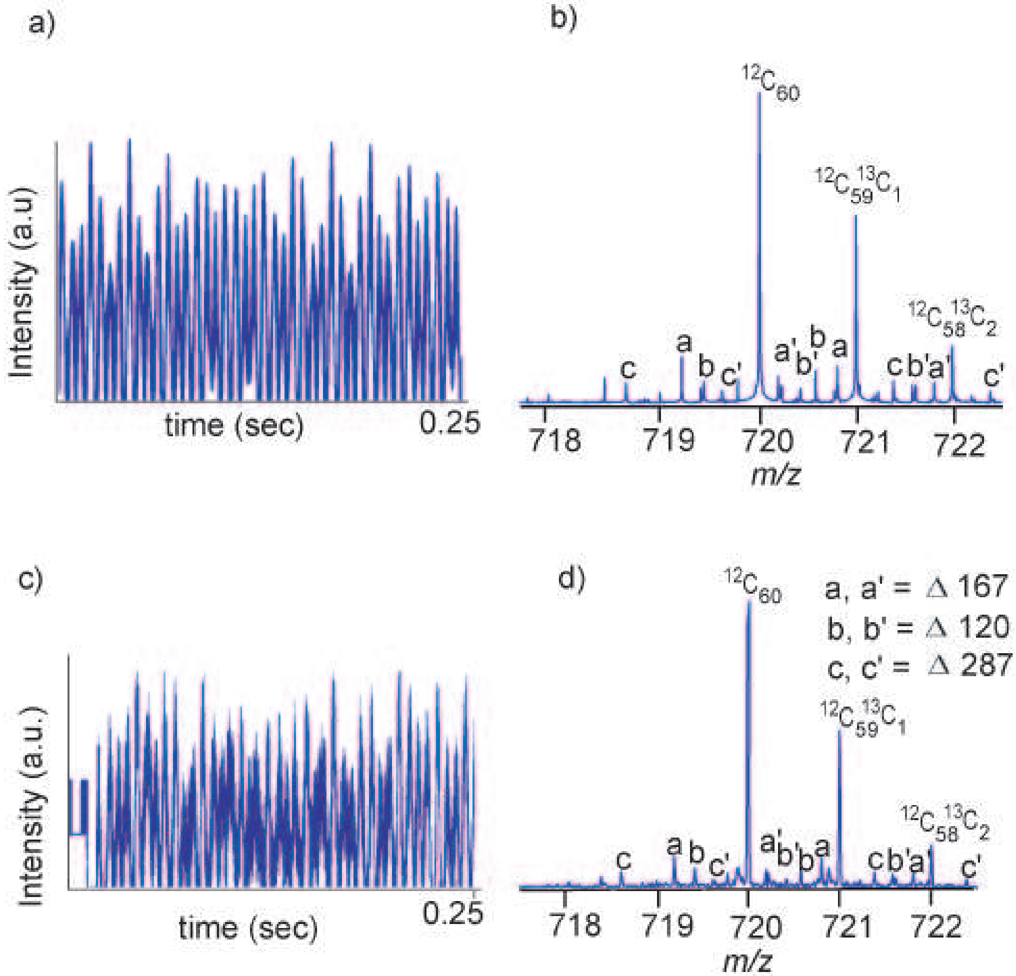

Figure 11·6: C_{60} transient with RFI at 120 Hz and 167 Hz. a) Simulated Transient clipped in negative half. b) Simulated MS showing peaks appearing at mixing frequencies of C_{60} isotopes and RFI signal. c) Experimental C_{60} transient obtained on MALDI-FTMS. d) Experimental MS obtained on MALDI-FTMS showing the intermodulation peaks.s

Chapter 12

Conclusions & Future Work

A Fourier Transform Mass Spectrometer (FTMS) that can reliably detect the presence of a single ion with unit charge in a sample can potentially revolutionize proteomics, and consequently our ability to discover new drugs for life-threatening diseases. One of the main challenges towards achieving this goal is the design of a low noise, wide-band, high gain amplifier that can work at cryogenic temperatures.

FTICRMS is based on the principle of inductive detection allowing longer observation times of the ions making it suitable for high precision experiments. The induced current on the detection electrodes (in the order of pA's) must be amplified using a transimpedance amplifier prior to digitization and data processing. The capacitance of the detection plates (20 pF) makes the task of designing a wide bandwidth, low noise amplifier non-trivial. Moreover, to reduce the thermal noise which is intrinsic to electrical devices the electrical circuit is to be cooled as close as to 0 K as possible. In conventional FTMS, cooling the electrical circuit turns out to be difficult, since a convenient thermal conductive path cannot be established between the coolant (liquid helium) and the electrical circuit, which is normally is situated in vacuum. However, in the design of the cryogenic FTICRMS developed at Boston University medical campus, the complete instrument is cooled to 4 K using liquid helium to reduce the base pressure (O'Connor, 2002). This new FTMS provided an opportunity for addressing the thermal noise issue using cryogenic electrical circuits. This dissertation is directed towards development of the cryogenic FTICRMS and the electronic components which were the part of this instrument.

The detection amplifiers have been designed with 2 stages: an in-vacuum preamplifier and an atmospheric pressure instrumentation amplifier. The detection of image current in the order of pA's requires minimization of leakage currents in the preamplifier input transistors. Both parameters, low noise and low leakage current, can be improved by cooling the amplifier circuit to cryogenic temperatures. Hence we have developed a low noise preamplifier which can be cooled to 4 Kelvin using GaAs MESFETs. In this research, 2 designs of such an amplifier circuit are developed, the room temperature version and the cryogenic version. The room temperature preamplifier uses low noise and low leakage Si-JFETs and the cryogenic version has GaAs MESFETs at its input stage. Performance of the room temperature design was evaluated on a custom MALDI-FTICRMS. Mass spectra of C60 desorbed using a ND-YAG laser showed a reduction in noise by 25 folds acquired using the room temperature amplifier as compared to the commercial Ionspec amplifier.

However development of a cryogenic amplifier is non-trivial and poses many challenges. One of the major limitation is the selection of the transistor. Low noise silicon JFETs do not work at 4 K and GaAs FETs which do, are generally fabricated for radio frequency applications in the GHz regime and mostly not suitable for FTICRMS frequency range (10 kHz - 1 MHz). Several tests on different versions of cryogenic preamplifier revealed that these RF devices are prone to oscillation at high frequencies and low temperature. The heat dissipation has to be minimized to limit the He boil-off. Conventional low noise Si transistors do not work at 4 K and moreover most of the electronic components such as capacitors and resistors do not function characteristically at cryogenic temperatures. Moreover, the layout of the components and traces requires careful mounting to prevent connection failures. In this doctoral work, we have resolved these issues, and developed and constructed such a cryogenic amplifier and characterize the resultant gain and noise performance in FTMS performance by conducting typical proteomic experiments. The cryogenic preamplifier designed in this work was mounted on the ICR cell, which is placed at 4 K. Mass spectra obtained from the cryogenic preamplifier are compared to the ones obtained previously with room temperature amplifier. The low temperature amplifier has shown a 25 times better SNR in a C60 mass spectrum obtained with similar experimental conditions.

The cryogenic preamplifier designed here showed superior performance, there are several improvements which are possible in the circuit.

- The GaAs MESFETs which are used here, are fabricated for microwave (GHz) applications and have small geometries with gate area $\approx 140 \mu m^2$. The 1/f noise cut-off frequency of these FETs is around 700 kHz, which appears in the bandwidth of interest in FTMS. Ideally, the gate area of the input FET for FTMS applications would be increased so that the input capacitance would match the capacitance of the detection plates, typically ≈10–15 pF; however, no such commercial FETs currently exist (Mathur et al., 2007). Larger FETs, such as the obsolete Sony 3SK164 exhibit lower 1/f noise and have shown ultra low noise performance at cryogenic temperatures (Lee, 1993). Moreover, the reduced leakage current of these Sony FETs (Alessandrello et al., 1990), would permit the use of a larger input bias resistor, thus reducing its noise contribution to a negligible level (Mathur et al., 2007). A collaboration has been set up with Dr. Randall Kirschman and GPD OptoElectronics (Salem, NH) to fabricate GaAs FETs for low frequency cryogenic applications. These FETs besides having larger geometry will have proprietary design features to achieve low noise.

- Further, in order to minimize the parasitic capacitance at the input terminals of the preamplifier, the FETs are being directly mounted onto the detect plates of the ICR cell. Finally, the cascode stage and the amplifier which use silicon-based components are being mounted inside a cold stage at temperatures around 80 K to reduce thermal noise.

- Various capacitors which are used on the cryogenic stage of the preamplifier and for RF coupling of inner trapping rings to excite plate, for linearizing the excitation field, failed to perform. The bypass capacitors supplied from Cryocircuits (Ballston Spa, NY), which are qualified for 4 K, are being added in the preamplifier circuit and on the ICR cell.

References

(2007). Online: http://machineshop.bu.edu/.

Aarstol, M. and Comisarow, M. B. (1987). Apodization of ft-icr spectra. *International Journal of Mass Spectrometry and Ion Processes*, 76:287–297.

Adamson, J. T. and Hakansson, K. (2007). Electron detachment dissociation of neutral and sialylated oligosaccharides. *Journal of the American Society for Mass Spectrometry*, 18(12):2162–2172.

Aebersold, R. and Mann, M. (2003). Mass spectrometry-based proteomics. *Nature*, 422(6928):198–207.

Aizikov, K. and O'Connor, P. B. (2006). Use of the filter diagonalization method in the study of space charge related frequency modulation in fourier transform ion cyclotron resonance mass spectrometry. *Journal of the American Society for Mass Spectrometry*, 17(6):836–843.

Alessandrello, A., Brofferio, C., Camin, D. V., Giuliani, A., Pessina, G., and Previtali, E. (1990). Cryogenic voltage-sensitive preamplifier using GaAs-Mesfets of low 1/f noise. *Nucl Instrum Meth A*, 295(3):405–410.

Amster, I. J. (1996). Fourier transform mass spectrometry. *Journal of Mass Spectrometry*, 31(12):1325–1337.

Analog Devices (2005). Online: http://www.analog.com/.

Anderson, G. A., Bruce, J. E., Hofstadler, S. A., Rockwood, A., and Smith, R. D. (1995). Low noise ICR detection electronics. In *43rd Annual Conference of the American Society for Mass Spectrometry*.

ASMS (2005). Online: http://www.asms.org".

Beavis, R. C. and Chait, B. T. (1990). Rapid, sensitive analysis of protein mixtures by mass-spectrometry. *Proceedings of the National Academy of Sciences of the United States of America*, 87(17):6873–6877.

Belov, M. E., Anderson, G. A., Wingerd, M. A., Udseth, H. R., Tang, K. Q., Prior, D. C., Swanson, K. R., Buschbach, M. A., Strittmatter, E. F., Moore, R. J., and Smith, R. D. (2004). An automated high performance capillary liquid chromatography-fourier transform ion cyclotron resonance mass spectrometer for high-throughput proteomics. *Journal of the American Society for Mass Spectrometry*, 15(2):212–232.

Belov, M. E., Zhang, R., Strittmatter, E. F., Prior, D. C., Tang, K., and Smith, R. D. (2003). Automated gain control and internal calibration with external ion accumulation capillary liquid chromatography-electrospray ionization-Fourier transform ion cyclotron resonance. *Analytical Chemistry*, 75(16):4195–4205.

Beu, S. C. and Laude, D. A. (1991). Modular data system for selective wave-form excitation and trapping experiments in Fourier-transform mass-spectrometry. *Analytical Chemistry*, 63(19):2200–2203.

Bodart, J. R., Garcia, B. M., Phelps, L., Sullivan, N. S., Moulton, W. G., and Kuhns, P. (1998). The effect of high magnetic fields on junction field effect transistor device performance. *Review of Scientific Instruments*, 69(1):319–320.

Brooks, D. (1998). Temperature rise in pcb traces. KeyWest, FL, USA. March 23-27, 1998.

Brown, L. S. and Gabrielse, G. (1986). Geonium theory: Physics of a single electron or ion in a Penning trap. *Review of Modern Physics*, 58:233–311.

Bruce, J. E., Anderson, G. A., Brands, M. D., Pasa-Tolic, L., and Smith, R. D. (2000). Obtaining more accurate fourier transform ion cyclotron resonance mass measurements without internal standards using multiply charged ions. *Journal of the American Society for Mass Spectrometry*, 11(5):416–421.

Budnik, B. A., Haselmann, K. F., and Zubarev, R. A. (2001). Electron detachment dissociation of peptide di-anions: an electron-hole recombination phenomenon. *Chemical Physics Letters*, 342(3-4):299–302.

Cermak, I. (2005). Compact radio-frequency power supply for ion and particle guides and traps. *Review of Scientific Instruments*, 76(6).

Comisarow, M. B. (1978). Signal modeling for ion cyclotron resonance. *Journal of Chemical Physics*, 69:4097–4104.

Comisarow, M. B. and Marshall, A. G. (1974). Frequency-sweep Fourier transform ion cyclotron resonance spectroscopy. *Chemical Physics Letters*, 26:489–490.

Comisarow, M. B. and Marshall, A. G. (1976). Theory of Fourier transform ion cyclotron resonance mass spectroscopy. *Journal of Chemical Physics*, 64:110–119.

Cooley, J. W. and Tukey, J. W. (1965). An algorithm for the machine calculation of complex Fourier series. *Math. Comput.*, 19:297301.

Cornell, E. A., Weisskoff, R. M., Boyce, K. R., Flanagan, R. W., Lafyatis, G. P., and Pritchard, D. E. (1989). Single-ion cyclotron-resonance measurement of M(CO+) M(N2+). *Physical Review Letters*, 63(16):1674–1677.

Cotter, R. J. (1997). *Time-of-flight mass spectrometry : instrumentation and applications in biological research.* American Chemical Society, Washington, DC.

Cronshaw, J. A., Krutchinsky, A. N., Zhang, W. Z., Chait, B. T., and Matunis, M. J. (2002). Proteomic analysis of the mammalian nuclear pore complex. *Journal of Cell Biology*, 158(5):915–927.

Difilippo, F., Natarajan, V., Bradley, M., Palmer, F., and Pritchard, D. (1995). Accurate Atomic Mass Measurements From Penning Trap Mass Comparisons Of Individual Ions. *Physica Scripta*, 63(9):144–154.

Dobson, C. M. (1999). Protein misfolding, evolution and disease. *Trends in Biochemical Sciences*, 24(9):329–332.

Duh, K., Pospieszalski, M., Kopp, W., Ho, P.and Jabra, A., & Chao, P., Smith, P., Lester, L., Ballingall, J., Weinreb, S., and Lee, A. T. (1988). Ultra-low-noise cryogenic high-electron-mobility transistors. *IEEE Transactions on Electron Devices*, 35(3):249 − 256.

Easterling, M. L., Mize, T. H., and Amster, I. J. (1999). Routine part-per-million mass accuracy for high-mass ions: Space-charge effects in maldi ft-icr. *Analytical Chemistry*, 71(3):624–632.

Elliot, R. The design of heat sinks. *"White Paper, Elliot Sound Products"*.

Eudyna Devices, Inc. (2005). Online: http://www.us.eudyna.com/.

Fourier, J. B. J. (1878). *The Analytical Theory of Heat.* Cambridge University Press, London.

Francl, T., Sherman, M. G., Hunter, R. L., Locke, M. J., Bowers, W. D., and McIver, R. T. (1983). Experimental determination of the effects of space charge on ion cyclotron resonance frequencies. *International Journal of Mass Spectrometry and Ion Processes*, 54:189–199.

Friar, M. E. and McClurg, R. H. (December 6, 1968). Printed circuits and high currents. *Design News*, 23:102–107.

Gabrielse, G., Fei, X., Orozco, L. A., Tjoelker, R. L., Haas, J., Kalinowsky, H., Trainor, T. A., and Kells, W. (1990a). Thousandfold improvement in the measured antiproton mass. *Physical Review Letters*, 65(11):1317–1320.

Gabrielse, G., Fei, X., Orozco, L. A., Tjoelker, R. L., Haas, J., Kalinowsky, H., Trainor, T. A., and Kells, W. (1990b). Thousandfold improvement in the measured antiproton mass. *Physical Review Letters*, 65(11):1317–1320.

Gao, H. Y., Shen, Y. F., Veenstra, T. D., Harkewicz, R., Anderson, G. A., Bruce, J. E., Pasa-Tolic, L., and Smith, R. D. (2000). Two-dimensional electrophoretic/chromatographic separations combined with electrospray ionization fticr mass spectrometry for high throughput proteome analysis. *Journal of Microcolumn Separations*, 12(7):383–390.

Gerald Gabrielse (2005). Online: http://www.physics.harvard.edu/gabrielse.htm.

Gerlich, D. (1992). Inhomogeneous rf fields: A versatile tool for the study of processes with slow ions. In *State-Selected and State-To-State Ion-Molecule Reaction Dynamics*, volume LXXXII of *Advances in Chemical Physics*, pages 1–176. John Wiley and Sons, Inc.

Gray, P., Hurst, P., Lewis, S., and Meyer, R. (2001). *"Analysis and Design of Analog Integrated Circuits"*. Wiley.

Gregg, J., Morris, I. D., and Wells, M. R. (1987). Cryogenic GaAs MESFET magnetic resonance spectrometer for use from 500 MHz to 3 GHz. *Journal of Physics E: Scientific Instruments*, 20:1223 – 1227.

Grosshans, P. B., Shields, P. J., and Marshall, A. G. (1990). Simple and accurate determination of ion translational energy in ion cyclotron resonance mass spectrometry. *Journal of the American Chemical Society*, 112:1275–1277.

Grosshans, P. B., Shields, P. J., and Marshall, A. G. (1991). Comprehensive theory of the Fourier transform ion cyclotron resonance signal for all ion trap geometries. *Journal of Chemical Physics*, 94:5341–5352.

Gygi, S. P., Han, D. K., Gingras, A. C., Sonenberg, N., and Aebersold, R. (1999). Protein analysis by mass spectrometry and sequence database searching: tools for cancer research in the post-genomic era. *Electrophoresis*, 20(2):310–319.

Hall, E. (1879). On a new action of the magnet on electric currents. *American Journal of Mathematics*, 2:287–292.

Hanyu, I., Asai, S., Nunokawa, M., Joshin, K., Hirachi, Y., Ohmura, S., Aoki, Y., and Aigo, T. (1988). Super Low-Noise HEMTs With A T-Shaped Wsix Gate. *Electronics Letters*, 24(21):1327–1328.

Harry, J. L., Wilkins, M. R., Herbert, B. R., Packer, N. H., Gooley, A. A., and Williams, K. L. (2000). Proteomics: Capacity versus utility. *Electrophoresis*, 21(6):1071–1081.

Henzel, W. J., Billeci, T. M., Stults, J. T., Wong, S. C., Grimley, C., and Watanabe, C. (1993). Identifying proteins from 2-dimensional gels by molecular mass searching of peptide-fragments in protein-sequence databases. *Proceedings of the National Academy of Sciences of the United States of America*, 90(11):5011–5015.

Hofstadler, S. A., Bruce, J. E., Rockwood, A. L., Anderson, G. A., Winger, B. E., and Smith, R. D. (1994). Isotopic beat patterns in Fourier transform ion cyclotron resonance mass spectrometry - implications for high resolution mass measurements of large biopolymers. *International Journal of Mass Spectrometry & Ion Processes*, 132(1-2):109–127.

Hofstadler, S. A., Wu, Q. Y., Bruce, J. E., Chen, R. D., and Smith, R. D. (1995). Enhanced accumulated trapping efficiency using an auxiliary trapping electrode in an external source fourier-transform ion-cyclotron resonance mass-spectrometer. *International Journal of Mass Spectrometry*, 142(3):143–150.

Horn, D. M., Zubarev, R. A., and McLafferty, F. W. (2000). Automated reduction and interpretation of high resolution electrospray mass spectra of large molecules. *Journal of the American Society for Mass Spectrometry*, 11(4):320–332.

Hu, B. H. and Yang, C. H. (2005). A cryogenic voltage amplifier with 36 MHz bandwidth using discrete GaAs metal-semiconductor field-effect transistors. *Review of Scientific Instruments*, 76(12).

Hu, Q., Noll, R. J., Li, H., Makarov, A., Hardman, M., and Graham Cooks, R. (2005). The orbitrap: a new mass spectrometer. *Journal of Mass Spectrometry*, 40(4):430–43.

Industries", A. C. E. Ipc - 2221a. generic standard on printed circuit board design.

Instruments, O. (2000). *Practical Cryogenics: An introduction to laboratory cryogenics*. Oxford Instruments Superconductivity Limited.

Itoh, Y., Nakahara, K.and Sakura, T., Yoshida, N., & Katoh, T., Takagi, T., and Ito, Y. (1995). W-band monolithic low noise amplifiers for advanced microwave scanning radiometer. *IEEE Microwave and Guided Wave Letters*, 5(2):59–61.

Jefferts, S. R. and Walls, F. L. (1987). A low-noise cascode amplifier. *Journal of Research of the National Bureau of Standards*, 92(6):383–386.

Jensen, O. N., Podtelejnikov, A. V., and Mann, M. (1997). Identification of the components of simple protein mixtures by high accuracy peptide mass mapping and database searching. *Analytical Chemistry*, 69(23):4741–4750.

Johnson, J. B. (1928). Thermal agitation of electricity in conductors. *Physical Review*, 32:97–109.

Jones, R. M., Gerlich, D., and Anderson, S. L. (1997). Simple radio-frequency power source for ion guides and ion traps. *Review of Scientific Instruments*, 68(9):3357–3362.

Jonsher, A. (1964). Semiconductors at cryogenic temperatures. *Proceedings of the IEEE*, 52(3):1092–1104.

Joshin, K., Mimura, T., Morei, M., Yamashita, Y., Kosemura, K., and J., S. (1983). Noise performance of microwave HEMT. pages 563–565, Boston, MA.

Kelly, J. W. (1998). The alternative conformations of amyloidogenic proteins and their multi-step assembly pathways. *Current Opinion in Structural Biology*, 8(1):101–106.

Keyes, R. W. (1977). Semiconductor devices at low temperature. *Comments on Solid State Physics*, 8(3):47–53.

Kirschman, R. K. (1986). *Low-Temperature Electronics*. IEEE Press.

Kirschman, R. K., Lemoff, S., and Lipa, J. (1992). Evaluation of GaAs FETs for crogenic readout. In *Proceedings of SPIE*, volume 1684, pages 110–130. Infrared Readout Electronics.

Kok, Y., Wang, H., Huang, T., Lai, R., Barsky, M., Chen, Y., & Sholley, M., Block, T., Streit, D., Allen, B., Samoska, L., and Gaier, T. (1999). 160-190-GHz monolithic low-noise amplifiers. *IEEE Microwave and Guided Wave Letters*, 9(8):311 – 313.

Krutchinsky, A. N. and Chait, B. T. (2002). On the nature of the chemical noise in maldi mass spectra. *Journal of the American Society for Mass Spectrometry*, 13(2):129–134.

Kwon, Y., Deakin, D., Sovero, E., and Higgins, J. (1996). High-performance Ka-band monolithic low-noise amplifiers using & 0.2-m dry-recessed GaAs PHEMTs. *IEEE Microwave and Guided Wave Letters*, 6(7):253 – 255.

Lawrence, E. O. and Livingston, M. S. (1932). The cyclotron. *Phys Rev*, 40:19.

Ledford, E. B., J., Rempel, D. L., and Gross, M. L. (1984). Mass calibration law for quadrupolar potential. *Analytical Chemistry*, 56:2744–2748.

Lee, A. T. (1989). Broadband cryogenic preamplifier incorporating GaAs MESFETs for use with low-temperature particle detectors. *Review of Scientific Instruments*, 80(10):3315–3322.

Lee, A. T. J. (1993). A low-power-dissipation broad-band cryogenic preamplifier utilizing GaAs-MESFETs in parallel. *Review of Scientific Instruments*, 64(8):2373–2378.

Lee, S. How to select a heat sink. *"White Paper, Aavid Thermalloy, Inc."*.

Lee, S. (1995). Optimum design and selection of heat sinks. *"IEEE Transactions on Components Packaging and Manufacturing Technology Part A"*, 18(4):812–817.

Lee, W. C. and Lee, K. H. (2004). Applications of affinity chromatography in proteomics. *Analytical Biochemistry*, 324(1):1–10.

Levinzon, F. A. (2000). Noise of the jfet amplifier. *IEEE Transactions on Circuits and Systems I-Fundamental Theory and Applications*, 47(7):981–985.

Lilienfeld, J. E. (1930). Method and apparatus for controlling electric currents. us patent 1877140.

Limbach, P. A., Grosshans, P. B., and Marshall, A. G. (1993). Experimental determination of the number of trapped ions, detection limit, and dynamic range in FT/ICR/MS. *Analytical Chemistry*, 65:135–140.

Lin, C., Mathur, R., Aizikov, K., and O'Connor, P. B. (2007). First signal on the cryogenic Fourier-Transform ion cyclotron resonance mass spectrometer. *Journal of the American Society for Mass Spectrometry*.

Maier, C. S., Yan, X. G., Harder, M. E., Schimerlik, M. I., Deinzer, M. L., Pasa-Tolic, L., and Smith, R. D. (2000). Electrospray ionization fourier transform ion cyclotron resonance mass spectrometric analysis of the recombinant human macrophage colony stimulating factor beta and derivatives. *Journal of the American Society for Mass Spectrometry*, 11(3):237–243.

Mann, M., Hojrup, P., and Roepstorff, P. (1993). Use of mass spectrometric molecular weight information to identify proteins in sequence databases. *Biological Mass Spectrometry*, 22(6):338–345.

March, R. E. and Todd, J. F. J. (2005). *Quadrupole ion trap mass spectrometry*. Wiley-Interscience, Hoboken, N.J., 2nd edition.

Marshall, A. G. and Comisarow, M. B. (1974). Fourier transform ion cyclotron mass spectroscopy. *Chemical Physics Letters*, 25:282–283.

Marshall, A. G. and Guan, S. H. (1996). Advantages of high magnetic field for Fourier transform ion cyclotron resonance mass spectrometry. *Rapid Commnications in Mass Spectrometry*, 10(14):1819–1823.

Marshall, A. G., Hendrickson, C. L., and Jackson, G. S. (1998). Fourier transform ion cyclotron resonance mass spectrometry - a primer. *Mass Spectrom Rev*, 17(1):1–35.

Marshall, A. G. and Verdun, F. R. (1990). Fourier transforms in NMR, optical, and mass spectrometry. pages 247–253. Elsevier, Amsterdam, The Netherlands.

Marshall, A. G., Wang, T. C. L., and Ricca, T. L. (1985). Tailored excitation for fourier-transform ion-cyclotron resonance mass-spectrometry. *Journal of the American Chemical Society*, 107(26):7893–7897.

Martinovic, S., Berger, S. J., Pasa-Tolic, L., and Smith, R. D. (2000). Separation and detection of intact noncovalent protein complexes from mixtures by on-line capillary isoelectric focusing-mass spectrometry. *Analytical Chemistry*, 72(21):5356–5360.

Mathur, R., Knepper, R. W., and O'Connor, P. B. (2007). A low-noise, wideband preamplifier for a Fourier tranform ion cyclotron resonance mass spectrometer. *Journal of the American Society for Mass Spectrometry*, 77(11):114101.

Mathur, R. and O'Connor, P. B. (2006). Design and implementation of a high power rf oscillator on a printed circuit board for multipole ion guides. *Review of Scientific Instruments*, 77(11).

McIver, R. T., J. U.S.A. Patent No. 4,523,235. Technical report. Apparatus and Method for Injection of Ions into an Ion Cyclotron Resonance Cell.

McLafferty, F. W. and Turecek (1993). *Interpretation of Mass Spectra.* University Science Books.

Miller, J. M. (1920). Dependence of the input impedance of a three-electrode vacuum tube upon the load in the plate circuit. *Scientific Papers of the Bureau of Standards*, 15(351):367–385.

Mize, T. H., Taban, I., Duursma, M., Seynen, M., Konijnenburg, M., Vijftigschild, A., Doornik, C. V., Rooij, G. V., and Heeren, R. M. A. (2004). A modular data and control system to improve sensitivity, selectivity, speed of analysis, ease of use, and transient duration in an external source FTICR-MS. *International Journal of Mass Spectrometry*, 235(3):243–253.

Moore, J. H., Davis, C. C., and Coplan, M. A. (2002). *Bulding Scientific Apparatus.* Westview.

Nettleton, E. J., Sunde, M., Lai, Z. H., Kelly, J. W., Dobson, C. M., and Robinson, C. V. (1998). Protein subunit interactions and structural integrity of amyloidogenic transthyretins: Evidence from electrospray mass spectrometry. *Journal of Molecular Biology*, 281(3):553–564.

Neubauer, G., Gottschalk, A., Fabrizio, P., Seraphin, B., Luhrmann, R., and Mann, M. (1997). Identification of the proteins of the yeast u1 small nuclear ribonucleoprotein complex by mass spectrometry. *Proceedings of the National Academy of Sciences of the United States of America*, 94(2):385–390.

Nikolaev, E. N. and Gorshkov, M. V. (1985). Dynamics of ion motion in an elongated cylindrical cell of an ICR spectrometer and the shape of the signal registered. *International Journal of Mass Spectrometry and Ion Processes*, 64(2):115–125.

O'Connor, P. B. (2002). Considerations for design of a Fourier transform mass spectrometer in the 4.2 K cold bore of a superconducting magnet. *Rapid Commnications in Mass Spectrometry*, 16(12):1160–1167.

O'Connor, P. B., Budnik, B. A., Ivleva, V. B., Kaur, P., Moyer, S. C., Pittman, J. L., and Costello, C. E. (2004). A high pressure matrix-assisted laser desorption ion source for Fourier transform mass spectrometry designed to accommodate large targets with diverse surfaces. *Journal of the American Society for Mass Spectrometry*, 15(1):128–32.

O'Connor, P. B., Costello, C. E., and Earle, W. E. (2002). A high voltage rf oscillator for driving multipole ion guides. *Journal of the American Society for Mass Spectrometry*, 13(12):1370–1375.

O'Connor, P. B., Pittman, J. L., Thomson, B. A., Budnik, B. A., Cournoyer, J. C., Jebanathirajah, J., Lin, C., Moyer, S., and Zhao, C. (2006). A new hybrid electrospray fourier transform mass spectrometer: design and performance characteristics. *Rapid Commnications in Mass Spectrometry*, 20(2):259–266.

Pan, T. Y., Poulson, R. H., and Blair, H. D. (1993). Current carrying capacity of copper conductors in printed wiring boards. pages 1061–1066, Orlando, FL; USA. June 01-04, 1993.

Pease Bob (1993). EDN Design News:What's All This Femtoampere Stuff, Anyhow?

Pitsenberger, C. C., Easterling, M. L., and Amster, I. J. (1996). Efficient ion remeasurement using broadband quadrupolar excitation FTICR mass spectrometry. *Analytical Chemistry*, 68(21):3732–3739.

Pospieszalski, M. and S., W. (1987). FETs and HEMTs at cryogenic temperatures - their properties and use in low-noise amplifiers. In *IEEE MTT-S International Microwave Symposium Digest.*, pages 955–958, Boston, MA.

Pospieszalski, M. and Wollack, E. (2000). Ultra-low-noise, InP field effect transistor radio astronomy receivers: state-of-the-art. volume 3, pages 23–32.

Pospieszalski, M., Wollack, E., Bailey, N., & Thacker, D., Webber, J., Nguyen, L., Le, N., and Lui, M. (2000). Design and performance of wideband, low-noise, millimeter-wave amplifiers for & Microwave Anisotropy Probe radiometers. volume 1, pages 25–28.

Prance, R., Long, A., and Goodall, F. (1982). UHF ultra-low-noise cryogenic FET preamplifier. *Journal of Physics E:Scientific Instruments*, 15.

Qian, W. J., Jacobs, J. M., Liu, T., Camp, D. G., and Smith, R. D. (2006). Advances and challenges in liquid chromatography-mass spectrometry-based proteomics profiling for clinical applications. *Molecular & Cellular Proteomics*, 5(10):1727–1744.

Ramsey, R. S., Goeringer, D. E., and Mcluckey, S. A. (1993). Active-chemical background-noise reduction in capillary electrophoresis/ion trap mass-spectrometry. *Analytical Chemistry*, 65(23):3521–3524.

Reinders, J., Lewandrowski, U., Moebius, J., Wagner, Y., and Sickmann, A. (2004). Challenges in mass spectrometry-based proteomics. *Proteomics*, 4(12):3686–3703.

Risacher, C. and Belitsky, V. (2003). GaAs HEMT Low-Noise Cryogenic Amplifiers from C-Band to X-Band with & 0.7K/GHz Noise Temperature. *IEEE Microwave and Guided Wave Letters*, 13(3).

Schottky, W. (1918). Über spontane stromschwankungen in verschiedenen elektrizitätsleitern. *Annaleu du Physik*, 57:541–548.

Senko, M. W., Canterbury, J. D., Guan, S. H., and Marshall, A. G. (1996). A high-performance modular data system for fourier transform ion cyclotron resonance mass spectrometry. *Rapid Communications in Mass Spectrometry*, 10(14):1839–1844.

Senko, M. W., Hendrickson, C. L., Emmett, M. R., Shi, S. D. H., and Marshall, A. G. (1997). External accumulation of ions for enhanced electrospray ionization fourier transform ion cyclotron resonance mass spectrometry. *Journal of the American Society for Mass Spectrometry*, 8(9):970–976.

Shen, Y. F., Berger, S. J., Anderson, G. A., and Smith, R. D. (2000). High-efficiency capillary isoelectric focusing of peptides. *Analytical Chemistry*, 72(9): 2154–2159.

Shen, Y. F. and Smith, R. D. (2000). High-resolution capillary isoelectric focusing of proteins using highly hydrophilic-substituted cellulose-coated capillaries. *Journal of Microcolumn Separations*, 12(3):135–141.

Shen, Y. F., Zhao, R., Belov, M. E., Conrads, T. P., Anderson, G. A., Tang, K. Q., Pasa-Tolic, L., Veenstra, T. D., Lipton, M. S., Udseth, H. R., and Smith, R. D. (2001). Packed capillary reversed-phase liquid chromatography with high-performance electrospray ionization fourier transform ion cyclotron resonance mass spectrometry for proteomics. *Analytical Chemistry*, 73(8):1766–1775.

Shi, S. D. H., Hendrickson, C. L., and Marshall, A. G. (1998). Counting individual sulfur atoms in a protein by ultrahigh-resolution fourier transform ion cyclotron resonance mass spectrometry - experimental resolution of isotopic fine structure in proteins. *Proceedings of the National Academy of Sciences of the United States of America*, 95(20):11532–11537.

Shockley, W. (1938). Currents to conductors induced by a moving point charge. *Journal of Applied Physics*, 9(10):635–636.

Shumaker, J., Basset, R., and Skuratov, A. (2001). High-power GaAs FET amplifiers: Push-pull versus balanced configurations. wcdma 2.11-2.17 GHz, 150w amplifiers. In *Wireless Symposium*.

Smith, C. D., Carney, J. M., Starkereed, P. E., Oliver, C. N., Stadtman, E. R., Floyd, R. A., and Markesbery, W. R. (1991). Excess brain protein oxidation and enzyme dysfunction in normal aging and in alzheimer-disease. *Proceedings of the National Academy of Sciences of the United States of America*, 88(23):10540–10543.

Smith, R. D. (2000). Probing proteomes - seeing the whole picture? *Nature Biotechnology*, 18(10):1041–1042.

Stadtman, E. R. and Berlett, B. S. (1998). Reactive oxygen-mediated protein oxidation in aging and disease. *Drug Metabolism Reviews*, 30(2):225–243.

Tanskanen, J., Kangaslahti, P., Ahtola, H., Jukkala, P., & Karttaavi, T., Lahdes, M., Varis, J., and Tuovinen, J. (2000). Cryogenic indium-phosphide HEMT low-noise amplifiers at V-band. *IEEE Transactions on Microwave Theory and Techniques*, 48(7):1283 – 1286.

Texas Instruments (2005). Online: http://www.ti.com.

Thomas, P. J., Qu, B. H., and Pedersen, P. L. (1995). Defective protein-folding as a basis of human-disease. *Trends in Biochemical Sciences*, 20(11):456–459.

Tonge, R., Shaw, J., Middleton, B., Rowlinson, R., Rayner, S., Young, J., Pognan, F., Hawkins, E., Currie, I., and Davison, M. (2001). Validation and development of fluorescence two-dimensional differential gel electrophoresis proteomics technology. *Proteomics*, 1(3):377–396.

Valaskovic, G. A., Kelleher, N. L., Little, D. P., Aaserud, D. J., and Mclafferty, F. W. (1995). Attomole-sensitivity electrospray source for large-molecule mass-spectrometry. *Analytical Chemistry*, 67(20):3802–3805.

Van Der Ziel, A. (1970). *Noise: Sources, Characterization, measurement.* Prentice-Hall.

Wang, H., Lai, R., Kok, Y.-L., Huang, T.-W., Aust, M., & Chen, Y., Siegel, P., Gaier, T., Dengler, R., and Allen, B. (1998). A 155-GHz monolithic low-noise amplifier. *IEEE Transactions on Microwave Theory and Techniques*, 46(11):1660 – 1666.

Warrick, J. M., Chan, H. Y. E., Gray-Board, G. L., Chai, Y. H., Paulson, H. L., and Bonini, N. M. (1999). Suppression of polyglutamine-mediated neurodegeneration in drosophila by the molecular chaperone hsp70. *Nature Genetics*, 23(4):425–428.

Weinreb, S. (1980). Low-noise cooled GaAs FET amplifiers. *IEEE Transactions on Microwave Theory and Techniques*, 28(10):1041 – 1054.

Weinreb, S., Fenstermacher, D., and Harris, R. (1982). Ultra-low-noise 1.2- to 1.7-GHz cooled GaAs FET amplifiers. *IEEE Transactions on Microwave Theory and Techniques*, 82(6):849 – 853.

Weisskoff, R. M., Lafyatis, G. P., Boyce, E. A., Cornell, R., Flangan, J., and Pritchard, D. E. (1988). rf SQUID detector for single-ion trapping experiments. *Journal of Applied Physics*, 63(9):4599–4604.

Wenger, J., Narozny, P., Dambkes, H., Splettstosser, J., and Werres, C. (1991). Dual gate cascode MESFETs and HEMTs with very high gain at low noise levels. London.

Williams, J. (1998). *The Art and Science of Analog Circuit Design.* Newnes.

Wilm, M., Shevchenko, A., Houthaeve, T., Breit, S., Schweigerer, L., Fotsis, T., and Mann, M. (1996). Femtomole sequencing of proteins from polyacrylamide gels by nano-electrospray mass spectrometry. *Nature*, 379(6564):466–469.

Winger, B. E., Hofstadler, S. A., Bruce, J. E., Udseth, H. R., and Smith, R. D. (1993). High-resolution accurate mass measurements of biomolecules using a new electrospray ionization ion cyclotron resonance mass spectrometer. *Journal of the American Society for Mass Spectrometry*, 4(7):566–577.

Yang, C. H. and Change, T. (2002). A low noise transimpedance amplifier for cryogenically cooled quartz tunig fork sensors. *Review of Scientific Instruments*, 73(7):2713–2716.

Zhang, L. K., Rempel, D., Pramanik, B. N., and Gross, M. L. (2005). Accurate mass measurements by Fourier transform mass spectrometry. *Mass Spectrometry Reviews*, 24(2):286–309.

CURRICULUM VITAE

Raman Mathur

Raman Mathur

Boston University, Department of Electrical & Computer Engineering

Email: rmathur@bu.edu **Phone:** 617-414-8234

Education

Ph.D., Electrical Engineering, expected May 2008
Boston University.

M.S., Computer Engineering, May 2003
Boston University.

B.E., Electrical Engineering, May 2000
M.B.M. Engineering College.

Peer-Reviewed Journal Publications

- M. G. Karpovsky, M. Mustafa, R. Mathur, "Fault-tolerant Unicast Wormhole Routing in Irregular Computer Networks", Proc. Of the 14th IASTED International Conference on Parallel and Distributed Computing and Systems, Cambridge, July 2002.
- R. Mathur, P.B. O'Connor, "Design and Implementation of a High Power rf Oscillator on a Printed Circuit Board", Review of Scientific Instruments, Vol.77 , 114101 (2006).
- Raman Mathur, Ronald W. Knepper, Peter B. O'Connor, "A Cryogenic Preamplifier for Fourier Transform Mass Spectrometer", Proc. Of the WOLTE-7, Noordwijk, June 2006.
- Raman Mathur, Ronald W. Knepper and Peter B. OConnor, "A Low-Noise, Wideband Preamplifier for a Fourier-Transform Ion Cyclotron Resonance Mass Spectrometer", Journal of American Society of Mass Spectrometry, Vol. 18, 12, 2233-2241 (2007).
- Cheng Lin, Raman Mathur, Kostantin Aizikov and Peter B. OConnor, "First Signal on the Cryogenic Fourier-Transform Ion Cyclotron Resonance Mass Spectrometer", Journal of American Society of Mass Spectrometry, Vol. 18, 12, 2090-2093 (2007).
- Raman Mathur, Ronald W. Knepper and Peter B. OConnor, "A Low Noise, Broadband Cryogenic Preamplifier operated in a High Field Superconducting Magnet", Submitted to IEEE transactions of applied superconductivity.
- R. Mathur, P.B. O'Connor, "Artifacts in Fourier Transform Mass Spectrometry", Submitted to Rapid Communications in Mass Spectrometry.

Invited Talks At National/International Conferences

- Raman Mathur. "Low Noise Amplifier for Cryogenic Fourier Transform Mass Spectrometry", Guest lecture at University of Bridgeport, School of Engineering, Bridgeport, CT, April 2007.
- Raman Mathur. "Design and testing of new high performance amplifier for Fourier Transform Mass Spectrometry", 9th NHLBI Proteomics Initiative Investigators Meeting, Boston, MA, April 2007.
- Raman Mathur, Ronald W. Knepper, Peter B. O'Connor, "Cryogenic Detection Circuit for a Fourier Transform Mass Spectrometer", IMAPS 2nd Advanced Technology Workshop on Reliability of Advanced Electronic Packages and Devices in Extreme Cold Environments, Arcadia, CA, Feb. 2007.
- Raman Mathur, Ronald W. Knepper, Peter B. O'Connor, "A Cryogenic Preamplifier for Fourier Transform Mass Spectrometer", 7th Workshop on Low Temperature Electronics, ESA/ESTEC Amsterdam, Netherlands, June 2006.
- Raman Mathur, Mark Karpovsky. "Fault Tolerant Routing in Computer Networks", The IASTED conference on Parallel and Distributed Computing Systems, Cambridge, MA, April 2002.

Poster Presentations At National/International Conferences

- Raman Mathur, Ronald W. Knepper, Peter B. O'Connor, "Low Noise High Performance Preamplifiers for Non-Destructive Detection of Ions in Precision Mass Spectrometry", 55th American Conference on Mass Spectrometry, Indianapolis, IN, May 2007.
- Raman Mathur, Ronald W. Knepper, Peter B. O'Connor, "A Low Noise Amplifier for Cryogenic Fourier Transform Mass Spectrometry", 6th North American FT-ICR MS Conference, Tahoe City, CA, April 2007.
- Raman Mathur, Ronald W. Knepper, Peter B. O'Connor, "A Comprehensive Design of the Electronics for the Cryogenic Fourier Transform Mass Spectrometry", 54th American Conference on Mass Spectrometry, Seattle, WA, May 2006.
- Raman Mathur, Ronald W. Knepper, Peter B. O'Connor, "A Low Noise Cryogenic Preamplifier for Fourier Transform Mass Spectrometer", 53rd American Conference on Mass Spectrometry, San Antonio, TX, May 2005.
- Raman Mathur, Ronald W. Knepper, Peter B. O'Connor, "A Low Noise Wideband Transimpedance Amplifier for Fourier Transform Mass Spectrometer", Boston University Science Day, Boston, MA, April 2005.
- Raman Mathur, Jason L. Pittman, Peter B. O'Connor, "Initial Design and Implementation of a Cryogenic Preamplifier for FTICRMS", 52nd American Conference on Mass Spectrometry, Nashville, TN, May 2004.

Technical Experience

- Electrical Design: Low noise circuits, cryogenic electronic design, RF and high voltage circuit design, etc.

- EDA Tools: Analog (Capture CIS, PSpice, TINA); PCB (Layout Plus, Allegro, Eagle); VLSI (Virtuoso, Magic, Spectre-RF); Virtual Instrumentation (LABVIEW, HPVEE); Verilog-XL.
- Programming: C, MATLAB, Unix shell scripts, TCL, HTML, etc.
- Other Tools: SIMION, 3D Autodesk Inventor.

Awards And Honors

- American Society of Mass Spectrometry Student Travel Award. (2005, 2006 and 2007).
- European Space Agency Student Travel Grant. (2006)
- Student Award, North American FT-ICR MS Conference (2007)

Professional Associations

- American Society of Mass Spectrometry.
- Institute of Electrical and Electronics Engineer.

April 13, 2008